The Yaou and Couriège gold mineralisations (Guiana Shield) : from primary enrichment to secondary processes

Vincent Combes

Ecole Doctorale SIReNa
Sciences et Ingénierie des Ressources Naturelles

THÈSE

Présentée pour l'obtention du grade de

Docteur de l'Université de Lorraine

Spécialité Géosciences

par

Vincent COMBES

Les minéralisations aurifères de Yaou et Couriège (Bouclier Guyanais) : des modalités de l'enrichissement primaire aux processus secondaires

Soutenue publiquement le 16 décembre 2020

Membres du Jury

Alain Chauvet, Directeur de Recherche, Géosciences Montpellier, CNRS	Rapporteur
Dominique Chardon, Directeur de Recherche, GET Toulouse, IRD	Rapporteur
Taija Torvela, Lecturer, School of Earth and Environment, University of Leeds	Examinatrice
Michel Cathelineau, Directeur de Recherche, GeoRessources, CNRS	Examinateur
Arnauld Heuret, Maître de Conférences, Université de Guyane	Invité
Pierre Gibert, Docteur, Auplata Mining Group	Invité
Anne-Sylvie André-Mayer, Professeur, GeoRessources, Univ. Lorraine	Directrice de thèse
Aurélien Eglinger, Maître de Conférences, GeoRessources, Univ. Lorraine	Co-directeur de thèse
Yoram Teitler, Docteur en Géosciences, GeoRessources, Université de Lorraine	Invité

Université de Lorraine - UMR 7359 GeoRessources - CREGU

Ecole Doctorale SIReNa
Sciences et Ingénierie des Ressources Naturelles

THÈSE

Présentée pour l'obtention du grade de

Docteur de l'Université de Lorraine

Spécialité Géosciences

par

Vincent COMBES

Les minéralisations aurifères de Yaou et Couriège (Bouclier Guyanais) : des modalités de l'enrichissement primaire aux processus secondaires

Soutenue publiquement le 16 décembre 2020

Membres du Jury

Alain Chauvet, Directeur de Recherche, Géosciences Montpellier, CNRS	Rapporteur
Dominique Chardon, Directeur de Recherche, GET Toulouse, IRD	Rapporteur
Taija Torvela, Lecturer, School of Earth and Environment, University of Leeds	Examinatrice
Michel Cathelineau, Directeur de Recherche, GeoRessources, CNRS	Examinateur
Arnauld Heuret, Maître de Conférences, Université de Guyane	Invité
Pierre Gibert, Docteur, Auplata Mining Group	Invité
Anne-Sylvie André-Mayer, Professeur, GeoRessources, Univ. Lorraine	Directrice de thèse
Aurélien Eglinger, Maître de Conférences, GeoRessources, Univ. Lorraine	Co-directeur de thèse
Yoram Teitler, Docteur en Géosciences, GeoRessources, Université de Lorraine	Invité

Université de Lorraine - UMR 7359 GeoRessources - CREGU

Résumé

Les minéralisations aurifères situées en Guyane (France, Amérique du Sud) sont localisées au sein de terrains d'âge rhyacien (2.3-2.05 Ga), témoins de l'orogenèse Transamazonienne. Ces gisements du Bouclier Guyanais sont masqués par une forêt dense sous laquelle des profils latéritiques bien développés laissent peu d'affleurement de roche non altérée (« *bedrock* »). Considérant ce contexte spécifique, cette thèse s'intéresse à définir (i) quels sont les processus de minéralisation d'or primaire et (ii) quel est leur préservation et enrichissement (ou non) au cours des processus supergènes secondaires et se base sur deux sites d'étude : le gisement de Yaou et le prospect de Couriège. L'approche scientifique retenue pour ces travaux de thèse est celle du système métallogénique qui nécessite une intégration dans le temps, dans l'espace et à différentes échelles des processus géologiques et métallogéniques. Ainsi, cette thèse intègre différentes disciplines des géosciences à savoir la géologie structurale (et microstructurale), la métallographie, la pétrographie, la géochimie, la géochronologie et la géophysique pour étudier la formation de ces objets minéralisés (primaires et secondaires), caractériser leur typologie et discuter des processus métallogéniques associés.

À Yaou, des corps intrusifs (quartz monzodiorite), encaissant principalement la minéralisation aurifère, sont alignés le long d'une zone de cisaillement à cinématique sénestre affectant un ensemble volcano-sédimentaire. Une évolution tectono-magmatique polyphasée, impliquant 5 phases de déformation, est proposée à l'échelle du camp minéralisé. Sont associés à cette séquence de déformation, deux événements aurifères (contrôlés pendant les phases D_{3YA} et D_{4YA} datée à 2105±25 Ma (Re-Os sur pyrite aurifère)) qui contrôlent le budget aurifère global du gisement. Cette étude confirme que des gisements d'or orogéniques peuvent être formés par remobilisation et/ou nouveaux apports d'or lors de multiples événements de déformation et de d'hydrothermalisme. L'intrusion porteuse de la minéralisation est datée à 2130,6 ± 5,8 Ma (U-Pb sur zircon). Une intégration à l'échelle du district est proposée où la mise en place de l'intrusion correspond à la transition entre les phases régionales D_1 et D_{2a}. Le modèle litho-structural défini à l'échelle du camp et du district montre que les minéralisations hébergées par des intrusions de type Yaou peuvent ainsi être ciblées le long de grands couloirs de cisaillement à l'échelle du district. Cette approche 4D associant géologie, géophysique et géochronologie relative/absolue aide à la prédiction de nouvelles cibles minéralisées jusqu'alors non reconnues dans la branche Sud de la ceinture de roche verte du Paramaca. Elle considère l'ensemble du système métallogénique d'or orogénique comprenant une architecture lithosphérique propice, un cadre géodynamique favorable, une fertilité géochimique en éléments sidérophiles et une préservation post-minéralisation.

Les modalités des processus supergènes sont étudiées dans le prospect de Couriège, qui comportent plusieurs indices aurifères associés soit à des veines de quartz riches en pyrite au sein de profils latéritiques en place, soit à des colluvions et alluvions. Deux profils latéritiques ont été étudiés pour évaluer le rôle des processus supergènes dans la modification des minéralisations primaires (hypogènes). Le profil du site d'Achman Giraud est caractérisé par un profil d'altération authigénique développé sur un protolithe d'amphibolite avec des veines de quartz aurifères. La dispersion verticale et latérale de l'or peu importante, le caractère principalement primaire des grains d'or et les preuves limitées de reprécipitation de l'or supergène, plaident en faveur d'une faible remobilisation supergène sans preuve évidente d'enrichissement au cours de la latéritisation. Le profil du site de Lupe expose un horizon colluvionnaire aurifère tronquant un profil latéritique stérile. L'or est présent sous forme d'inclusions d'électrum dans des cristaux de pyrite détritiques centimétriques partiellement goethitisés et sous forme de grains d'or libres qui présentent une forme subarrondie, des marques de transport mécanique et des bordures appauvries en Ag, suggérant un transport significatif ainsi qu'une altération supergène. Ces observations remettent en question l'évaluation du caractère proximal à distal de la source de cet or allogénique.

Abstract

Gold deposits located in French Guiana (France, South America) within Rhyacian terranes (2.3-2.05 Ga), are the witnesses of the Trans-Amazonian orogeny. These deposits, in the Guiana Shield, are covered by a dense rainforest where well-developed lateritic profiles leave little outcrop of unaltered bedrock. Considering this specific context, this thesis is interested in defining (i) what are the primary gold mineralisation processes and (ii) what is their preservation and enrichment (or not) during secondary supergene processes and is based on two case studies: the Yaou deposit and the Couriège prospect. The scientific approach adopted for this work follow the mineral system concept, which requires integration in time, space and at different scales of geological and metallogenic processes. Thus, this thesis integrates different disciplines of geosciences namely structural geology (and microstructural), metallography, petrography, geochemistry, geochronology and geophysics in order to study the formation of these mineralised (hypogene and supergene) objects, characterise their typology and discuss the associated metallogenic processes.

At Yaou, intrusive bodies (quartz monzodiorite), mainly hosting gold mineralisation, are aligned along a sinistral shear zone affecting a volcano-sedimentary sequence. A polyphase tectono-magmatic evolution, of 5 deformation phases, is proposed at the scale of the mineralized camp. Associated with this deformation framework are two gold events (controlled during phases D_{3YA} and D_{4YA} dated at 2105±25 Ma (Re-Os on Au-bearing pyrite)) which control the overall gold budget of the deposit. This study confirms that orogenic gold deposits can be formed by remobilisation and/or new gold inputs during multiple deformation phases, veining and hydrothermal events. The intrusion hosting the mineralisation is dated at 2130.6 ± 5.8 Ma (U-Pb on zircon). An integration at the district-scale is proposed where the emplacement of the intrusion is at the transition between the regional phases D_1 and D_{2a}. The litho-structural model defined at the camp- and district-scale shows that mineralisation hosted by Yaou-type intrusions can thus be targeted along shear zones within the Yaou district. This 4D approach combining geology, geophysics and relative/absolute geochronology helps to define new targets previously unrecognised in the Southern Paramaca greenstone belt. It considers the whole orogenic gold mineral system encompassing a favourable lithospheric architecture, a favourable geodynamic framework, a geochemical fertility in siderophile elements and a post-mineralisation preservation.

The modalities of supergene processes are studied at the Couriège prospect, which includes several gold occurrences associated either with pyrite-rich quartz veins within in situ lateritic profiles, or with colluvial and alluvial horizons. Two profiles were studied to assess the role of supergene processes in the modification of primary (hypogene) mineralisation. The Achman Giraud site is characterised by an authigenic alteration profile developed on an amphibolite protolith with gold-bearing quartz veins. The weak vertical and lateral dispersion of gold, the predominantly primary character of the gold grains, and the limited evidence of supergene gold reprecipitation, argue for minor supergene remobilisation without clear evidence for gold enrichment during lateritisation. The Lupe site exposes a gold-bearing detrital horizon truncating a barren lateritic profile. Gold is present as electrum inclusions in partially goethitised detrital pyrite crystals and as free gold grains exhibiting a sub-rounded shape, mechanical transport marks and Ag-depleted rim, suggesting transport and exposure to weathering over significant distance and time, respectively. These observations question the evaluation of the proximal to distal character of transported gold.

Remerciements

J'adresse mes sincères remerciements à mes directeurs de thèse, Anne-Sylvie André-Mayer et Aurélien Eglinger qui ont accepté de m'encadrer pendant les trois années qu'a duré ma thèse. Je les remercie pour leur encadrement, leur bienveillance, leurs conseils et leur disponibilité même à 7 325 km de distance. Ce fut un plaisir de travailler et échanger avec eux, notamment pendant les fameux Gold Team meetings. Je remercie également Yoram Teitler qui a rejoint l'encadrement de ma thèse en fin de première année lorsqu'un expert latéritique était nécessaire. Merci pour son aide précieuse et implication dans tous les chapitres de cette thèse et pas seulement pour le supergène. Je lui dois ma nouvelle passion pour l'étude de la saproshit, passion partagée depuis avec Aurélien Eglinger.

Je tiens à remercier chacun des membres de mon jury, en commençant par Alain Chauvet et Dominique Chardon qui ont accepté de réviser mon manuscrit. Merci également à Michel Cathelineau, Taija Torvela et Arnauld Heuret d'avoir accepté notre invitation pour venir juger ce travail.

Je remercie Auplata Mining Group (AMG) pour le financement de cette thèse ainsi que son VP Exploration, Karim Robo.

Merci à Pierre Gibert, référent de cette thèse, collègue et ami, pour son soutien pendant ces trois années.

Un grand merci à Frédéric Tona, pour tous ses conseils depuis maintenant 8 ans mais également de m'avoir mis en relation avec les membres de GeoRessources.

Je remercie également Didier Tamagno de m'avoir autorisé à faire cette thèse sans aucune hésitation lors de ma demande.

Merci à Arnauld Heuret pour son aide lors des missions terrain et suivi au cours de ces années.

Je remercie également Nathalie Foucal pour la gestion administrative de cette thèse.

Sont également remerciés, Christophe Scheffer, Anthony Pochon, Didier Béziat, François Turlin, Philippe Marion et Marc Jessell pour leur aide et nombreuses discussions pendant cette thèse.

Je ne peux continuer ces remerciements sans mentionner Hilaire Dakouré et Julien Perret, amis de la Gold Team ayant partagé de très nombreuses pizzas, Chouffes et autres pains au chocolat. Bon courage pour ces derniers mois de thèse !

Merci à mes collègues géologues d'Auplata, Valentin *Ggn* Ilboudo, Julienne Mian, Mohamed le benguiste Diallo, Maxence de Witasse et Souleymane Sall. Merci également à Hamel Ibbari pour son aide dans le comptage de pyrite tous les 10 cm.

Rodney Sacks, CEO de Monster Beverage Corporation est également remercié et félicité.

Pour finir, je voudrais remercier mes amis Valentin Alain, Julia Grimm et Yohan Thiebaut ainsi que ma famille, mes parents et mon frère Pierre qui m'ont soutenu tout au long de ma thèse, et pour finir merci à mon épouse Kelly.

Sommaire

Liste des figures

Liste des Tableaux

Introduction

Thématique et problématique

Les gisements d'or orogéniques Précambriens sont spatialement et temporellement associés à des ceintures de roches vertes (Fig. 1 ; Dubé & Gosselin, 2007). Les minéralisations aurifères situées en Guyane (France, Amérique du Sud) sont ainsi localisées au sein de terrains d'âge Rhyacien (2.3-2.05 Ga), témoins de l'orogenèse transamazonienne (Hurley et al., 1967 ; Vanderhaeghe et al., 1998 ; Delor et al., 2003a, b ; Kroonenberg et al., 2016). Ces dépôts aurifères du Bouclier Guyanais (*Guiana Shield*) sont masqués par une forêt amazonienne dense sous laquelle des profils latéritiques bien développés laissent peu d'affleurement de roche non altérée (« *bedrock* »).

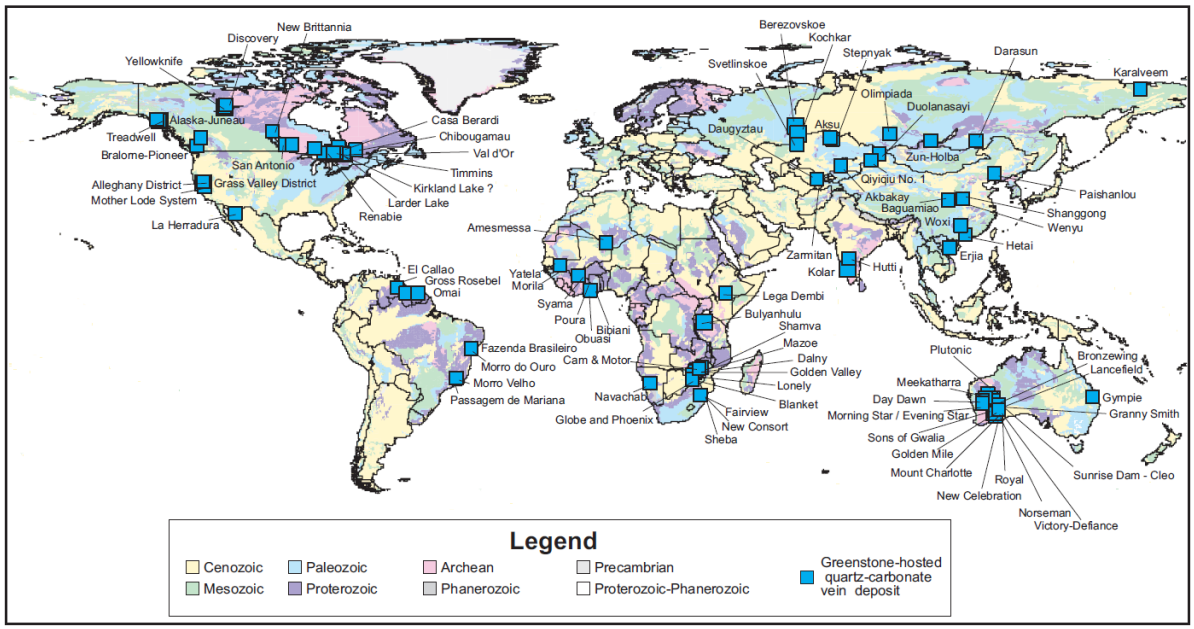

Figure 0-1 Distribution des gisements d'or orogénique (> 30 t Au) et âges des terrains associés dans le monde (Dubé et Gosselin, 2007).

Ces terrains Paléoprotérozoïques affleurant au Nord de l'Amérique du Sud sont relativement sous-explorés en comparaison avec le Craton Ouest Africain par exemple, et les études métallogéniques et pétro-structurales sont peu nombreuses. Une dizaine d'étude à l'échelle du gisement d'or est dénombrée avec les travaux de Voicu et al. (2001) à Omai au Guyana ; Tedeschi et al. (2018, 2019) à Karouni au Guyana ; Daoust et al. (2011) à Rosebel au Surinam ; Velasquez et al. (2014) à El Callao au Vénézuela ; Padoan et al. (2014) à Choco 10 au Vénézuela ; Guiraud et al. (2017, 2020) à Montagne d'or en Guyane ou Lafrance et al. (1999) à St. Elie en Guyane. Les travaux portant sur l'étude des profils latéritiques en Guyane sont également peu nombreux (Girard et al., 2000 ; Freyssinet & Farah, 2000, ou Théveniaut & Freyssinet, 2002) et ne sont pas focalisés sur la minéralisation supergène en domaine latéritique.

Des données récentes sur ces possibles enrichissements supergènes sont quasi-inexistantes en Guyane alors que l'ensemble des indices aurifères connus actuellement sont affectés en subsurface par des processus de latéritisation.

A l'échelle du Bouclier Guyanais, les travaux publiés se concentrent sur des études à l'échelle du gisement sans prendre en compte le concept de *système métallogénique* (McCuaig & Hronsky, 2014 ; Wyman et al., 2016 ; Groves et al., 2020), qui cherche à déterminer les contrôles fondamentaux essentiels pour la génération de gisements aurifères à différentes échelles de temps et d'espace.

Concernant la caractérisation géodynamique au Paléoprotérozoïque du Bouclier Guyanais et ses lithologies associées, les modèles actuels sont basés sur les travaux de Gibbs (1980), Ledru et al. (1991), Gibbs and Barron (1993), Vanderhaeghe et al. (1998), Voicu et al. (2001), Delor et al. (2003a, b), Enjolvy (2008) et Kroonenberg et al. (2016).

La définition d'un cadre litho-structural précis dans lequel des gisements aurifères peuvent être placés en termes de phases de déformation, évènements aurifères et hydrothermaux ; ainsi que des modélisations en 4D des minéralisations sont donc à actualiser en Guyane en considérant les processus primaires hypogènes et secondaires supergènes associés.

Objectifs et organisation du manuscrit

Ce travail de doctorat se propose ainsi d'étudier les modalités d'enrichissements primaires et secondaires d'or dans des ceintures de roche vert Précambrienne en Guyane, à différentes échelles de temps et d'espace, par une approche multi-méthode. Le gisement de Yaou ainsi que le prospect de Couriège sont utilisés comme cas d'étude pour cette thèse (Fig. 2).

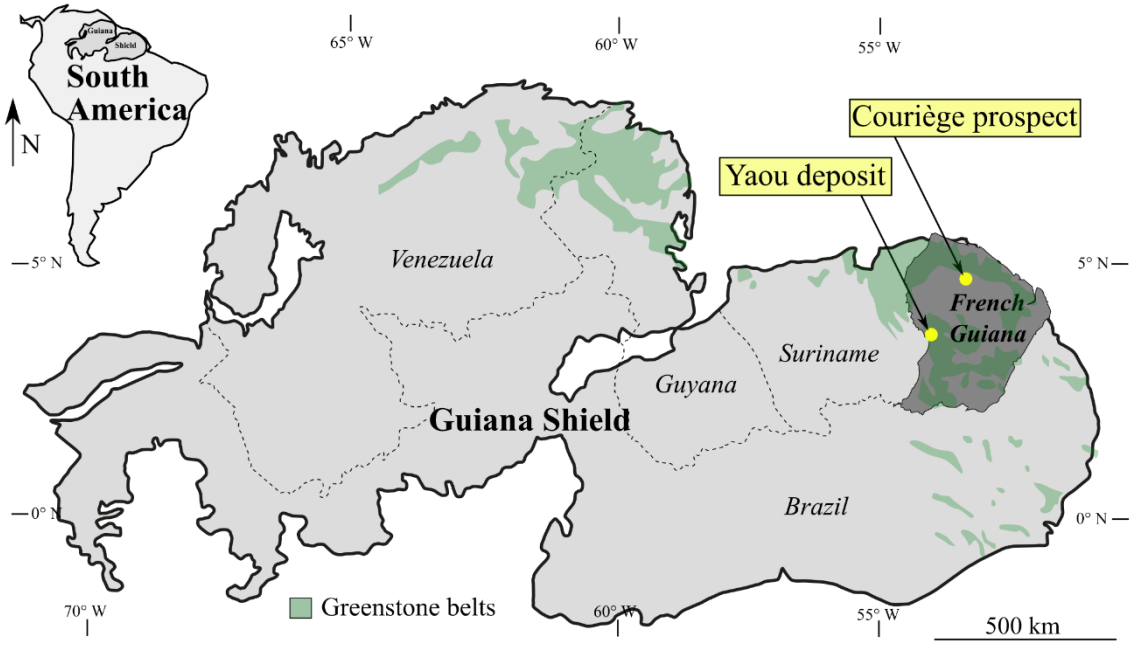

Figure 0-2 Localisation des deux zones d'étude de cette thèse, au sein du Bouclier Guyanais (limites du Bouclier Guyanais et ceintures de roches vertes associées, d'après Kroonenberg et al., 2016).

Considérant le contexte spécifique du Bouclier Guyanais, la problématique sera plurielle (1) quel est le cadre pétro-structural des possibles phases de minéralisation à l'échelle du gisement, (2) quelle est l'architecture litho-structurale et son évolution temporelle à l'échelle du district et (3) quels sont les processus d'enrichissement hypogènes et supergènes associés. Cette approche intégrée offre donc une vision spatio-temporelle d'un système minéralisé, ici celui de l'or, en étudiant la typologie des objets minéralisés et les processus métallogéniques associés, à savoir minéralisation primaire *versus* minéralisation secondaire.

Les modalités d'enrichissement primaires seront discutées sur le site de Yaou, un gisement exploré depuis les années 1980, successivement par le BRGM, Guyanor et Auplata Mining

Group (AMG) totalise plus de 30 km de forages disponibles pour l'étude et l'échantillonnage de *bedrock*.

Les modalités d'enrichissement secondaires seront étudiées sur le site de Couriège, un prospect peu exploré par ces mêmes compagnies minières, où des occurrences d'or dans les profils latéritiques ont été documentées par Auplata Mining Group. Durant cette thèse, aucun affleurement de la minéralisation de Yaou n'était accessible à l'échantillonnage pour une étude de la minéralisation dans l'horizon latéritique.

Ce manuscrit de thèse va donc présenter successivement (1) **les modalités d'enrichissement primaire à différentes échelles depuis l'échelle du gisement** (*deposit-scale*, chapitre 2) **à celles du camp à district** (*camp- to district- scale*, chapitre 3), puis (2) **les modalités d'enrichissement secondaire** (*prospect-scale*, chapitre 4), pour finir sur une discussion et conclusion (chapitre 5).

Le **chapitre 1** présente **l'état de l'art** concernant les processus primaires (source, transport, dépôt, polyphasage, remobilisation) de l'or orogénique et secondaires (caractérisation des profils d'altération latéritique et enrichissements supergènes). Dans ce chapitre est aussi présentée une synthèse bibliographique de la géologie du Bouclier Guyanais, du modèle d'évolution géodynamique et métallogénique de la Guyane, de ses unités lithologiques principales et différents types de gisements aurifères. L'organisation de ce chapitre s'appuiera sur notre récente publication dans le volume spécial Géologues, Les ressources des Guyanes, édité par la Société Géologique de France (Eglinger et al., 2020) discutant des processus minéralisateurs primaires et secondaires comme traceurs géologiques du cycle orogénique transamazonien en Guyane française.

Les chapitres suivants sont présentés sous forme d'articles scientifiques acceptés ou en préparation, écrits en anglais et pour lesquels le doctorant en est le premier auteur. Chaque chapitre est précédé d'une introduction en français composée d'une présentation du contexte et d'un résumé du chapitre. Ces chapitres s'articulent ainsi :

Minéralisation primaire (*deposit-scale*), (chapitre 2 ; Fig. 3)

Dans le **chapitre 2**, les observations pétro-structurales et les données géochimiques (EPMA et LA-ICP-MS sur pyrite) sont intégrées en utilisant une approche multi-échelles (des échelles macro- à microscopiques) combinée à une approche multidisciplinaire pour (i) établir la relation spatiale et temporelle entre phases de déformation, générations de veines, occurrences

éventuelles de sulfures, faciès d'altération hydrothermale et événements aurifères, (ii) comprendre l'influence des différentes unités (corps intrusifs, métasédiments, métavolcanites) et des différentes phases tectoniques dans la formation et l'évolution du gisement et (iii) définir la nature, la distribution et la (re) mobilisation de l'or dans le temps et l'espace relatifs afin de discuter du caractère monophasé *versus* polyphasé du gisement. Ce chapitre 2 correspond à un article accepté en septembre 2020 dans la revue de la Société Géologique de Londres (GSL) pour une publication spéciale sur l'or orogénique intitulée « *Recent Advances in Understanding Gold Deposits: From Orogeny to Alluvium* »

En annexe, une étude complémentaire sur la distribution des teneurs en or est présentée.

Minéralisation primaire (*camp- to district-scale),* (chapitre 3 ; Fig. 3)

Dans le **chapitre 3**, de nouvelles données géologiques (géochimie en roche totale, isotopie Lu-Hf et datation U-Pb sur zircon) concernant l'intrusif de Yaou, interprété comme une quartz monzodiorite, hébergeant la minéralisation principale sont présentées, permettant une corrélation temporelle avec l'évolution orogénique transamazonienne. De nouvelles cartes structurales et lithologiques à l'échelle du district, du camp et du gisement, basées sur des données géophysiques aéroportées, y compris la magnétométrie et la radiométrie (Th, U et K), aideront à définir la relation entre le cisaillement, le magmatisme et la minéralisation aurifère. Ces données géologiques et géophysiques sont intégrées et discutées dans un modèle 4D visant à cibler de nouveaux gisements d'or (de type *intrusion-hosted*) dans un domaine paléoprotérozoïque mal exploré. L'interprétation qui en résulte peut améliorer les stratégies d'exploration minière en Guyane et dans le Bouclier Guyanais. Ce chapitre 3 correspond à un manuscrit prochainement soumis à *Precambrian Research*.

En annexe, sont présentés les autres unités intrusives de Yaou, non associées à la minéralisation ainsi qu'une tentative de caractérisation des altérations en terme bilan de masse

Minéralisation secondaire (*prospect-scale),* (chapitre 4 ; Fig. 3)

Le **chapitre 4** se focalise sur les profils latéritiques aurifères du prospect de Couriège. Les données pétrographiques (observations optiques et MEB) et géochimiques (analyse en roche totale, µXRF, XRD, EPMA, LA-ICP-MS) seront ici intégrées pour (i) documenter les changements minéralogiques et géochimiques associés aux processus de latéritisation, (ii) déterminer dans quelle mesure les processus supergènes peuvent conduire à la dispersion verticale et latérale de l'or depuis les veines aurifères, (iii) évaluer l'évolution de la composition

et de la morphologie des grains d'or lors de la latérisation et (iv) discuter des processus supergènes associés. Une attention particulière sera ici apportée à la distribution *in situ* de l'or dans les horizons de *latosol*, argiles tachetées et saprolite, qui représentent des cibles importantes pour l'exploration de l'or latéritique au sein du Bouclier Guyanais (Dardenne & Schobbenhaus, 2003) et ailleurs (Freyssinet et al., 2005 ; Béziat et al., 2016 ; Butt, 2016 entre autres). Ce chapitre 4 correspond à un manuscrit soumis dans la revue de la Société Géologique de Londres (GSL) pour une publication spéciale sur l'or orogénique intitulée « *Recent Advances in Understanding Gold Deposits: From Orogeny to Alluvium* » .

Enfin, le **chapitre 5** du manuscrit fournit une discussion-conclusion qui intègre les conclusions principales de chaque chapitre. Nous menons une réflexion globale s'appuyant sur les éléments critiques du concept de système métallogénique, (*mineral system)*, (McCuaig & Hronsky, 2014 ; Wyman et al., 2016 ; Groves et al., 2020), à savoir l'architecture de la lithosphère/croûte à différentes échelles, le contexte géodynamique, la fertilité et la préservation de la minéralisation primaire, ici pour le cas Guyane au cours du cycle transamazonien.

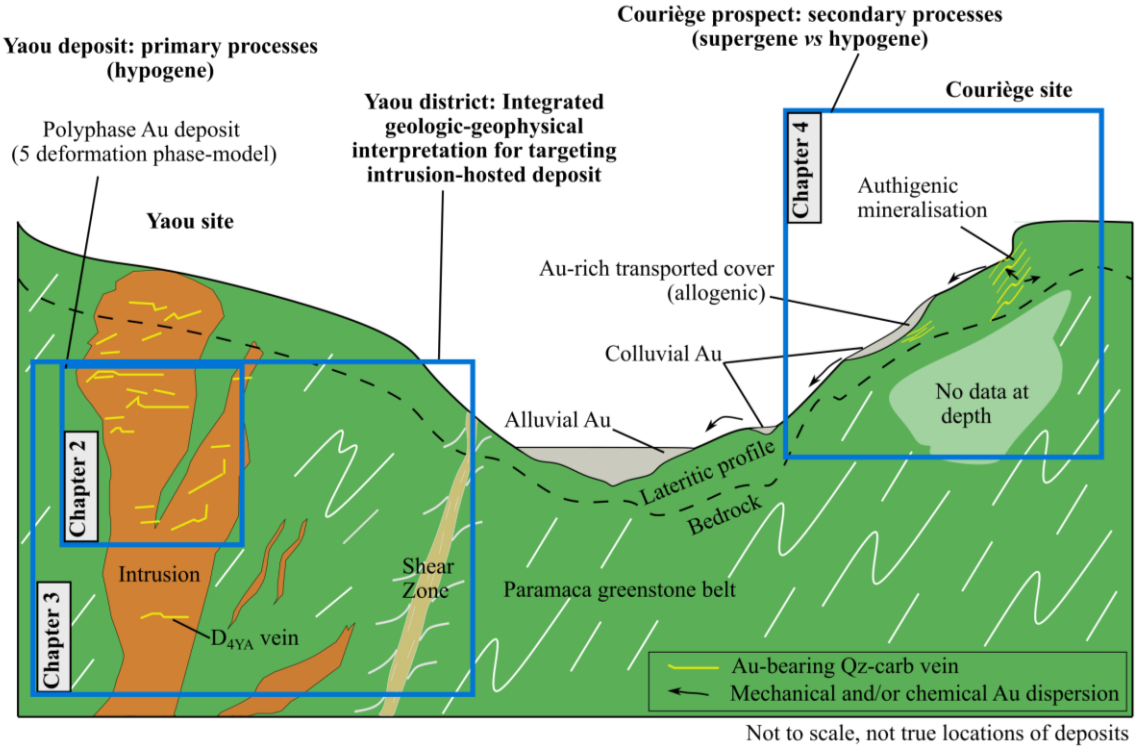

Figure 0-3 Représentation schématique des thématiques de cette thèse et lien entre les chapitres.

Echantillonnage et méthodes analytiques

Sur le site de Yaou, l'échantillonnage a été réalisé sur des carottes de forages d'Auplata Mining Group alors que sur le site de Couriège, il est effectué sur des fronts de profils excavés à l'aide d'une pelle mécanique sur d'anciennes zones de tranchées d'exploration.

Chacune des méthodes analytiques utilisées est décrite dans le chapitre correspondant.

Elles incluent:

- Des observations pétrographiques et micro-structurales optiques associées à de l'imagerie MEB (Microscopie électronique à balayage) et analyses EDS (Energy-Dispersive X-ray Spectroscopy), (tous les chapitres)
- Des analyses géochimiques en roche totale des éléments majeurs et traces (Chapitre 3 et 4)
- Des analyses en microfluorescence X (cartographie chimique) sur des échantillons issus des profils latéritiques (Chapitre 4)
- Des analyses à la microsonde électronique (Chapitre 2, 3 et 4)
- De la géochronologie U-Pb couplée isotopie Hf sur zircon en LA-ICPMS (Chapitre 3)
- De la géochronologie Re-Os sur pyrite (Chapitre 3)
- Des analyses des éléments traces par LA-ICPMS (Laser Ablation-Inductively Coupled Plasma Mass Spectrometry) sur des grains de pyrite (Chapitre 3) ainsi que sur des grains d'or (Chapitre 2)
- Des analyses en diffractométrie des rayons X sur des poudres des différents horizons de profils latéritiques (Chapitre 4).

Références

Béziat, D., Siebenaller, L., Salvi, S., Chevalier, P., 2016. A weathered skarn-type mineralization in Ivory Coast: the Ity gold deposit. Ore Geol. Rev. 78, 724–730.

Butt, C.R.M., 2016. The development of regolith exploration geochemistry in the tropics and sub-tropics. Ore Geol. Rev. 73, 380–393.

Daoust, C., Voicu, G., Brisson, H. and Gauthier, M., 2011, Geological setting of the Paleoproterozoic Rosebel gold district, Guiana Shield, Suriname. J South Am Earth Sci. 32, 222–245.

Dardenne, M.A., Schobbenhaus, C., 2003. Metallogeny of the Guiana Shield. Geol. Fr. 2–4, 291–319.

Delor, C., Lahondère, D., Egal, E., Lafon, J.-M., Cocherie, A., Guerrot, C., Rossi, P., Truffert, C., Théveniaut, H., Phillips, D., Avelar, V.G.d., 2003b. 2-3-4 In: Transamazonian crustal growth and reworking as revealed by the 1:500000 scale geological map of French Guiana. Géol Fr, 5–57.

Delor, C., de Roever, E.W.F., Lafon, J.-M., Lahondère, D., Rossi, P., Cocherie, A., Guerrot, C., Potrel, A., 2003a. The Bakhuis ultrahigh-temperature granulite belt (Suriname) : II. Implications for late Transamazonian crustal stretching in a revised. Géol Fr. 2-3- 4, 207–230.

Dubé, B., and Gosselin, P., 2007, Greenstone-hosted quartz-carbonate vein deposits, in Goodfellow, W.D., ed., Mineral Deposits of Canada: A Synthesis of Major Deposit-Types, District Metallogeny, the Evolution of Geological Provinces, and Exploration Methods: Geological Association of Canada, Mineral Deposits Division, Special Publication No. 5, 49-73.

Eglinger, A., André-Mayer, A.-S., Combes, V., Teitler, Y., Heuret, A. 2020. Les gisements d'or de la Guyane française. Géologues. 206, 36-40.

Enjolvy R, 2008. Processus d'accrétion crustale et régimes thermiques dans le bouclier des Guyanes : signatures géochimiques et thermochronologiques au transamazonien (2250-1950 Ma) : Phd thesis, Université - Sciences et Techniques du Languedoc Montpellier II. 305 p.

Freyssinet, P., Butt, C.R.M., Morris, R.C., Piantone, P., 2005. Ore-forming processes related to lateritic weathering. Econ. Geol. 100th Anniversary volume. 681-722

Freyssinet, P., Farah, A., 2000. Geochemical mass balance and weathering rates of ultramafic schists in Amazonia. Chem Geol. 170. 133-151.

Gibbs, A.K., 1980. Geology of the Barama-Mazaruni Supergroup of Guyana: Unpublished Ph.D. thesis, Cambridge, Harvard University, p. 385.

Gibbs, A.K., Barron, C.N., 1993. The Geology of the Guiana Shield. Oxford University Press, pp. 246.

Girard, J.P., Freyssinet, P., Chazot, G., 2000. Unraveling climatic changes from intraprofile variation in oxygen and hydrogen isotopic composition of goethite and kaolinite in laterites: an integrated study from Yaou, French Guiana. Geochim. Cosmochim. Acta 64, 409– 426.

Groves, D.I., Santosh, M., Zhang, L., 2020b. A scale-integrated exploration model fororogenic gold deposits based on a mineral system approach.. Geosci. Front 11 (3),719–738

Guiraud, J., Tremblay, A., and Jebrak, M., 2017. The Rhyacian Montangne d'Or auriferous volcanogenic massive sulphide deposit, French Guiana, South America: Stratigraphy and geochronology [ext. abs.]: Society for Geology Applied to Mineral Deposits, 14th Biennial Meeting, Québec City, August 20–23, 2017, Extended Abstracts, 237–240.

Guiraud, J., Tremblay, A., Jébrak, M., Ross, P-S., Lefrançois, R., 2020. Stratigraphic setting and timing of the Montagne d'Or deposit, a unique Rhyacian Au-rich VMS deposit of the Guiana Shield, French Guiana, Precambr. Res. 337, 105551.

Hurley, P.M., de Almeida, F.F.M., Melcher, G.C., Cordani, U.G., Rand, J.R., Kawashita, K., Vandoros, P., Pinson, W.H. & Fairbairn, H.W., 1967. Test of continental drift by comparison of radiometric ages. Science 157: 495–500.

Kroonenberg, S.B., de Roever, E.W.F., Fraga, L., Reis, N., Faraco, T., Lafon, J.-M., Cordani, U., Wong, T., 2016. Paleoproterozoic evolution of the Guiana Shield in Suriname: a revised model. Neth. J. Geosci. 95, 491–522.

Lafrance, J., Bardoux, M., Voicu, G., Stevenson, R., Machado, N., 1999. Geological and metallogenic environments of gold deposits of the Guiana Shield; a comparative study between St-Elie (French Guiana) and Omai (Guyana). Explor. Min. Geol. 8, 117–135.

Ledru, P., Lasserre, J.L., Manier, E., and Mercier, D., 1991, Révision de la lithologie du Paléoprotérozoïque du craton guyanais. Tectonique transcurrente et dynamique des bassins sédimentaires. Bull Soc Geol Fr. 162, 627–636.

McCuaig, T.C., Hronsky, J.M.A., 2014. The mineral system concept: The key to exploration targeting: Society of Econ Geol. Special Publication. 18, 153–175.

Milesi, J., Lerouge C, Delór C, Ledru P, Billa M, Cocherie A, Egal E, Fouillac A, Lahondère D, Lasserre J, Marot A, Martel-Jantin B, Rossi P, Tegyey M, Théveniault H, Thiéblemont D, Vanderhaeghe, O., 2003. Gold deposits (gold-bearing tourmalinites, gold-bearing conglomerates, and mesothermal lodes), markers of the geological evolution of French Guiana: geology, metallogeny, and stable isotope constraints. Géol Fr, 2-3-4:257-290.

Padoan, M., Rossetti, P., Rubatto, D., 2014. The Choco 10 gold deposit (El Callao, Bolivar State, Venezuela): petrography, geochemistry and U-Pb geochronology. Precambrian Res. 252, 22–38.

Siddorn, J. P., Williams, P. R., Isles, D. J., Rankin, L. R., 2020. Integrated Geologic-Geophysical Interpretation of District-Scale Structural Frameworks: Systematic Approaches for Targeting Mineralizing Systems. Reviews in Econ Geol. 21, 271–313

Tedeschi, M., Hagemann, S.G., Davis, J., 2018. The Karouni Gold Deposit, Guyana, South America: part I. Stratigraphic Setting and Structural Controls on Mineralization. Econ Geol. 113, 1679–1704.

Tedeschi, M., Hagemann, S.G., Roberts, M.P. and Evans, N.J., 2018b. The Karouni Gold Deposit, Guyana, South America: Part II. Hydrothermal Alteration and Mineralization. Econ Geol. 113, 1705-1732.

Tedeschi, M. T., Hagemann, S. G., Kemp, A. I. S., Kirkland, C. L., Ireland, T. R., 2019. Geochronological constrains on the timing of magmatism, deformation and mineralization at the Karouni orogenic gold deposit: Guyana, South America. Precambr. Res. 105329.

Théveniaut, H & Freyssinet, Ph., 2002. Timing of lateritization on the Guiana Shield: Synthesis of paleomagnetic results from French Guiana and Suriname. Palaeogeography, Palaeoclimatology, Palaeoecology. 178. 91-117.

Vanderhaeghe, O., Ledru, P., Thiéblemont, D., Egal, E., Cocherie, A., Tegyey, M., Milesi, JP., 1998. Contrasting mechanism of crustal growth: Geodynamic evolution of the Paleoproterozoic granite–greenstone belts of French Guiana. Precambrian Res. 92:165–193.

Velásquez, G., Béziat, D., Salvi, S., Siebenaller, L., Borisova, A.Y., Pokrovski, G.S., and De Parseval, P., 2014, Formation and deformation of pyrite and implications for gold mineralization in the El Callao district, Venezuela. Econ Geol. 109, 457–486.

Voicu, G., Bardoux, M., Stevenson, R., 2001. Lithostratigraphy, geochronology and gold metallogeny in the northern Guiana Shield, South America: a review: Ore Geol Rev.18, 211–236.

Wyman, D.A., Cassidy, K.F., Hollings, P., 2016. Orogenic gold and the mineral systems approach: resolving fact, fiction and fantasy. Ore Geol Rev. 78, 322–335.

Chapitre 1

Considérant les processus minéralisateurs primaires et secondaires comme traceurs géologiques du contexte géodynamique, ce chapitre vise à présenter les processus primaires (source, transport, dépôt, polyphasage, remobilisation) et secondaires (caractérisation des profils d'altération latéritique, enrichissements supergènes, préservation/modification de la minéralisation primaire) de l'or dans le cycle transamazonien en Guyane française. Dans ce chapitre est présentée une synthèse bibliographique de la géologie du Bouclier Guyanais, de ses unités lithologiques principales, du modèle d'évolution géodynamique et métallogénique de la Guyane et des différents types de gisements aurifères identifiés.

In this thesis, the following scale-related terms are used following Jebrak & Marcoux (2008) definitions: (1) a *deposit* is a set of mineralised bodies relatively closed to each other (less than a km), (2) a *camp* is a cluster of deposits with dimensions varying from 1 to 10 km while (3) a *district* is an aggregate of mineralised camps with dimensions ranging from 10 to 100 km. At higher scales, the term *province* can be used together with *continental/cratonic* scale.

Primary processes

Precambrian orogenic gold deposits within greenstone belts are characterised by a series of key parameters (Table 1).

The most recent models of the formation of orogenic gold deposit (Groves et al., 2019 after Goldfarb & Groves, 2005) is presented in Figure 1A. This subduction-based model states that over-pressured ore fluids released from the slab and sediments intersect deep crustal faults, and then move upwards to form orogenic gold deposits in second-order structures or hydraulically fractured rock bodies (Groves et al., 2019). A schematic representation of ore-fluid source models for orogenic gold deposits (Groves et al., 2019 after Groves & Santosh, 2016) is presented in Figure 1C. According to these authors, the metamorphic fluids are channelled by crustal-scale faults with metals associations controlled by depth of deposition. At the ductile-brittle transition, gold is associated with As, Te or W (Groves and Santosh, 2016 and references therein). Moreover, regarding the key parameters for the formation of an orogenic gold deposit, Gaboury (2019) proposes the conceptual representation (after Cox, 2016), as visible in Figure 1C, where the formation of such deposit, from bottom to top and in time, requires a succession of processes in order to build a deposit. The key parameters considered are *"the fluid sources, the appropriate ligands and their sources, the solubility of gold and its potential sources, the function of faults as conduits, and the mechanisms for precipitating gold"* (Gaboury, 2019).

Table 1-1 Key parameters related to Precambrian orogenic gold deposits

Key parameter	***Characteristics***	**References**
Definition	*Greenstone-hosted quartz-carbonate vein deposits,* *Gold-only deposits*	Groves (1993); Groves et al. (1998); Dube & Gosselin, (2007), Groves et al. (2019) and references therein
Type/ formation	*Hydrothermal in character, formed from gold-bearing fluids focused into structural traps during metamorphism and deformation*	Groves (1993); Groves et al. (1998, 2003, 2019); Goldfarb et al. (2001, 2005)
Geodynamic	*Associated with accretional and collisional regimes*	
Precise location	*Along major compressional to trans-tensional crustal-scale fault zones* *In deformed greenstone terranes* *At margins of major lithological boundaries*	Groves et al. 1998 ; Goldfarb et al. 2001
Control	*Mainly structurally controlled, epigenetic deposits* *Pre-existing structures predating a gold input are important for locating ore shoots, while deformation phases postdating gold event are significant for remobilisation processes*	*Chauvet, (2019b), Blenkinsop et al. (2020*) and references therein; *Tomkins & Mavrogenes, 2002; Cook et al., 2013; Fougerouse et al., 2016, among others*
Timing	*Archaean to Phanerozoic, mainly from ca. 2.8 to 2.5 Ga, from 2.15 to 1.75 Ga, and during the most recent 650 Ma* *(Paleoproterozoic in the Guiana Shield)*	Goldfarb et al., 2001, 2010) For the Guiana Shield: Gibbs & Barron, (1993); Ledru et al. (1991); Vanderhaeghe et al. (1998) among others
Depth of formation	*Formed at intermediate depth (5- 10 km).*	Groves et al. (1998); Dube & Gosselin, (2007)
Associated structure	*Moderately to steeply dipping, compressional brittle-ductile shear zones and faults*	Groves et al. (1998); Dube & Gosselin, (2007) ; Perret et al., 2020
Gold-bearing veining	*Laminated fault filled veins, shear veins, shallow-dipping extensional veins, hydrothermal breccias.*	Groves et al. (1998); Dube & Gosselin, (2007),
Metamorphism	*Greenschist to locally amphibolite-facies metamorphic rock*	Tomkins and Grundy (2009)
Timing compared to deformation	*The mineralisation is syn- to late-deformation*	Groves (1993), Groves et al. (1998, 2019), Goldfarb & Groves (2015), Dube & Gosselin, (2007), Goldfarb et al. (2001, 2005)
Mineralogy associated with Au	*Quartz-dominant, with 3–5 vol. % sulfide minerals mainly Fe-sulfides.* *and 5–15% carbonate minerals.* *Common: Albite, white mica or fuchsite, chlorite, scheelite and tourmaline as gangue phases in veins and in greenschist-facies host rocks.*	
Proximal alteration	*Iron-carbonatization (e.g. ankerite), sericitisation, sulphidation, albitisation*	
Gold is largely confined	*To the quartz-carbonate vein network* *Within iron-rich sulphidised wall-rock selvages* *Within silicified and arsenopyrite-rich replacement zones.*	
Fluids precipitation	*As vein material or wall-rock replacement in second and third order structures at higher crustal levels.*	
Auriferous quartz veins formation	*Formed along deep and seismically active faults as the result of a fault valve cycle (cycling fluctuations in shear stress and fluid pressure over the time within faults, coupled with interactions between fluids and the host rock)*	Sibson et al. (1988); Cox (1995); Peterson and Mavrogenes (2014).

Source of Au

What is/are the source(s) of metal (Au) is a crucial interrogation when studying such deposit. Currently, from isotopic labelling, the proposed metal sources are linked to the metamorphic devolatilisation of metasedimentary sequences and/or metavolcanic rocks (Phillips and Groves, 1983; Groves et al. 1998 ; Pitcairn et al., 2006 ; Large et al., 2007 ; Phillips and Powell, 2010; Gaboury et al. 2013 ; Tomkins et al. 2013 ; LaFlamme et al., 2018). While it is now largely accepted that metasedimentary rocks are sources of Au (Pitcairn et al. 2017), Large et al. (2009, 2012 and reference therein) together with Pitcairn et al. (2010) confirm that gold in arsenic-bearing syngenetic to diagenetic pyrite are crucial primary sources for orogenic gold deposits. Magmas have also been identified as gold sources (Burrows and Spooner, 1987; Tomkins, 2013; Xue et al., 2013). Regarding the fluids transporting gold, Pokrovski et al. (2015) demonstrate that the trisulfur ions form very stable and soluble complexes with Au^{+} enabling extraction, transport, and focused precipitation of gold by sulfur-rich fluids more efficiently than sulfide and chloride only, as previously stated.

Continuum vs metamorphic model

Regarding the link between gold endowment and the tectono-metamorphic evolution of the crust, two main models of orogenic gold deposition are discussed. The continuum model, originally proposed by Colvine et al. (1988), states that gold deposition occurs at the peak of metamorphism (Groves et al., 1990; Groves et al., 2019 and references therein). Alternatively, the metamorphic model (Fig. 1D) proposed by Phillips and Powell (2009, 2010) emphasises the importance of gold deposition before peak metamorphism. Although both models account, to some extent, for gold remobilisation processes during the retrograde history, the metamorphic model highlights the potential of the retrograde metamorphism to spatially redistribute gold through local remobilisation of early gold. For the metamorphic model, Tomkins (2010) used thermodynamic computer programs THERMOCALC and PerpleX in order to constrain the *P-T* range of pyrite breakdown to pyrrhotite, a reaction which liberates sulphur. This study suggests that pressure constraints on metamorphic sulphur liberation implie tectonic settings that allow prograde metamorphism to follow low pressure *P-T-t* paths in an occasionally compressional or transpressional environment. Inverted back-arc basins are interpreted to be the most favourable.

Polyphase gold deposit

Various gold deposits have been identified as having a polyphase or progressive deformation history of gold with protracted history of precipitation, remobilisation and sometimes new input, as evidenced by Couture et al. (1994), Bucci et al. (2002), Kolb et al. (2005), Simard et al. (2013), Lawley et al. (2013), Meffre et al. (2016), Fougerouse et al. (2017), Augustin et al. (2018) ; Gourcerol et al. (2020) and Perret et al. (2020) among others. Thébaud et al. (2018) define a model of protracted and polyphase gold mineralisation through multiple hydrothermal events channelled through identical structures at distinct times. In a broader sense, polyphase gold deposits can express various mineralisation types corresponding to different geodynamic settings as recently evidenced within the West African Craton (WAC; Mc Farlane et al., 2011; Le Mignot et al., 2017a, Le Mignot et al., 2017b; Eglinger et al., 2017; Thébaud et al., 2020). As an example of a polyphase gold deposit within the WAC, the Bonikro deposit, in Ivory Coast, displays an intrusion-related gold system (dated at ca. 2086 Ma) emplaced during the tectonic accretion, followed by a lode gold veining event dated at ca. 2074 Ma interpreted as part of a late orogenic system (Masurel et al., 2019). At the Morila deposit in Mali, McFarlane et al. (2011) propose the superimposition of two gold events. The first event is classified as an intrusion-related gold system while the second is considered as an orogenic. Another key example of polyphase system is the Wassa gold deposit in Ghana where a disseminated gold mineralisation stage (dated at ca. 2145 Ma) during magmatic accretion is followed by a lode gold veins deposit dated at ca. 2055 Ma during tectonic accretion (Le Mignot et al., 2017).

Polyphase characters are also demonstrated at micro- to nanoscopic scale with gold remobilisation and formation of high-grade shoots. For example, Fougerouse et al. (2016) demonstrate that two economic styles of mineralisation occurred at Obuasi (Ghana) with pseudomorphic dissolution-reprecipitation, driven by small volumes of infiltrating fluids in microstructures and intragranular microfractures. The development of anomalously gold-rich fluid controls the formation and distribution of high-grade ore shoots.

Superimposed gold mineralisation phases are not necessarily diachronous as presented above but can also be contemporaneous as evidenced at the Dead Bullock Soak mining camp, Australia (Petrella et al., 2019) with two contrasting styles of mineralisation, defined as a vein-hosted and a stratabound system.

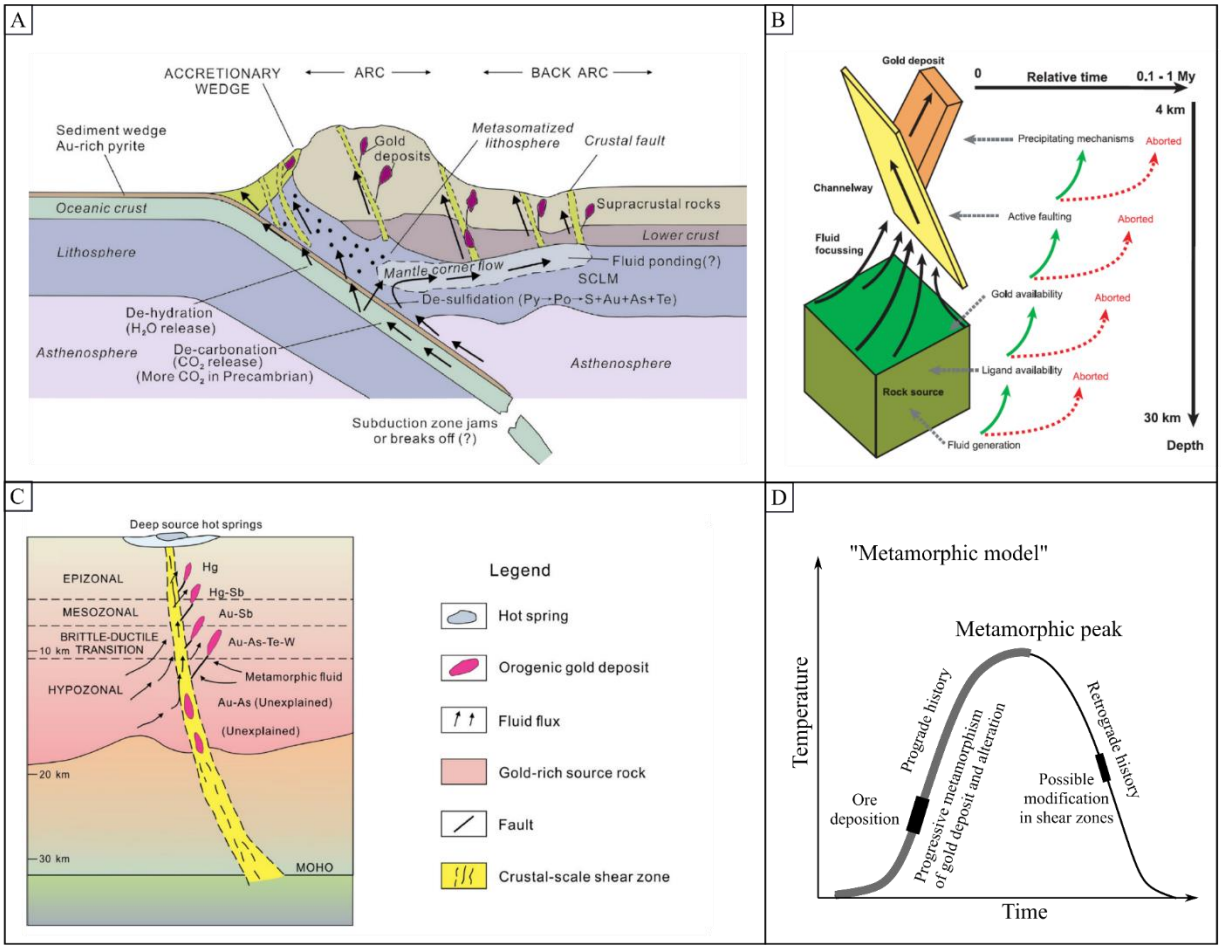

Figure 1-1 A. Model of the formation of orogenic gold deposit (Groves et al., 2019 after Goldfarb & Groves, 2005). B. Anatomy of an orogenic gold hydrothermal system with the key parameters (Gaboury, 2019 after Cox 2016). C. Schematic representation of ore-fluid source models for orogenic gold deposits (Groves et al., 2019 after Groves & Santosh, 2016). D. Metamorphic model of Phillips & Powell (2009) for the formation of gold deposits.

Gold and pyrite association

Commonly associated with orogenic gold deposits (see previous section), the pyrite grains discriminated as generations and types need to be characterised with great details regarding texture, morphology, trace elements contents, trace elements associations in the lattice, types of gold inclusions and infills in fractures (e.g.Velasquez et al., 2014, Gourcerol *et al*., 2018a, b); as detailed in chapter 2. Gold types are illustrated by Eglinger et al. (2020) where gold can be observed within pyrite grains as (1) lattice gold, (2) nano-particles, micro-inclusions, (3) infilling micro-fractures and cracks or (4) within the quartz-carbonate vein as free gold. These different gold typologies have been documented by Sung et al. (2009), Velasquez et al. (2014) or Hastie et al. (2020) for example.

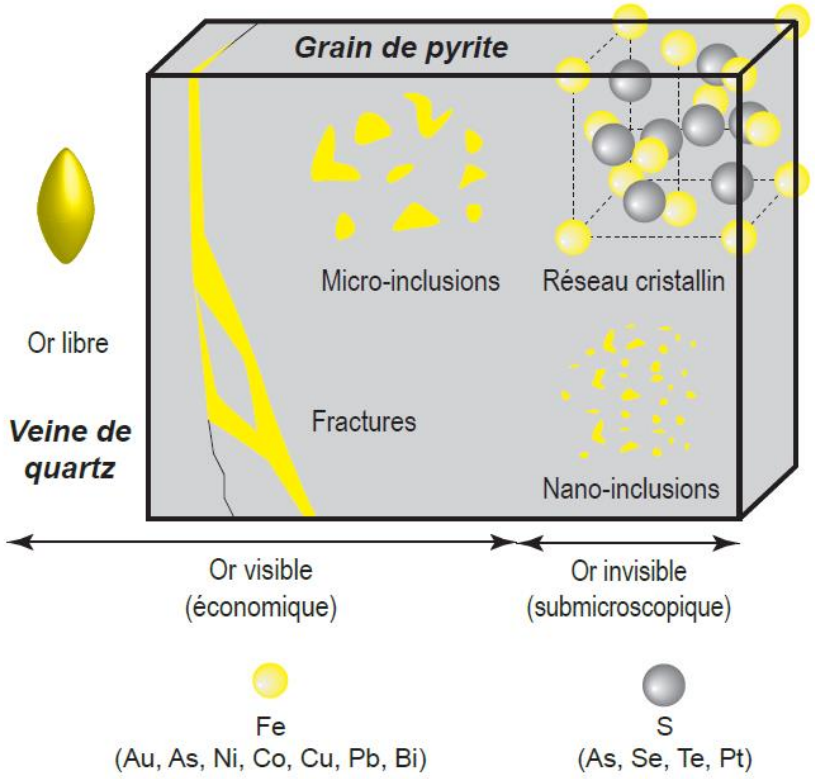

Figure 1-2 Types of gold observed in an orogenic gold deposit (Eglinger et al., 2020)

From studies focused on pyrite, the gold remobilisation processes are observed from the pyrite core to the rim with oscillatory zoning associated with As zoning (Simard et al., 2013; Velásquez et al., 2014; among others) or from lattice gold to visible gold associated with coupled dissolution-reprecipitation processes (Putnis, 2009, Hastie et al., 2020) and deformation in sulphide associated with "aseismic refinement" (Voisey et al., 2020). Pyrite geochemistry studies also provide information on the source of gold, for example Large et al. (2011; 2009) demonstrate the importance of sedimentary-hosted diagenetic pyrite which contain elevated Au and As contents.

Mineral system concept and targeting

The mineral systems approach (Wyborn et al., 1994; McCuaig and Hronsky, 2014; Wyman et al., 2016; Hronsky, 2019 et Groves et al., 2020) considers critical parameters for the formation of orogenic deposit (fertility, favourable geodynamics, favourable architecture, favourable post-formation conditions-preservation; Fig. 3) at various scales from continental (craton) to province to district to camp to deposit to ore-shoot. Coupled geological and geophysical studies are then essential when targeting orogenic gold mineralisation linked in time and space to tectonic triggers (Groves et al., 2020) and predicting models for mineral exploration.

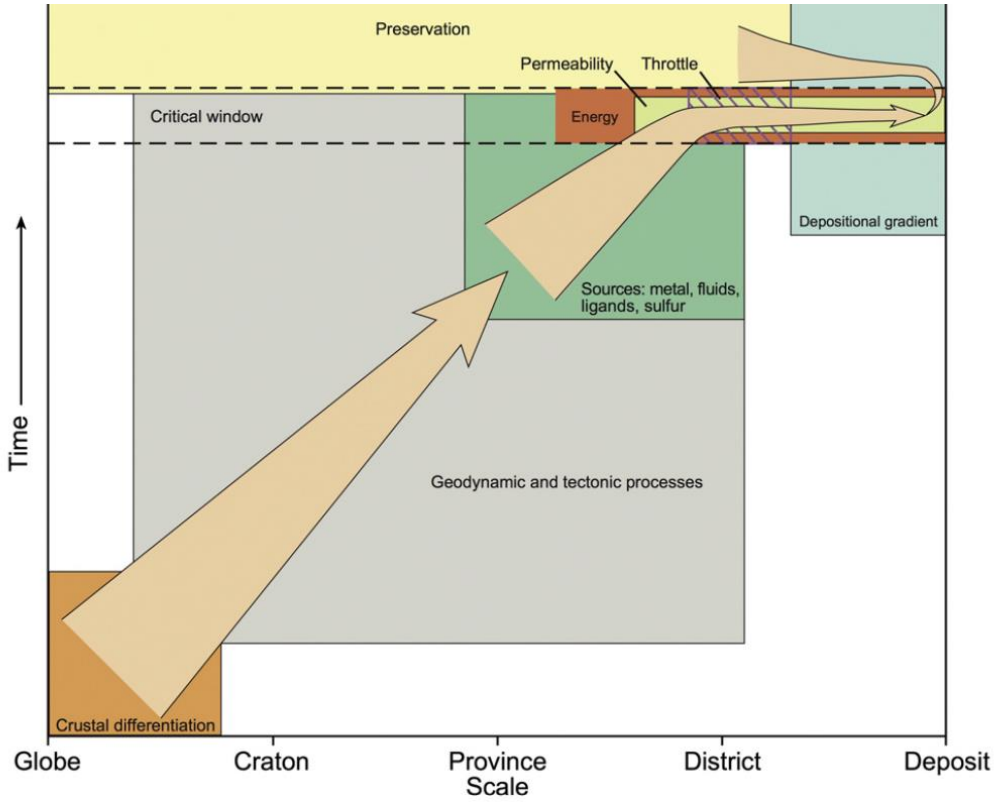

Figure 1-3 Space-time diagram showing important features and processes of a mineral system (Wyman et al., 2016).

Secondary processes

The preservation or modification of a primary gold deposit is controlled by supergene processes. The characterisation of these secondary processes is therefore essential in lateritic domains.

The weathering process of lateritisation takes place under warm and humid climates leading to the dissolution of the most soluble elements (e.g. K, Na, Mg, Ca) while elements such as Fe, Al or Au can be accumulated (Butt, 2001; Collin et al., 2011 and references therein). In tropical and sub-tropical environments, on top of the bedrock, the lateritic weathering profile, as illustrated by Chardon et al. (2018) in Figure 4, typically consists of a saprock transition to a saprolite (isovolumetrically transformed rock which has preserved rock structure), a pedolith, i.e., residuum horizons which have lost rock structure with from bottom to top a mottled zone, a Fe-carapace and a ferricrete). On truncated profiles, the mottled zone, or the saprolite, can be covered by latosol horizons or transported covers (see next section).

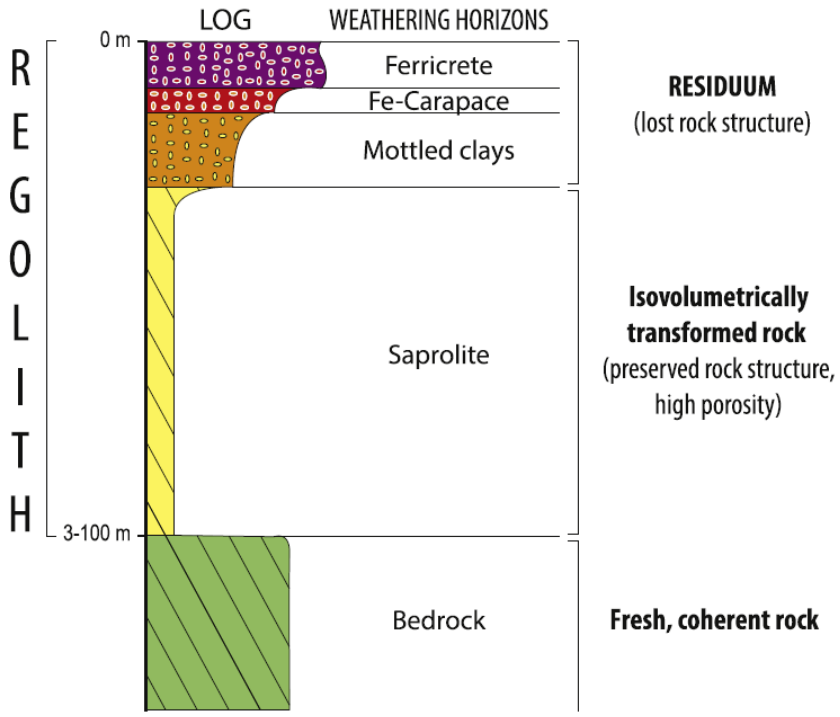

Figure 1-4 Elements of a comprehensive lateritic weathering profile (Chardon et al., 2018).

Primary gold deposits can be modified and/or upgraded during lateritisation. Indeed, secondary deposits are the result of physical accumulation, chemical mobilisation, and redistribution of Au during the weathering of primary mineralisation (Butt, 1998). Regarding distribution of Au in savanna, rainforest and arid regions, Webster and Mann, (1984); Freyssinet et al., (1989, 2005); Lecomte and Colin (1989); Bowell et al. (1993); Colin et al. (1993); Hough et al. (2007); Fairbrother et al. (2012); Butt (2001, 2016); Anand et al. (2017, 2019) among others state that gold can be residually enriched after leaching of mobile cations, but also mobilised physically and/or chemically, depending on geomorphology and climatic conditions. Experimental studies of gold solubility, transport and precipitation mechanisms support the assumption that gold is, to some extent, remobilised during weathering as gold chloride and thiosulfate complexes (Benedetti & Boulègue, 1991; Pokrovski et al., 2014; Perera et al., 2005; Zotov et al., 2018), although some authors argue for limited gold mobility and thus limited migration/dispersion (Bowell et al., 1993; Vishiti et al., 2015; Horbe et al., 2019). So far, the effectiveness of gold migration and redeposition from primary ore zones, and the role of geochemical barriers, require further investigations.

However, a number of studies have demonstrated that lateritisation processes are associated with active gold remobilisation through dissolution-reprecipitation, grain coarsening and

increase in fineness with formation of Ag-poor rims (Colin and Lecomte, 1989; Freyssinet et al., 1989; Collin et al., 1991; Bamba et al., 2002; Larizatti et al., 2008; Falconer and Crow, 2009; Fairbrother et al., 2012). Spherulite of secondary gold can be observed on the surface of primary grains as evidenced by Bamba et al. (2002), commonly of high fineness due to the preferential leaching of Ag during weathering (Freyssinet et al., 2005).

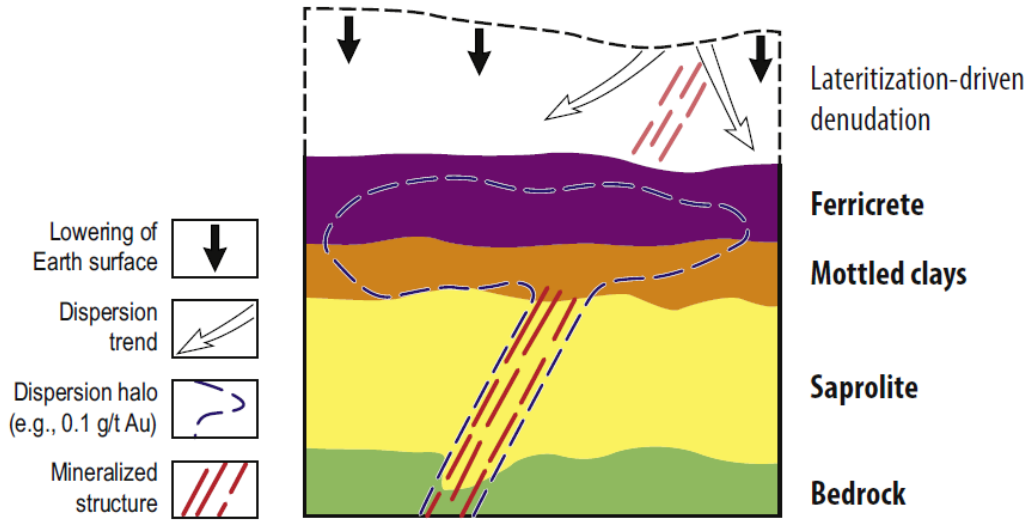

Figure 1-5 Gold dispersion model through the in situ or autochthonous regolith for ferricrete-capped West African landscapes (Chardon et al., 2018; adapted from Freyssinet et al., 2005).

In ferricrete-capped regolith developed after primary gold mineralisation, a dispersion halo may be identified within the residuum (Fig. 5) together with a dispersion trend from top to bottom and laterally due to lateritisation-driven denudation and lowering of the Earth paleo-surface (Freyssinet et al., 2005). Such haloes are generally narrow (Freyssinet et al., 2005).

When dealing with gold-bearing laterites, the evaluation of the mechanical transport component is essential together with the study of the geomorphology of the studied area in lateritic domain where primary mineralisation can be hidden.

Anand and Butt (2010) identify three regolith-landform regimes which are lateritic residuum, erosional plains/slopes and depositional sediments covering the weathering profile. Chardon et al. (2018) and Sawadogo et al. (2020) among others, highlight the importance of defining, in a studied area the erosional surfaces, the depositional surfaces and associated transported pediment material.

As illustrated in Figure 6 by Sawadogo et al. (2020), it is challenging to target the primary sources in a transported regolith environment. Indeed, the primary mineralisation can be (a)

truncated by a glacis/pediment and therefore be covered. The gold-bearing structure may (b) crops out in a truncated area and therefore no dispersion halo is encountered. As previously illustrated by Freyssinet et al. (2005), in the case of a complete profile (c) with a lateritic residuum on top, a mushroom-shape halo may form where an *in situ* geochemical anomaly may be detected. Finally, if a mechanical transport of mineralised material occurs in the pediment detrital cover, subsurface (d) to surface (e) gold anomalies are not indicative of underlying mineralisation in the basement. .

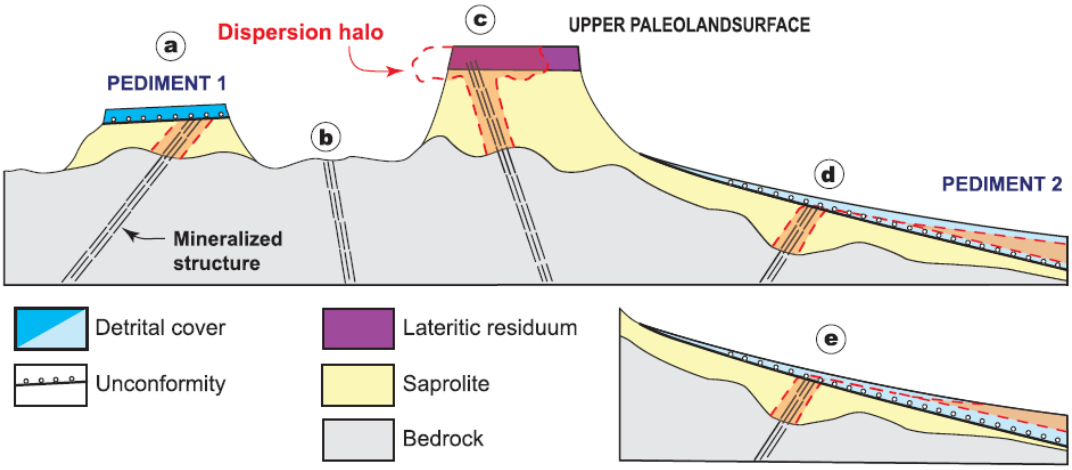

Figure 1-6 Sketch of each possibilities to hide, transport or disperse an Au-bearing (Sawadogo et al., 2020).

In French Guiana and more generally across the Guiana Shield, the formation of lateritic and placer gold deposits is assumed to be related to the recent (i.e., Phanerozoic) geomorphological and weathering history that shaped the modern landscape of the region. Lateritisation and erosion cycles affected primary gold occurrences and deposits, resulting in the development of deeply weathered gold-bearing regolith and placers. Across French Guiana, Theveniaut and Freyssinet (2002) recognised a succession of lateritisation and erosion phases associated with the formation of secondary gold deposits, including (1) early (Paleocene-Eocene) lateritic weathering corresponding to the Sul Americano lateritisation cycle at ca. 40-50 Ma (resulting from the warm and perhumid conditions that prevailed during the Paleocene–Eocene Thermal Maximum (PETM)), (2) a strong erosion period during the Oligocene (ca. 23-30 Ma) and (3) a late Miocene lateritisation event (Late Velhas cycle, 5-13 Ma). Regarding the time scale of lateritisation, Freyssinet & Farah (2000) estimated, along a lateritic profile at Yaou, a saprolitisation and a latosol development rate of 7.5 and 4.5 m/Ma, respectively, thus resulting in a chemical thickening rate of 3 m/Ma

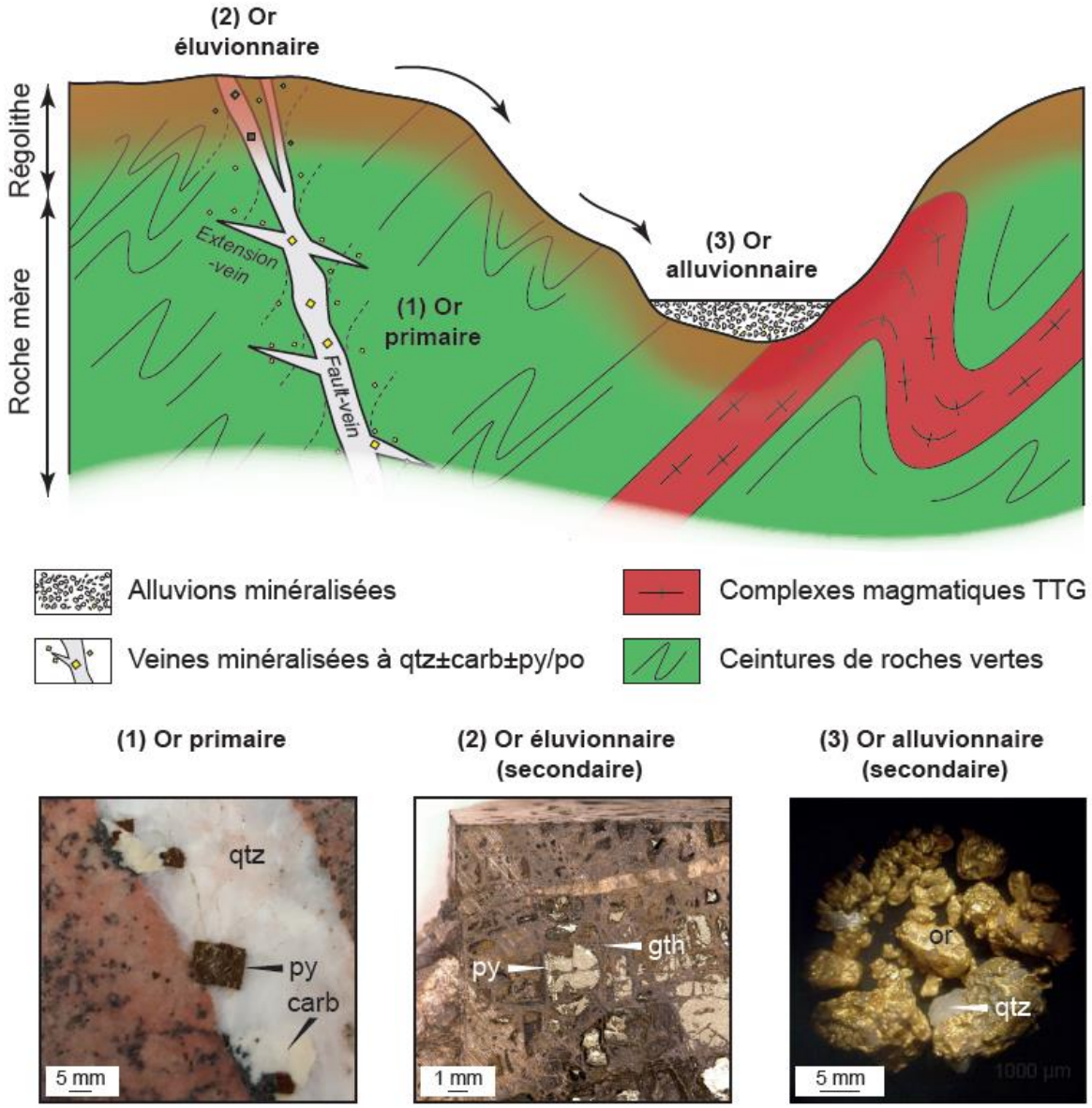

Figure 1-7 Overview of the primary and secondary gold mineralisation with examples from French Guiana (Eglinger et al., 2020)

The Paleoproterozoic Guiana Shield

The Guiana Shield (NE of South America), part of the Amazon craton (with the Guaporé Shield at its south), is the counterpart of the West African Craton in Africa. Both share an history of crustal growth and collision phase related to the Trans-Amazonian orogeny in South America and the Eburnean orogeny in West Africa (Onstott et al., 1984; Vanderhaeghe et al., 1998, Goldfarb et al., 2017).

A paleo-reconstruction of the Guiana and West Africa shields, during the Cretaceous is presented in Figure 8 (modified from Goldfarb et al., 2017 after Frimmel et al., 2014) where location of greenstone belt-hosted orogenic gold deposits (yellow) and conglomerate-hosted gold deposits (orange) are mentioned.

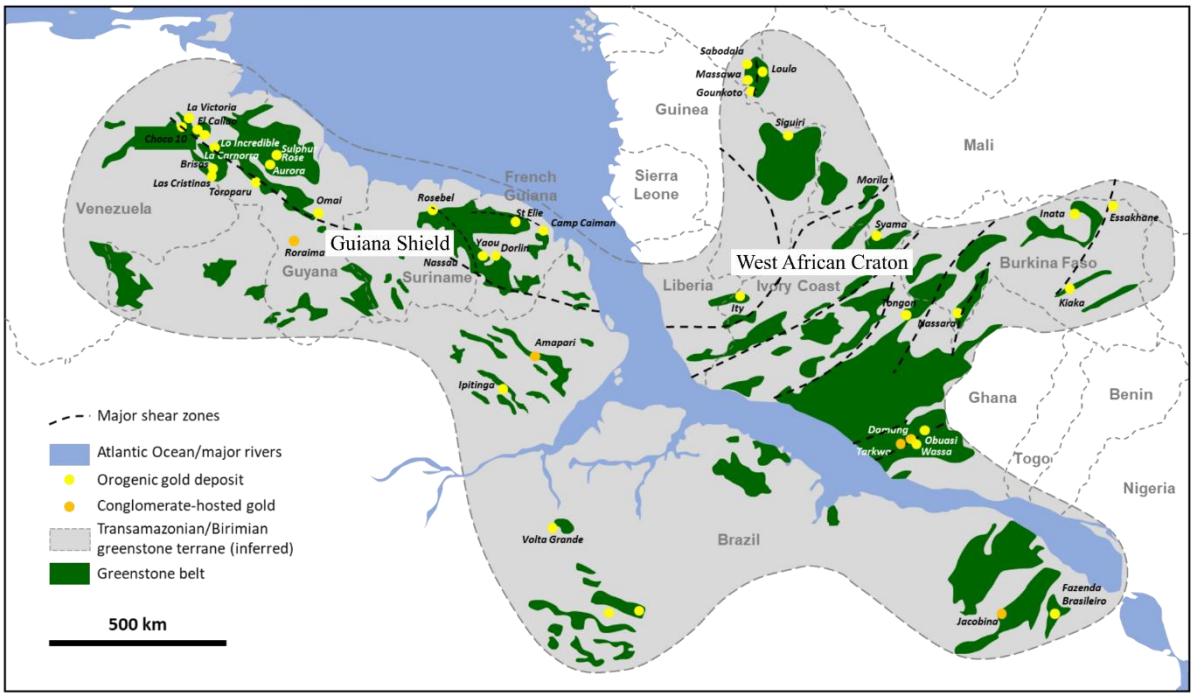

Figure 1-8 Paleo-reconstruction of the Guiana Shield and West African Craton during the Cretaceous (pre-rift fit of Africa and South America), (modified from Goldfarb et al., 2017 after Frimmel et al., 2014)

Chardon et al. (2020) propose a new reconstruction during the Neoproterozoic of the two cratons (Fig. 9) using paleomagnetic data. This model, displaying a 37° anticlockwise rotation of the Guiana Shied, highlights the main fabrics and main shear zones (orogen-scale) across both cratons.

Main geotectonic units within the Guiana Shield

The Guiana Shield which forms the northern part of the Amazonian Craton displays different geotectonic units as reviewed by Kroonenberg et al. (2016). These units are presented in the simplified map of the Guiana Shield (Fig. 10) modified after Kroonenberg et al. (2016) where two major Archean nuclei are mapped, the Imataca block in the west and the Amapa block in the East (Gaudette et al., 1978; Kroonenberg et al., 2016). The Trans-Amazonian belt, located in the North, is composed of volcano-sedimentary formations, TTG complexes and late intrusions.

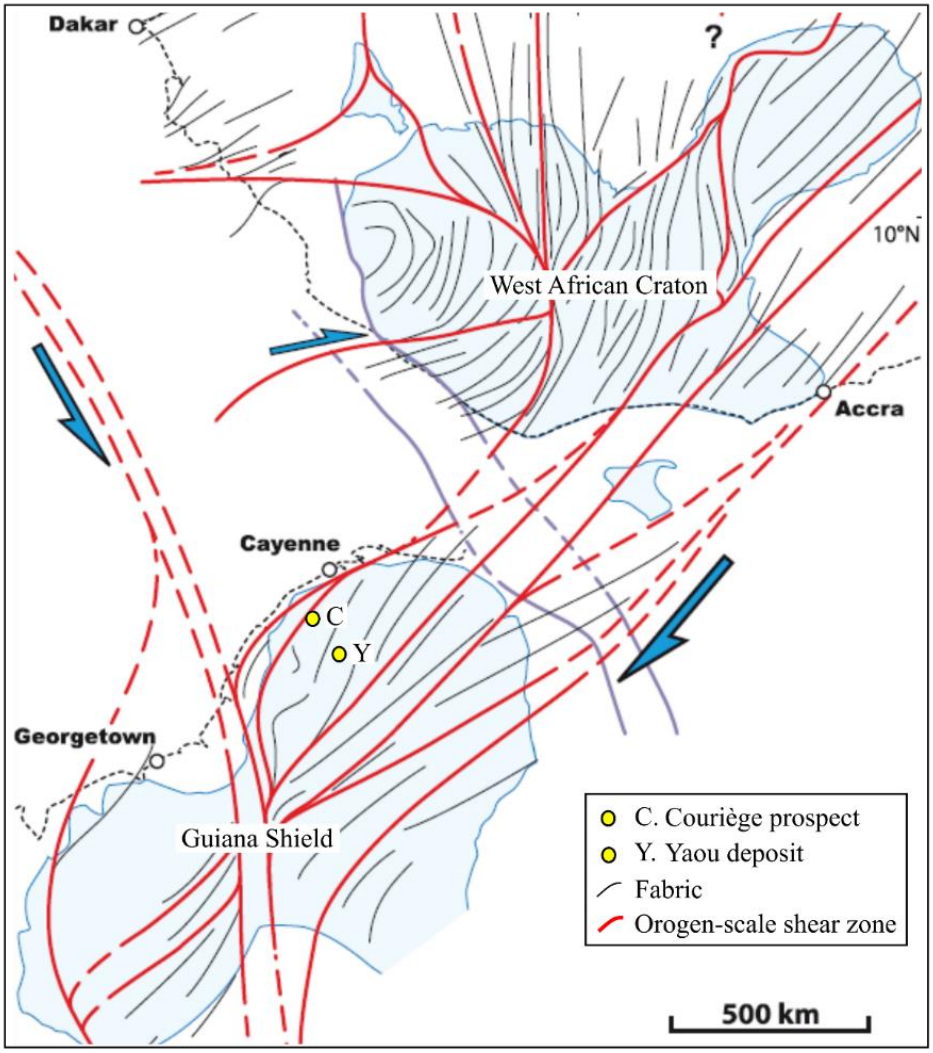

Figure 1-9 Structural pattern of the Eburnean-Trans-Amazonian orogens from Chardon et al. (2020) with addition of the Yaou and Couriège site.

Geodynamic evolution model for the Guiana Shield terranes witnessed by the tectono-metamorphic features

The Guiana Shield corresponds to a vast Precambrian domain that spans over 1.5 million km^2 delimited by two Archean cores (e.g. the blocks Imataca and Amapá outcropping in Venezuela and Brazil respectively) forming Paleoproterozoic domains during the Trans-Amazonian orogeny between ca. 2.26 and 1.95 Ga (Tassinari and Macambira, 1996). In French Guiana, geological formations are dated mainly between ca. 2.26 and 2.06 Ga and can be divided into four large lithotectonic units (Vanderhaeghe et al., 1998; Delor et al., 2003a, b; Fig. 11): (1) the Paramaca greenstone belts dominated by volcano-sedimentary rocks; (2) the magmatic complexes of the TTG type (Tonalite-Trondhjemite-Granodiorite) coeval with the greenstone belts; (3) the Upper Detrital Unit dominated by conglomerates, pelites and sandstones and (4) granitic metaluminous to peraluminous suites.

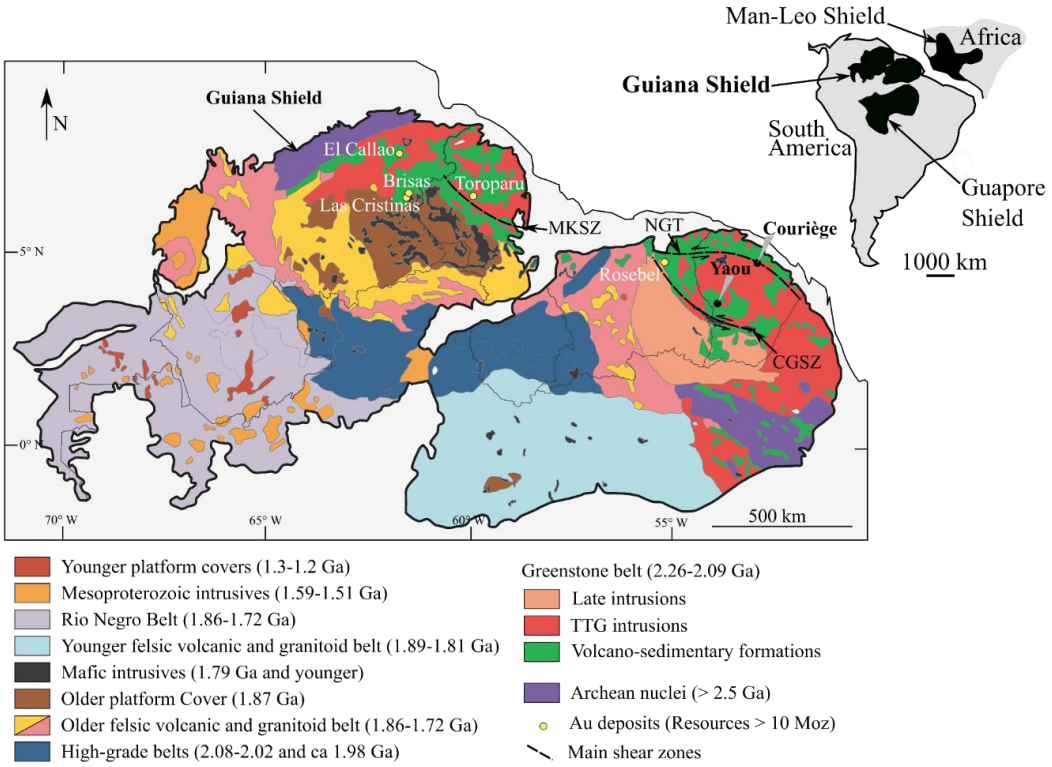

Figure 1-10 Simplified geological map of the Guiana Shield modified after Kroonenberg et al. (2016).

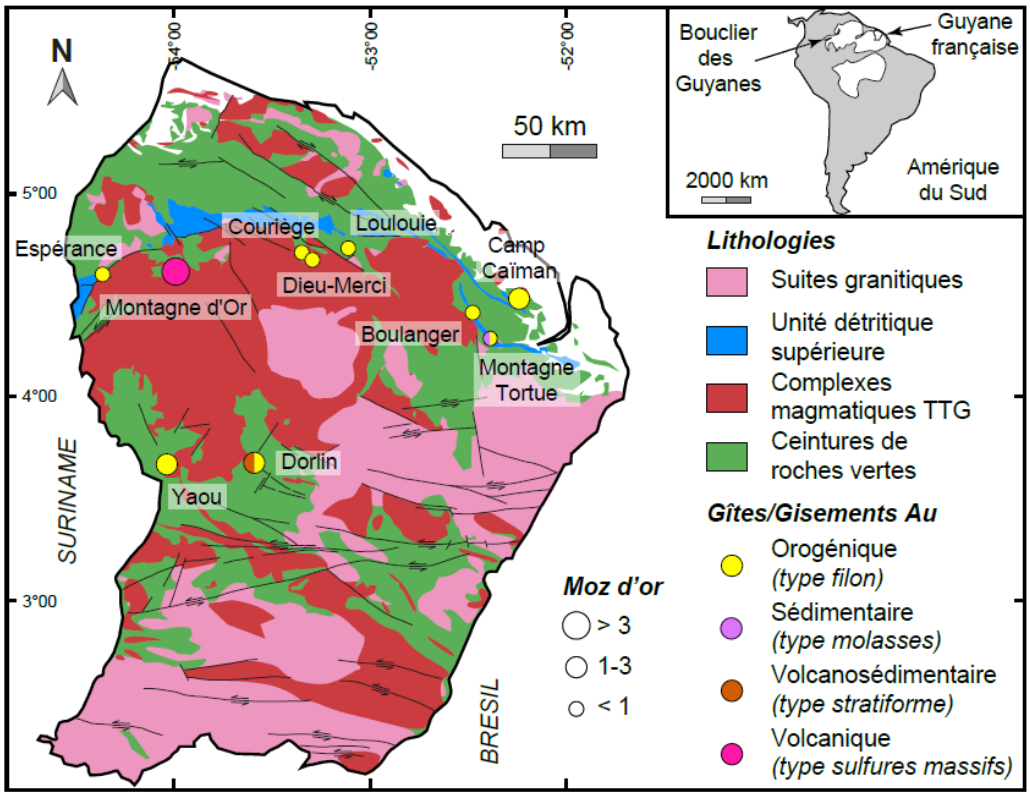

Figure 1-11 Geological map of French Guiana with location of the main Au deposits including the Yaou deposit and Couriège prospect. Modified from Delor et al. (2003b) and Eglinger et al. (2020).

All these units were deformed and metamorphosed during a complete orogenic cycle (Fig. 12) at the Rhyacian period. The Trans-Amazonian cycle begins with the formation of an oceanic lithosphere at the Eorhyacian (ca. 2.26-2.20 Ga) between Archean cratons of the West Africa and North Amazonia (Vanderhaeghe et al., 1998; Delor et al., 2003a). The closure of this oceanic domain by subduction (ca. 2.18-2.13 Ga), generates the establishment of TTG type intrusions in context of magmatic arcs and synchronous filling by volcano-sediments from the back-arc basin (Paramaca). The Eorhyacian and the Mesorhyacian mark a period of juvenile magmatic accretion and therefore of major crustal growth in the Paleoproterozoic (Vanderhaeghe et al., 1998).

The end of the subduction period is marked by the tectonic accretion of these different sets of magmatic arcs and closure of these basins during the Neorhyacian period (ca. 2,11-2.06 Ga) which is accommodated by large-scale sinistral sliding. The transcurrent tectonics allows the development of late sedimentary basins of pull-apart type (Ledru et al., 1991). The conglomerate series with sandstone which constitute the Upper Detrital Unit should be considered as unconformable deposits in these extensional basins. This period of crustal thickening is accompanied by the emplacement of granite suites (metaluminous to peraluminous) of potassium affinity showing a period of crustal remobilisation by partial melting of the juvenile crust formed by TTG sets and associated greenstone belts.

According to Milesi et al. (2003) and Delor et al. (2003b), it is possible to highlight two key parameters that control the location of gold mineralisation in French Guiana namely (1) associated with the Paramaca Greenstone Belts (PGB) and magmatic TTG complexes and (2) formed in a distinct geodynamic context, which are the subduction period (expressed by the presence of magmatic arcs and back-arc basins) and the collision zones (underlined by the development of syn- to late-orogenic structures).

Gold deposits in French Guiana can then be considered as markers of geodynamic environments in which they formed or were remobilised during the Rhyacian period. Indeed, for example, the deposit of Montagne d'Or (5 Moz at 1.5 g/t Au; Guiraud et al., 2020) is closely associated with the establishment of a bimodal volcanic and volcanoclastic sequence coeval with arc magmatism (Guiraud et al., 2020).

There, mineralisation is expressed as a VMS (Volcanogenic Massive Sulphide) Au-rich type deposit dated between ca. 2.15 and 2.12 Ga, i.e., Mesorhyacian (Guiraud et al., 2020).

Other deposits, such as the Dorlin deposit (45Mt @ 1.1-1.2 g/t Au), were interpreted as syngenetics, in the same context of basin and island arc. Gold mineralisation is associated with intense tourmalinisation and this deposit is classified as stratiform/stratabound and associated with volcano-sedimentary series of the Paramaca (Lerouge and al., 1998). Based on relative timeline data, it would be earlier than ca. 2.13 Ga (Milési et al., 2003). The particularity of Dorlin lies in the fact that this deposit has been overprinted by a brittle late-orogenic deformation with the formation of a network of gold veins of quartz-carbonate and a strong associated pyritisation, dated to ca. 2.06 Ga (Marcoux et Milesi, 1993). The Montagne Tortue gold occurrence is characterised by mainly disseminated gold mineralisation in deformed polygenic conglomerates belonging to the Upper Detrital Unit and emplaced by infilling of the syn-orogenic basins of the North Guiana Trough (Ledru et al., 1991; Milési et al., 1995). The mineralisation is polyphase with a second expression of orogenic gold associated with quartz-tourmaline veins (Milési et al., 2003). In this context of tectonic accretion, other syn- to late-deformation gold deposits have also been described as corresponding to discordant vein mineralisation (mainly veins and stockworks). The gold mineralised system described in French Guiana shares strong similarities with the geodynamics and metallogeny of the West African Craton (Goldfarb et al., 2017; Masurel et al., 2020; Thébaud et al. al., 2020). Indeed, the Amazonian and West African cratons were amalgamated while forming the supercontinent Columbia between 2.1-1.8 Ga during the orogenic cycles of the Eburnean in West Africa and Trans-Amazonian in South America (Rogers and Santosh, 2002), hence similar geodynamics, tectonics and metallogenic very close components.

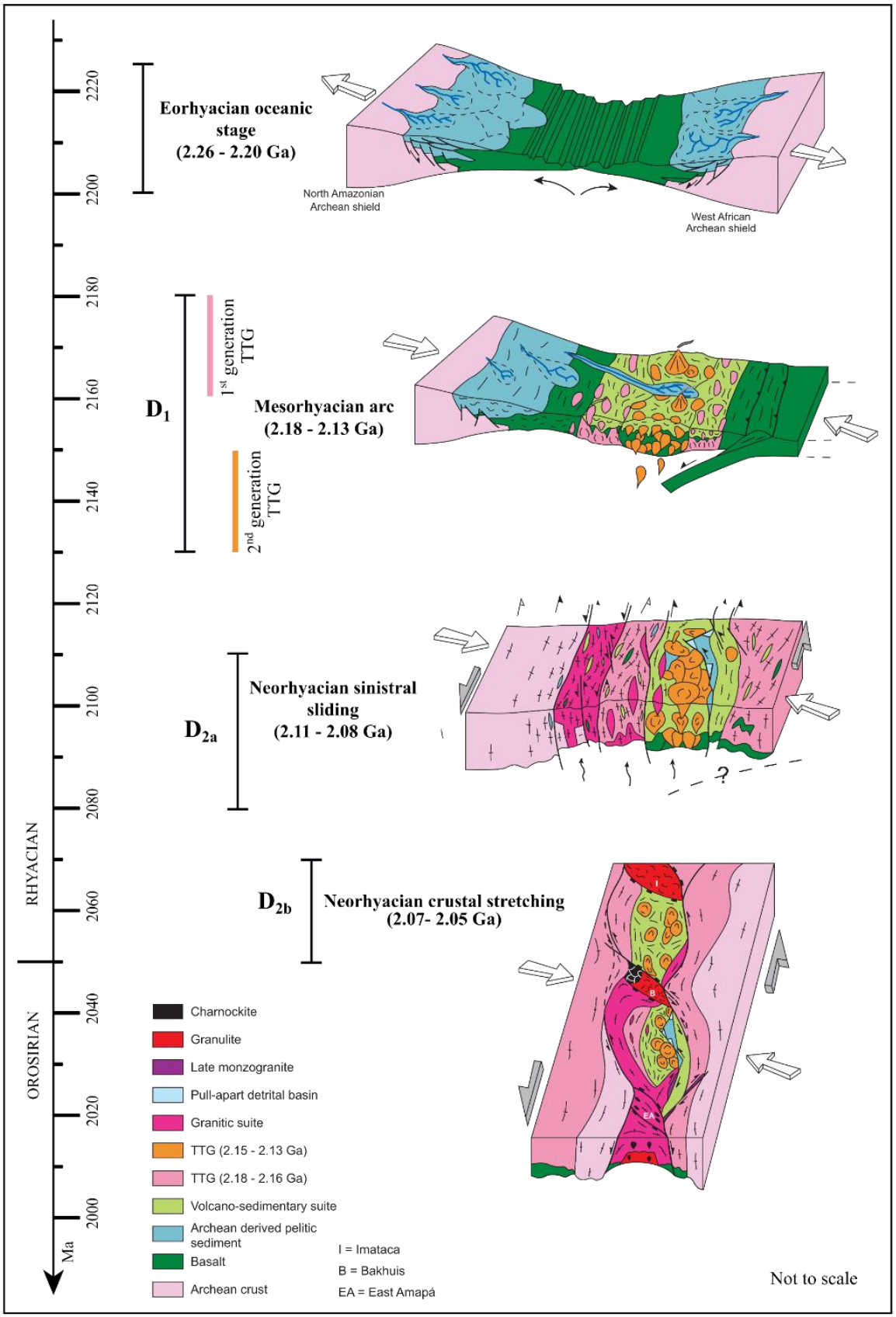

Figure 1-12 Geodynamic evolution model for the Guiana Shield terranes modified after Delor et al. (2003b).

References

Anand, R., Lintern, M., Hough, R., Noble, R., Verrall, M., Salama, W., Balkau, J., Radford, N., 2017. The dynamics of gold in regolith change with differing environmental conditions over time. Geology 45, 127–130.

Anand, R.R., Hough, R.M., Salama, W., Aspandiar, M.F., Butt, C.R.M., Gonzalez-Alvarez, I., Metelka, V., 2019. Gold and pathfinder elements in ferricrete gold deposits of the Yilgarn Craton of Western Australia: a review with new concepts. Ore Geol Rev. 104, 294-355.

Augustin, J., Gaboury, D., 2018. Multi-stage and multi-sourced fluid and gold in the formation of orogenic gold deposits in the world-class Mana district of Burkina Faso - Revealed by LA-ICP-MS analysis of pyrites and arsenopyrites. Ore Geol Rev. 104:495-521.

Bamba, O., Parisot, J.C., Grandin, G., Beauvais, G., 2002. Ferricrete genesis and supergene gold behaviour in Burkina Faso, West Africa. Geochem. Explor. Environ. Anal. 2, 3–14.

Benedetti, M., Boulegue, J., 1991. Mechanism of Au transfer and deposition in a supergene environment. Geochim. et Cosmochim Ac. 55, 1539–1547.

Blenkinsop, T. G., Oliver, N.H.S., Dirks, P.G.H.M, Nugus, M. Tripp, G., Sanislav, I., 2020. Structural Geology Applied to the Evaluation of Hydrothermal Gold Deposits. Society of Economic Geologists. Reviews in Econ. Geol. 21, 1–23.

Bowell, R.J., Foster, R.P., Gize, A.P., 1993. The mobility of gold in tropical rain forest soils. Econ. Geol. 88, 999–1016.

Bucci, L.A., Hagemann, S., Groves, D.I., and Standing, J.G., 2002. The Archean Chalice gold deposit: a record of complex, multistage, high temperature hydrothermal activity and gold mineralisation associated with granitic rocks in the Yilgarn Craton, Western Australia. Ore Geol Rev. 19,.23–6.

Burrows, D.R., Spooner, E.T.C., 1987. Generation of a magmatic H2O-CO2 fluid enriched in Mo, Au, and W within an archean sodic granodioritic stock, Mink Lake, Northwestern Ontario. Econ. Geol. 82, 1931–1957

Butt, C.R.M., 1998. Supergene gold deposits. AGSO J. Geo. Geophys. 17, 89–96.

Butt, C.R.M., Lintern, M., Anand, R.R., 2000. Evolution of regoliths and landscapes in deeply weathered terrain - implications for geochemical exploration. Ore Geol. Rev. 16, 167–183.

Butt, C.R.M., 2016. The development of regolith exploration geochemistry in the tropics and sub-tropics. Ore Geol. Rev. 73, 380–393.

Chardon, D., Grimaud, J.-L., Beauvais, A., Bamba, O., 2018. West African lateritic pediments:landform-regolith evolution processes and mineral exploration pitfalls. Earth- Sci. Rev. 179, 124–146.

Chardon, D., Bamba, O., Traoré, K., Eburnean deformation pattern of Burkina Faso and the tectonic significance of shear zones in the West African craton, 2020. BSGF-Earth Sci Bull. 191, 2.

Chauvet, A., 2019b. Structural Control of Ore Deposits: The Role of Pre-Existing Structures on the Formation of Mineralised Vein Systems. Minerals, 9, 56.

Colin, F., Lecomte, P., Boulange, B., 1989. Dissolution feature of gold particles in a lateritic profile at Dondo Mobi, Gabon. Geoderma 45, 241–250.

Colin, F., and Vieillard, P., 1991, Behavior of gold in lateritic equatorial environment: Weathering and surface dispersion of residual gold particles at Dondo Mobi, Gabon. J. Appl. Geochem. 6, 279–290.

Colin, F., Vieillard, P., and Ambrosi, J. P., 1993. Behavior of gold in lateritic equatorial environment: Mass transfer and thermodynamic study. Earth and Planetary Sci. Lett. 114, 269–285

Colvine, A.C., Fyon, J.A., Heather, K.B., Marmont, S., Smith, P.M. & Troop, D.G., 1988. Archean lode gold deposits in Ontario. Ontario Geological Survey Miscellaneous Paper, 139, 136.

Cook, N.J., Ciobanu, C.L., Meria, D., Silcock, D., and Wade, B., 2013. Arsenopyrite–pyrite association in an orogenic gold ore: tracing mineralization history from textures and trace elements. Econ Geol. 108, 1273–1283.

Couture, J.F., Pilote, P., Machado, N., and Desrochers, J.P., 1994. Timing of gold mineralization in the Val-d'Or district, southern Abitibi belt: Evidence for two distinct mineralizing events. Econ Geol. 89, 1542–1551.

Cox, S. F., 1995. Faulting processes at high fluid pressures: an example of fault-valve behaviour from the Wattle Gully Fault, Victoria, Australia. J. Geophys. Res. 100, 12,841–12,859.

Cox S.F., 2016. Injection-driven swarm seismicity and permeability enhancement: implications for the dynamics of hydrothermal ore systems in high fluid-flux, over-pressured faulting regimes-an invited paper. Econ. Geol. 111, 559–588.

Delor, C., Lahondère, D., Egal, E., Lafon, J.-M., Cocherie, A., Guerrot, C., Rossi, P., Truffert, C., Théveniaut, H., Phillips, D., Avelar, V.G.d., 2003b. 2-3-4 In: Transamazonian crustal growth and reworking as revealed by the 1:500000 scale geological map of French Guiana. Géol Fr, 5–57.

Delor, C., de Roever, E.W.F., Lafon, J.-M., Lahondère, D., Rossi, P., Cocherie, A., Guerrot, C., Potrel, A., 2003a. The Bakhuis ultrahigh-temperature granulite belt (Suriname) : II. Implications for late Transamazonian crustal stretching in a revised. Géol Fr. 2-3- 4, 207–230.

Dubé B, Gosselin P., 2007. Greenstone-hosted quartz-carbonate vein deposits, In Goodfellow, W.D., ed., Mineral deposits of Canada: a synthesis of major deposit types, district metallogeny, the evolution of geological provinces, and exploration methods. Geological Association of Canada, Mineral Deposits Division Spec Publ. 5, 49–73.

Eglinger, A., Thébaud, N., Zeh, A., Davis, J., Miller, J., Loucks, R., McCuaig, C., Belousova, E., 2017. New insights into the crustal growth of the Paleoproterozoic margin of the Archean Kéména-Man domain, West African craton (Guinea): Implications for gold mineral system. Precambrian Res. 292, 258–289.

Eglinger A., André-Mayer A.-S., Combes V., Teitler Y., Heuret A., 2020. Les gisements d'or de la Guyane française. Géologues. 206:36-40.

Fougerouse, D., Micklethwaite, S., Tomkins, A. G., Mei, Y., Kilburn, M., Guagliardo, P., Howard, D. L., 2016. Gold remobilisation and formation of high-grade ore shoots driven by dissolution-reprecipitation replacement and Ni substitution into auriferous arsenopyrite. Geochim. Cosmochim. Acta. 178, 143-159. https://doi.org/10.1016/j.gca.2016.01.040

Jébrak, M., Marcoux, E., 2008. Géologie des ressources minérales. Ministère des ressources naturelles et de la faune.

Jessell MW, Begg GC, Miller MS. 2016. The geophysical signatures of the West African Craton. Precambrian Res 274: 3–24.

Fairbrother, L., Brugger, J., Shapter, J., Laird, J.S., Southam, G., Reith, F., 2012. Supergene Au transformation: Biogenic secondary and nano-particulate Au from arid Australia. Chem. Geol. 320, 17–31.

Falconer, D., Craw, D., 2009. Supergene gold mobility: a textural and geochemical study from gold placers in southern New Zealand. Econ Geol. Spec. Publ. 14, 77–93.

Fougerouse D, Micklethwaite S, Ulrich S, Miller J, Godel B, Adams DT, McCuaig TC., 2017. Evidence for two stages of mineralization in West Africa's largest gold deposit: Obuasi, Ghana. Econ Geol. 112: 3–22.

Freyssinet, Ph., Lecomte, P., Edimo, A., 1989. Dispersion of gold and base metals in the Mborguene laterite profile. J. Geochem. Explor. 32, 99–116.

Freyssinet, P., Farah, A., 2000. Geochemical mass balance and weathering rates of ultramafic schists in Amazonia. Chem Geol. 170. 133-151.

Freyssinet, Ph., Butt, C.R.M., Morris, R.C., Piantone, P., 2005. Ore-forming processes related to lateritic weathering. In: Hedenquist, J.W., Thomson, J.F.H., Goldfarb, R.J., Richards, J.P. (Eds.), Econ Geol. 681–722

Frimmel, H., 2014, Giant Mesoarchean crustal gold-enrichment episode: Possible causes and consequences for exploration. Geol. Soc. Spec. Publ. 18, 209–234.

Gaboury, D., 2013. Does gold in orogenic deposits come from pyrite in deeply buried carbon-rich sediments?: Insight from volatiles influid inclusions. Geology. 41, 1207–1210.

Gaboury, D., 2019. Parameters for the formation of orogenic gold deposits. Appl. Earth Sci. 1-10. https://doi.org/10.1080/25726838.2019.1583310

Gaudette, H.E., Hurley, P.M., Espejo, A., Dahlberg, E.H., 1978. Older Guiana basement south of the Imataca Complex in Venezuela and in Suriname. Geol. Soc. Am. Bull. 89: 1290–1294.

Gibbs, A.K., Barron, C.N., 1993. The Geology of the Guiana Shield. Oxford University Press, USA, pp. 246.

Goldfarb, R. J., Groves, D. I., and Gardoll, S., 2001, Orogenic gold and geological time: a global synthesis. Ore Geol Rev. 18, 1–75.

Goldfarb, R.J., Bradley, D., Leach, D.L., 2010, Secular variations in economic geology. Econ. Geol. 105, 459-466.

Goldfarb R.J., Groves, D.I., 2015. Orogenic gold: common vs evolving fluid and metal sources through time. Lithos 223:2–26

Goldfarb, R.J., Baker, T., Dubé, B., Groves, D.I., Hart, C.J.R., Gosselin, P., 2005. Distribution, character, and genesis of gold deposits in metamorphic terranes. Econ. Geol. 100th Anniversary Volume. 407–450.

Goldfarb, R.J., André-Mayer, A.-S., Jowitt, S.M., Mudd, G.M., 2017. West Africa: The World's Premier Paleoproterozoic Gold Province. Econ. Geol. 112, 123-143.

Gourcerol B., Kontak D.J., Thurston P.C., Petrus J.A., 2018a. Gold and trace element distribution in sulfides from mineralized gold Algoma-type BIFs; Implications for nature of mineralizing fluids, metal sources and deposit models. Miner. Depos. 53:871-894.

Gourcerol, B., Kontak, D.J., Thurston, P.C., et Petrus, J.A. 2020, Application of LA ICP-MS analysis of arsenopyrite to gold metallogeny of the Meguma Terrane, Nova Scotia, Canada. Gondwana Res. 81, 265-290.

Groves D.I., 1993. The crustal continuum model for late-Archaean lode-gold deposits of the Yilgarn Block, Western Australia. Miner. Depos. 28:366–374

Groves, D.I., Goldfarb R.J., Gebre-Mariam, M., Hagemann S.G., Robert, F., 1998. Orogenic gold deposits–a proposed classification in the context of their crustal distribution and relationship to other gold deposit types. Ore Geol. Rev. 13, 7–27.

Groves, D.I., Santosh, M., Zhang, L., 2020b. A scale-integrated exploration model fororogenic gold deposits based on a mineral system approach. Geosci. Front. 11 (3), 719–738

Groves D.I., Santosh, M., 2016. The giant Jiaodong gold province: the key to a unified model for orogenic gold deposits? Geosc. Front. 7, 409–418

Groves, D. I., Santosh, M., Deng, J., Wang, Q., Yang, L., & Zhang, L., 2019. A holistic model for the origin of orogenic gold deposits and its implications for exploration. Miner. Depos. https://doi.org/10.1007/s00126-019-00877-5

Guiraud, J., Tremblay, A., Jébrak, M., Ross, P-S., Lefrançois, R., 2020. Stratigraphic setting and timing of the Montagne d'Or deposit, a unique Rhyacian Au-rich VMS deposit of the Guiana Shield, French Guiana. Precambr Res. 337, 105551.

Hastie, E., Kontak, D., Lafrance, B., 2020. Gold Remobilization: Insights from Gold Deposits in the Archean Swayze Greenstone Belt, Abitibi Subprovince, Canada. Econ Geol. 115. 241-277.

Horbe, A.M.C., Martins-Ferreira, M.A.C., Lima, R.S., 2019. Supergene gold characterization by geochemistry, grain morphology and Au-Ag-Cu-Te classification. J. S. Am. Earth Sci. 95, 102315.

Hough, R., Noble, R., Reich, M., 2011. Natural gold nanoparticles. Ore Geol Rev. 42. 55-61. 10.1016/j.oregeorev.2011.07.003.

Hronsky, J.A., 2019. Deposit-scale structural controls on orogenic gold deposits: an integrated, physical process-based hypothesis and practical targeting implications. Miner. Depos. https://doi.org/10.1007/s00126-019-00918z

Kolb, J., Rogers, A., Meyer, F.M., 2005, Relative timing of deformation and two-stage gold mineralization at the Hutti mine, Dharwar craton, India. Miner. Depos. 40, 156–174.

Kroonenberg, S.B., de Roever, E.W.F., Fraga, L., Reis, N., Faraco, T., Lafon, J.-M., Cordani, U., Wong, T., 2016. Paleoproterozoic evolution of the Guiana Shield in Suriname: a revised model. Neth. J. Geosci. 95, 491–522.

LaFlamme, C., Hollis, S. P., Jamieson, J. W., Fiorentini, M. L., 2018.Three-dimensional spatially constrained sulfur isotopes highlight processes controlling sulfur cycling in the near surface of the Iheya North hydrothermal system, Okinawa Trough. Geochem Geophys. 19, 2798–2812.

Large, R.R., Maslennikov, V., Robert, F., Danyushevsky, L.V., Chang, Z., 2007. Multistage sedimentary and metamorphic origin of pyrite and gold in the giant Sukhoi Log deposit, Lena gold province, Russia. Econ. Geol. 102, 1232-1267

Large, R.R., Danyushevsky, L.V., Hollit, C., Maslennikov, V., Meffre, S., Gilbert, S., Bull, S., Scotte, R., Emsbo, P., Thomas, H., Foster, J., 2009. Gold and trace element zonation in pyrite using a laser imaging technique: implications for the timing of gold in orogenic and Carlin-style sediment-hosted deposits. Econ. Geol. 104, 635–668.

Large, R.R., Thomas, L., Craw, D., Henne, A., Henderson, S., 2012. Diagenetic pyrite as a source for metals in orogenic gold deposits, Otago Schist, New Zealand. New Zealand J. Geol. Geophys. 55:2, 137-149,

Lawley, C.J.M., Selby, D., and Imber, J. 2013, Re-Os molybdenite, pyrite and chalcopyrite geochronology, Lupa Goldfield, southwestern Tanzania: Tracing metallogenic time scales at midcrustal shear zones hosting orogenic Au deposits. Econ Geol. 108, 1591–1613.

Larizzatti, H., Oliveria, S.M.B., Butt, C.R.M., 2008. Morphology and composition of gold in a lateritic profile, Fazenda Pison "Garimpo", Amazon, Brazil. J. S. Am. Earth Sci. 25, 359–376

Ledru P., Lasserre J.L., Manier E., Mercier D., 1991. Révision de la lithologie du Paléoprotérozoïque du craton guyanais. Tectonique transcurrente et dynamique des bassins sédimentaires. Bull. Soc. Geol. Fr., 162(4), 627-636

Le Mignot E, Reisberg L, Andre-Mayer AS, Bourassa Y, Fontaine A, Miller J.2017a, Re-Os geochronological evidence for multiple Paleoproterozoic gold events at the scale of theWest African craton. Econ Geol 112:145–168.

Le Mignot, E., Siebenaller, L., Béziat, D., André-Mayer, AS., Reisberg, L., Salvi, S., Velásquez, G., Zimmermann, C., Naré, A., Franceschi, G. 2017b. The Paleoproterozoic Copper-Gold Deposits of the Gaoua District,

Burkina Faso : Superposition of Orogenic Gold on a Porphyry Copper Occurrence? Econ Geol. 112. 99-122. 10.2113/econgeo.112.1.99.

Marcoux E., Milesi J.P., 1993. Lead isotope signature of Early Proterozoic ore deposit in Western Africa: comparison with gold deposits in French Guiana. Econ Geol. 88, 1862-1879.

Masurel, Q., Thébaud, N., Allibone, A., André-Mayer, A.-S., Hein, K. A. A., Reisberg, L., Bruguier, O., Eglinger, A., Miller, J. 2019. Intrusion-related affinity and orogenic gold overprint at the Paleoproterozoic Bonikro Au–(Mo) deposit (Côte d'Ivoire, West African Craton). Miner. Depos. 10.1007/s00126-019-00888-2

Masurel Q., Eglinger A., Thébaud N., Allibone A., André-Mayer A.S., McFarlane H., Miller J., Jessell M., Aillères L., Vanderhaeghe O., Salvi S., Baratoux L., Perrouty S., Begg G., Fougerouse D., Hayman P., Ousmane W., Tshibubudze A., Parra-Avila L., Kouamelan A., Ofori P. (in review). Gold metallogeny of the Paleoproterozoic part of the southern West African Craton: capturing distinct pulses within a Paleoproterozoic orogenic cycle. Miner. Depos.

McCuaig, T.C., Hronsky, J.M.A., 2014. The Mineral System Concept: the Key to Exploration Targeting. SEG 2014: Building Exploration Capability for the 21st Century. 153–175.

McFarlane, C.R.M., Mavrogenes, J., Lentz, D., King, K., Allibone, A., and Holcombe, R., 2011, Geology and intrusion-related affinity of the Morila gold mine, southeast Mali. Econ Geol. 106, 727–750.

Meffre S, Large RR, Steadman JA, Gregory DD, Stepanov AS, Kamenetsky VS, Ehrig K, Scott RJ., 2016. Multi-stage enrichment processes for large gold-bearing ore deposits. Ore Geol Rev 76:268–279.

Milesi, J., Lerouge C, Delór C, Ledru P, Billa M, Cocherie A, Egal E, Fouillac A, Lahondère D, Lasserre J, Marot A, Martel-Jantin B, Rossi P, Tegyey M, Théveniault H, Thiéblemont D, Vanderhaeghe, O., 2003. Gold deposits (gold-bearing tourmalinites, gold-bearing conglomerates, and mesothermal lodes), markers of the geological evolution of French Guiana: geology, metallogeny, and stable isotope constraints. Géol Fr, 2-3-4:257-290.

Onstott, T.C., Hargraves, R.B., York, D. and Hall, C., 1984. Constraints on the notions of South America and African Shields during the Proterozoic: 40Ar/39Ar and paleomagnetic correlations between Venezuela and Liberia. Geol. Soc. Am. Bull. 95, pp. 1045–1054.

Perera, W., Senanayake, Ga., Nicol, M., (2005). Interaction of gold(I) with thiosulfate–sulfite mixed ligand systems. Inorg Chim Acta. 358. 2183-2190.

Perret, J., Eglinger, A., André-Mayer, A.S., Aillères, L., Feneyrol, J., Hartshorne C., Abanyin, E., Bosc, R.., 2020. Subvertical, linear and progressive deformation related to gold mineralization at the Galat Sufar South deposit, Nubian Shield, NE Sudan. J. Struct. Geol. 135. 104032. 10.1016/j.jsg.2020.104032.

Peterson E, Mavrogenes J., 2014. Linking high-grade gold mineralization to earthquake-induced fault-valve processes in the Porgera gold deposit, Papua New Guinea. Geology 42:383–386

Petrella, L., Thébaud, N., LaFlamme, C., Miller, J., McFarlane, C., Occhipinti, S., Turner, S., Perazzo, S., 2019. Contemporaneous formation of veinhosted and stratabound gold mineralization at the world-class Dead Bullock Soak mining camp, Australia. Miner. Depos. 1–18. https://doi.org/10.1007/s00126-019-00902-7

Phillips G. N., Groves D. I., 1983. The nature of Archaean gold-bearing fluids as deduced from gold deposits of Western Australia. Aust. J. Earth Sci. 30:1-2, 25-39, DOI: 10.1080/00167618308729234

Phillips, G.N., and Powell R., 2010, Formation of gold deposits: a metamorphic devolatization model. J Metamorph Geol. 28, 689–718.

Phillips, G.N. & Powell, R., 2009. Formation of gold deposits: review and evaluation of the continuum model. Earth-Sci. Rev. 94, 1–21.

Pitcairn, I., Teagle, D.A.H., Craw, D., Olivo, G.R., Kerrich, R. and Brewer, T.S., 2006. Sources of metals and fluids in orogenic gold deposits: insights from the Otago and Alpine schists, New Zealand. Econ Geol. 101 (8), 1525-1546.

Pitcairn, I.K., Olivo, G.O., Teagle D.A.H., Craw, D., 2010. Sulfide evolution during prograde metamorphism of the Otago and Alpine Schists, New Zealand. Can Mineral. 48 (5), 1267-1295

Pitcairn, IK, Leventis, N, Beaudoin, G, Faure S, Dubé, B, 2017. A metasedimentary source of Au for the Abitibi? 15th Biennal SGA Conference, 20-23rd August 2017, Quebec, Canada.

Pokrovski, G., Akinfiev, N., Borisova, A., Zotov, A., Kouzmanov, K., 2014. Gold speciation and transport in geological fluids: Insights from experiments and physical-chemical modelling. 10.1144/SP402.4.

Pokrovski, G., Dubessy, J., 2015. Stability and abundance of the trisulfur radical ion S^{3-} in hydrothermal fluids. Earth and Planetary Science Letters. 411. 10.1016/j.epsl.2014.11.035.

Putnis, A., Mineral replacement reactions, 2009. Rev. Mineral. Geochem. 70, no. 1, 87–124.

Rogers, J.J.W., Santosh, M., 2002. Configuration of Columbia, a Mesoproterozoic supercontinent. Gondwana Res. 5, 5–22.

Sawadogo, B., Bamba, O., Chardon, D., 2020. Landform-regolith mapping in the West African context. Ore Geol Rev.126, 103782.

Sibson, R.H., Robert, F., Poulsen, K.H., 1988. High-angle reverse faults, fuid-pressure cycling, and mesothermal gold-quartz deposits. Geology 16, 551–555.

Simard, M., Gaboury, D., Daigneault, R., Mercier-Langevin, P., 2013, Multistage gold mineralization at the Lapa mine, Abitibi Subprovince: Insights into auriferous hydrothermal and metasomatic processes in the Cadillac-Larder Lake Fault Zone. Miner. Depos. 48, 883–905.

Sung, Y.-H., Brugger, J., Ciobanu, C.L., Pring, A., Skinner, W., and Nugus, M., 2009, Invisible gold in arsenian pyrite and arsenopyrite from a multistage Archaean gold deposit: Sunrise Dam, Eastern Goldfields province, Western Australia. Miner. Depos. 44, 765–791.

Tassinari, C.C.G., Macambira, M.J.B., 1999. Geochronological provinces of the Amazonian 1083 Craton. Episodes 22, 174–182

Thébaud, N., Sugiono, D., LaFlamme, C., Miller, J., Fisher, L., Voute, F., Tessalina, S., Sonntag, I., Fiorentini, M., 2018. Protracted and polyphased gold mineralisation in the Agnew District (Yilgarn Craton, Western Australia). Precambrian Res 310:291–304.https:// doi.org/10.1016/j.precamres.2018.02.013

Thébaud N., Allibone A., Masurel Q., Eglinger A., Davis J., André- Mayer A.S., Miller J. et Jessell M., 2020. The Paleoproterozoic (Rhyacian) gold deposits of West Africa. Economic Geology, in press.

Théveniaut, H., Freyssinet, Ph.,2002. Timing of lateritization on the Guiana Shield: Synthesis of paleomagnetic results from French Guiana and Suriname. Palaeogeography, Palaeoclimatology, Palaeoecology. 178. 91-117.

Tomkins, A.G. & Mavrogenes, J., 2002. Mobilization of Gold as a Polymetallic Melt during Pelite Anatexis at the Challenger Deposit, South Australia: A Metamorphosed Archean Gold Deposit. Econ Geol. 97. 1249-1271. 10.2113/gsecongeo.97.6.1249.

Tomkins, A.G., Grundy, C., 2009. Upper temperature limits of orogenic gold deposit formation: constraints from the granulite-hosted Griffin's Find Deposit, Yilgarn Craton. Econ. Geol. 104, 669–685

Tomkins A.G. (2013) On the Source of Orogenic Gold. Geology, 41 (12), 1255–1256

Vanderhaeghe, O., Ledru, P., Thiéblemont, D., Egal, E., Cocherie, A., Tegyey, M., Milesi, JP., 1998. Contrasting mechanism of crustal growth: Geodynamic evolution of the Paleoproterozoic granite–greenstone belts of French Guiana. Precambrian Res. 92:165–193.

Velásquez, G., Béziat, D., Salvi, S., Siebenaller, L., Borisova, A.Y., Pokrovski, G.S., De Parseval, P., 2014, Formation and deformation of pyrite and implications for gold mineralization in the El Callao district, Venezuela. Econ Geol. 109, 457–486.

Vishiti, A., Suh, C., Lehmann, B., Egbe, J.A., Shemang, E., 2015. Gold grade variation and particle microchemistry in exploration pits of the Batouri gold district, SE Cameroon. J Afr Earth Sci. 111. 1-13.

Voisey C.R., Willis, D., Tomkins, A.G., Wilson, C.J.L., Micklethwaite, S., Salvemini, F., Bougoure, J., Rickard, W.D.A., 2020. Aseismic Refinement of Orogenic Gold Systems. Econ. Geol. 115, 33-50.

Webster, J. G.; Mann, A. W., 1984. The influence of climate, geomorphology and primary geology on the supergene migration of gold and silver. Geochem. Explor. 22: 21-42.

Wyborn, L.A.I., Heinrich, C.A., Jaques, A.L., 1994. Australian Proterozoic Mineral Systems: Essential Ingredients and Mappable Criteria. Australasian Institute of Mining and Metallurgy Annual Conference, Melbourne, 109–115.

Wyman, D.A., Cassidy, K.F., Hollings, P., 2016. Orogenic gold and the mineral systems approach: resolving fact, fiction and fantasy. Ore Geol. Rev. 78, 322–335.

Xue Y, Campbell IH, Ireland TR, Holden P, Armstrong R., 2013. No mass-independent sulfur isotope fractionation in auriferous fluids supports a magmatic origin for Archean gold deposits. Geology 41:791-794

Zotov, A., Kuzmin, N., Reukov, V., Tagirov, B., 2018. Stability of AuCl2− from 25 to 1000 °C at Pressures to 5000 bar and Consequences for Hydrothermal Gold Mobilization. Minerals. 8. 286.

Chapitre 2

La minéralisation aurifère polyphasée du gisement de Yaou en Guyane. Résumé en français

Le gisement de Yaou, situé en Guyane française dans le Bouclier Guyanais, est l'un des gisements aurifères les plus prometteurs des ceintures de roches vertes Paléoprotérozoïque dite du Paramaca. Il présente de nombreux corps intrusifs alignés le long d'une zone de cisaillement à cinématique senestre où un modèle à cinq phases de déformation est établi lors de cette étude à l'échelle du camp. La phase ductile $D_{1/2YA}$ est responsable de la schistosité pénétrative principale tandis que la phase D_{3YA} est associée au cisaillement. Un événement magmatique est identifié comme étant pré à syn-D_{3YA}. La phase suivante D_{4YA} représente un ensemble de veines de quartz-carbonate exprimées dans le régime cassant, hébergées préférentiellement dans des corps intrusifs et le long de la zone de cisaillement. Une bréchification D_{5YA} recoupe les veines D_{4YA}. Sont associés à cet historique de déformation, deux événements aurifères (D_{3YA} et D_{4YA}) qui contrôlent le budget global aurifère du gisement de Yaou. Plus précisément, la majeure partie de l'or est associée au principal événement économique D_{4YA}, où l'or est visible et lié à la pyritisation Py_4 localisée dans un halo d'altération riche en ankérite et hématite. À l'échelle microscopique, les résultats d'analyses *in situ* de LA-ICP-MS sur la pyrite montrent que la pyrite Py_0 hébergé par des métasédiments est une source principale d'or submicroscopique ayant une faible contribution à la dotation totale. La pyrite Py_3 montre une certaine teneur en or due à une remobilisation probable de l'Au_{D0YA} ou à un nouveau dépôt. L'or dans la pyrite Py_4 se trouve sous forme d'or submicroscopique, de micro-inclusions et de remplissage de micro-fracture en association avec des éléments tels que le Te, Ag et Bi. La majeure partie de la contribution en Au provient de micro-inclusions et, dans une moindre mesure, d'or libre et submicroscopique. Concernant la localisation de la minéralisation, on définit un contrôle lithologique pour Au_{D0YA} (hébergé dans les métasédiments), structural (zone de cisaillement) pour Au_{D3YA} et rhéologique pour Au_{D4YA} (veines aurifères hébergées par des corps intrusifs). Le gisement est clairement polyphasé à la fois à l'échelle macroscopique et microscopique, l'or invisible est associé à l'Arsenic alors que l'or visible est observé sous forme d'inclusions dans la pyrite à haute teneur en Ag, Te et Bi. Nous définissons un enrichissement précoce à faible teneur de Au_{D0YA} en Au_{D3YA} suivi d'un événement ultérieur à haute teneur, Au_{D4YA} impliquant des processus de minéralisation polyphasés. Cette étude confirme que des gisements d'or orogéniques peuvent être formés par remobilisation et / ou nouveaux apports d'or lors de multiples événements de déformation, de systèmes de veines et d'hydrothermalisme.

Publication #1

(Accepted 09/2020 in the Geological Society London-Special Publication)

Polyphase gold mineralisation at the Yaou deposit, French Guiana

Vincent Combes[1, 2, *], Aurélien Eglinger[1], Anne-Sylvie Andre-Mayer[1], Yoram Teitler[1], Arnauld Heuret[3], Pierre Gibert[2], Didier Béziat[4]

[1]Université de Lorraine-CNRS, CREGU, laboratoire GeoRessources, 54500 Nancy, France
[2]AMG, Auplata Mining Group, ZI Dégrad des Cannes, 97354, Rémire Montjoly, France
[3]Université de Guyane / Géosciences Montpellier (UMR 5243), 97300 Cayenne, France
[4]Géosciences Environnement Toulouse (GET), Université Paul Sabatier, CNRS, IRD, OMP, 14 avenue Edouard Belin, 31400 Toulouse, France

* correspondence (vincent.combes@univ-lorraine.fr)

Abstract

The Yaou deposit, located in French Guiana within the Guiana Shield, is one of the most promising gold deposits of the regional Palaeoproterozoic greenstone belt. It displays numerous quartz monzodiorite bodies aligned along a sinistral shear zone where a five-deformation phases model is established at the camp scale. The ductile $D_{1/2YA}$ phase is responsible for the main penetrative foliation while the D_{3YA} phase is related to shearing. An intrusive event is identified as being pre to syn-D_{3YA}. The following phase D_{4YA} represents a brittle quartz-carbonate veining set hosted preferentially within intrusive bodies and along the shear zone. A local D_{5YA} brecciation event crosscuts the D_{4YA} veins. Among this deformation history, two auriferous events (D_{3YA} and D_{4YA}) control the overall grade of the Yaou gold deposit. More specifically, most of the Au grade is associated with the main economic D_{4YA} veining event, where the gold is visible and linked to Py_4 within an ankerite/hematite rich alteration halo. At the microscopic scale, results of *in situ* analyses using LA-ICP-MS on pyrite show that metasediment-hosted Py_0 is a primary source of submicroscopic gold having a low contribution to the total endowment. Py_3 shows some gold content due to possible remobilisation of Au_{D0YA}. Gold in Py_4 is found as submicroscopic gold, as micro-inclusions and as infilling fractures in association with elements such as Te, Ag and Bi. Most contribution to the Au grade is from micro-inclusions and, to a lesser extent, from free and submicroscopic gold. The ore shoot

locations are lithologically controlled for Au_{D0YA} (metasedimentary unit-hosted), structurally controlled (shear zone-hosted) for Au_{D3YA} and rheologically controlled for the Au_{D4YA} (intrusion-hosted). The deposit is clearly polyphase both at the macroscopic and the microscopic scales, invisible gold is associated with As whereas visible gold is observed as inclusions in pyrite with high contents of Ag, Te and Bi. We define an early low-grade enrichment of Au_{D0YA} to Au_{D3YA} followed by a later high-grade event, Au_{D4YA} supporting polyphase mineralisation processes. This study confirms that orogenic gold deposits can be formed by remobilisation and/or new gold inputs during multiple deformation, veining and hydrothermal events.

Keywords: Polyphase deposit-Deformation phases-Pyrite generation-Invisible Gold-Guiana Shield

Introduction

To link auriferous pulses with the spatial/temporal tectono-metamorphic evolution of granitoid-greenstone belts remains challenging (Golfarb *et al*., 2001; Goldfarb *et al*., 2005; Dubé & Gosselin, 2007; Phillips & Powell, 2009 ; Groves *et al*., 2020; Thébaud *et al*., accepted; Masurel *et al*., in review). The polyphase and/or progressive history of deformation and metamorphism associated with any possible protracted magmatic activity is used as a framework to answer key questions pertaining to orogenic gold systems, such as the polyphase *versus* monophase deposition of Au; the potential contribution of spatially associated intrusions the timing and type of ore shoot control (e.g., rheological, lithological or structural); the possible remobilisation of gold associated with local deformation; and the identification of metal sources. This kind of multi-scale and multi-method approach, integrating structural, petrological and geochemical data, has been used by Thebaud *et al*. (2018) from camp to deposit scale at the Agnew district in Western Australia.

It is important to investigate the deformation phases and associated vein sets, with great details at the deposit scale, while considering possible progressive deformation (Fossen *et al*., 2019; Perret *et al*., 2020). Pre-existing structures predating a gold input are important for locating ore shoots (Chauvet, 2019b) while deformation phases postdating gold event are significant for remobilisation processes (Tomkins & Mavrogenes, 2002; Cook *et al*., 2013; Fougerouse *et al*., 2016, among others). Based on camp-scale structural framework, various gold deposits have been identified as having a polyphase release of gold with protracted history of precipitation, remobilisation and sometimes new input, as evidenced by Couture *et al*. (1994), Bucci *et al*.

(2002), Kolb *et al*. (2005), Simard *et al*. (2013), Lawley *et al*. (2013), Meffre *et al*. (2016), Fougerouse *et al*. (2017), Augustin *et al*. (2018) and Gourcerol *et al*. (2020) among others. Thébaud *et al*. (2018) define a model of protracted and polyphase gold mineralisation through multiple hydrothermal events channeled through identical structures at distinct times. In a broader sense, polyphase gold deposits can express various mineralisation types corresponding to different geodynamic settings as recently evidenced within the West African Craton (WAC; Mc Farlane *et al*., 2011; Le Mignot *et al*., 2017a, Le Mignot *et al*., 2017b; Eglinger *et al*., 2017). As an example of a polyphase gold deposit within the WAC, the Bonikro deposit, in Ivory Coast, displays an intrusion-related gold system (dated at ca. 2086 Ma) emplaced during the tectonic accretion, followed by a lode gold veining event dated at ca. 2074 Ma interpreted as part of a late orogenic system (Masurel *et al*., 2019).

The robust deciphering of deformation phases expressed at the deposit scale in the framework of the regional evolution is therefore mandatory to unravel gold events that contribute to the overall gold endowment within a deposit. It relies, in addition to detailed petrographic investigation, on the identification of ductile *vs* ductile-brittle *vs* brittle nature of macro- and microstructures (Tikoff *et al*., 2013). Brittle deformation is associated with faulting/fracturing, while ductile deformation corresponds to folding and penetrative fabrics (Twiss & Moores, 2007; Fossen 2010). The resulting petro-structural framework is then based on cross-cutting features and kinematic markers, such as shear bands or strain fringes on porphyroclasts/porphyroblasts (Passchier & Trouw, 2005). Once this framework is established, the gold deposition needs to be assessed in the light of the associated deformation history. Following the evolution of gold deposition through time, in orogenic gold deposits is challenging due to the variable nature of gold observed in such environments (e.g., invisible *versus* visible gold). Invisible gold, also referred as submicroscopic gold, encompasses (1) Au^{+} solid-solution within pyrite or arsenopyrite, (2) Au^{0} nanoparticles (nano-inclusions) (Cabri *et al*., 1989; Cook and Chryssoulis, 1990, Wu *et al*., 2019) and (3) Au^{+} adsorbed on to these mineral surfaces (Becker *et al*., 2010). Contrastingly, visible gold occurs as micro-inclusions and/or as infills in pre-existing fractures and cracks within sulphides together with free gold (e.g., in quartz), (Mumin *et al*., 1994; Reich *et al*., 2005; Large *et al*., 2009; Sung *et al*., 2009; Deditius *et al*., 2014. Dubosq *et al*., 2018). Both invisible and visible Au are intimately associated with iron sulphides (Groves *et al*., 1998 ; Dubé and Gosselin, 2007; Dubosq *et al*., 2018). It is therefore important to define and discriminate pyrite generations in order to decipher gold ore genesis. The different pyrite generations are best discriminated from their textural

characteristics and structural position. Trace element compositions of pyrite may also prove to be useful to further discriminate pyrite generations, providing that each generation has a specific geochemical signature.

Optical studies coupled with in situ Laser Ablation Inductively Coupled Plasma Mass Spectrometry (LA-ICP-MS) analyses of trace elements in pyrite allow the identification and discrimination of associated gold typologies, as well as Au-bearing pyrite generations through the study of gold and other trace element distributions (sector zoning, oscillatory zoning, and irregular patches) in pyrite (Wu *et al*., 2019; Velasquez *et al*., 2014; Gourcerol *et al*., 2018a, b).

From these microscale observations, the role of deformation in remobilising the Au can be investigated: deformation at the microscale can drive and/or facilitate the Au-upgrading as discussed by Fougerouse *et al*. (2016) and Dubosq *et al*. (2018). High-grade ore shoots are typically synchronous with pervasive deformation as stated by Bleeker, 2015 and mostly associated with coupled dissolution – reprecipitation processes (Putnis, 2009, Fougerouse *et al*., 2016 and Hastie *et al*., 2020).

Currently, the proposed sources for gold-bearing fluids are linked to the metamorphic devolatilisation of metasedimentary and metavolcanic rocks (Phillips and Groves, 1983; Groves *et al*. 1998; Pitcairn *et al*., 2006, 2010, 2017; Large *et al*., 2007; Phillips and Powell, 2010; Gaboury *et al*. 2013; Tomkins *et al*. 2013; LaFlamme *et al*., 2018) or magmatic hydrothermal fluids (Burrows and Spooner, 1987; Tomkins, 2013; Xue *et al*., 2013). When intrusions are spatially associated with gold deposits, they can be either referred to as (1) intrusion-related with an important fluid contribution from the intrusive event (low sulphide content, low Au grade) as mentioned by Thompson *et al*. (1999) ; Lang *et al*. (2000) ; Lang and Baker (2001) and Hart 2005 ; or as (2) intrusion-hosted where the mineralised veins are located preferably within the fractures of the more competent intrusive body highlighting a rheological control (as example in the Guiana Shield at the Omai deposit by Voicu *et al*. (1999)). In such deposit the contribution of the intrusion is only mechanical with typical characteristics of orogenic gold deposit.

In such a challenging context of tracking and constraining the evolution of the gold endowment regarding (i) the recorded deformation history and (ii) geochemical processes involved in gold segregation (both spatially and temporally) in a Palaeoproterozoic orogenic environment, the Yaou deposit, represents an attractive case study. Historically, two styles of mineralisation have been identified at Yaou (Milesi *et al*., 2003), with no indication of their spatial/temporal

relationships. This deposit provides therefore an excellent opportunity to discuss the polyphase and/or protracted character of gold mineralisation, the contribution of each lithological unit/deformation phase and the possible Au sources.

Petro-structural observations and geochemical (EPMA and LA-ICP-MS on pyrite) data are here integrated using a multiscale approach (from macro- to microscopic scales) combined with a multidisciplinary approach (i) to establish the spatial and temporal relationship between deformation phases, vein generations, possible sulphide occurrences, hydrothermal alteration features and gold events, (ii) to understand the influence of the different units (granitoid, metasediment, metavolcanite) and the different tectonic phases (shearing, veining) in building/upgrading the deposit and (iii) to define the nature, the distribution and the (re-) mobilisation of gold through relative time and space in order to discuss the single phase *versus* polyphase character of the Yaou deposit and its spatial and temporal integration within the Guiana Shield.

Geological background

Regional geology

The Amazonian Craton, encompassing the Guiana Shield to the north and the Guapore Shield to the south, constitutes one of the largest pieces of the Columbia 'puzzle' (Bispo-Santos et al., 2014 and references therein), (Fig. 1A). The Guiana and Guapore Shields are separated by the Phanerozoic Amazonas sedimentary basin (Lacerda-Filho et al., 2004). The Guiana Shield was amalgamated to the West Africa Craton around 2000-1970 Ma during the Transamazonian-Eburnean tectono-thermal events (Bispo-Santos et al., 2014), in a configuration where the Guri (Guiana Shield) and Sassandra (West Africa) lineaments were aligned (Onstott and Hargraves, 1981). A large number of world class gold deposits formed during these events, including Las Cristinas (Ristorcelli et al., 2007) and El Callao in Venezuela (Velasquez et al., 2014); Omaï and Karouni in Guyana (Voicu et al., 1999; Tedeshi et al., 2018a, 2018b, 2019); Rosebel in Suriname (Daoust et al., 2011) and Montagne d'Or (Guiraud et al., 2017, 2020), Camp Caïman, Yaou and Dorlin in French Guiana (Milesi et al., 2003), for the Guiana Shield. For the West Africa Craton, refer to the synthesis of Masurel et al. (2020, in review). French Guiana belongs to the Guiana Shield which extends from northwest to southeast from eastern Venezuela to northern Brazil (Fig. 1A) and consists of a Palaeo- to Neoproterozoic granite-greenstone terrane (Santos et al., 2000).

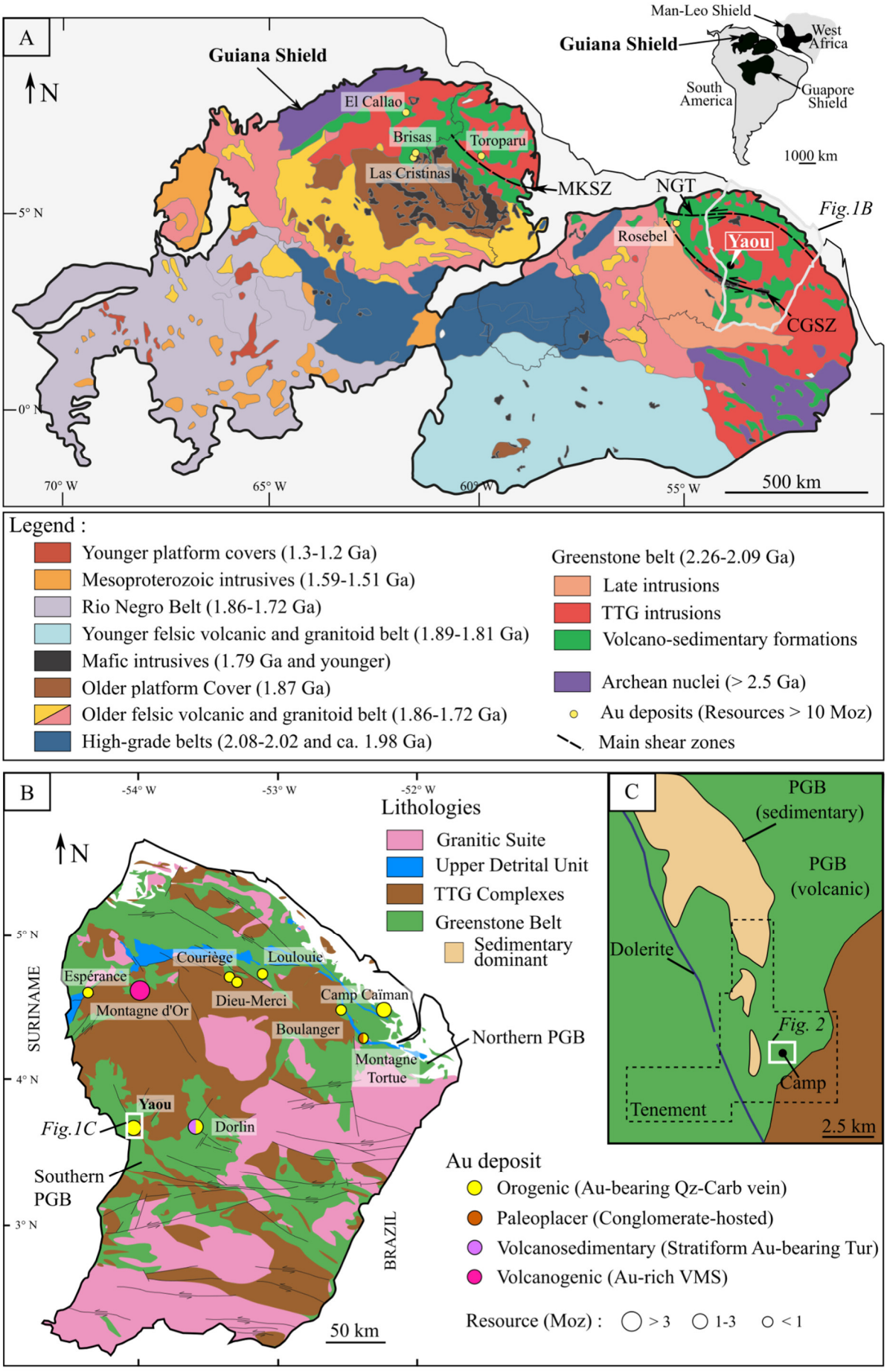
A
Guiana Shield
N
El Callao
Brisas
Toroparu
Las Cristinas
MKSZ
NGT
Fig.1B
Rosebel
Yaou
CGSZ
5° N
0° N
70° W
65° W
60° W
55° W
500 km
Man-Leo Shield
Guiana Shield
West Africa
South America
Guapore Shield
1000 km
Legend :
Younger platform covers (1.3-1.2 Ga)
Mesoproterozoic intrusives (1.59-1.51 Ga)
Rio Negro Belt (1.86-1.72 Ga)
Younger felsic volcanic and granitoid belt (1.89-1.81 Ga)
Mafic intrusives (1.79 Ga and younger)
Older platform Cover (1.87 Ga)
Older felsic volcanic and granitoid belt (1.86-1.72 Ga)
High-grade belts (2.08-2.02 and ca. 1.98 Ga)
Greenstone belt (2.26-2.09 Ga)
Late intrusions
TTG intrusions
Volcano-sedimentary formations
Archean nuclei (> 2.5 Ga)
Au deposits (Resources > 10 Moz)
Main shear zones
B
-54° W
-53° W
-52° W
Lithologies
Granitic Suite
Upper Detrital Unit
TTG Complexes
Greenstone Belt
Sedimentary dominant
N
5° N
4° N
3° N
SURINAME
BRAZIL
Couriège
Loulouie
Espérance
Montagne d'Or
Dieu-Merci
Camp Caïman
Boulanger
Montagne Tortue
Northern PGB
Yaou
Fig.1C
Dorlin
Southern PGB
50 km
C
PGB (sedimentary)
PGB (volcanic)
Dolerite
Fig. 2
Camp
Tenement
2.5 km
Au deposit
Orogenic (Au-bearing Qz-Carb vein)
Paleoplacer (Conglomerate-hosted)
Volcanosedimentary (Stratiform Au-bearing Tur)
Volcanogenic (Au-rich VMS)
Resource (Moz) : > 3 1-3 < 1

*Figure 2-1 (**a**). Geology of the Guiana Shield (modified from Kroonenberg et al., 2016). Gold deposits presented have total resources > 10 Moz. MKSZ: Makapa-Kuribrong Shear Zone, NGT: Northern Guiana Trough, CGSZ: Central Guiana Shear Zone. Geographic coordinates are reported as WGS 84. (**b**). Map of simplified Palaeoproterozoic formations located in French Guiana (modified from Delor et al., 2003a;). Main gold deposits are spatially associated with the two Paramaca Greenstone belts (PGB) and at contacts with the TTG complexes, deposit types from Marcoux & Milesi, (1993), Milesi et al. (2003). (Abbreviations are Tur = tourmalinite, VMS = Volcanogenic Massive Sulphide). (**c**). Yaou district lithology map (AMG internal map). The deposit is situated at the contact between the Southern Paramaca Greenstone Belt and the central TTG complex.*

Within French Guiana, four types of gold-bearing deposits are currently identified (Fig 1B): (1) Au-rich VMS (Volcanogenic Massive Sulphide) deposits as characterised by Franklin et al. (2000) and Guiraud et al. (2017, 2020) at Montagne d'Or; (2) stratiform/stratabound gold-bearing tourmalinites with disseminated sulphides as observed at Dorlin (Milesi et al., 2003) with an overprinting of late orogenic gold mineralization dated at 2.06 Ga (Marcoux and Milési, 1993); (3) gold-bearing polygenic conglomerates within the Upper Detrital Unit, exemplified by Montagne Tortue (Milesi et al., 1995) where the mineralisation is polyphase with an orogenic gold overprinting expressed by quartz-tourmaline veining (Milesi et al., 2003); and (4) orogenic gold deposits as observed at Yaou, Esperance, Loulouie, Boulanger and Camp Caïman (Milesi et al., 2003). The type and the distribution of these gold deposits are intimately related to the Transamazonian geodynamic evolution from ca. 2.25 Ga to 1.95 Ga (Enjolvy et al., 2008), which is characterised by a first stage of crustal growth/recycling followed by a stage of crustal reworking (Vanderhaerghe et al., 1998). The first stage is associated with the formation of an oceanic crust giving tholeiitic volcanic rocks dated at ca. 2.26 - 2.20 Ga (Vanderhaeghe et al., 1998; Delor et al., 2003a, b). Following the formation of juvenile crust, an early stage of arc construction in a compressional context occurred at ca. 2.18-2.13 Ga, by TTG (Tonalite-trondhjemite-granodiorite) complexes exhibiting calc-alkaline geochemical signatures (Vanderhaeghe et al., 1998; Delor et al., 2003 a, b). The onset of deformation D_1 is linked to this first period of crustal growth by magmatic accretion interpreted as a successive formation of magmatic arcs (Vanderhaeghe et al., 1998) or a protracted TTG process operating relatively continuously from ca. 2.18 Ga to 2.13 Ga (Delor et al., 2003a, b). The second period of crustal reworking is characterised by tectonic accretion and erosion/sedimentation/partial melting processes. Deformation D_{2a} is accommodated by sinistral strike-slip shear zones and records oblique convergence between crustal blocks (Vanderhaeghe et al., 1998). Syntectonic granitic intrusions emplaced between ca. 2.11 Ga and 2.08 Ga and foreland pull-apart basins initiated during D2a deformation event witness of this period of crustal thickening and partial

melting (Ledru et al., 1991; Delor et al., 2003b). A late D_{2b} deformation event dated at ca. 2.07-2.06 Ga is recorded by metamorphosed detrital sediments buried and exhumed during the final oblique collision between newly formed continental blocks (Vanderhaeghe et al., 1998; Delor et al., 2003 a, b). Regarding this geodynamic evolution, terranes in French Guiana (Fig. 1B) are defined as follows. A lower volcanic and sedimentary unit is composed of metagreywacke, flysch, meta-basalt, meta-andesite, meta-dacite, meta-rhyolite and meta-pyroclastics (Delor et al. 2003b). All these rocks constitute the two East-West-trending Paramaca Greenstone Belts (PGB) of Gibbs (1980), (Southern and Northern Greenstone belt, Fig. 1B). Along these units, TTG complexes are identified in the north, at the centre and in the south of French Guiana (Fig. 1B), together with a younger granitic formation. Finally, an Upper Detrital Unit which is composed of sandstones and fluvial conglomerates (Milesi et al., 1995) is located at the northern extremity of the Central TTG Complex (Fig. 1B).

Deposit geology

Gold endowment in the Yaou district has been investigated by the French Geological Survey (BRGM) and by the exploration companies Guyanor Resources/Cambior/Auplata/AMG almost continually since 1981. Yaou is currently owned by the gold exploration and mining company Auplata Mining Group. Orebodies are currently identified along a 4.5 km-long structure, giving an average inferred resource tonnage and grade of 22.9 Mt at 2.1 g/t. Three drilling campaigns have been completed since 1989, with a total length of drilled core exceeding 32 000 linear meters. The deposit is located within the southern branch of the Paramaca Greenstone Belt (PGB), (Fig. 1B and C) with a TTG Complex to the southeast and a sedimentary unit to the north of the Yaou camp. A Neoproterozoic dolerite dyke (Delor *et al*., 2003b) cuts the western part of the deposit. Milesi *et al*. (2003) defines the deposit as an Au-Fe-Cu stratabound and epigenetic deposit, with disseminated sulphides associated with two sets of veins: an early folded quartz-carbonate vein system followed by a late, unfolded quartz-carbonate vein set. These unfolded veins, interpreted as a late D_{2YA}, are associated with widespread albitisation and chloritisation (Milesi *et al*., 2003) and are spatially related to small intermediate intrusive bodies historically interpreted as trondjhemite. Three types of pyrite are described by these authors: Py_1 is disseminated and shows pressure shadows; coarse Py_2 is associated with veining; whereas Py_3 is disseminated and fine-grained without pressure shadows. An Au-Te association is mentioned by internal reports on the auriferous pyrite associated with veins. Regarding deformation phases, historically a folding stage is identified, followed by a simple shearing stage associated with the rotation of magmatic bodies.

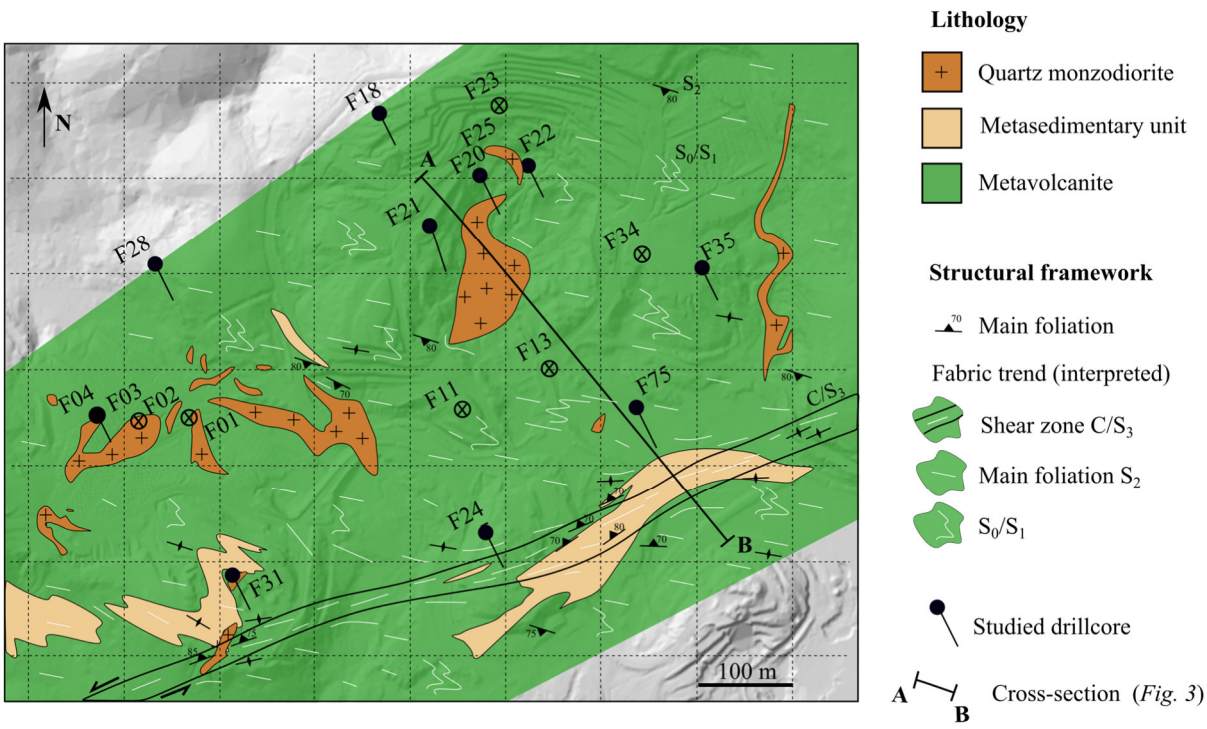

Figure 2-2 Geological map of the central part of the deposit including field observations, drilling, trenching and saprolite extraction with studied drillcore location, fabrics and main lithologies. Quartz monzodiorite bodies are aligned along a N60° trend parallel to a sinistral shear zone. The main hostrock is a metavolcanite transposed in a pervasive foliation S_2 striking N100°-120°E. Locally the schist has a metasedimentary protolith. Location of the cross-section represented in the next figure is visible in the map.

Lithology description

Detailed relogging carried out in 2017-2019 shows that, at the camp scale, the Yaou deposit is mainly hosted by three lithologies (Figs. 2 and 3). The dominant host lithology consists of a fine-grained, strongly foliated and locally folded, dark greenish chloritic schist displaying evidence of a volcano-sedimentary origin and referred to as metavolcanite. The pervasive foliation is defined by chlorite. Centimetre-scale, lense-shaped calcite aggregates are locally observed. The second most common lithology is a brownish to greyish, fine- to medium-grained intrusive unit, displaying a phaneritic texture. The intrusive bodies locally present a porphyritic texture, with primary alkali-feldspar phenocrysts. In the Q-A-P normative classification diagram, the unaltered (very rare) intrusive rock plots in the quartz monzodiorite field. A second type of intrusive rock, exhibiting a dark grey coloration, is locally observed and plots in the diorite field of the Q-A-P normative classification diagram. The third lithological unit is a fine-grained, greyish to brownish, laminated and strongly schistosed metasediment displaying a primary bedding that is defined by alternating layers of dark- and light-coloured matrix. Such

layering, together with the presence of millimetric lithic clasts of quartz and plagioclase, attest to a sedimentary origin. This lithofacies is commonly strongly foliated, with pyrite porphyroclasts and locally exhibit ultramylonite features, although primary textures remain locally preserved distal to high-strain zones. Other, less common lithologies include a strongly carbonate-altered, magnetite-rich, dark green ultramafic schist and a mafic tuff, interpreted as two minor facies of the metavolcanite. The metavolcanite and the metasedimentary units belong to the Lower volcanic and sedimentary formation of the Paramaca Greenstone Belt (Milesi *et al*., 2003). Whether the intrusive unit belongs to the TTG complex or to the granitic formation is not clearly determined. Regional metamorphism is of greenschist facies with a great abundance of chlorite, sericite and carbonate in the volcanosedimentary host rocks (Delor *et al*., 2003b, Milesi *et al*., 2003).

Deposit geometry

The main studied area displays a truncated lateritic profile with saprolite exposed at surface and our investigations are therefore restricted to fresh-rock drill cores. The depth of the bedrock-saprock interface varies from 10 to 80 m below the topographic surface. Nevertheless, in order to characterise the regional strain pattern, a detailed foliation trajectory map was constructed at the deposit scale from structural measurements on saprolite, where structure and fabric of the parent rocks are preserved. A good overall correspondence is observed between regional foliation trajectories and the structural grain observed on the aeromagnetic map of the area. Trajectories highlight some heterogeneities in the strain pattern, as follows:

1. Regional fabric trajectories appear locally folded (or refolded) and transposed within the main regional fabric. The area is characterised by a steeply dipping regional foliation which strikes mainly N100°-N120° (Fig. 2). Simple shear features are well expressed from camp to mineral scale with the presence of C/S_3 shear band cleavage mostly recorded by the metasedimentary unit.
2. In the southern area, foliation trajectories tend to converge toward an ENE–striking, high-strain zone with a sinistral shear component (Fig. 2).
3. Parallel to the shear zone, a series of intrusive bodies (Fig. 2 and 3) occur as small dykes and locally as wider plutons varying from 1 to 120 m in thickness along a N60° trend and exceeding 4.5 km in length along strike. These structural features suggest close relationships between shear zone development and emplacement of melts.

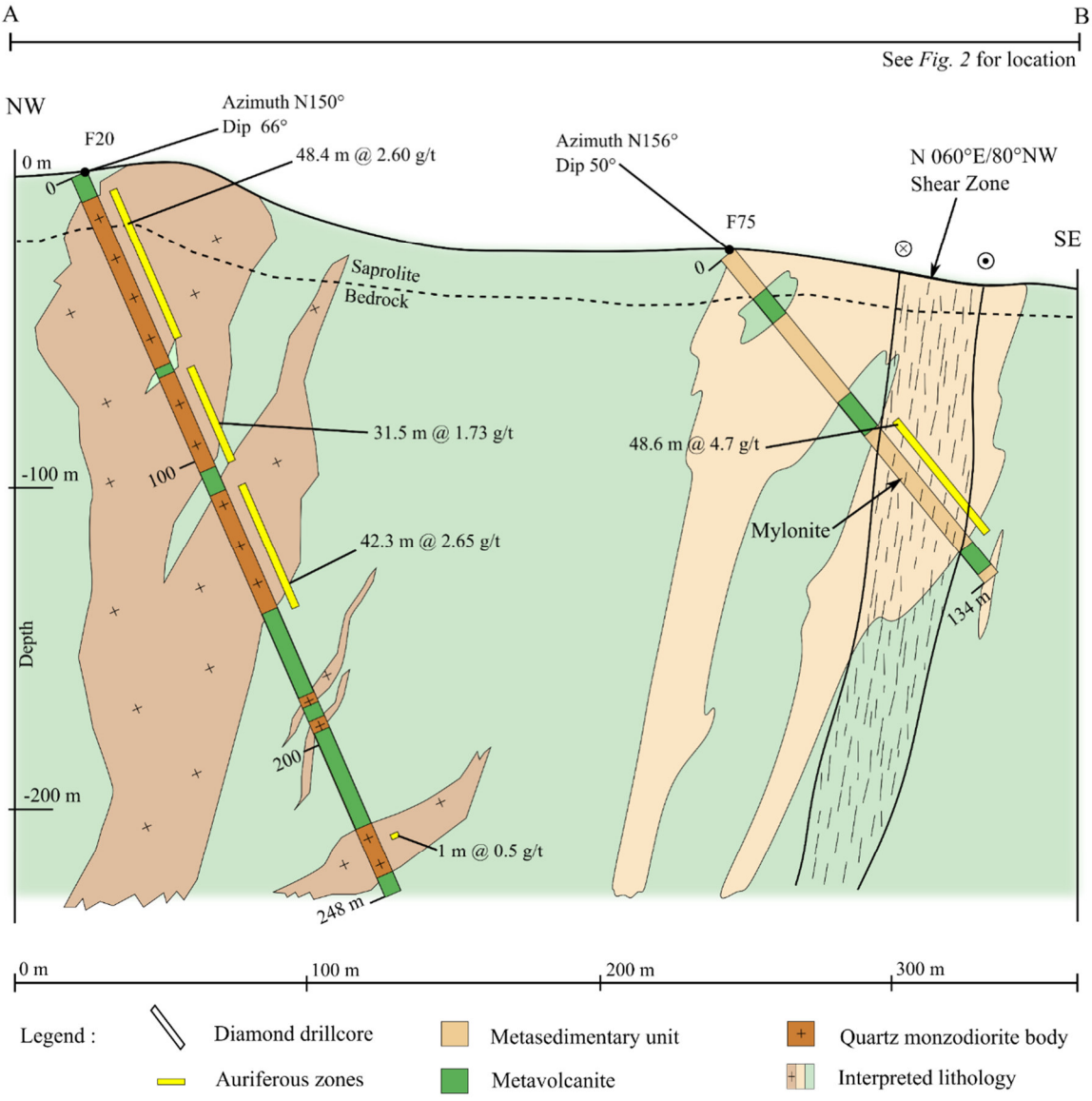

Figure 2-3 Interpreted NW-SE cross-section through the studied area displaying the geometry of the deposit with typical orebodies and associated gold grade in ppm obtained from AMG exploration database. Auriferous zones are mainly associated with the intrusive bodies and the sinistral shear zone. Pale colours show the interpreted envelopes of the studied bodies.

This geometry is best expressed on a NW-SE cross-section through the studied area from drill-core information (Fig. 3). The deposit consists of multiple, discontinuous mineralised bodies spatially associated both with the intrusions and with the 30-40 m wide mylonitic Central Yaou shear zone. Currently drilled to a maximum depth of 315 m, the orebodies remain open at depth and along strike. The mineralisation is essentially confined to the pyrite-bearing facies. Auriferous drill intersects show up to 55 m @ 5.1 g/t Au within the intrusion and 48.6 m @ 4.7

g/t Au within the shear zone. Mineralisation located within the intrusion accounts for approximately 70 % of the total Au budget of the currently identified resource.

Sample material and analytical methods

Logging and sample selection

Few structural measurements in the open-pit exposures were possible as presented in Figure 2 where different foliations have been measured and mapped. Detailed logging of entire or specific representative sections of 32 unoriented drill cores (about 6200 m in total) was carried out (Figs. 2 and 3).

Drill cores were logged in terms of their rock type, mineralogy and structural characteristics, with a step of 10 cm or 50 cm depending on core, in order to accurately document variations within the different lithologies and alteration assemblages of (1) the pyrite abundance and (2) the cumulated corrected thickness of the veins associated with deformation phases. These detailed measurements are combined with whole-rock gold assays to provide a comprehensive documentation of gold distribution with regards to pyrite and vein thicknesses. A total of 88 samples were collected providing a representative material for laboratory work. A total of 43 thin sections for petrographic and metallographic studies were prepared from different facies and deformation features. Microfabric characterisation, mineral identification, overprinting relationships, and ore parageneses were studied with optical, reflected and transmitted light microscopy at the GeoRessources laboratory (Nancy, France).

Scanning electron microscopy (SEM) and electron microprobe (EPMA)

A total of 20 polished thin sections and 8 mounts were prepared from the collected samples and examined using reflected/transmitted light and scanning electron microscopy (SEM) to characterise ore assemblages and pyrite morphology for each generation. The SEM analyses were conducted using the backscattered electron mode (BSE) with typical beam conditions of 15 kV and 10 nA on a Hitachi FEG S4800 equipped with an Energy-dispersive X-ray spectrometer (EDS) at the GeoRessources laboratory (Nancy, France). About 80 pyrite crystals were examined for this study. Pyrite crystals were analysed using a CAMECA SX-100 electron microprobe (EPMA) at the GeoRessources laboratory (Nancy, France) with an acceleration voltage of 20 kV and beam current of 20 nA. Elements and X-ray lines used for the analysis are Fe (Ka), S (Ka), As (La), Pb (Ma) and Co (Ka), with acquisition time of 10 s per element. Standard specimens used for calibration were FeS_2 (for Fe and S) and pure metals for As, Co

and Pb. A total of 221 spot analyses were conducted to provide internal standard calibration of Fe grade for LA-ICP-MS data processing but are not presented here. The occurrence of chemical zonation in each pyrite generation was tested by X-ray maps of the following elements: Fe, S, As, Co and Pb; using an acceleration voltage of 20 kV, a 100 nA beam current and a 1 μm^2 electron beam focused on the sample surface.

Laser Ablation-Inductively Coupled Plasma-Mass Spectrometry (LA-ICP-MS)

A total of 70 spots located on 8 mounts were ablated by LA-ICP-MS at the Géosciences Environnement Toulouse Laboratory (GET) using a Thermo Finnigan (Element XR) coupled to a Ti: sapphire femtosecond (fs) laser operating at 800 nm and providing 55-fs pulses with a maximum output of 12 mJ $pulse^{-1}$ (Borisova *et al*., 2008, 2010; Freydier *et al*., 2008). In total, 26 selected individual pyrite grains representative of the 7 identified generations and types of pyrite were analysed for which the major element concentration is known from EPMA analysis. Ablation time and spot sizes were 60 seconds and 30 microns, respectively. Trace element concentrations were calculated using pyrrhotite Po-726 (Sylvester *et al*., 2005), USGS sulphide MASS-1, NIST SRM 610 and 612 (Pearce *et al*., 1997) as external standards, and using ^{57}Fe as the internal calibrator (detailed method in Velásquez *et al*., 2012). Raw data were reduced with the limits of detection calculated using the commercial version of the GLITTER software package (e.g., Van Achterbergh *et al*., 2001). A total of 28 elements were measured and the following isotopes were monitored: ^{32}S, ^{33}S, ^{34}S, ^{56}Fe, ^{57}Fe, ^{59}Co, ^{60}Ni, ^{62}Ni, ^{63}Cu, ^{65}Cu, ^{66}Zn, ^{68}Zn, ^{69}Ga, ^{75}As, ^{77}Se, ^{95}Mo, ^{101}Ru, ^{103}Rh, ^{105}Pd, ^{107}Ag, ^{109}Ag, ^{115}In, ^{121}Sb, ^{123}Sb, ^{125}Te, ^{130}Te, ^{138}Ba, ^{185}Re, ^{187}Re, ^{189}Os, ^{193}Ir, ^{194}Pt, ^{195}Pt, ^{197}Au, ^{205}Tl, ^{208}Pb,^{209}Bi. The accuracy is calculated for each element for each analysis as a function of the uncertainty of the reference standard, the absolute element content and the time of integration. Detection limit was below 1 ppm for most trace elements.

All observations and data acquired by these methods allow us to synthesise and integrate deformation phases, alteration stages and mineralisation.

Results

Deformation phases and hydrothermal alteration features

1. Early fabrics S_0/S_1

The S_0/S_1 fabrics are expressed within the metasedimentary unit. Primary features are locally well preserved with the presence of angular plagioclase-quartz clasts together with bedding (Fig. 4) and graded bedding.

2. D_{1YA}/D_{2YA} phase

These deformation phases are well expressed in metavolcanites and in the metasedimentary unit (Fig. 4). The D_{2YA} ductile event is defined by the dominant penetrative fabric S_2 representing the principal foliation oriented N100°-120° in the study area. The earliest deformation D_{1YA} is not clearly discriminated and is defined by the S_1 foliation visible in cm-scale D_{2YA} kink folds. The principal foliation S_2 is defined by axial planes of these folds. S_0/S_1 fabrics are transposed by the D_{2YA} event. S_2 is a crenulation cleavage superposed on S_1, defined by chlorite and sericite (Fig. 5A). The veins associated with D_{1YA} and D_{2YA} are folded and/or refolded, testifying of the ductile regime. Pre- to syn-folding veins are referred as $D_{1/2YA}$ veins in this study. They are boudinaged and transposed within the S_2 fabric and mainly hosted by metavolcanite. Their thickness is ranging from 0.1 to 15 cm (Fig. 6 and 7). This vein population displays a milky coloration and presents a composite mineral assemblage consisting of quartz and calcite, with the calcite being developed at the vein margins. Quartz grains display evidence of recrystallisation by Grain Boundary Migration (GBM) (Fig. 8A) and grain elongation. The main characteristic of this vein population is the heterogeneous grain size distribution (Fig. 8B) with grain size of quartz and calcite varying from 50 to 1000 µm. Locally, barren sulphides are present within the veins (Fig. 9).

3. D_{3YA} phase

This deformation phase is represented by ductile, ENE-striking shear zones observed at all scales (from regional-scale to micro-scale) and showing components of sinistral strike slip (Fig. 2). The D_{3YA} shearing event is mostly recorded by the metasedimentary unit (Fig. 4) and rarely by the metavolcanite. One occurrence of intrusive body affected by D_{3YA} has been identified at the margins of the major shear zone. The sinistral character of the D_{3YA} shear zone is well expressed by the deflection of the regional S_2 foliation into the shear zone. At the microscopic scale, the non-coaxial character of the D_{3YA} deformation phase is expressed by the C/S_3 fabric (Fig. 5B), mylonitic texture and fringe structures around pre-D_{3YA} pyrite grains (Fig. 5C). These pyrite crystals show antitaxial and asymmetric fringes developed in simple shear matrix flow, interpreted to be formed during the non-coaxial D_{3YA} shearing (Ramsay and Huber, 1983) Fringes display elongated and fibrous quartz and chlorite rims. Rarely, some pyrite crystals

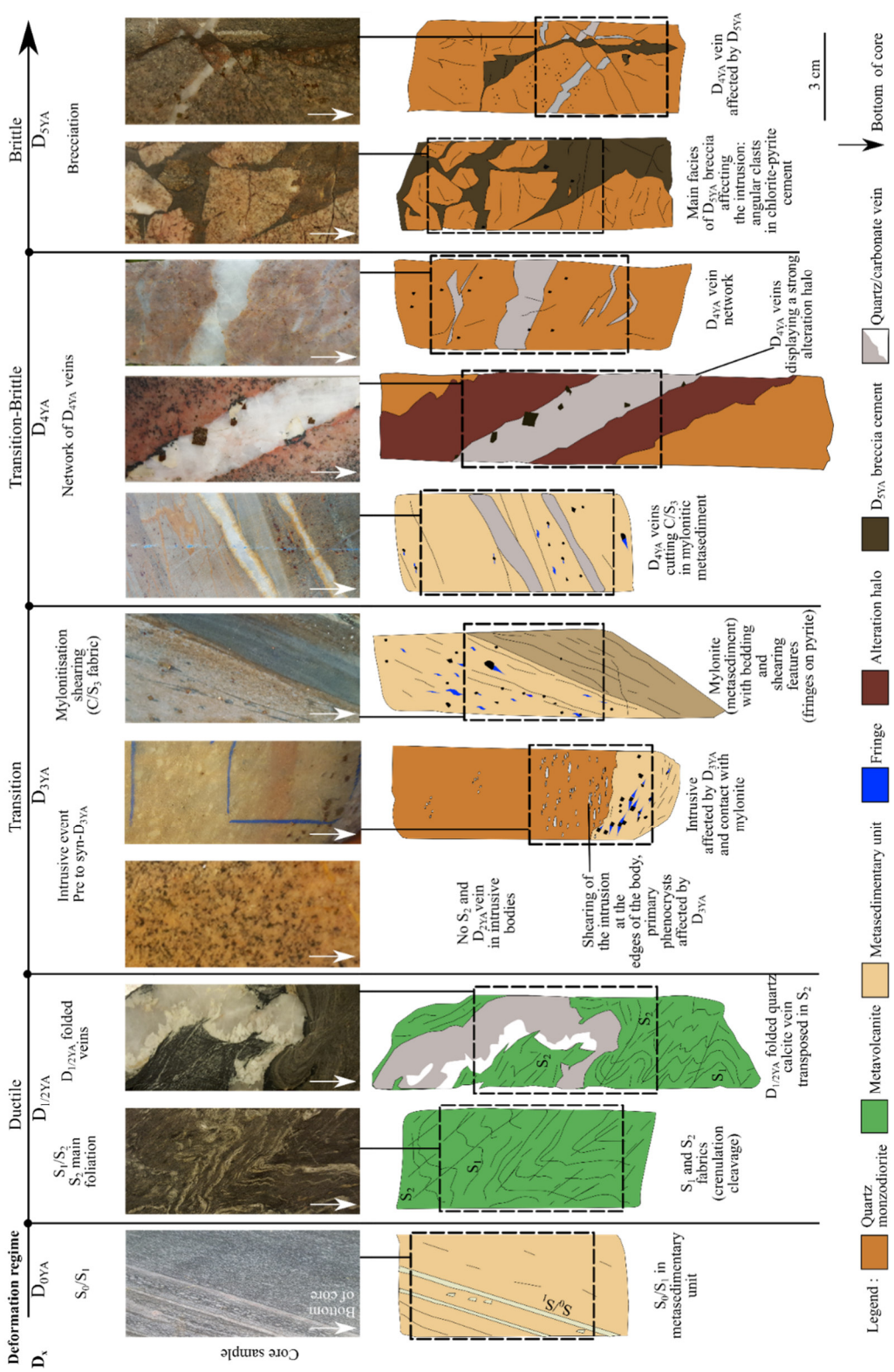

Figure 2-4 Photographs and corresponding sketches of drillcore intervals exemplifying the interpreted deformation phases set on a relative timing sequence. Five deformation phases are defined with a progressive evolution of the deformation style, from ductile ($D_{1/2YA}$ phase) to transitional (D_{3YA} to D_{4YA} phase) to brittle (D_{4YA} to D_{5YA} phase).

exhibit a late calcite fringe near the pyrite grain. The D_{3YA} deformation phase is not associated with any veining (Fig. 6).

The intrusive event is interpreted as pre to syn-D_{3YA} (see discussion section). The quartz monzodiorite bodies are clearly not affected by the regional penetrative S_2 foliation nor by the $D_{1/2YA}$ veining event. S_2 fabric is locally disturbed by the intrusive bodies. In the F31 drill core (Fig. 6), the intrusion is clearly affected by D_{3YA}. The intrusion and the mylonitisation may therefore be synchronous. Xenoliths of the metavolcanite are encountered within the plutons. Regarding hydrothermal alteration, the D_{3YA} phase in the metasedimentary unit is marked by a sericite, chlorite and calcite alteration assemblage. Apatite and rutile are present in the matrix. Some sericite is also observed within the D_{3YA}-altered metavolcanite (Fig. 9).

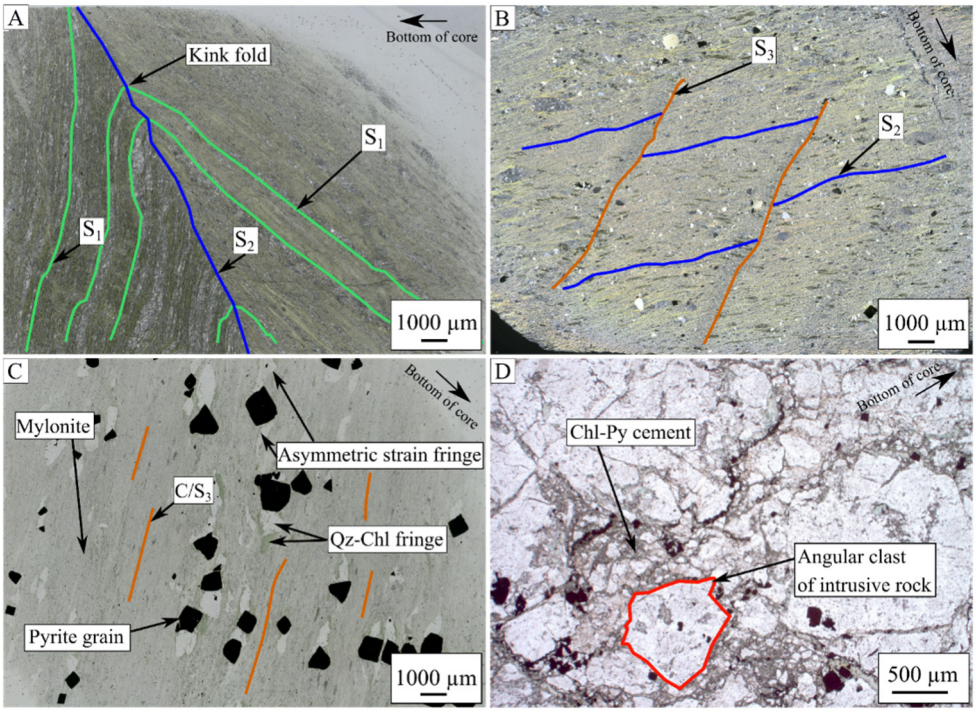

*Figure 2-5 Optical microphotographs of the microtectonics features. **(a)**. Crenulation cleavage in chlorite-sericite metavolcanite with S_1 and S_2 fabrics. **(b)**. Relationship of the S_2 fabric and the CS_3 shear bands in a D_{3YA} mylonitic metasediment (unoriented core and thin section). **(c)**. D_3 mylonitic metasediment with shear indicators such as strain fringes around pyrite grains (unoriented core and thin section). **(d)**. Brecciation D_{5YA} with angular clasts of quartz monzodiorite in a pyrite-chlorite cement.*

4. D_{4YA} phase

The D_{4YA} phase is expressed by shallow-dipping, dilational quartz-calcite veins forming a network (Fig. 4). These veins are preferentially located within the intrusive bodies (Fig. 6), at

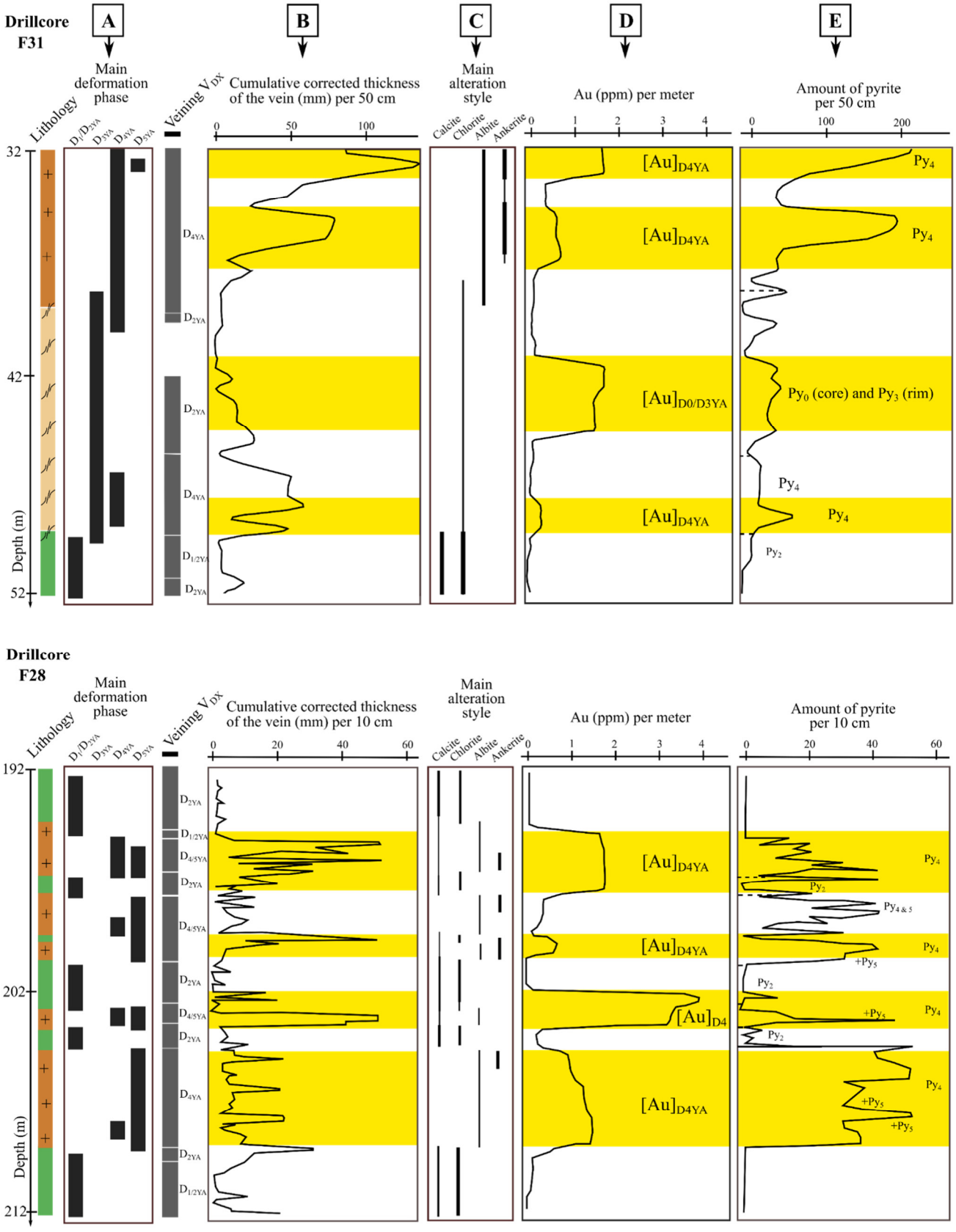
Drillcore F31
A
B
C
D
E
Main deformation phase
Lithology
Veining V_DX
Cumulative corrected thickness of the vein (mm) per 50 cm
Main alteration style
Calcite
Chlorite
Albite
Ankerite
Au (ppm) per meter
Amount of pyrite per 50 cm
Depth (m)
32
42
52
[Au]D4YA
[Au]D0/D3YA
Py4
Py0 (core) and Py3 (rim)
Py2
Drillcore F28
Cumulative corrected thickness of the vein (mm) per 10 cm
Amount of pyrite per 10 cm
192
202
212
Py4 & 5
+Py5
Legend :
Quartz monzodiorite
Metavolcanite
Metasedimentary unit
Shear zone
Auriferous zones [Au]DX

*Figure 2-6 Logs of drillcores representative the lithologies; (**a**) the main deformation phase; (**b**) the cumulative corrected thicknesses of veins; (**c**) the main alteration assemblages; (**d**) the associated Au grades from whole-rock analyses and (**e**) the amount of pyrite. The Au grade is associated with the shearing event mentioned as D_{3YA} (C/S_3 mylonitisation) and not with the $D_{1/2YA}$ vein system which is always associated with low or no grade when alone and thus interpreted as barren. Whole-rock gold assays are from 1 m core interval, some minor $D_{1/2}$ veins were logged but not responsible for the Au grade. $Au_{D0/D3}$ is not correlated to any veining.*

their contacts, or more rarely in the metavolcanite and within the sinistral D_{3YA} shear zone). The D_{4YA} event can be distinguished from D_{3YA} event as some D_{4YA} veins clearly crosscut the S/C_3 shear zone. D_{4YA} veins have also been observed cross-cutting the regional penetrative S_2 in metavolcanite and also the lithological contacts between the quartz monzodiorite and the metavolcanite. It is worth noticing that the D_{4YA} veins not only crosscut the D_{3YA} fabric but also locally re-use it. The density of veins is strongly lithology-dependent creating a distributed damage zone, with a higher density of veins in the intrusive bodies than in the metasedimentary unit and the metavolcanite (Fig. 6). The vein thickness ranges from 0.1cm to 4 cm, with rare occurrences up to 20 cm thick. These veins are mostly composed of quartz with minor carbonates and display fracturation, within the vein, often perpendicular to the edges. The low carbonate content differs from D_{1YA} and D_{2YA} vein generations. At the macroscopic scale, the quartz can be either glassy, smoky, or milky. The grain size is relatively homogeneous, with quartz grains sizes ranging from 100 to 3000 µm. Evidence of recrystallisation includes subgrain rotation, subgrain boundaries, few bulging (Fig. 8C) and intense undulose extinction (Fig. 8D). The degree of recrystallisation is lower for this generation than for the D_{2YA} vein generation. Sulphides can be observed within the veins (up to 3 vol. %), (Fig. 6). Locally, 30-40 µm-large free gold grains with a 5.6 to 6.1 weight % silver are observed within the quartz grain boundaries in the D_{4YA} veins. The dominant, D_{4YA} hydrothermal alteration event is associated with bleaching of the intrusive wallrock, forming mm- to m-thick alteration haloes (Fig. 10). The proximal alteration assemblage consists of ankerite, hematite and albite together with a strong pyritisation and hematite between the albite crystals (Fig. 9). The intermediate assemblage is composed of albite, ankerite, sericite and pyrite. For both assemblages, albite is overprinted by ankerite followed by sericite. The distal assemblage is characterised by albite, sericite and chlorite. A progressive replacement of magnetite by pyrite towards the ore zone is observed from distal to proximal zones. D_{4YA} veins in the mylonite and the metavolcanite display an alteration halo characterised by strong pyritisation and weak sericitisation.

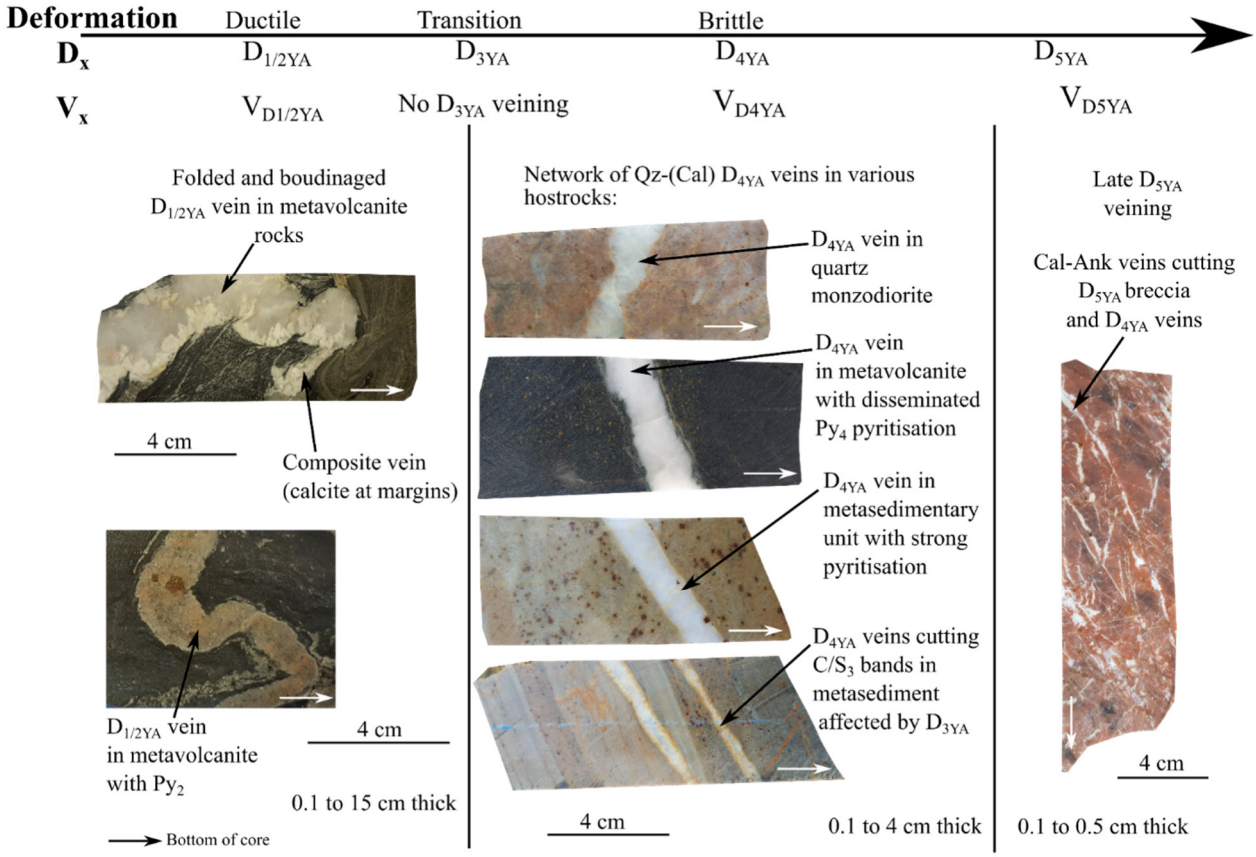

Figure 2-7 Photographs of core intervals of each vein type and generation associated with a deformation phase. Three generations are being identified. The $D_{1/2YA}$ veins are folded and boudinaged, the D_{4YA} veins are mainly observed within intrusive bodies.

5. D_{5YA} phase

A late brecciation phase D_{5YA} affects the intrusive unit (Fig. 4) and, more rarely, the metavolcanite. This breccia displays more than 30 % of angular clast of intrusive rocks (Fig. 5D) with a space between clasts ranging from 10 µm to 1 cm. The cement between clasts is composed of chlorite, pyrite and ankerite (Fig. 9). These monogenic cataclastites cut the D_{4YA} veins. Late veinlets composed of carbonates, mainly calcite and ankerite, generally hosted in the intrusive and the metavolcanite units and not exceeding 5 mm in thickness, crosscut the D_{5YA} breccia and the D_{4YA} veins and are barren, with no sulphide observed (Fig. 7). At the microscopic scale, the calcite shows type II deformation twins, which are tabular thick twins of 20 µm. The D_{5YA} phase is characterised by an intense chloritisation, carbonatisation and pyritisation, as observed in the cement of the breccia.

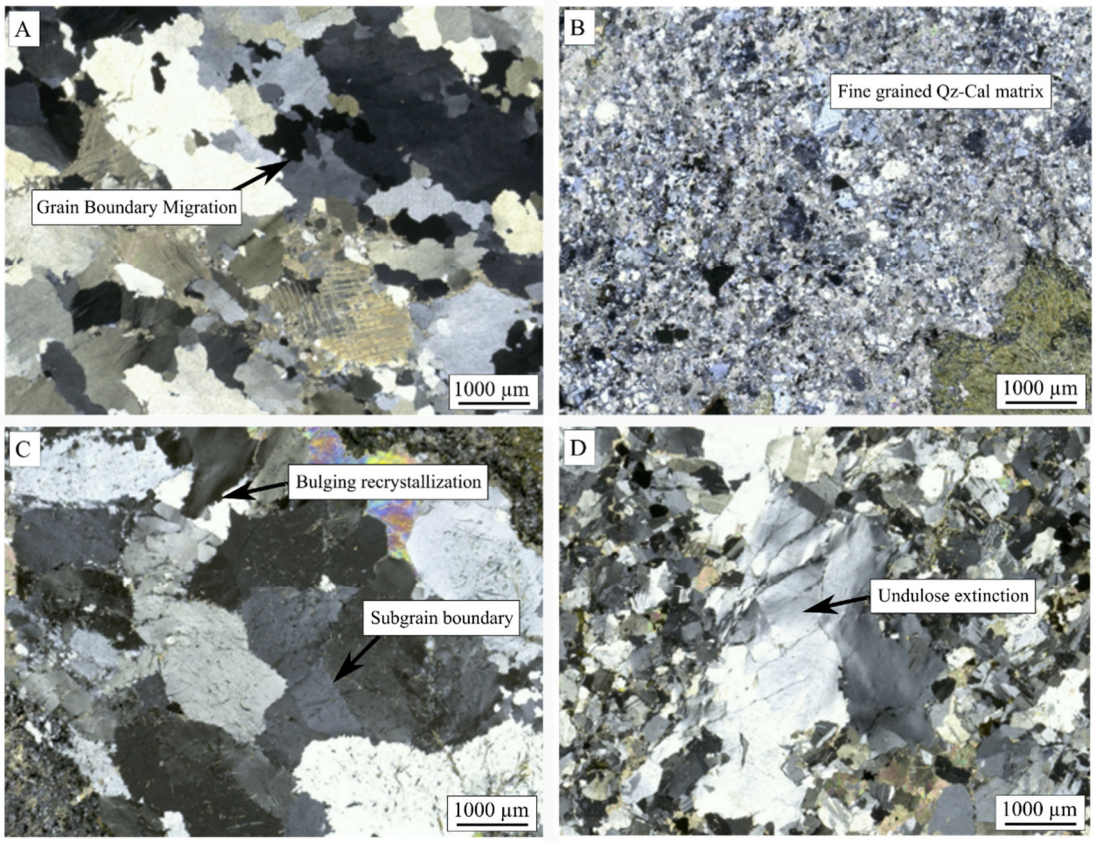

*Figure 2-8 Representative optical microphotographs of veins. (**a**). $D_{1/2YA}$ vein hosted in a metavolcanite with Grain Boundary Migration of quartz evidencing of a ductile deformation regime. (**b**). $D_{1/2YA}$ vein hosted in a metavolcanite displaying a fine-grained matrix of quartz and carbonate. (**c**). D_{4YA} vein hosted in intrusive rock with quartz subgrains and bulging. (**d**). D_{4YA} vein hosted in intrusive rock showing undulose extinction.*

Whole-rock gold grade *vs.* deformation-hydrothermal stages

The deformation and vein stages and their related alteration mineral assemblages have been compared with gold grades obtained from whole-rock drill core analyses (Fig. 6 A, B, C and D, where systematic logging is presented for two core intervals from drill cores F31 and F28, located in Figure 2). Core F31 intersects the D_{3YA} shear zone, whilst F28 is located outside it. The spatial correlation between elevated gold grades and D_{4YA} veins (average values of 1 to 4 g/t) in core F28, clearly illustrates the critical influence of D_{4YA} veins in formation of the economic gold grades. To a lesser extent, D_{3YA} shear zones are also associated with elevated gold grades (up to 1.5 g/t) as demonstrated by core F31. The D_{2YA} event is not auriferous (below 0.1 g/t) while D_{5YA} brecciation grades less than 0.5 g/t when distal to D_{4YA} veins. Highest Au grades are found where both D_{3YA} shear zones and D_{4YA} veins co-exist (e.g. the F75 drill core with 45-metre-long interval grading above 9 g/t at -75m). It is worth noting that rare D_{4YA} in

the metavolcanite return positive Au grades (about 0.5 g/t) but are not frequent enough to build an ore zone.

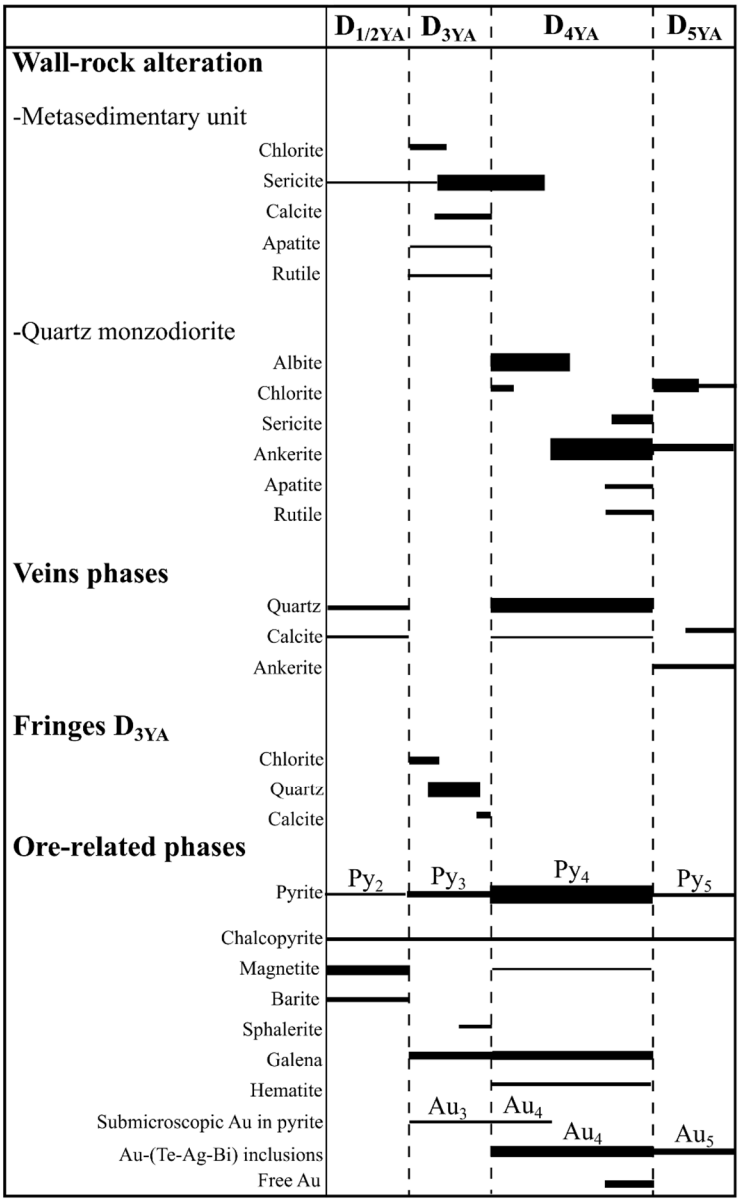

Figure 2-9 Hydrothermal and ore paragenetic sequence chart for the quartz monzodiorite and the metasedimentary unit against deformation phases based on petrographic observation.

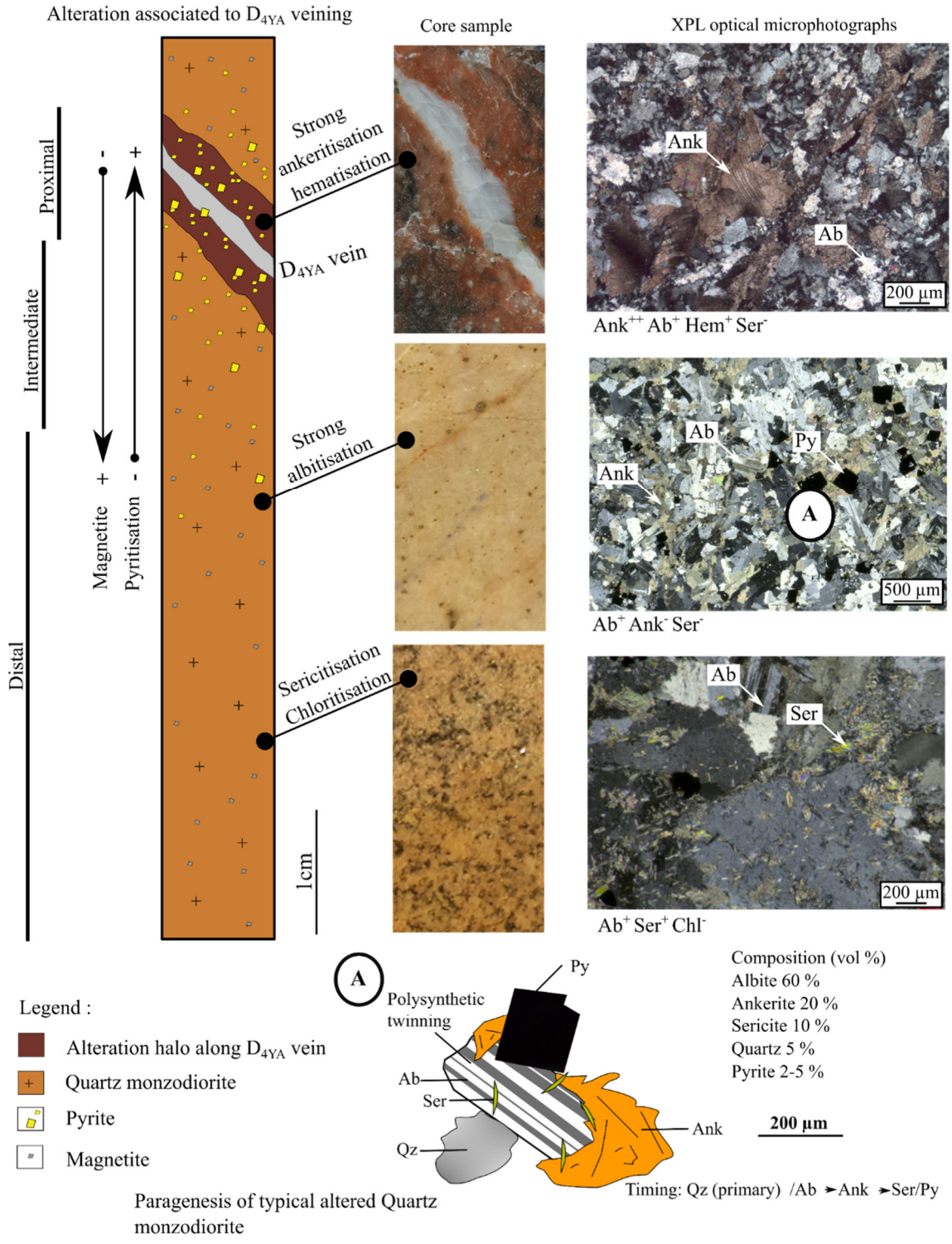

Figure 2-10 Representative micrographs of ore-related hydrothermal alteration focusing on the D_{4YA} event with proximal ankeritisation followed by a strong albitisation and a more distal chloritisation. A negative correlation of pyrite and magnetite contents toward the vein is observed.

Pyrite types, generations, and their trace elements distribution

As gold mineralisation and pyritisation are intimately associated at the Yaou deposit, a detailed study of morphology, texture, inclusion, and associated minerals of pyrite were conducted. Pyrite generations were interpreted and assigned to separate deformation and veining events (Fig. 6 and 11). Each pyrite generation was investigated for (i) zonation using EPMA mapping (Fig. 12); and (ii) geochemical composition using combined EPMA and LA-ICP-MS analyses, especially for gold (Fig. 13 and table 1 for row data) and related trace element tracking (Fig. 14). For this study, LA-ICPMS analyses do not allow to determine whether trace elements are present as nanoparticles or as solid solution in the pyrite lattice substituting Fe. However, gold micro-inclusions can be deciphered from lattice gold/nanoparticles based on the spectrum pattern, i.e. plateau-like versus pulselike (Fig. 13C). A total of five pyrite generations are proposed, mostly based on textural, structural, and relative chronology criteria.

Table 2-1 . Major and trace element composition analyses of pyrite using EPMA (S, Fe) and LA-ICP-MS (Bi, Te, Ag, Ni, Co, As, Au)

Spot ID	Py	Bi (ppm) LA-ICP-MS	Te (ppm) LA-ICP-MS	Ag (ppm) LA-ICP-MS	Ni (ppm) LA-ICP-MS	Co (ppm) LA-ICP-MS	As (ppm) LA-ICP-MS	Au (ppm) LA-ICP-MS	S (wt %) EPMA	Fe (wt %) EPMA
SP1	Py0	<0.221	22.58	<0.206	376.62	184.81	2351.59	0.636	52.83	47.88
SP2	Py0	0.0112	55.22	<0.043	6.22	23.59	2330.07	0.288	53.76	47.83
SP3	Py0	0.713	36.41	3.54	640.9	256.21	13704.09	66.55	51.01	46.5
SP4	Py0	5.96	35.18	11.7	303.69	178.75	14476.78	55.25	52.65	47.31
SP5	Py0	<0.085	8.79	<0.066	171.73	381.85	240.64	<0.01	53.42	47.54
SP6	Py0	1.18	58.09	0.386	11.44	8.49	2504.02	1.152	53.64	47.61
SP7	Py0	4.6	30.83	0.658	144.05	37.8	3076.48	1.96	53.35	47.85
SP8	Py0	6.51	7.69	0.466	255.26	58.64	224.74	0.503	53.53	47.09
SP9	Py0	20.51	13.42	4.13	2721.27	576.28	487.42	1.52	53.93	47.18
SP10	Py0	7.15	15.66	0.196	467.92	124.48	4546.65	0.965	53.76	47.83
SP11	Py0	4.46	5.09	0.196	122.44	103.8	4966.2	0.597	52.63	45.95
SP12	Py2	0.0433	<0.064	<0.0234	2251.28	778.59	143.64	<0.001	53.36	47.57
SP13	Py2	2.67	<0.066	0.069	738.7	195.16	125.62	0.0036	53.34	47.15
SP14	Py2	0.0093	<0.051	<0.0255	362.5	55.16	148.76	<0.001	51.23	46.64
SP15	Py2	0.0056	<0.0258	<0.0248	763.94	430.72	172.45	<0.0027	53.11	47.72
SP16	Py2	62.58	10.93	22.81	121.95	1514.09	135.54	0.105	53.51	47.22
SP17	Py2	0.0616	<0.076	<0.030	1921.4	839.76	125	<0.0032	52.88	47.17
SP18	Py2	1.117	0.177	0.202	827.18	450.84	142.15	0.0147	53.58	47.89
SP19	Py3	0.222	11.82	0.125	49.04	79.99	558.48	0.194	53.86	47.82
SP20	Py3	<0.049	0.75	0.101	15.22	2278.74	116.62	0.18	53.57	47.33
SP21	Py3	0.54	11.93	0.422	46.42	196.05	417.57	0.386	53.78	48.02

SP22	Py3	0.233	22.83	0.098	94.42	795.67	1555.17	0.622	53.29	47.8
SP23	Py3	<0.055	5.31	<0.062	31.66	225.04	3115.84	0.173	53.42	47.61
SP24	Py3	2.59	3.13	<0.20	102.39	4653.3	26.28	0.042	53.47	47.64
SP25	Py3	<0.045	1.98	<0.045	34.15	40.25	101.65	0.037	53.54	47.89
SP26	Py3	0.466	25.83	0.338	145.52	204.72	154.04	0.216	53.68	47.7
SP27	Py3	0.142	3.03	<0.069	72.38	415.96	122.96	0.023	53.51	47.84
SP28	Py4	12.43	10.74	1.46	130.12	203.66	35.59	0.87	53.4	47.9
SP29	Py4	18.41	20.19	3.86	75.83	74.03	45.68	1.15	53.05	47.44
SP30	Py4	2.59	1.17	0.159	279.03	55.08	45.49	<0.01	51.23	46.64
SP31	Py4	<0.70	<2.70	0.76	124.66	119.73	46.74	0.72	53.26	47.31
SP32	Py4	9.02	16.15	2.54	106.29	87.5	49.04	1.17	53.52	47.54
SP33	Py4	131.19	50.03	14.37	289.24	357.55	50.38	47.96	53.29	47.62
SP34	Py4	4.97	4.75	1.681	83.45	1136.72	71.1	0.0147	53.79	47.94
SP35	Py4	0.45	1.46	0.066	102.77	3.22	58.61	0.039	53.42	47.68
SP36	Py4	13.77	140.52	28.87	368.99	241.25	51.52	58.88	53.76	47.64
SP37	Py4	0.296	0.156	0.0261	162.06	322.56	167.86	0.0012	53.38	47.23
SP38	Py4	0.026	0.192	<0.0207	364.17	111.39	144.92	<0.01	53.42	47.54
SP39	Py4	32.08	41.02	1.671	160.55	451.66	130.85	7.41	53.16	47.79
SP40	Py4	0.47	0.589	<0.0219	343.08	107.71	137.32	0.0036	53.34	47.47
SP41	Py4	4.91	10.72	0.42	222.85	260.46	157.97	0.284	53.1	47.72
SP42	Py4	43.59	62.52	6.51	164.53	486.82	145.63	1.318	52.66	46.89
SP43	Py4	2.28	7.24	0.714	85.53	1443.44	143.99	0.185	53.13	48.18
SP44	Py4	57.44	60.94	2.047	155.91	50.29	125.8	0.403	53.72	47.17
SP45	Py4	8.37	23.74	1.87	48.06	175.31	68.41	0.758	53.81	47.3
SP46	Py4	5.77	12.4	0.801	49.51	45.41	46.4	1.3	53.55	47.76
SP47	Py4	0.267	1.81	<0.093	69.34	181.6	51.88	<0.094	53.08	47.63
SP48	Py4	15.14	86.46	23.36	520.81	426.21	66.09	6.21	53.44	47.01
SP49	Py4	1.91	15.21	0.51	52.42	121.67	70.24	0.253	53.07	46.94
SP50	Py4	<0.0247	169.68	0.07	34.1	48.19	289.36	<0.029	53.28	47.26
SP51	Py4	0.056	237.15	0.083	35.72	38.88	295.79	0.088	54.03	47.36
SP52	Py4	<0.026	34.95	<0.057	362.01	932.54	148.09	0.116	53.52	47.09
SP53	Py4	0.147	65.99	0.132	17.74	12.6	125.73	<0.01	53.87	47.57
SP54	Py4	132.84	38.08	29.64	12.72	5.48	90.19	0.7	53.57	47.85
SP55	Py4	37.31	103.96	8.33	119.82	401.6	147.19	2.48	53.63	47.03
SP56	Py5	10.43	21.35	2.03	61.09	155.41	47.66	1.43	52.78	47.34
SP57	Py5	7.8	15.96	1.59	187.83	79.75	44.66	0.93	53.67	47.73
SP58	Py5	7.82	68.93	0.95	171.88	168.55	58.03	0.396	53.69	47.43
SP59	Py5	9.65	3.7	0.305	291.56	327.7	53.38	0.245	53.79	46.73

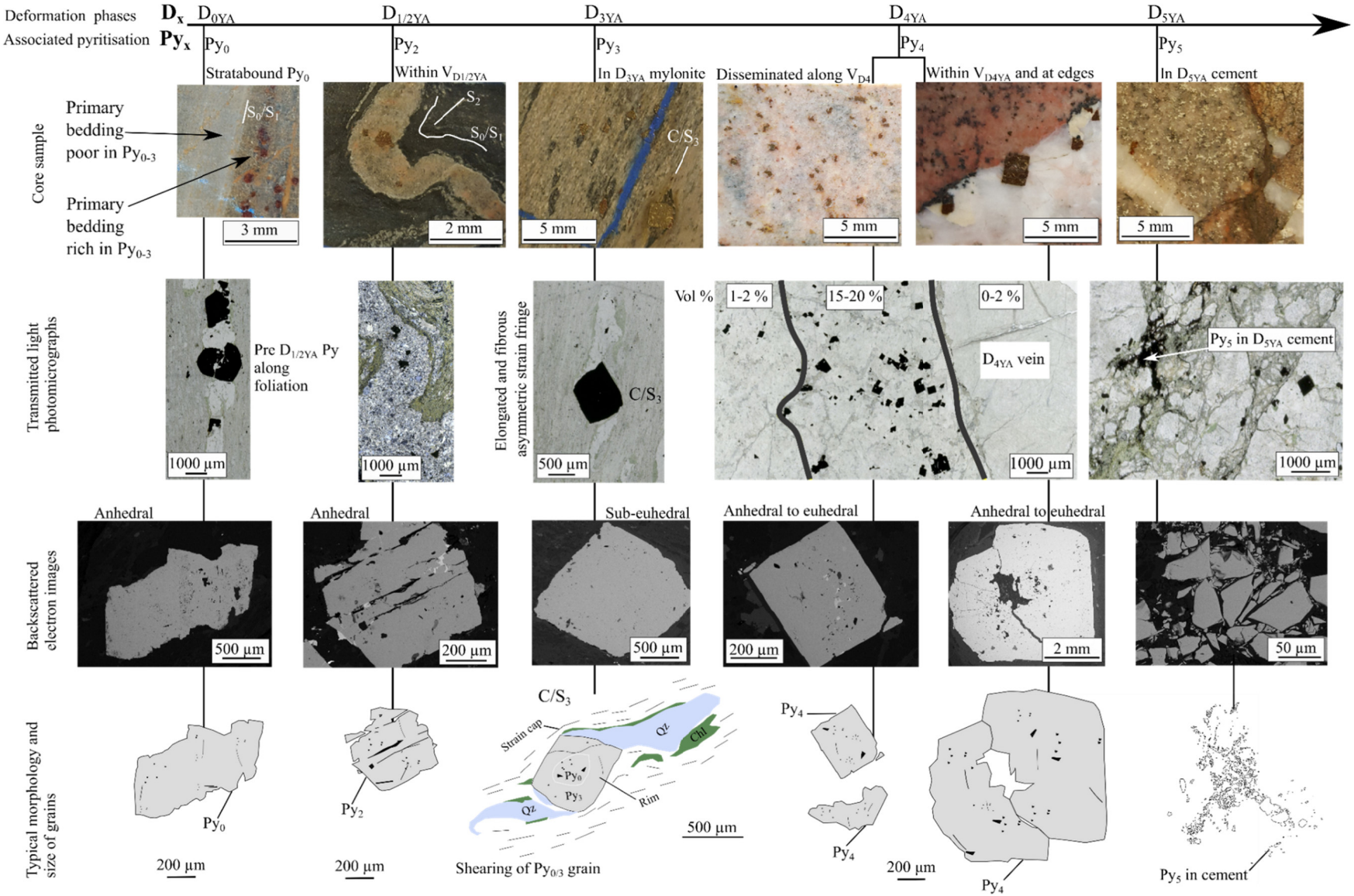
Deformation phases
Dx
D0YA
D1/2YA
D3YA
D4YA
D5YA
Associated pyritisation
Pyx
Py0
Py2
Py3
Py4
Py5
Stratabound Py0
Within VD1/2YA
In D3YA mylonite
Disseminated along VD4
Within VD4YA and at edges
In D5YA cement
Core sample
Primary bedding poor in Py0-3
Primary bedding rich in Py0-3
S0/S1
S2
C/S3
3 mm
2 mm
5 mm
5 mm
5 mm
5 mm
Transmitted light photomicrographs
Pre D1/2YA Py along foliation
Elongated and fibrous asymmetric strain fringe
Vol %
1-2 %
15-20 %
0-2 %
D4YA vein
Py5 in D5YA cement
1000 µm
1000 µm
500 µm
1000 µm
1000 µm
Backscattered electron images
Anhedral
Anhedral
Sub-euhedral
Anhedral to euhedral
Anhedral to euhedral
500 µm
200 µm
500 µm
200 µm
2 mm
50 µm
Typical morphology and size of grains
Py0
Py2
C/S3
Strain cap
Qz
Chl
Py0
Py3
Rim
Qz
Py4
Py4
Py4
Py5 in cement
200 µm
200 µm
500 µm
Shearing of Py0/3 grain
200 µm

Figure 2-11 Synthetic representation of each pyrite generation interpreted from photomicrographs (reflected light microscopy and BSE images) highlighting the various textures, morphologies, and characteristics of pyrite grains.

Pyrite Py_0

Primary Py_0 is only observed within the metasedimentary unit. This generation, relatively rare in the studied area, occurs as stratiform, layered or banded grains with a grain size ranging from 250 µm to 1.5 mm (Fig. 11). Observed as cores of $Py_{0/3}$ associated with D_{3YA} and as oriented chips in the main foliation S_2, Py_0 grains are anhedral, irregular and fractured with barite infills. When forming the core of $Py_{0/3}$, Py_0 grains present a rounded shape with abundant inclusions such as galena and plagioclase resulting in a poikilitic texture. Geochemically, two types of Py_0 can be discriminated based on their As content in the core (high versus low content, Fig. 12) from 6 EPMA X-rays maps. Highest submicroscopic gold values are found in both types of Py_0 with a median value of 1.1 ppm (Fig. 13B) and outliers above 50 ppm. These outliers represent analyses of the core of As-rich pyrite grains. The gold nature constrained by the spectrum pattern (as exampled in Fig. 13C) is submicroscopic. For this study, LA-ICPMS analyses do not allow to determine whether trace elements are present as nanoparticles or as solid solution in the pyrite lattice substituting Fe. However, micro-inclusions can be deciphered from lattice gold/nanoparticles. Both Py_0 subtypes return high arsenic content above 200 ppm with a median value of 2800 ppm (Fig. 14).

Pyrite Py_2

Anhedral, highly fractured, Py_2 grains are located within folded $D_{1/2YA}$ veins only (Fig. 11). No inclusions nor zonation are observed within these 200 to 500 µm large grains, although barite and chalcopyrite are identified in fractures. In metavolcanite, Py_2 is spatially associated with magnetite and chalcopyrite. No pyritisation is observed within the halo of the $D_{1/2YA}$ veins. This hydrothermal pyrite generation is rare at Yaou. Gold concentration of analysed Py_2 is below the detection limits. This generation shows high a Ni content (mean value of 8000 ppm) together with a lower As and Te content compared with Py_0 (Fig. 14).

Pyrite Py_3

Sub-euhedral (early-D_{3YA}) to euhedral (syn- to late-D_{3YA}) Py_3 pyrite grains formed during the D_{3YA} shearing of the metasedimentary unit, grows around pre-existing Py_0 clasts and presents a grain size typically ranging from 1 to 3 mm. Py_3 is commonly associated with minerals such as rutile, apatite and chalcopyrite within the shear zone. The Py_3 porphyroblasts around Py_0

porphyroclasts exhibit asymmetrical quartz-chlorite strain fringes in agreement with a C/S_3 shearing (Fig. 11). Oscillatory, Co and/or As chemical zonation are commonly observed in Py_3, with overgrowth sequences repeated up to seven times with complete and straight rims of alternating rich and depleted bands observed on EPMA mapping (Fig. 12). Cobalt concentrations in Py_3 vary from 40 to 4800 ppm (Fig. 14). Cobalt-rich bands are observed at the core-rim (Py_0-Py_3) boundary and at edges of the grain. Py_3 displays an As content ranging from 25 ppm in As-depleted rims up to 3000 ppm in As-rich rims. The median value of invisible Au is of 0.25 ppm for this generation.

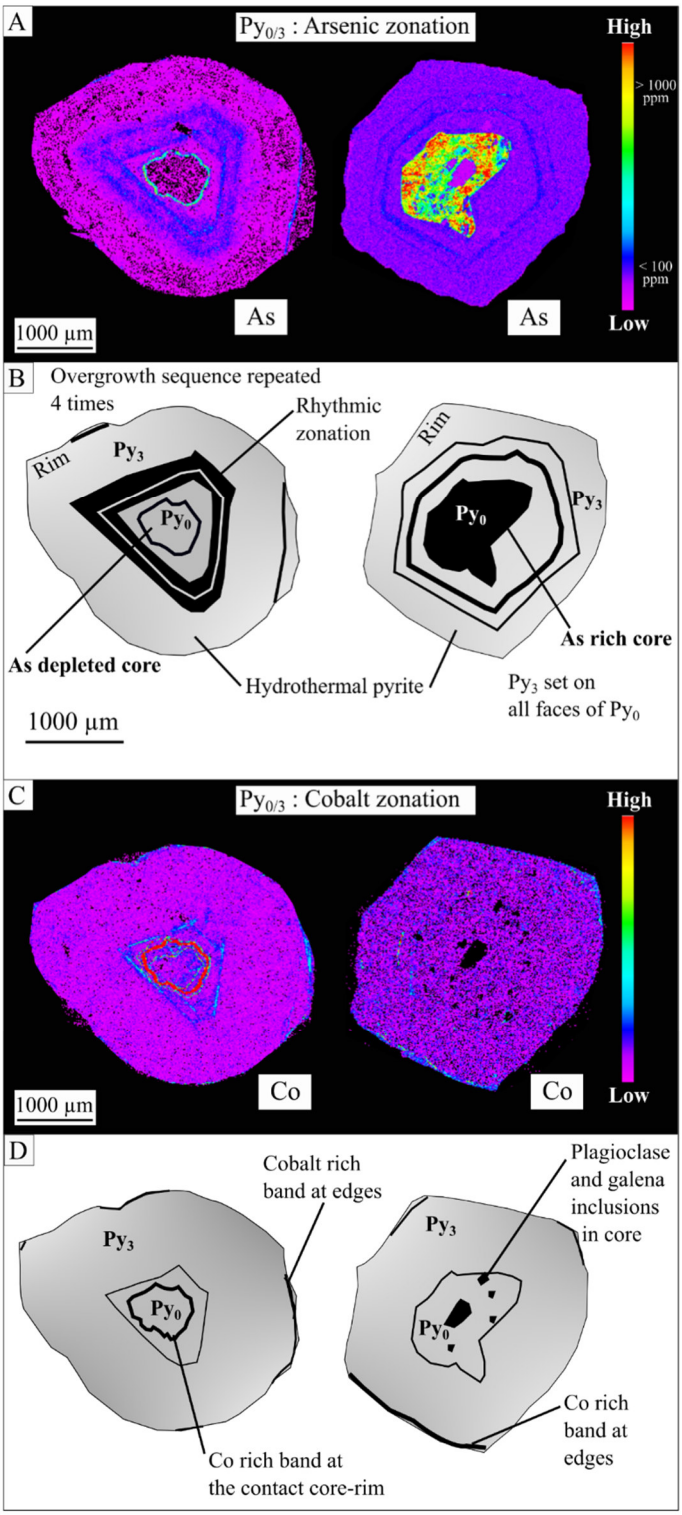

Figure 2-12 EPMA mapping of arsenic and cobalt concentration on typical Py_{0-3} with core-rim identification and oscillatory zonation. Two types are presented, As rich core and As depleted core with typical rhythmic zonation.

Pyrite Py_4

Two types of Py_4 are interpreted in association with the D_{4YA} event. The first subtype of Py_4 is developed within the D_{4YA} veins, whereas the second type, representing the most abundant sulphide at Yaou, corresponds to disseminated pyritisation of the host rock proximal to the D_{4YA}

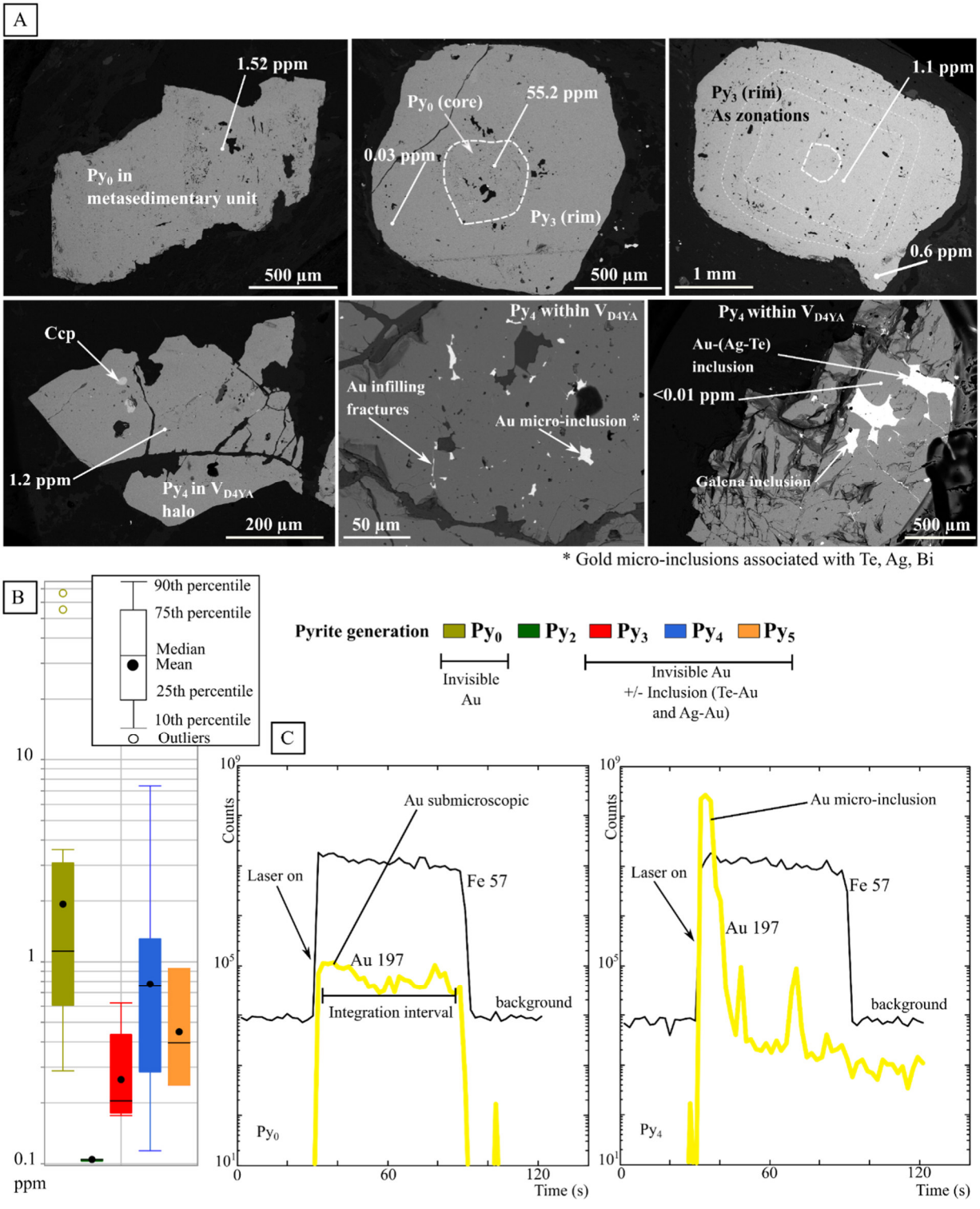

*Figure 2-13 (**a**). BSE images with examples of spot analyses and corresponding gold assays in ppm. (**b**). Statistical representation of submicroscopic gold contents for each pyrite generation (grades below 0.01 ppm are not represented). (**c**). Typical LA-ICP-MS pattern outputs for inclusions and submicroscopic gold discrimination.*

veins. The vein-hosted pyrite (subtype 1) is fractured, anhedral to subhedral, with grain size ranging from 1 mm to 8 mm, and less fractured compared to other pyrite generation (Py_0 to

Py_3). Various micro-inclusions within the pyrite grains are observed (Fig. 13A) including: Au-Te, Au-Ag (electrum), Au-Ag-Te, Bi-Ag, Ag-Te, PbS (galena) and Te-Bi. Also, a significant number of LA-ICP-MS analyses of gold in Py_4 return pulselike patterns, indicating the presence of a micro-inclusion in the ablated volume (Fig. 13C). The disseminated pyrite (subtype 2 of Py_4) is mostly euhedral, ranging from 100 to 500 µm in size. These grains contain inclusions of chalcopyrite, galena and tellurides. In addition, apatite and rutile are identified in association with pyrite but not as inclusions. The observed modal abundance of pyrite decreases with increasing distance from the veins, from 15-20 vol.% in the halo, to less than 2 vol.% in the intermediate (1 to 5 cm away from the vein) to distal zone. Contrary to Py_3, no chemical zonation (e.g. As, Co or Pb) of the Py_4 grains has been identified by EPMA mapping. Importantly, gold is found in Py_4, as micro-inclusions with average size of 10 µm, and as infilling micro-fractures (in both pyrite subtypes). The gold content of Py_4 ranges from 0.3 to 7.5 ppm, with a median value of 0.75 ppm of invisible gold. Py_4 displays a lower content of As than the pre-existing generations. Te (average grade of 15 ppm) and Bi (average grade of 3 ppm) contents are similar to that of Py_0 and higher than that of Py_2 and Py_3.
Importantly, LA-ICP-MS analyses located at the vicinity of the gold micro-inclusions return low (below average detection limit of 0.068 ppm) gold values (Fig. 13A). Eight ablation spots were targeted at selected gold micro-inclusions larger than 30 µm displaying relatively high average concentrations of Te (2207 ppm), Ag (1309 ppm), and Bi (1326 ppm).

Pyrite Py_5

Py_5 occurs in the cement of D_{5YA} breccia both as fractured and as euhedral grains. When not spatially associated with D_{4YA} veins, the D_{5YA} breccia still displays Py_5 grains. On the other hand, a late D_{4YA} pyritisation can be considered. Chalcopyrite and galena inclusions are observed within Py_5 pyrite. Py_5 has trace elements composition relatively similar to that of the Py_4 generation but with a lower gold content (median value of 0.4 ppm) and a higher Ni content (median value of 190 ppm). Few occurrences of undeformed euhedral pyrite with Bi infilling fractures have been identified. This rare, homogeneous type of pyrite, with no internal tectonic fabric is a late to post D_{5YA} pyrite.

In summary, trace element analyses of different pyrite generations indicate that Py_0, Py_3, Py_4 and Py_5 are gold-bearing (Table 1). Only Py_2 shows no gold content. Py_0 and Py_3 yield the highest As contents of all pyrite generations, and an Au-As association is suggested in pyrite related to $D_{0/3YA}$ (Fig. 14). Although all pyrite generations are displaying relatively similar

concentration ranges for Bi, Te, Co, Ag and Ni, a significative increase of the Te content is observed from Py_2 to Py_5. $D_{4/5YA}$ gold inclusions in pyrite yield outstanding Te, Ag and Bi contents (> 1000 ppm) compared to all pyrite generations.

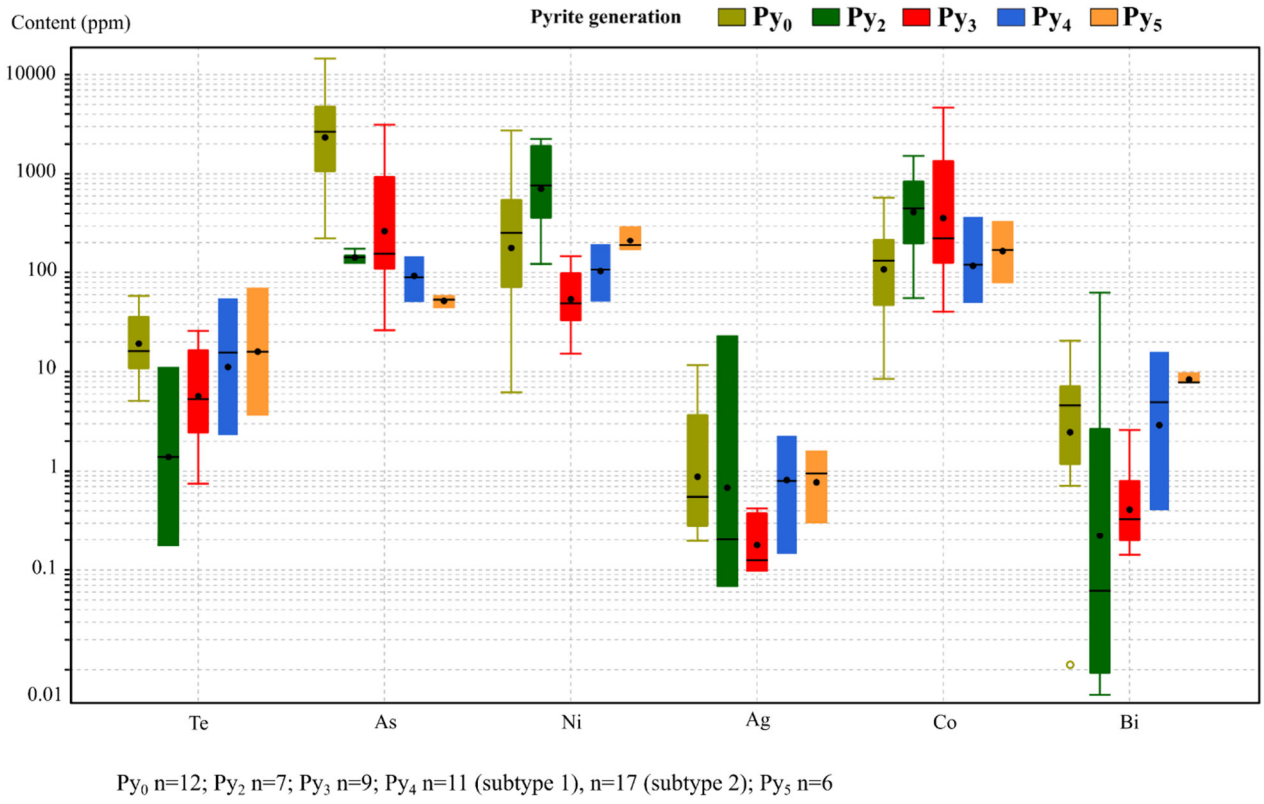

Figure 2-14 Statistical representation of trace element (Te, As, Ni, Ag, Co, Bi) distribution in ppm for each pyrite generation. Concentrations are in logarithmic scale.

Discussion

Relative chronology of the multi-phase deformation, magmatic and hydrothermal activity

Based on the petro-structural and relative petro-chronological features described at macro- and microscale, we can establish the following framework at the Yaou deposit scale. First, Py_0 pyrite grains are: (1) hosted only in a metasedimentary unit; (2) disseminated in sulphide-rich layers alternating with sulphide-poor bands and identified along the S_0/S_1 fabric (i.e. stratiform); and (3) not related to any veining (and related pyritisation event). Py_0 is interpreted as a sediment-hosted pyrite being either (i) diagenetic; (ii) hydrothermal; or (iii) the product of recrystallisation of diagenetic pyrite during prograde greenschist facies metamorphism. Py_0 with an average content of 2500 ppm of As, can be defined as arsenian (Fleet *et al.*, 1988). The

presence of mineral inclusions such as albite and galena and porosity could suggest that Py_0 is the product of a replacement process (Putnis, 2009) that could be associated with recrystallisation of diagenetic pyrite.

The D_{1YA}/D_{2YA} deformation phases are characterised by the S_1 and S_2 fabrics witnessing a ductile regime and by folded (or re-folded) $D_{1/2YA}$ veins which can be distinguished from others vein generations as being the only one transposed within the S_2 foliation.

The D_{2YA} phase is interpreted as having occurred during peak metamorphism, as evidenced by the greenschist-facies mineral assemblage of chlorite-sericite underlining the regional S_2 foliation. The intrusive phase is interpreted as post-D_{2YA}. Indeed, the intermediate dykes and plutons locally contain metavolcanite xenoliths witnessing S_2 fabrics, and no clear penetrative foliation has been developed within intrusive bodies at macroscopic or at microscopic scale, except within the later shear zone.

The relative chronology between the subsequent D_{3YA} shearing phase and the intrusive phase is not clearly constrained in this study. D_{3YA} shearing has affected the intrusive bodies located at the margin of the N60°-striking shear zone, where the intrusive rocks are mylonitic showing ductile albite recrystallisation. The most likely relative timing of the intrusion would be pre- to early syn-D_{3YA}. The shearing could have enabled the magma to rise and emplace as various intrusive bodies. This igneous intrusion mechanism resolves the space needed for the emplacement's issue as example in Hutton *et al*. (1990) and references therein. The D_{3YA} deformation phase is evidenced by (1) the N60°E C/S_3 fabrics, (2) the mylonitic texture of the host rock within the shear zone and (3) the asymmetrical strain fringes around $Py_{0/3}$. The shear zone is interpreted as continuous across the Yaou Central zone where three studied drillcores intersect the sheared metasediments (F31 and F75) and rarely metavolcanite (F24). In the F24 drillcore, the shearing is less defined within the metavolcanite, as no porphyroclast are present to evidence the kinematics.

The shear zone and the related C/S_3 fabrics are crosscut by the D_{4YA} quartz-calcite veins (Fig. 4). The interpretation of a separate D_{4YA} deformation phase is further supported by the fact that when D_{4YA} veins and associated pyritisation are observed within the mylonitic zone, the Py_4 do not show any fringes or pressure shadows. These D_{4YA} veins are, therefore, clearly not affected by the D_{3YA} shearing. Not laminated, they are interpreted as dilational. D_{4YA} veins can be clearly distinguished from other vein generations by the strong associated pyritisation at selvages. At the camp scale, a system with a continuum between the D_{3YA} and D_{4YA} could be considered and classified as a progressive deformation with two end-members: an early sinistral shearing phase

characterized by pre- to syn-tectonic intrusions and a later brittle veining phase in a transcurrent regime. However, following Fossen (2019) concept of deformation phases *versus* progressive deformation, we do not have (i) the relative age (no U-Pb or Re-Os dating) of the different structures related to each deformation phases (e.g., shearing for D_{3YA} and veining for D_{4YA}) and (ii) the orientation of the local stress for each deformation phases (as no oriented drillcore have been done), and therefore we did not identify the regional or far-field stress to discuss a large-scale tectonic model. Thus, without any structural measurements on the D_{4YA} vein system, it is difficult to consider if the D_{3YA}-D_{4YA} deformation phases result from a single progressive deformation (single deformation phase) or a two-stage deformation.

Regarding the hydrothermal alteration paragenesis adjacent to the different vein systems, no alteration is associated with D_{1YA}/D_{2YA}, whereas a reddish alteration selvage characterised by an ankerite-albite-pyrite-hematite assemblage is a key alteration footprint for the D_{4YA}-related hydrothermal event. The D_{4YA} veins are locally offset by a late brittle D_{5YA} deformation phase. Following the classification of Jébrak (1997) and Chauvet (2019b), the brecciation is interpreted to result from hydraulic fracturation with jigsaw geometry and monogenic angular clasts, formed under high fluid overpressure with no evidence for clast rotation. A late carbonate dominated D_{5YA} veining crosscut all the deformation features at Yaou.

Comparing our pyrite generation interpretation with that made at Yaou by Milesi *et al*. (2003) and unpublished internal report (Khuns, 1992), their disseminated Py_1 with pressure shadows corresponds to the Py_{0-3} of the present study, whilst their coarse pyrite Py_2 associated with veining, and the fine grained disseminated Py_3, correspond to the Py_4 types 1 and 2 of the present study. Regarding deformation phases, we agree with the historical internal report of Bardoux (1994) which identifies a folding phase (the D_{1YA}/D_{2YA} phase of this work) followed by a simple shear event (the D_{3YA} phase).

The Yaou gold deposit: a polyphase gold system

No single mineralisation event may explain the formation of the Yaou deposit (see characteristics in Table 2). Indeed, histogram logs presented in Figure 6 emphasise that the whole-rock gold content in drillcore intercepts are correlated to: (1) the frequency of D_{4YA} veins; (2) the amount of Py_4 pyrite; and (3) the abundance of Py_{0-3} pyrite. Low grade intercepts

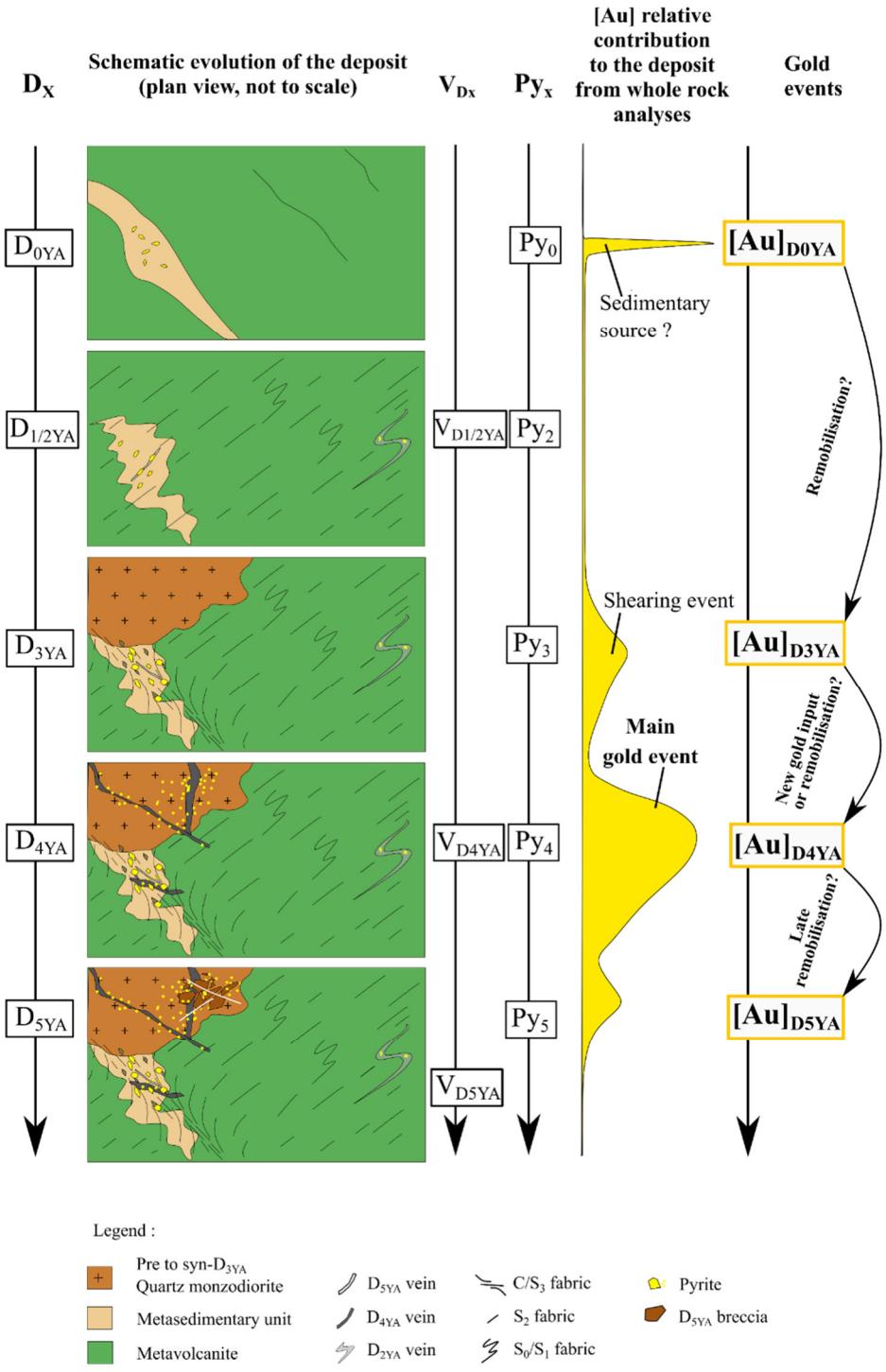

Figure 2-15 Five-phases model for the formation of the Yaou polyphase gold mineralisation with interpreted contribution of each gold events. Possible gold remobilisation and/or new gold input are associated with each deformation phase. The main gold stage is related to the D_{4YA} deformation phase.

coincide with D_{1YA}/D_{2YA} veins and associated Py_2 pyrite. Therefore, two auriferous events are recorded and are related to the D_{3YA} shearing and D_{4YA} veining. The main ore zones are delineated by the high density of D_{4YA} veins (Fig. 6). It is worth noticing that these two

auriferous stages can be discriminated by the whole-rock gold grades: the gold content is ranging from 0.5 to 5 g/t for the D_{4YA} related mineralisation intercepts while the grade associated with D_{3YA} is below 1.5 g/t. Contrastingly, gold grades associated with $D_{1/2YA}$ veins fall below 0.1 g/t.

The estimation of the amount of gold attributed to each event (Fig. 15) is only relative due to a lack of precise mapping, precluding accurate volume quantification:

(1) At the microscopic scale (Fig. 16), the D_0-related, stratabound sediment-hosted Py_0 grains could represent a primary source of gold. However, from both drillcore and outcrop observation, this unit is relatively infrequent in the studied area. Their contribution in the total gold endowment of Yaou deposit is therefore considered as weak. Either way, the D_{0YA} can be interpreted as an early gold event, characterised by invisible gold (i.e., nano-inclusions and/or solid solution in the lattice of the sediment-hosted pyrite), as evidenced by time-resolved depth-concentration spectra patterns from LA-ICP-MS with no spikes observed in the profile (Fig. 13C), (e.g., Reich *et al*., 2005; Cook *et al*., 2009; Large *et al*., 2011, Velasquez *et al*., 2014 and Wu *et al*. 2019). Similar arsenian pyrites displaying submicroscopic gold have been described by several authors (e.g., Cook and Chryssoulis, 1990; Reich *et al*., 2005; Sung *et al*., 2009).

(2) No contribution to the gold budget has been evidenced for the $D_{1/2YA}$-related pyritisation.

(3) The D_{3YA} shearing has a major influence on the deposit formation. The shear zone probably acted as a channel conduit for both magma and hydrothermal fluids. However, the contribution of Au_{D3YA} to the total resource is relatively minor as Py_3 is only present within the 30 m-large D_{3YA} shear zone. Core-rim relationships (Fig. 11) and the associated gold imply that during the D_{3YA} shearing phase, Py_0 recrystallised to form a coarser-grained pyrite $Py_{0/3}$ with remobilization and re-concentration of submicroscopicAu_{D0YA}. Au and As rich rims grew around pyrite core, with multiple redistribution of gold towards the rims (Velasquez *et al*., 2014 and 2018; Mumin *et al*., 1994.). The oscillatory zoning of Co and As within the grains is interpreted to be associated with crystallisation in an episodic fluid flow regime in which fluid composition fluctuated due to fault-valve behaviour (Mishra *et al*., 2018). The remobilisation process may give Au and As-depleted cores and Au and As-rich margins while some grains have been observed with Au and As-rich cores and poorly developed rims, but this statement in only based on LA-ICPMS spot analyses of gold and not from Au mapping, we have therefore not a global image of the whole pyrite grain Au spatial distribution. Regarding the As content fluctuation, the high geochemical variation in sedimentary/diagenetic pyrite (Large *et al*., 2007) can be enhanced through further hydrothermalism and metamorphism (Gregory *et al*., 2019).

(4) The D_{4YA} phase is the main gold deposition event, outlined by elevated grade intercepts that likely result from new gold input and/or remobilisation (Fig. 6). The D_{4YA} veins clearly postdate the intrusive event. Auriferous D_{4YA} veins are mostly hosted by the plutonic and sub-volcanic rocks which acted as brittle, reactive host rocks receptive to fracturing and mineralisation. Indeed, the brittle rheology of the intrusions compared to the adjacent volcanic and sedimentary country rocks is inferred to be a key factor that controls the distribution of the gold in granitoid-hosted deposit type. Several other Palaeoproterozoic granitoid-hosted gold deposits are known in West Africa (e.g. the Chirano deposit in Ghana (Allibone *et al*., 2004), the Telem deposit in the Syama District (Traoré *et al*., 2015)). It is worth noticing that rare D_{4YA} veins within metavolcanite, locally observed in drill cores, are auriferous. Although the distance between these veins and the nearest intrusive bodies is unknown, it is possible that these veins may be located in the vicinity of a buried quartz monzodiorite body. The D_{4YA} event represents a major contribution to the total resource, involving a potentially new gold input related to hydrothermal fluids, together with some interpreted remobilisation of older gold. The gold grade of Py_4 ranges from 0.3 to 7.5 ppm, with a median value of 0.75 ppm. Such a high variability in gold content relates to the presence of gold nano- to micro-inclusions within pyrite. Micro-inclusion is the most common gold species as supported by SEM observations together with the pulse like patterns of LA-ICP-MS spectra (Fig. 13C). Contrastingly, free gold in the veins is rare, as only one occurrence of free gold in quartz has been observed. The relatively low content of invisible gold is tentatively resulting from remobilisation of invisible gold within pyrite Py_4 which reprecipitates as micro-inclusions and as infills within internal fractures of pyrite by coupled dissolution reprecipitation processes that liberate Au from the pyrite structure (Mumin *et al*., 1994; Oberthür *et al*., 1997b; Cook *et al*., 2009; Large *et al*., 2009; Sung *et al*., 2009, Cook *et al*., 2013; Simard *et al*., 2013; Fougerouse *et al*., 2016 a, b; Velasquez *et al*., 2018 and Hastie *et al*., 2020). The visible free gold flakes type displays a high purity with fineness of ~940 and silver contents ranging from 5.6 to 6.1 wt % whereas the average gold fineness for micro-inclusions within Py_4 is ~904. These fineness values are typical of orogenic gold deposits with a fineness > 900 (Morrison *et al*., 1991).

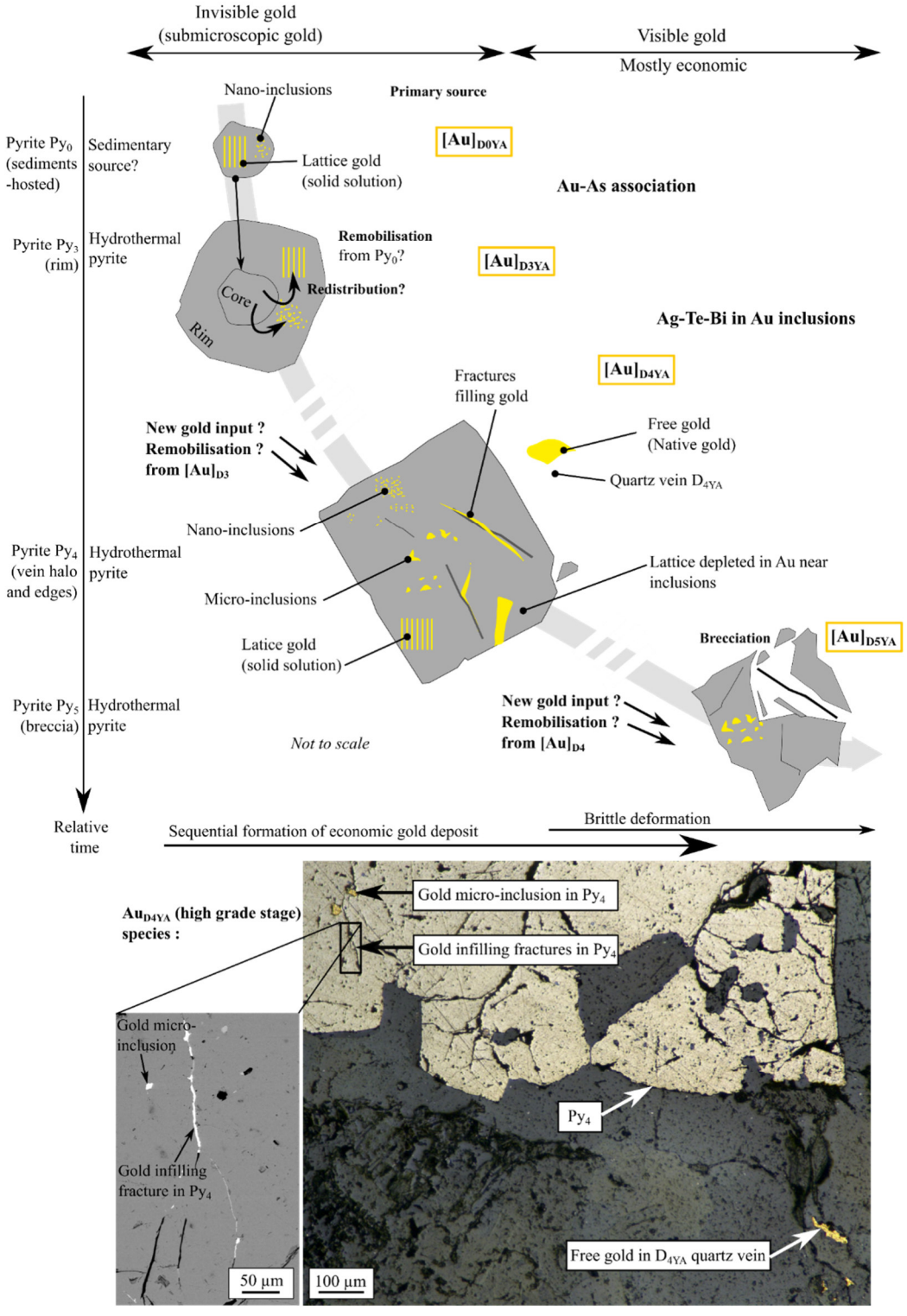

Figure 2-16 Interpretation at the microscopic scale of the evolution of gold species and behaviours through time associated with defined pyritisation events. The two types of submicroscopic gold (gold nano-inclusions and lattice gold), have not been clearly discriminated in this study. Gold micro-inclusions in Py4 are responsible for the bulk of the mineralisation.

To summarise, three gold types can be described associated with the main gold D_{4YA} event (Fig. 16): (1) anhedral gold micro-inclusions in Py_4, with an average gold fineness of 904, (2) gold infilling cracks in Py_4 and (3) free gold flakes in a D_{4YA} quartz-carbonate vein at the edge of Py_4 pyrite with an average fineness of 940. These high finenesses (>900) may correspond to remobilised gold, contrasting with the lower values that characterise primary by gold (as proposed Oberthür *et al*., 1997b and Velasquez *et al*., 2014). There is therefore a potential but unproven input from remobilised gold. Trace elements signatures within the Au_{D4YA} micro-inclusions provide evidence for the presence of Ag, Te and Bi-bearing minerals. Also, Ag, Te, and Bi concentrations in Py_4 grains are higher than in Py_3. These two observations suggest that such elements have been introduced, together with Au, as a new metal input by the D_{4YA} hydrothermal event.

(5) Finally, Au_{D5YA} is found as micro-inclusions and its relative contribution to the system is minor. Py_5 are auriferous but whole-rock gold assays are below 0.5 g/t for D_{5YA} breccia.

Table 2-2. Summarised ore characterisation of the Yaou deposit

Deformation phase	**D_{0YA}**	**$D_{1/2YA}$**	**D_{3YA}**	**D_{4YA}**	**D_{5YA}**
Gold event	Au_{D0YA}	ø	Au_{D3YA}	Au_{D4YA}	Au_{D5YA}
Ore shoot hostrock	Metasedimentary unit	ø	Metasedimentary unit	Mylonite and quartz monzodiorite	Quartz monzodiorite
Ore control	Lithological	ø	Structural	Rheological/ intrusion-hosted	Rheological/ intrusion-hosted
Contribution to the budget	Low	No	Low	High	Low
Gold typology	Submicroscopic in Py_0	No gold	Submicroscopic in Py_3	Submicroscopic, micro-inclusion/ infills in Py_4 and free gold	Micro-inclusion
Gold behaviors	Early source	No gold	New input and/or remobilisation	New input and/or remobilisation	New input and/or remobilisation
Typical whole-rock gold grade (ppm)	No data	<0.01	0.1 to 1.8 (Au_{D0YA} +Au_{D3YA})	0.5 to 10	0.5
Median submicroscopic gold value within pyrite (ppm)	1.1	<0.01	0.2	0.75	0.4
Bulk of the mineralisation	Submicroscopic gold-rich arsenian core Py_0	ø	Submicroscopic gold-rich rims in pyrite Py_3	Mostly micro-inclusions in pyrite Py_4 and rare free gold grains in veins	Py_5 in cement
Trace element	As	ø	As	Te, Ag, Bi	Te, Ag, Bi

Overall, the Yaou deposit is characterized by an early, low-grade enrichment (from Au_{D0YA} to Au_{D3YA}) followed by a later, higher-grade episode (Au_{D4YA}). From trace elements and gold content variation along this polyphase history, we identify two main geochemical associations: invisible gold is linked to arsenic (association largely evidenced in orogenic gold deposits; Pitcairn *et al*. 2006; Large *et al*., 2007, 2009, 2011) and visible gold is associated with Te-Ag-Bi rich inclusions.

The fluid source and metal association are different for pyrite related to shearing (Au-As) with the mineralising fluid that can be buffered by the (meta-) sediments (Large *et al*., 2007); when the pyrite related to veining (with Au-Te-Bi-Ag micro-inclusions), may have the geochemical footprints of the intrusion (Jowitt *et al*., 2014).

When dealing with the ore shoots control, we identify (1) a lithological control for Au_{D0YA} with a stratabound deposition within sediments, now metamorphosed in the greenschist facies; (2) a syngenetic, structural control (sinistral shearing) for Au_{D3YA} along the N60°E trend; (3) a rheological control for the Au_{D4YA} where ore shoots are located preferentially within the intrusive bodies, this latter control being epigenetic and (4) a structural control for those D_{4YA} veins which locally are re-using the pre-existing N60° striking C/S_3 foliation.

The distribution of gold clearly illustrates the geometrical and spatial relationships between auriferous zones and the D_{3YA}-D_{4YA}-D_{5YA} features, highlighting a polyphase system at both the macroscopic and microscopic scales. This property is critical for exploration as gold can be located in various settings characterised by multiple possible gold remobilisation and new gold inputs.

An intrusion-hosted high-grade event responsible for the bulk of the Yaou gold mineralisation

When dealing with the deposit type definition of mineralised system spatially associated with intrusion, it is not easy to decipher between orogenic gold deposit, (intrusion-hosted within or near major low-grade shear zones) and intrusion-related gold system. The Yaou deposit present several typical characteristics of orogenic gold deposit as evidenced by authors like Groves *et al*. (1998); Goldfarb *et al*. (2001); Robert and Poulsen, (2001), Groves *et al*. (2003); Goldfarb *et al*. (2005); Dubé and Gosselin, (2007): a gold-only metal suite, hosted in deformed and metamorphosed (to greenschist facies) units belonging to greenstone belts (Paramaca Greenstone Belt), a low sulphide content (less than 5 volume percent of pyrite) with an increase

near quartz-carbonate veins (pyritisation at the selvage of the D_{4YA} quartz-carbonate veins), a spatial association / control with transcurrent structures (D_{3YA} shear zone), a carbonate-sericite-albite alteration assemblage (with proximal hydrothermal ankerite), a ductile-brittle transitional regime (from D_{3YA} to D_{4YA}) and a geochemical signature, with elements such as Ag, Te, Bi and Pb. Taken apart, the strong correlation between intrusive bodies and mineralisation could equally argue for an intrusion-related gold system or IRGDs (Sillitoe *et al*., 1991; Lang *et al*., 2000, Baker *et al*., 2002; McFarlane *et al*., 2011), or for an intrusion-hosted system wherein mineralisation is rheologically controlled by the intrusive bodies. At Yaou, geological and geochemical observations do not support an IRGD setting as (1) IRGD deposits are typically low-grade deposits from 0.8 to 1.5 g/t (Goldfarb *et al*., 2005; Goldfarb and Groves 2015; Groves *et al*., 2019) whereas the gold grades at Yaou are frequently above 4 g/t; (2) there is no zonation of the ore and alteration systems observed around intrusions (Hart *et al*. 2002). The Au-Te-Bi assemblage do not help here to discriminate the deposit type; indeed these geochemical signatures characterise intrusion-related mineralisation, but also hydrothermal deposits (Hart and Goldfarb, 2005). The source of Te may come from metasediments or magma (Keith *et al*., 2018). Lang and Baker (2001) and Pulz *et al*. (1991), on the other hand, highlight the association Au-Bi as a key feature of IRGD. Also, Jowitt *et al*. (2014) mention that W, Mo, Be, Li, Sn, Fe and Bi-tellurides assemblages reflect magmatic affinities. Except the Bi-Te association, such assemblage is not observed here and scheelite, as well as molybdenite, has not been described at Yaou. Therefore, we interpret the D_{4YA} gold event as being mostly intrusion-hosted, with potential local geochemical buffering of the hydrothermal fluid with by the magmatic host rock with no genetic intrusion-related component.

The Yaou polyphase gold system in the metallogenic evolution of the Guiana Shield

Without absolute dating of the deformation stages, a comparison of the deposit scale deformation phases documented at Yaou and the regional scale deformation sequence proposed by Delor *et al*. (2003a, b) and Vanderhaeghe *et al*. (1998) remains challenging. Nevertheless, the following correlation may be proposed: (1) D_{1YA}/D_{2YA} would refer to the regional D_1 deformation phase defined as a compressional regime, in the context of the first period of crustal growth and recycling by magmatic accretion; (2) D_{3YA} could be related to the sinistral shearing (D_{2a}) with the transcurrent shear zones associated with the oblique convergence during the tectonic accretion between crustal blocks; and (3) D_{4YA}/D_{5YA} may correspond to the regional D_{2b} characterised by the final oblique collision between newly formed continental blocks.

Polyphase gold systems have been suggested within the Guiana Shield: Voicu *et al*. (1999) define a polyphase system with an early gold deposition associated with tungsten (unlike at Yaou where scheelite has not been observed) followed by a main gold event associated with Te during stages 2 and 3. Velasquez *et al*. (2014, 2018) define a polyphase system at the El Callao gold deposit in Venezuela with an early stage under the ductile and ductile-brittle transition characterised by invisible gold, followed by a primary gold remobilisation under brittle conditions. When comparing the gold associations defined at Yaou to the other deposits within the Guiana Shield, the Au-As association defined at Merian in Suriname (Kioe-A-Sen *et al*., 2016; Bardoux 2017) can be consistent with the $Au_{D0/D3YA}$ and As association described at Yaou within the metasedimentary unit. Assemblage of gold and telluride minerals similar to the one observed for the D_{4YA} is described in Guyana, at the Karouni deposit (Tedeshi *et al*., 2019) but also at the Omai deposit (Voicu *et al*., 1999) where an intrusion-hosted mineralisation is also identified.

Conclusions

Coupled petro-structural and geochemical approach demonstrates that gold mineralisation at the Yaou deposit, French Guiana, is a polyphase system at both macroscopic and microscopic scales with a total of four pyrite generations and gold deposition. Py_0 hosted by the metasedimentary unit is interpreted as diagenetic in origin, forming cores of hydrothermal Py_3 overgrowths developed during a subsequent D_{3YA} sinistral shearing event. Hydrothermal Py_4 are observed as disseminated crystals proximal to quartz-carbonate D_{4YA} veins (within ankerite/hematite-rich alteration haloes), at the edges and within D_4 veins. The last event is represented by Py_5 within the matrix of the D_{5YA} brecciation. At the microscopic scale, Py_0 is interpreted as a possible primary source of submicroscopic gold with a relatively weak contribution to the total resource. The hydrothermal and shear-hosted Py_3 exhibits gold content above > 0.2 ppm after possible remobilisation of Au_{D0YA}. Most of the high-grade mineralisation is associated with one set of hydrothermal quartz-calcite veins formed during the brittle D_{4YA} phase. Gold micro-inclusions within Py_4 are the primary contributors to the gold system together with minor contribution from both free and submicroscopic gold. The ore shoot locations during the various stages are lithologically controlled for Au_{D0YA} (metasedimentary unit), structurally controlled (sinistral shearing) for Au_{D3YA} and rheologically controlled for the Au_{D4YA} (intrusion-hosted). We identify two main geochemical associations: invisible gold is linked to arsenic whereas visible gold is observed as inclusions with high contents of Ag, Te and Bi. The camp-scale petro-structural framework proposed at Yaou witnesses therefore the

polyphase gold endowment of the Rhyacian crust throughout the Trans-Amazonian orogeny within the Guiana Shield, where the main gold event could be associated with the regional D_{2b} phase (local $D_{3/4YA}$ phase) related to strike slip shearing at ca. 2.07-2.05 Ga (Delor *et al*., 2003a).

Acknowledgements

This study is part of Vincent Combes's Ph.D. research at the Université de Lorraine within the GeoRessources laboratory, in Nancy, France. This work greatly benefited from discussions and friendly support from F. Tona. We are grateful to D. Tamagno for allowing this Ph.D research, to the GET Laboratory in Toulouse, France, for LA-ICP-MS analyses, to O. Rouer and A. Lecomte at the SCMEM and to A. Flammang for thin sections manufacturing at the GeoRessources laboratory in Nancy, France. We gratefully acknowledge B. Gourcerol and one anonymous reviewer for their constructive comments that helped to greatly improve the manuscript as well as T. Torvela for the final corrections and editing work.

Funding

This research was funded by Auplata Mining Group (AMG). This work has also benefited from the framework of both CREGU and the LabEx RESSOURCES21 (supported by the French National Research Agency through the national program 'Investissements d'avenir', reference ANR-10-LABX-21–LABEX RESSOURCES 21)

References

Allibone AH, McCuaig TC, Harris D, Etheridge MA, Munroe S, Byrne D, Amanor J, Gyapong W. 2002a. Structural controls on gold mineralization at the Ashanti gold deposit, Obuasi, Ghana. Econ Geol Spec Pub 9:65–93.

Allibone AH, Hayden P, Cameron G, Duku F., 2004. Paleoproterozoic gold deposits hosted by albite- and carbonate-altered tonalite in the Chirano district, Ghana, West Africa. Econ Geol 99:479–497.

Augustin J, Gaboury D., 2018. Multi-stage and multi-sourced fluid and gold in the formation of orogenic gold deposits in the world-class Mana district of Burkina Faso - Revealed by LA-ICP-MS analysis of pyrites and arsenopyrites. Ore Geol Rev 104:495-521.

Becker, U., Reich, M., and Biswas, S.,2010. Nanoparticle–host interactions in natural systems. In F. Brenker, and G. Jordan, Eds., Nanoscopic Approaches in Earth and Planetary Sciences: EMU Notes in Mineralogy, 8, 1–52.

Bardoux, M., 1994, Internal report on structural features observed at Yaou. Unpublished report for Guyanor Resources.

Bardoux, M., 2017, Gold mineralization of the Guiana Shield, Guiana, and Suriname, South America: Society for Geology Applied to Mineral Deposits, 14th Biennial Meeting, Québec City, Canada, August 20–23, 2017, Excursion Guidebook FT-03, p. 19–21.

Bispo-Santos F, D'Agrella-Filho MS, Janikian L, Reis NJ, Trindade, RIF, Reis, MAAA., 2014. Towards Columbia: Paleomagnetism of 1980–1960 Ma Surumu volcanic rocks, Northern Amazonian Craton. Precambrian Res 244:123–138.

Borisova A., Thomas R., Salvi S., Candaudap F., Lanzanova A. and Chmeleff J., 2012. Tin and associated metal and metalloid geochemistry by femtosecond LA-ICP-QMS microanalysis of pegmatite-leucogranite melt and fluid inclusions: New evidence for melt-melt-fluid immiscibility. Mineralogical Magazine, 76, 91–113.

Bleeker, W., 2015. Synorogenic gold mineralization in granite greenstone terranes: The deep connection between extension, major faults, synorogenic clastic basins, magmatism, thrust inversion, and long-term preservation. In Targeted Geoscience Initiative 4: Contributions to the Understanding of Precambrian Lode Gold Deposits and Implications for Exploration. Edited by B. Dubé and P. Mercier-Langevin. Geological Survey of Canada, Open File 7852, pages 25-47

Bucci, L.A., Hagemann, S., Groves, D.I., and Standing, J.G., 2002. The Archean Chalice gold deposit: a record of complex, multistage, high temperature hydrothermal activity and gold mineralisation associated with granitic rocks in the Yilgarn Craton, Western Australia. Ore Geol Rev. 19, 23–67.

Chauvet A., 2019b. Structural Control of Ore Deposits: The Role of Pre-Existing Structures on the Formation of Mineralised Vein Systems. Minerals, 9, 56.

Cabri, L., Chryssoulis, S.L. Villiers, J., Laflamme, J.H.G., Buseck, P.R., 1989. The nature of "invisible" gold in arsenopyrite. Canad Mineral. 27. 353-362.

Cook, N.J., and Chryssoulis, S.L., 1990. Concentrations of invisible gold in the common sulfides. Canad Mineral. 28, 1–16.

Cook, N.J., Ciobanu, C.L., Mao, J., 2009. Textural control on gold distribution in As-free pyrite from the Dongping, Huangtuliang and Hougou gold deposits, North China craton (Hebei Province, China). Chem Geol. 264, 101–121.

Cook, N.J., Ciobanu, C.L., Meria, D., Silcock, D., and Wade, B., 2013. Arsenopyrite–pyrite association in an orogenic gold ore: tracing mineralization history from textures and trace elements. Econ. Geol. 108, 1273–1283.

Couture, J.F., Pilote, P., Machado, N., Desrochers, J.P., 1994. Timing of gold mineralization in the Val-d'Or district, southern Abitibi belt: Evidence for two distinct mineralizing events. Econ. Geol. 89, 1542–1551.

Daoust, C., Voicu, G., Brisson, H. and Gauthier, M., 2011. Geological setting of the Paleoproterozoic Rosebel gold district, Guiana Shield, Suriname. Neth. J. Geosci. 32, 222–245.

Deditius, A.P., Reich, M., Kesler, S.E., Utsunomiya, S., Chryssoulis, S.L., Walshe, J., and Ewing, R.C., 2014. The coupled geochemistry of Au and As in pyrite from hydrothermal ore deposits. Geochim. Cosmochim. Acta. 140, 644–670.

Delor, C., Lahondère, D., Egal, E., Lafon, J.-M., Cocherie, A., Guerrot, C., Rossi, P., Truffert, C., Théveniaut, H., Phillips, D., Avelar, V.G.d., 2003b. 2-3-4 In: Transamazonian crustal growth and reworking as revealed by the 1:500000 scale geological map of French Guiana. Géol Fr, 5–57.

Delor, C., de Roever, E.W.F., Lafon, J.-M., Lahondère, D., Rossi, P., Cocherie, A., Guerrot, C., Potrel, A., 2003a. The Bakhuis ultrahigh-temperature granulite belt (Suriname) : II. Implications for late Transamazonian crustal stretching in a revised. Géol Fr. 2-3- 4, 207–230.

Dubé B, Gosselin P., 2007. Greenstone-hosted quartz-carbonate vein deposits, In Goodfellow, W.D., ed., Mineral deposits of Canada: a synthesis of major deposit types, district metallogeny, the evolution of geological provinces, and exploration methods. Geological Association of Canada, Mineral Deposits Division Spec Publ. 5, 49–73.

Dubosq, R., Lawley, C.J.M., Rogowitz, A., Schneider, D.A., and Jackson, S., 2018. Pyrite deformation and connections to gold mobility: Insight from micro-structural analysis and trace element mapping: Lithos. 310–311, 86–104.

Eglinger, A., Thébaud, N., Zeh, A., Davis, J., Miller, J., Loucks, R., McCuaig, C., Belousova, E., 2017. New insights into the crustal growth of the Paleoproterozoic margin of the Archean Kéména-Man domain, West African craton (Guinea): Implications for gold mineral system. Precambrian Res. 292, 258–289.

Enjolvy R, 2008. Processus d'accrétion crustale et régimes thermiques dans le bouclier des Guyanes : signatures géochimiques et thermochronologiques au transamazonien (2250-1950 Ma) : Phd thesis, Université Montpellier II-Sciences et Techniques du Languedoc 305 p.

Fleet, M.E., MacLean, P.J., and Barbier, J., 1989. Oscillatory-zoned As-bearing pyrite from strata-bound and stratiform gold deposits, an indicator of ore fluid evolution. In R.R. Keays, W.R.H. Ramsay, and D.I. Groves, Eds., The Geology of Gold Deposits: The perspective in 1988. Econ. Geol. 6, 356–362.

Ferrill, D.A., Morris, A.P., Evans, M.A., Burkharrd, M., Groshong Jr., R.H., Onasch, C.M., 2004. Calcite twin morphology: a low temperature deformation geothermometer J. Struct. Geol. 26, 1521–1529.

Fossen H., Cavalcante G.C.G., Pinheiro R.V.L., Archanjo C.J., 2019. Deformation Progressive or multiphase? J. Struct. Geol. 125: 8299.http://dx.doi.org/10.1016/j.jsg.2018.05.006

Fossen, H., 2010. Structural Geology. Cambridge University Press, Cambridge, 463. https://doi.org/10.1017/CBO9780511777806.

Fougerouse D, Micklethwaite S, Ulrich S, Miller J, Godel B, Adams DT, McCuaig TC., 2017. Evidence for two stages of mineralization in West Africa's largest gold deposit: Obuasi, Ghana. Econ Geol. 112: 3–22.

Fougerouse, D., Micklethwaite, S., Tomkins, A. G., Mei, Y., Kilburn, M., Guagliardo, P., Howard, D. L., 2016. Gold remobilisation and formation of high-grade ore shoots driven by dissolution-reprecipitation replacement and Ni substitution into auriferous arsenopyrite. Geochim. Cosmochim. Acta. 178, 143-159. https://doi.org/10.1016/j.gca.2016.01.040

Franklin, J., Bertoni, C., Boudrie, M., Bout, J., Costelloe, D., Lillie, F., Millo, L., Sauvage, J., 2000. The Paul Isnard gold–copper occurrence, French Guiana: the first volcanogenic massive sulphide occurrence in the Guiana Shield? In: Sherlock, R., Logan, M.A.V. (Eds.), VMS Deposits of Latin America, Geological Association of Canada, Mineral Deposits Division. Spec Publ. pp. 509–542.

Freydier R., Candaudap F., Poitrasson F., Arbouet A., Chatel B. and Dupré B., 2008. Evaluation of infrared femtosecond laser ablation for the analysis of geomaterials by ICP-MS. J. Anal. At. Spectrom. 23, 702–710.

Gibbs, A.K., 1980, Geology of the Barama-Mazaruni Supergroup of Guyana: Unpublished Ph.D. thesis, Cambridge, Harvard University, p. 385.

Goldfarb, R. J., Groves, D. I., and Gardoll, S., 2001, Orogenic gold and geological time: a global synthesis. Ore Geol Rev. 18, 1–75.

Goldfarb R.J., Groves, D.I., 2015. Orogenic gold: common vs evolving fluid and metal sources through time. Lithos 223:2–26

Goldfarb, R.J., Baker, T., Dubé, B., Groves, D.I., Hart, C.J.R., Gosselin, P., 2005. Distribution, character, and genesis of gold deposits in metamorphic terranes. Econ. Geol. 100th Anniversary Volume. 407–450.

Goldfarb, R.J., André-Mayer, A.-S., Jowitt, S.M., Mudd, G.M., 2017. West Africa: The World's Premier Paleoproterozoic Gold Province. Econ. Geol. 112, 123-143

Gourcerol B., Kontak D.J., Thurston P.C., Petrus J.A., 2018a. Gold and trace element distribution in sulfides from mineralized gold Algoma-type BIFs; Implications for nature of mineralizing fluids, metal sources and deposit models. Miner. Depos. 53:871-894.

Gourcerol, B., Kontak, D.J., Thurston, P.C., et Petrus, J.A., 2018b. Application of LA-ICP-MS sulfide analysis and methodology to deciphering elemental paragenesis and associations in addition to multi-stage processes in metamorphic gold settings. Canad Mineral. 56, 1-18.

Gourcerol, B., Kontak, D.J., Thurston, P.C., et Petrus, J.A. 2020, Application of LA ICP-MS analysis of arsenopyrite to gold metallogeny of the Meguma Terrane, Nova Scotia, Canada. Gondwana Res. 81, 265-290.

Gregory, D.D., Cracknell, M.J., Large, R.R., McGoldrick, P.J., Kuhn, S., Maslennikov, V.V., Baker, M.J., Fox, N.A., Belousov, I., Figueroa, M.C., Steadman, J., Fabris, A.J., & Lyons, T.W., 2019. Distinguishing ore deposit type and barren sedimentary pyrite using laser ablation-inductively coupled plasma-mass spectrometry trace element data and statistical analysis of large data sets. Econ. Geol. 114, 771-786.

Groves, D.I., Goldfarb R.J., Gebre-Mariam, M., Hagemann S.G., Robert, F., 1998. Orogenic gold deposits–a proposed classification in the context of their crustal distribution and relationship to other gold deposit types. Ore Geol. Rev. 13, 7–27.

Groves, D.I., Goldfarb, R.J., Robert, F., and Hart, C.J.R., 2003, Gold deposits in metamorphic belts: Overview of current understanding, outstanding problems, future research, and exploration significance. Econ. Geol. 98, 1–29.

Groves, D. I., Santosh, M., Deng, J., Wang, Q., Yang, L., & Zhang, L., 2019. A holistic model for the origin of orogenic gold deposits and its implications for exploration. Miner. Depos. https://doi.org/10.1007/s00126-019-00877-5

Guiraud, J., Tremblay, A., and Jebrak, M., 2017. The Rhyacian Montangne d'Or auriferous volcanogenic massive sulphide deposit, French Guiana, South America: Stratigraphy and geochronology [ext. abs.]: Society for Geology Applied to Mineral Deposits, 14th Biennial Meeting, Québec City, August 20–23, 2017, Extended Abstracts, p. 237–240.

Guiraud, J., Tremblay, A., Jébrak, M., Ross, P-S., Lefrançois, R., 2020. Stratigraphic setting and timing of the Montagne d'Or deposit, a unique Rhyacian Au-rich VMS deposit of the Guiana Shield, French Guiana. Precambr Res. 337, 105551.

Hart CJR, McCoy D, Goldfarb RJ, Smith M, Roberts P, Hulstein R, Bakke AA, Bundtzen TK., 2002. Geology, exploration and discovery in the Tintina gold province, Alaska and Yukon. Econ Geol Spec Pub 9:241–274.

Hart, C. & Goldfarb, R., 2005. Distinguishing intrusion-related from orogenic gold systems. Proceedings of Scientific Conference on Minerals, New Zealand.

Hastie, E., Kontak, D., Lafrance, B., 2020. Gold Remobilization: Insights from Gold Deposits in the Archean Swayze Greenstone Belt, Abitibi Subprovince, Canada. Econ Geol. 115. 241-277.

Hutton, D., Ingram, G., 1992. The Great Tonalite Sill of southeastern Alaska and British Columbia: Emplacement into an active contractional high angle reverse shear zone (extended abstract). Earth and Environmental Science Transactions of the Royal Society of Edinburgh, 83(1-2), 383-386.

Jébrak, M., 1997. Hydrothermal breccias in vein-type ore deposits: a review of mechanisms, morphology and size distribution. Ore Geol Rev. 12, 111–134.

Jowitt, S. M., Cooper, K. M., Squire, R. J., Thebaud, N. J. M., Fisher, L. A., Cas, R. A. F., & Pegg, I., 2014. Geology, mineralogy, and geochemistry of magnetite-associated Au mineralization of the ultramafic-basalt greenstone hosted Crusader Complex, Agnew Gold Camp, Eastern Yilgarn Craton, Western Australia; a late Archean intrusion-related Au deposit? Ore Geol Rev. 56(SI), 53 - 72.

Keith, M., Haase, K.M., Klemd, R., 2018. Constraints on the source of Cu in a submarine magmatic-hydrothermal system, Brothers volcano, Kermadec island arc. Contrib Mineral Petrol 173, 40.

Kioe-A-Sen, N.M., van Bergen, M.J., Wong, T.E., Kroonenberg, S.B., 2016. Gold deposits of Suriname: Geological context, production, and economic significance. Neth. J. Geosci. 95, 429–445.

Kolb, J., Rogers, A., Meyer, F.M., 2005, Relative timing of deformation and two-stage gold mineralization at the Hutti mine, Dharwar craton, India. Miner. Depos. 40, 156–174.

Kroonenberg, S.B., de Roever, E.W.F., Fraga, L., Reis, N., Faraco, T., Lafon, J.-M., Cordani, U., Wong, T., 2016. Paleoproterozoic evolution of the Guiana Shield in Suriname: a revised model. Neth. J. Geosci. 95, 491–522.

Kuhns, R. J., 1992. Geologic and structural progress report on the gold mineralization at Yaou, French Guiana. Internal report BHP, unpublished.

Lacerda Filho J.V., Abreu Filho W., Valente C.R., Oliveira C.C, Albuquerque M.C. 2004. Geologia e Recursos Minerais do Estado de Mato Grosso. Escala 1:1.000.000. Goiânia. CPRM 235p.

Laflamme, Crystal & Jamieson, John & Fiorentini, Marco & Thébaud, Nicolas & Caruso, Stefano & Selvaraja, Vikraman., 2018. Investigating sulfur pathways through the lithosphere by tracing mass independent fractionation of sulfur to the Lady Bountiful orogenic gold deposit, Yilgarn Craton. Gondwana Res. 58.

Lang, J. R., Baker, T., Hart, C. J. R., and Mortensen, J. K., 2000. An exploration model for intrusion-related gold systems. Soc Econ Geol Newsletter, 40.

Lang, J.R., Baker, T., 2001, Intrusion-related gold systems: the present level of understanding. Min Dep 36, 477–489.

Large, R.R., Maslennikov, V., Robert, F., Danyushevsky, L.V., Chang, Z., 2007. Multistage sedimentary and metamorphic origin of pyrite and gold in the giant Sukhoi Log deposit, Lena gold province, Russia. Econ. Geol. 102, 1232-1267

Large, R.R., Danyushevsky, L.V., Hollit, C., Maslennikov, V., Meffre, S., Gilbert, S., Bull, S., Scotte, R., Emsbo, P., Thomas, H., Foster, J., 2009. Gold and trace element zonation in pyrite using a laser imaging technique: implications for the timing of gold in orogenic and Carlin-style sediment-hosted deposits. Econ. Geol. 104, 635–668.

Large, R.R., Bull, S.W., Maslennikov, V.V., 2011. A carbonaceous sedimentary source-rock model for Carlin-type and orogenic gold deposits. Econ. Geol. 106 (3), 331–358.

Large R. R., Maslennikov V. V., 2020. Invisible Gold Paragenesis and Geochemistry in Pyrite from Orogenic and Sediment-Hosted Gold Deposits. Minerals. 10, 339; doi:10.3390/min10040339

Lawley, C.J.M., Selby, D., and Imber, J. 2013, Re-Os molybdenite, pyrite and chalcopyrite geochronology, Lupa Goldfield, southwestern Tanzania: Tracing metallogenic time scales at midcrustal shear zones hosting orogenic Au deposits. Econ Geol. 108, 1591–1613.

Ledru P., Lasserre J.L., Manier E., Mercier D., 1991. Révision de la lithologie du Paléoprotérozoïque du craton guyanais. Tectonique transcurrente et dynamique des bassins sédimentaires. Bull. Soc. Geol. Fr., 162(4), 627-636

Le Mignot E, Reisberg L, Andre-Mayer AS, Bourassa Y, Fontaine A, Miller J.2017a, Re-Os geochronological evidence for multiple Paleoproterozoic gold events at the scale of theWest African craton. Econ Geol 112:145–168.

Le Mignot, E., Siebenaller, L., Béziat, D., André-Mayer, AS., Reisberg, L., Salvi, S., Velásquez, G., Zimmermann, C., Naré, A., Franceschi, G. 2017b. The Paleoproterozoic Copper-Gold Deposits of the Gaoua District, Burkina Faso : Superposition of Orogenic Gold on a Porphyry Copper Occurrence? Econ Geol. 112. 99-122. 10.2113/econgeo.112.1.99.

Marcoux E., Milesi J.P., 1993. Lead isotope signature of Early Proterozoic ore deposit in Western Africa: comparison with gold deposits in French Guiana. Econ Geol. 88, 1862-1879.

Masurel, Q., Thébaud, N., Allibone, A., André-Mayer, A.-S., Hein, K. A. A., Reisberg, L., Bruguier, O., Eglinger, A., Miller, J. 2019. Intrusion-related affinity and orogenic gold overprint at the Paleoproterozoic Bonikro Au–(Mo) deposit (Côte d'Ivoire, West African Craton). Miner. Depos. 10.1007/s00126-019-00888-2

Masurel Q., Eglinger A., Thébaud N., Allibone A., André-Mayer A.S., McFarlane H., Miller J., Jessell M., Aillères L., Vanderhaeghe O., Salvi S., Baratoux L., Perrouty S., Begg G., Fougerouse D., Hayman P., Ousmane W., Tshibubudze A., Parra-Avila L., Kouamelan A., Ofori P. (in review). Gold metallogeny of the Paleoproterozoic part of the southern West African Craton: capturing distinct pulses within a Paleoproterozoic orogenic cycle. Miner. Depos.

McFarlane, C.R.M., Mavrogenes, J., Lentz, D., King, K., Allibone, A., and Holcombe, R., 2011, Geology and intrusion-related affinity of the Morila gold mine, southeast Mali. Econ Geol. 106, 727–750.

Meffre S, Large RR, Steadman JA, Gregory DD, Stepanov AS, Kamenetsky VS, Ehrig K, Scott RJ., 2016. Multi-stage enrichment processes for large gold-bearing ore deposits. Ore Geol Rev. 76:268–279.

Milesi, J.-P., Egal, E., Ledru, P., Vernhet, Y., Thiéblemont, D., Cocherie, A., Tegyey, M., Martel-Jantin, B., Lagny, P., 1995. Les minéralisations du Nord de la Guyane française dans leur cadre géologique. Chronique de la recherche Miniere 518, 5–59.

Milesi, J., Lerouge C, Delór C, Ledru P, Billa M, Cocherie A, Egal E, Fouillac A, Lahondère D, Lasserre J, Marot A, Martel-Jantin B, Rossi P, Tegyey M, Théveniault H, Thiéblemont D, Vanderhaeghe, O., 2003. Gold deposits (gold-bearing tourmalinites, gold-bearing conglomerates, and mesothermal lodes), markers of the geological evolution of French Guiana: geology, metallogeny, and stable isotope constraints. Géol Fr, 2-3-4:257-290.

Mishra, B., Pruseth, K., Hazarika, P., Chinnasamy, S., 2017. Nature and source of the ore-forming fluids associated with orogenic gold deposits in the Dharwar Craton. Geosci. Front.. 9. 10.1016/j.gsf.2017.09.005.

Morey, A. A., Tomkins, A. G., Bierlein, F., Weinberg, R. F., Davidson, G. J., 2008. Bimodal distribution of gold in pyrite and arsenopyrite: Examples from the archean boorara and bardoc shear systems, Yilgarn Craton, Western Australia. Econ. Geol., 103(3), 599 - 614.

Morrison, G. W., Rose, W. J., Jarieth, S., 1991, Geological and geochemical controls on the silver content (fineness) of gold in gold-silver deposits. Ore Geol Rev Ore. 6, 333-364.

Mumin, A.H., Fleet, M.E., Chryssoulis, S.L., 1994. Gold mineralization in As-rich mesothermal gold ores of the Bogosu-Prestea mining district of the Ashanti gold belt, Ghana: Remobilization of "invisible" gold. Miner. Depos. 29, 445–460.

Oberthür, T., Weiser, T., Amanor, J.A., and Chryssoulis, S.L., 1997b. Mineralogical sitting and distribution of gold in quartz veins and sulfide ores of the Ashanti mine and other deposits in the Ashanti belt of Ghana: Genetic implications Miner. Depos. 32, 2–15.

Oberthür T, Vetter U, Davis DW, Amanor JA., 1998. Age constraints on gold mineralization and Paleoproterozoic crustal evolution in the Ashanti belt of southern Ghana. Precambr Res. 89:129–143.

Onstott, T. and Hargraves, R.B., 1981. Proterozoic transcurrent tectonics. Nature, 289:131-136.

Passchier, C.W., and Trouw, R.A., 2005, Microtectonics: Berlin, Springer, 382 p.

Pearce, N.J.G., Perkins, W.T., Westgate, J.A., Gorton, M.P., Jackson, S.E., Neal, C.R., Chenery, S.P., 1997, A compilation of new and published major and trace element data for NIST SRM 610 and NIST SMR 612 glass reference materials: Geostandards Newsletter, v. 21, p. 115–144.

Perret, J., Eglinger, A., André-Mayer, A.S., Aillères, L., Feneyrol, J., Hartshorne C., Abanyin, E., Bosc, R.., 2020. Subvertical, linear and progressive deformation related to gold mineralization at the Galat Sufar South deposit, Nubian Shield, NE Sudan. J. Struct. Geol. 135. 104032. 10.1016/j.jsg.2020.104032.

Phillips G. N., Groves D. I., 1983. The nature of Archaean gold-bearing fluids as deduced from gold deposits of Western Australia. Aust. J. Earth Sci. 30:1-2, 25-39, DOI: 10.1080/00167618308729234

Phillips, G.N., and Powell R., 2010, Formation of gold deposits: a metamorphic devolatization model. J Metamorph Geol. 28, 689–718.

Pitcairn, I., Teagle, D.A.H., Craw, D., Olivo, G.R., Kerrich, R. and Brewer, T.S., 2006. Sources of metals and fluids in orogenic gold deposits: insights from the Otago and Alpine schists, New Zealand. Econ Geol. 101 (8), 1525-1546.

Pulz, G.M., Jost, H., Michel, D., Giuliani, G., 1991a. The Archaean Maria Lizara gold deposit, Goias, Brazil: example of Au-Bi-Te-S metallogeny related to shear zones intruded by synkinematic granitoids. In: E.A. Ladeira (Editor), Brazil Gold'9 1. Balkema, Rotterdam, pp. 385-387.

Putnis, A., Mineral replacement reactions, 2009. Rev. Mineral. Geochem. 70, no. 1, 87–124.

Ramsay JG, Huber MI., 1983. The techniques of modern structural geology, 1: Strain analysis. Academic Press, London.

Reich, M., Kesler, S.E., Utsunomiya, S., Palenik, C.S., Chryssoulis, S.L., and Ewing, R.C., 2005. Solubility of gold in arsenian pyrite. Geochim. Cosmochim. Acta. 69, 2781–2796.

Ristorcelli, S., Spencer, R., Dyer, T., Goode, J., Evans, D., Josic, L., Sangam, H and Jackson, H., 2007, Technical report update on the Las Cristinas project, Bolivar State, Venezuela: Unpublished technical report prepared for Cystallex International Corporation by Mine Development Associates, November 7, 2007. p. 51-64.

Santos J.O.S., Hartmann L.A, Gaudette H.E., Groves D.I., McNaughton N.J., Fletcher I.R., 2000. A new understanding of the provinces of the Amazon Craton based on integration of field mapping and U-Pb and Sm-Nd geochronology. Gondwana Res., 3 (4), 453-488.

Sillitoe, R.H., McKee E.H. and Vila, T., 1991. Reconnaissance K-Ar geochronology of the Maricunga gold-silver belt, northern Chile. Econ. Geol. 86, 1261-1270.

Simard, M., Gaboury, D., Daigneault, R., Mercier-Langevin, P., 2013, Multistage gold mineralization at the Lapa mine, Abitibi Subprovince: Insights into auriferous hydrothermal and metasomatic processes in the Cadillac-Larder Lake Fault Zone. Miner. Depos. 48, 883–905.

Sung, Y.-H., Brugger, J., Ciobanu, C.L., Pring, A., Skinner, W., and Nugus, M., 2009, Invisible gold in arsenian pyrite and arsenopyrite from a multistage Archaean gold deposit: Sunrise Dam, Eastern Goldfields province, Western Australia. Miner. Depos. 44, 765–791.

Sylvester, P.J., Cabri, L.J., Tubrett, M.N., McMahon, G., Laflamme, J.H.G., and Peregoedova, A., 2005, Synthesis and evaluation of a fused pyrrhotite standard reference material for platinum group element and gold analysis by laser ablation-ICPMS, in Törmänen, T.O., and Alapieti, T.T., eds., 10th International Platinum Symposium: Oulu, Geological Survey of Finland, Extended Abstracts, p. 16–20.

Tedeschi, M., Hagemann, S.G., Davis, J., 2018. The Karouni Gold Deposit, Guyana, South America: part I. Stratigraphic Setting and Structural Controls on Mineralization. Econ Geol. 113, 1679–1704.

Tedeschi, M., Hagemann, S.G., Roberts, M.P. and Evans, N.J., 2018b. The Karouni Gold Deposit, Guyana, South America: Part II. Hydrothermal Alteration and Mineralization. Econ Geol. 113(8), 1705-1732.

Tedeschi, M. T., Hagemann, S. G., Kemp, A. I. S., Kirkland, C. L., Ireland, T. R., 2019. Geochronological constrains on the timing of magmatism, deformation and mineralization at the Karouni orogenic gold deposit: Guyana, South America. Precambr. Res. 105329.

Thébaud, N., Sugiono, D., LaFlamme, C., Miller, J., Fisher, L., Voute, F., Tessalina, S., Sonntag, I., Fiorentini, M., 2018. Protracted and polyphased gold mineralisation in the Agnew District (Yilgarn Craton, Western Australia). Precambrian Res 310:291–304.https:// doi.org/10.1016/j.precamres.2018.02.013

Thébaud N., Allibone A., Masurel Q., Eglinger A., Davis J., André- Mayer A.S., Miller J. et Jessell M., 2020. The Paleoproterozoic (Rhyacian) gold deposits of West Africa. Economic Geology, in press.

Tikoff, B., Blenkinsop, T., Kruckenberg, S.C., Morgan, S., Newman, J., Wojtal, S., 2013. A Perspective on the Emergence of Modern Structural Geology: Celebrating the Feedbacks between Historical-Based and Process-Based Approaches. The Web of Geological Sciences: Advances, Impacts, and Interactions. Geological Society of America, pp. 65–119. https://doi.org/10.1130/2013.2500(03.

Tomkins, A.G. & Mavrogenes, J., 2002. Mobilization of Gold as a Polymetallic Melt during Pelite Anatexis at the Challenger Deposit, South Australia: A Metamorphosed Archean Gold Deposit. Econ Geol. 97. 1249-1271. 10.2113/gsecongeo.97.6.1249.

Tomkins A.G., 2013. On the Source of Orogenic Gold. Geology, 41 (12), 1255–1256.

Traoré, D.Y., Siebenaller, L., Salvi, S., Béziat, D., Bouaré, M.L., 2016. Progressive gold mineralization along the Syama corridor, southern Mali (West Africa). Ore Geol. Rev. 78, 586–598.

Twiss, R.J., Moores, E.M., 2007. Structural Geology. WH Freeman and Company, New York, p. 532

Van Achterbergh, E., Ryan, C.G., Jackson, S.E. and Griffin, W.L., 2001. Data reduction software for LA-ICP-MS: appendix; In Sylvester, P.J. (ed.), Laser Ablation–ICP-Mass Spectrometry in the Earth Sciences: Principles and Applications, Mineralogical Association of Canada Short Course Series, Ottawa, Ontario, Canada, v. 29, pp. 239-243.

Vanderhaeghe, O., Ledru, P., Thiéblemont, D., Egal, E., Cocherie, A., Tegyey, M., Milesi, JP., 1998. Contrasting mechanism of crustal growth: Geodynamic evolution of the Paleoproterozoic granite–greenstone belts of French Guiana. Precambrian Res. 92:165–193.

Velásquez, G., Borisova, A.Y., Salvi, S., and Béziat, D., 2012, In situ determination of Au and Cu in natural pyrite by near-infrared femtosecond laser ablation-inductively coupled plasma-quadrupole mass spectrometry: No evidence for matrix effects. Geostand. Geoanalytical Res. 36, 315–324.

Velásquez, G., Béziat, D., Salvi, S., Siebenaller, L., Borisova, A.Y., Pokrovski, G.S., De Parseval, P., 2014, Formation and deformation of pyrite and implications for gold mineralization in the El Callao district, Venezuela. Econ Geol. 109, 457–486.

Velásquez, G.; Salvi, S.; Siebenaller, L.; Béziat, D.; Carrizo, D. 2018. Control of Shear-Zone-Induced Pressure Fluctuations on Gold Endowment: The Giant El Callao District, Guiana Shield, Venezuela. Minerals., 8, 430.

Voicu, G., 1999. The Geology, Geochemistry and Metallogeny of the Omai Gold Deposit, Guyana, South America. PhD Thesis. Université du Québec à Montréal, pp. 271.

Voicu, G., Bardoux, M., Stevenson, R., 2001. Lithostratigraphy, geochronology and gold metallogeny in the northern Guiana Shield, South America: a review. Ore Geol Re. 18, 211–236.

Wu, Y.-F., Fougerouse, D., Evans, K., Reddy, S.M., Saxey, D.W., Guagliardo, P., and Li, J.-W., 2019. Gold, arsenic, and copper zoning in pyrite: A record of fluid chemistry and growth kinetics. Geology. 47, 641–644.

Xue Y, Campbell IH, Ireland TR, Holden P, Armstrong R., 2013. No mass-independent sulfur isotope fractionation in auriferous fluids supports a magmatic origin for Archean gold deposits. Geology 41:791-794

Complementary discussion: Whole-rock gold grade distribution study

A Yaou, a study regarding the whole rock gold grade distribution has been carried out following the publication presented in chapter 2. It has not been submitted to any journal and can be considered as an unfinished work for publication. It was initially a section of an intended paper dealing with gold grade distribution and structural characterisation of associated gold-bearing veins based on the work of Turlin et al. (2019). However, this research was aborted as the drilling campaign providing a new dataset for this study was cancelled.

With the help of François Turlin (postdoc researcher at UQAM, Montréal, Canada), we follow the work of Taner & Trudel (1991) who used a statistical approach focusing on gold content in Au deposits in order to discuss the gold grade distribution. The main objective was to find out if different populations of gold grade are present and if the shear zone has an influence in the distribution. To do so, this study uses data from the Auplata Mining Group database of exploration drilling assays.

The methodology is as follow, 1409 analyses are considered, after a careful selection of drillholes, depending on their emplacement and distance from the shear zone. As an example, two representative drillcores are presented in Figure 17 with a drillhole cross-cutting the ore zone associated with D_{4YA} vein sets (Fig. 17A) and a drillhole cross-cutting the ore zone associated with D_{3YA} (i.e. the shear zone). The grade statistics are presented in the figure, the Au_{D4YA} mean grade is of 2.53 g/t while the one for the combination of $Au_{D0/3/4}$ within the shear zone is of 4.38 g/t.

Plots of cumulative frequency *vs* log of gold grades in ppm for all data are presented in Figure 18. The selected sections are considered in the figure : (A) 500 m away from the shear zone with the ore associated with D_{4YA} veins (514 analyses are considered); (B) 150 m away from the shear zone with the ore associated with D_{4YA} veins (460 analyses are considered); (C) Within the shear zone with $Py_{0/3}$ and Py_4 where D_{4YA} veins are cross-cutting the mylonite (185 analyses are considered); (D) Within the shear zone with the ore associated with D_{4YA} veins, with mylonitised intrusion and some metasediment (250 analyses are considered).

Plots indicate the presence of two or three statistical populations as explained by Taner & Trudel (1991) and references therein where “inflection point occurs in the cumulative curve at a percentage that coincides with the amounts of the two populations present”.

We observe for the analysed cores (1) two statistical populations of grade when 500 m away from the shear zone (Fig. 18A within the intrusion with two populations noted A and B), (2) two statistical populations of grade when 150 m away from the shear zone (Fig. 18B within the intrusion with two populations noted A and B), (3) three statistical populations of grade when inside the shear zone (Fig. 18C with three population noted A, B and C) and (4) two statistical populations of grade when inside the shear zone with an intrusion (Fig. 18D with two populations noted A and B). According to graphs interpretations of Taner & Trudel (1991), population are depleted, normal or enriched. Following this scheme, we would have for A, B and D, normal and enriched (from nuggets effect?) population while for the section C, within the shear zone with no intrusion, a depleted, a normal and an enriched population may be considered.

No clear interpretation can be made at this point but the presence of both Py_3 and Py_4 gives three populations instead of two when only Py_4 are present. It needs further work however it can be used as a tool to check where the analyses of gold grades come from and how many generations of pyrite are involved.

From the pattern presented in Figure 18, with two or three populations, we may discriminate drillhole within or away from the shear one.

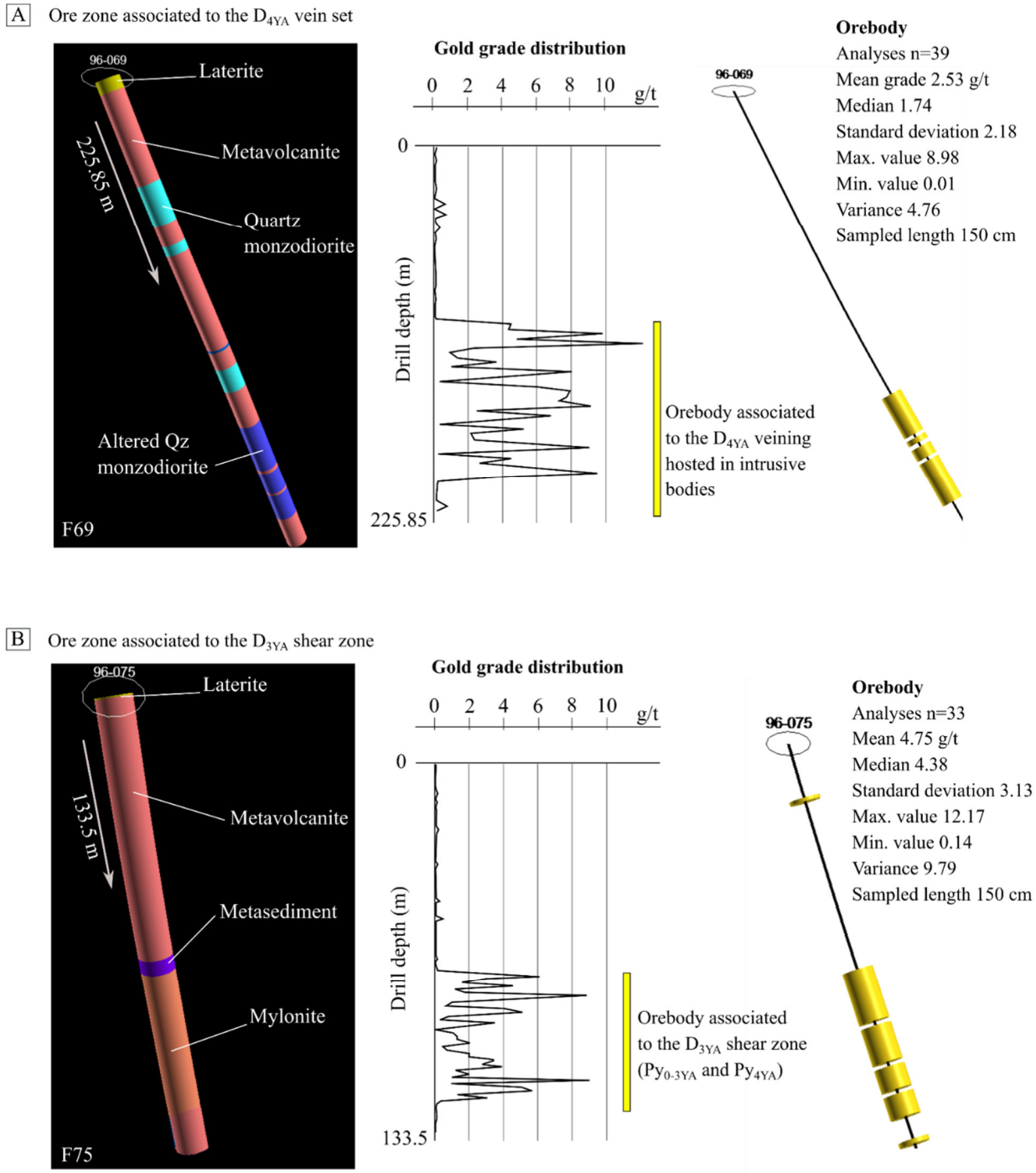

Figure 2-17 Selected drillhole with gold grade variations along the core and statistics regarding the ore intervals. A. Crosscutting the Au_{D4YA} orebody and B. Crosscutting the shear zone.

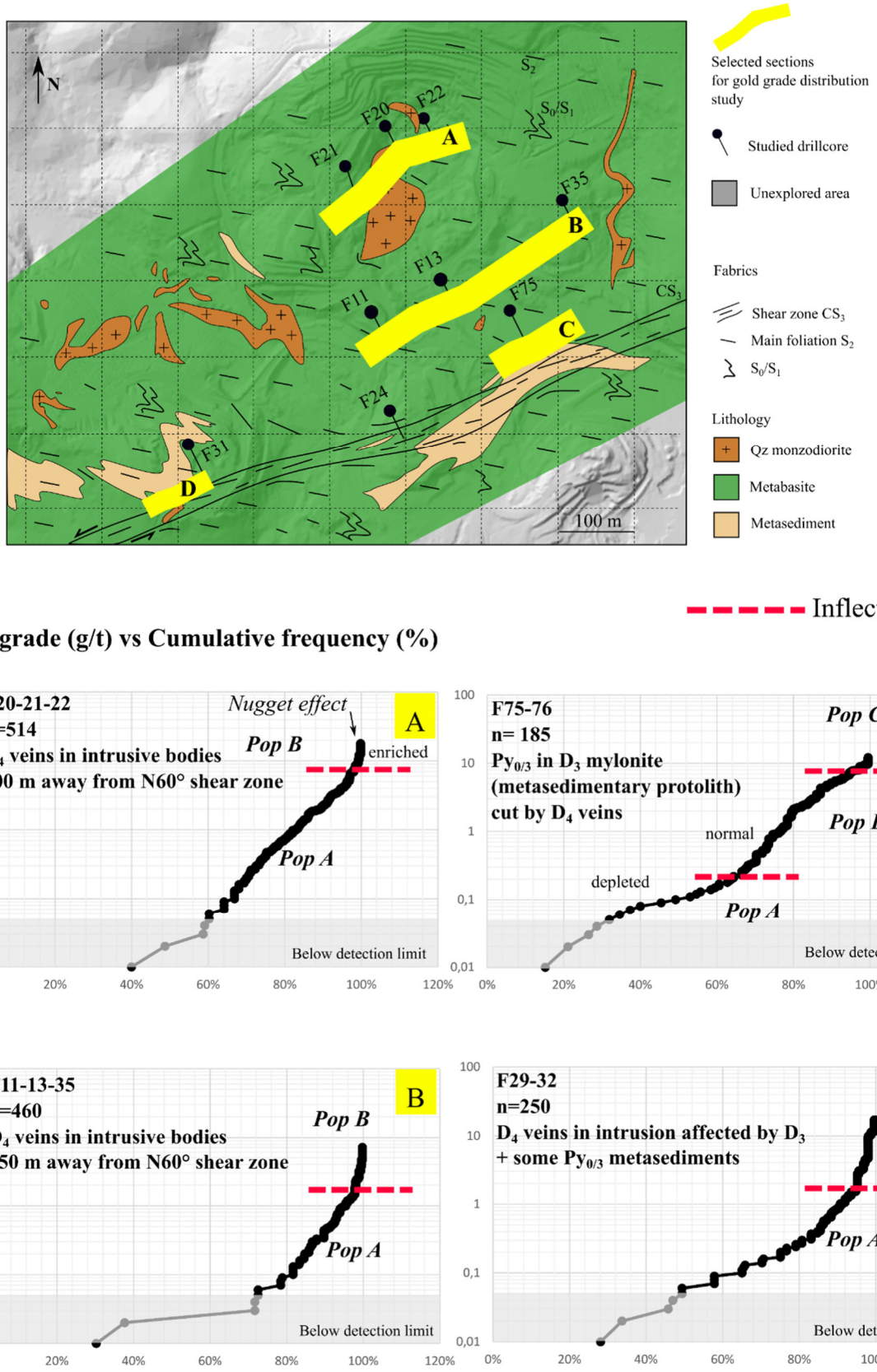

Figure 2-18 Plots cumulative frequency-probability vs log Au in ppm for 4 different sections of drillholes.

References

Taner, M. F., Trudel, P., 1991. Gold distribution in the Val-d'Or Formation and a model for the formation of the Lamaque-Sigma mines, Val-d'Or, Quebec. Can. J. Earth Sci. 28, 706-720.

Turlin, F., Jébrak, M., De Souza, S., Turcotte, J., 2019. Topological characterization of a polyphased gold-bearing vein network. J Struct Geol. 128, 103872

Chapitre 3

Etude géologique et géophysique, de l'échelle du gisement à l'échelle du district, des intrusions Rhyaciennes porteuse de la minéralisation aurifère de Yaou en Guyane.

Résumé en français

L'approche du système métallogénique avec des études couplées géologiques et géophysiques est très prometteuse pour localiser / prédire les structures et les lithologies éventuellement associées à la minéralisation aurifère à toutes les échelles (de l'échelle cratonique à l'échelle du gisement). Le gisement de Yaou, situé en Guyane française au sein des terrains Rhyaciens associés à l'orogenèse trans-amazonienne, est ici utilisé comme étude de cas. Il présente de nombreux corps intrusifs portant la majeure partie de la minéralisation aurifère polyphasée. Spatialement associé à la zone de cisaillement centrale de Yaou (CYSZ), l'événement intrusif est daté dans cette étude à 2130,6±5,8 Ma (U-Pb sur zircon) et montre un εHft supra-chondritique indiquant que la quartz monzodiorite provient du remaniement de la crustale trans-amazonienne juvénile vieille de 2,6-2,4 Ga. La phase aurifère principale à Yaou, portée par ces intrusions, est datée à 2105±25 Ma (Re-Os sur pyrite aurifère) ce qui représente la première datation d'un événement aurifère en Guyane. A partir d'une étude comparée de la géochimie de tous les types de roches magmatiques de Guyane avec celle de la quartz monzodiorite de Yaou, et ces nouvelles datations absolues, une intégration à l'échelle du craton est proposée où la mise en place des corps intrusifs se produit entre les phases régions D_1 et D_{2a}.

Dans un contexte de forêt amazonienne dense avec un profil latéritique bien développé et une quasi-absence d'afffleurement, une approche multi-échelles utilisant des données magnétiques et radiométrique permet de mieux définir la distribution spatiale des intrusions et des possibles zones de cisaillement associées. Les deux sont interprétés ici comme étant parallèles suivant la direction N60° et répliqués latéralement vers le NO. Une association temporelle est définie entre le cisaillement et l'événement magmatique, tous deux étant synchrones avec une possibilité d'intrusion pré-cisaillement et un événement intrusif prolongé lors du cisaillement. La minéralisation aurifère hébergée par des intrusions de type Yaou peut être ciblée le long de linéaments N60° dans le district de Yaou. Cette approche intégrée peut définir de nouvelles cibles jusque-là non reconnues dans la ceinture Sud du Paramaca.

Publication #2 *(In preparation)*

Integrated geological-geophysical investigation, from the deposit- to the district-scale, of gold-hosting Rhyacian intrusions, Yaou, French Guiana

Vincent Combes[1, 2, *], Aurélien Eglinger[1], Anne-Sylvie Andre-Mayer[1], Yoram Teitler[1], Mark Jessell[3], Armin Zeh[4], Laurie Reisberg[5,] Arnauld Heuret[6], Pierre Gibert[2]

[1]Université de Lorraine-CNRS, CREGU, laboratoire GeoRessources, 54500 Nancy, France

[2]AMG, Auplata Mining Group, ZI Dégrad des Cannes, 97354, Rémire Montjoly, France

[3]University of Western Australia, CET, 35 Stirling Highway, 6009 Crawley, Australia

[4]Karlsruher Institut für Technologie (KIT), 76131 Karlsruhe, Germany

[5]Centre de Recherches Pétrographiques et Géochimiques (CRPG), UMR 7358 CNRS-Université de Lorraine, BP 20, 54501 Vandoeuvre-lès-Nancy Cedex, France

[6]Université de Guyane / Géosciences Montpellier (UMR 5243), 97300 Cayenne, France

* corresponding author (vincent.combes@univ-lorraine.fr)

Abstract

The mineral system approach with coupled geological and geophysical studies is highly promising to localise/predict structures and lithologies possibly associated with gold mineralisation at all scales (i.e., upscaling from craton- to district- to camp- to deposit-scale). The Yaou deposit, located in French Guiana within Rhyacian terranes associated with the Trans-Amazonian orogeny, is used here as a case study. It displays numerous intrusive bodies hosting the bulk of the polyphase gold mineralisation. Spatially associated with the Central Yaou Shear Zone (CYSZ), the intrusive event is dated at 2130.6±5.8 Ma (U-Pb on zircon) and shows supra-chondritic εHft indicating that the quartz monzodiorite derives from the reworking of juvenile Trans-Amazonian crustal components as old as ca. 2.6-2.4 Ga. Using geochemical comparison (REE patterns) of all types of magmatic rocks from French Guiana, an integration of the deposit-scale framework is proposed where the intrusion is emplaced between the regional D_1 and D_{2a}. The main gold event hosted by this intrusion is dated at 2105±25 Ma (Re-Os on Au-bearing pyrite) which represents the first dating of a gold event in French Guiana. From airborne magnetic and radiometric data, the multi-scale approach helps to better understand the spatial distribution of the intrusions and associated shear zones, both related to gold mineralisation events. Both are interpreted as being parallel along a N60° trend and replicated laterally toward the NW. A temporal association is defined between the shearing

deformationand the magmatic event, both being synchronous with a possibility of pre-shearing intrusion and a protracted intrusive event while shearing. The Yaou-type intrusion hosted mineralisation can be targeted along the N60°-striking structures and where possible occurrences of intrusive bodies are defined. This integrated approach opens some targeting options, previously unrecognised within the southern Paramaca Greenstone Belt.

1. Introduction

Ore deposits are generated from a variety of natural processes, from lithospheric to nano- scale, that concentrate elements into a small volume that can be economically mined (Jenkin et al. 2015). Mineral deposits are by definition geographically small in extent compared to the surface and thickness of the crust, even if they result from geological and geodynamic processes that occur, and can be mapped at, a variety of larger scales (McCuaig et al., 2010; Hronsky et al., 2012). Ore mobilisation, transfer and deposition are linked to geological processes leading to the concept of mineral systems, which encompasses "*all geological factors that control the generation and preservation of mineral deposits*" (Wyborn et al., 1994; McCuaig and Hronsky, 2014 and references therein). Although there are a variety of interpretations of what a mineral system is (e.g., Wyborn et al. 1994; McCuaig et al., 2010; Huston et al. 2012), most include factors such as the geological setting, the timing and duration of deposition, the source(s) and nature of mineralising fluids (including magmas), the pathways used by the respective fluids and fluid flow drivers, the depositional site, mechanisms of metal transport and deposition, and post-depositional modifications. Unravelling the structural and lithological settings of a gold deposit at various scale, from deposit to lithosphere, is thus a key for understanding the mineral system and enhancing exploration targeting.

For regional exploration, an understanding of mineral systems is important when zooming in from (1) lithospheric-scale (connection between lithospheric processes and metal endowment when studying plumbing structures as discussed by Bierlein et al. (2006, 2009), Begg et al. (2010), Hronsky et al. (2012), or Motta et al. (2019); to (2) district-scale architecture of structural networks (Siddorn et al., 2020). This scalability in mineral exploration requires the integration of a large set of geophysical, geological and geochemical data (Niiranen et al., 2019; Nykänen et al., 2017). At the district-scale, aeromagnetic data are particularly useful. Indeed, the integrated interpretation of aeromagnetic data (Jessell et al 1993; Jessell and Valenta 1996) helps to localise/predict which structures and lithologies could be associated with gold. Working both on the structural and lithological framework combining geological (structural

geology, geochemistry, and geochronology) and geophysical (magnetometry, gamma-ray spectrometry, remote sensing, and gravimetry) techniques, in accordance with 3D models of Au deposits at the camp scale will deliver insights of the deposit to district scale of such mineral system.

Integration of regional geological and geophysical datasets is particularly useful in regions characterised by dense vegetation and/or thick lateritic profiles above primary orebodies such as the Guiana Shield in NE South America or the West African Craton. Such integration provides insights on both (1) the lithospheric architecture and (2) the evolution (e.g., deformation phases, gold events) of mineralised orogenic belts. This approach has been carried out recently in the West African craton, regarding the litho-structural patterns such as shear zone geometries and kinematics (Metelka et al., 2011; Jessell et al., 2016; Chardon et al., 2020) and their links with the gold deposit distribution (Perrouty et al., 2012; Baratoux et al., 2015). In the Amazonian craton, such integration of regional geological and geophysical datasets has been applied to highlight the control of the lithosphere geometry on the copper and gold mineral systems using satellite gravity, constrained by airborne potential field data (gravity and magnetics) with validation with information from passive seismic (wave speeds, crustal and lithospheric thickness) and geochronologic data (model, crystallisation ages, and Neodymium isotope ratio determinations, Motta et al., 2019).

This study will develop a similar approach in the Guiana Shield, focusing on the Yaou district located in French Guiana (Fig. 1). The Yaou deposit, which displays a polyphase gold mineralisation where the main orebodies are defined as intrusion-hosted along the Central Yaou Shear Zone (CYSZ), (Eglinger et al., 2020; Combes et al., 2021), is a typical undercover deposit with its dense Amazonian forest and thick lateritic profiles (Théveniaut & Freyssinet, 2002), representing a suitable ground for the application of such an integrated geological and geophysical approach. New geological data (geochemistry, Lu-Hf isotopy and zircon U-Pb) for the Yaou quartz monzodiorite hosting the main economic gold vein system (dated here using the Re-Os geochronometer on pyrite) will allow time correlation with the Trans-Amazonian orogenic evolution. New district-, camp- and deposit-scale structural and lithological maps based on airborne geophysical data including airborne magnetometry and radiometry (Th, U and K), will help to define the relation between shearing, magmatism, and gold mineralisation. All these collected geological and geophysical data are discussed and integrated in a 4D model aiming to target new intrusion-hosted gold deposits in a poorly exposed Paleoproterozoic

domain. The resultant interpretation can improve mineral exploration strategies in French Guiana and in the whole Guiana Shield.

2. Geological background

Regional geology

The Guiana Sheild, with at the South the Guapore Shield, and at the East its counterpart, the Man Leo Sheild in West Africa (Fig. 1), is spatially and temporally associated with the Trans-Amazonian orogeny (2600-1950 Ma), (Delor et al., 2003a; Enjolvy, 2008; Kroonenberg et al., 2016) which is characterised by a period of crustal growth followed by a crustal reworking phase (Vanderhaeghe et al., 1998).

Regarding main formations identified within the Guiana Shield, Archean terranes referred to as the Imataca Complex in Venezuela and the Amapá Block in Brazil (Gibbs and Barron, 1993) are present along with Rhyacian Volcano-sedimentary formations (greenstone belts), TTG complexes, late intrusions, and late Rhyacian High grade belt (see Fig. 1 and synthesis by Kroonenberg et al., 2016 and references therein).

While moving from an oceanic-arc environment to an intracratonic basin environment, the tectonic framework established by Ledru et al. (1991), Gibbs and Barron (1993) and updated by Vanderhaeghe et al. (1998), Delor et al. (2003a, b) and Kroonenberg et al. (2016) defines an early D_1 phase, associated with a compressional regime in a subduction context. This D_1 phase, dated at 2180-2130 Ma, produced TTG-type intrusions and volcanosedimentary formations within an oceanic volcanic arc or back-arc environment (Vanderhaeghe et al., 1998; Delor et al., 2003a). A North-South block convergence is proposed for this early phase. The following D_{2a} phase (2110-2080 Ma) in a collisionnal context and ending of subduction is marked by trans-tension and sinistral sliding together with folding of the volcano-sedimentary formation (Vanderhaeghe et al., 1998 ; Delor et al., 2003a, b). The North Guiana Trough (NGT) shear zone (Fig. 1 and 2) (Egal et al., 1991) is formed during this deformation phase (Ledru et al.,1991, Vanderhaeghe et al., 1998). The D_{2b} deformation phase dated at 2070- 2060 Ma (Delor et al., 2003a, b) is responsable for dextral strike slip shearing (Vanderhaeghe et al., 1998; Delor et al., 2003a) together with a crustal stretching. Regarding kinematic directions, a North East-South West convergence for D_{2a} is proposed by Delor et al. (2003a, b). Delor et al. (2003b) define a late D_{2c} phase associated with granulite facies metamorphism which is currently not defined in French Guiana and dated at 2110-1990 Ma (DeRoever et al., 2003 ; Klaver et al., 2015).

From the GIS-based lithological map of the BRGM, a simplified geological map of French Guiana is produced for this study (Fig. 2) where all dating information is from Delor et al. (2003a, b and references therein).

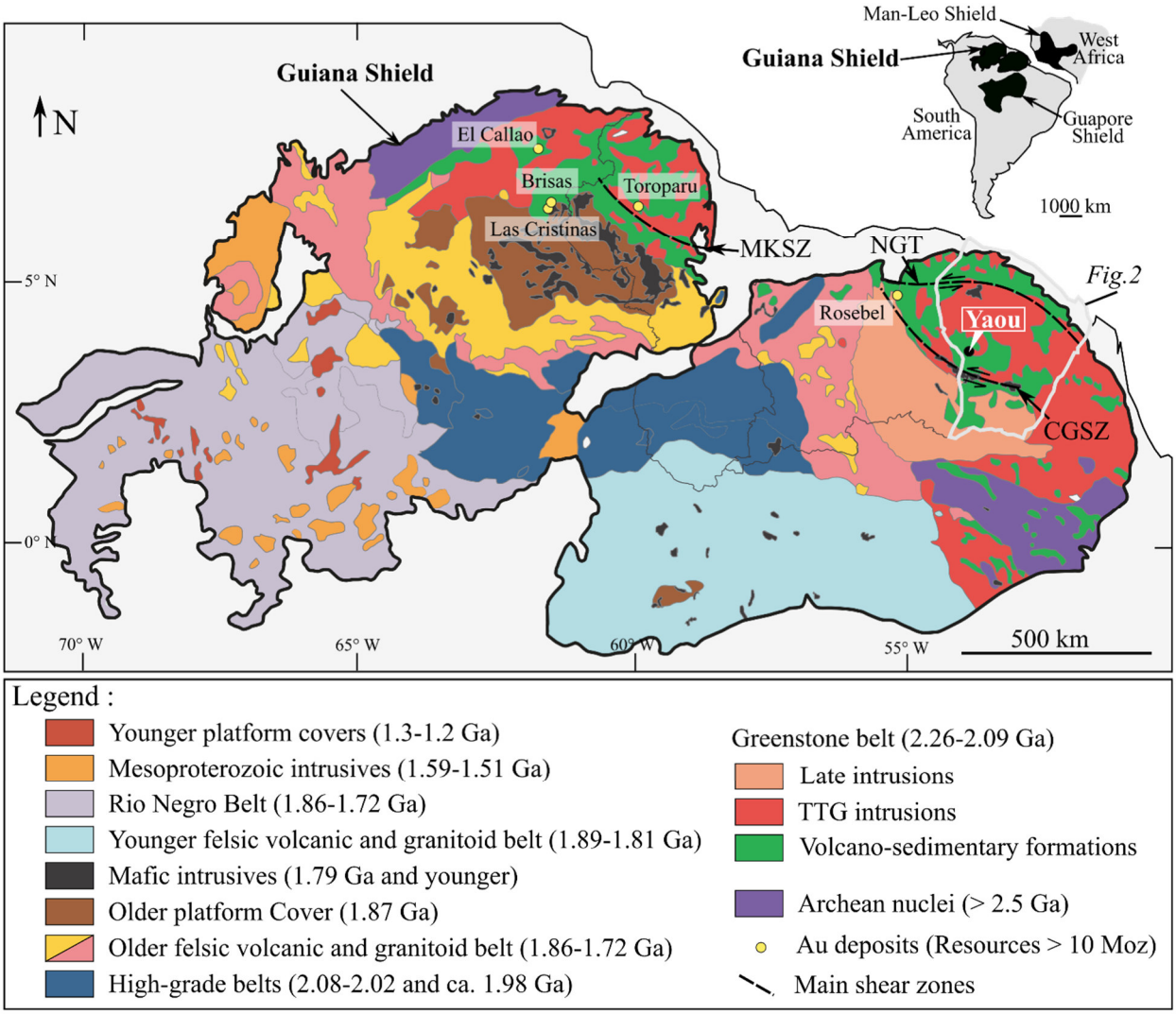

Figure 3-1 Geology of the Guiana Shield (modified from Kroonenberg et al., 2016). Gold deposits presented have total resources > 10 Moz. MKSZ: Makapa-Kuribrong Shear Zone, NGT: Northern Guiana Trough, CGSZ: Central Guiana Shear Zone. Geographic coordinates are reported as WGS 84.

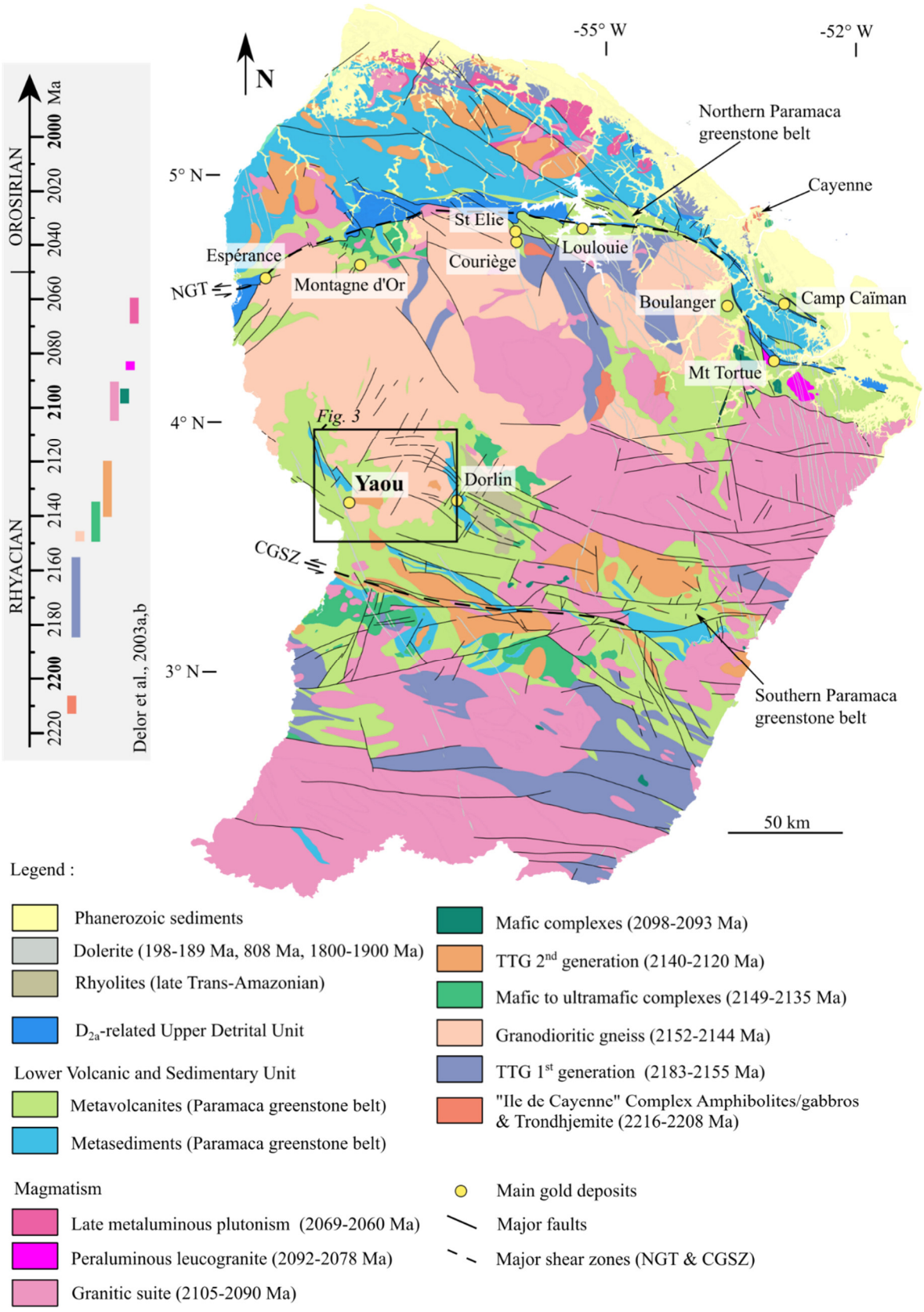

Figure 3-2 Geological map of French Guiana with location of the main Au deposits including the Yaou deposit. Modified from Delor et al. (2003b). All geochronology data are from Delor et al. (2003b) and references therein.

The oldest complex, the « Ile de Cayenne » has an age of 2216-2208 Ma based on dating of two suites, an amphibolite/gabbroic and a trondhjemitic. Later, a first generation of TTG (dated at 2183-2155 Ma) was emplaced both in the northern part of French Guiana and in the south (Fig. 2). The Central TTG complex, situated in the central part of French Guiana between the two E-W greenstone belts is composed of a granodioritic gneiss unit (dated at 2152-2144 Ma) and undifferentiated TTGs dated at 2140-2120 Ma which are also encountered in the northern part of French Guiana. Minor mafic to ultramafic complexes are identified and dated at 2149-2135 and 2090-2093 Ma. A granitic suite dated at 2105-2090 Ma is mostly displayed at the south and central east parts of the region (Fig. 2) followed by late Rhyacian units defined as peraluminous leucogranite (2092-2078 Ma) and late metaluminous plutonism (2069-2060 Ma). Apart from plutonism, the main units include the Lower volcanic and sedimentary unit (Paramaca greenstone belt) with its two East-West belts (Fig. 2) where all gold occurences are currently known (Milesi et al., 2003) and the D_{2a}-related Upper Detrital Unit associated with pull-apart basins composed of pelites, sandstones and conglomerats. Post-Trans-Amazonian units includes mafic dykes (dolerites dated at 1900-1800 Ma, ca. 808 Ma and 198-189 Ma) and phanerozoic sediments, mostly mapped in the northern part of French Guiana, along the Atlantic coast (Fig. 2).

Geological features at the district-scale

In the Yaou district, many gold occurrences are known within 50-60 km around the Yaou camp (Fig. 3), such as Dorlin, Bois Blanc, Chaina, and Tomantoni (among others). Each Au occurrence is located within either the metasediments or the metavolcanites of the southern Paramaca Greenstone Belt (PGB). The historical BRGM surveys and the updated geological map from Delor et al. (2003), mainly based on airborne geophysical interpretations, define a lithologic distribution map (Fig. 3) with a dominant metavolcanite unit (PGB), some metasediments (PGB) in the north west part of the Yaou district, two plutonic complexes in the east and north east, (TTG 2nd generation dated at 2140-2120 and older granodioritic gneiss dated at 2152-2144 Ma ; Delor et al., 2003b) and a Neoproterozoic dolerite (Delor et al., 2003b) striking N165°E, crosscutting the western part of the Yaou deposit. The Central Yaou Shear Zone (CYSZ) is located within the PGB, at the border with the eastern TTG complex. Regional structures, drawn mostly from aeromagnetic interpretations, strike NW-SE and NNE-SSW (Fig. 3).

Intrusion and deformation features at the camp- and deposit-scale

At the deposit- to the camp-scale a five-phase deformation model is established (Combes et al., 2021). Considering all mineralised bodies within the central part of the Yaou deposit, a model is presented in Figure 4 where quartz monzodiorite bodies are aligned along the sinistral CYSZ. The ductile $D_{1/2YA}$ phase is responsible for the main penetrative foliation (S_2 striking N90°-N120° with a subvertical dip) while the D_{3YA} phase is related to shearing (sinistral CYSZ; N60°E, 70°NW; Fig. 4). An intrusive quartz monzodiorite event is identified as being pre- to syn-D_{3YA}. The following phase D_{4YA} represents a brittle quartz-carbonate veining set hosted preferentially within intrusive bodies and along the shear zone. A strong rheological control is interpreted for this main auriferous event (see Combes et al., 2021). The D_{5YA} brecciation event locally affect the D_{4YA} veins.

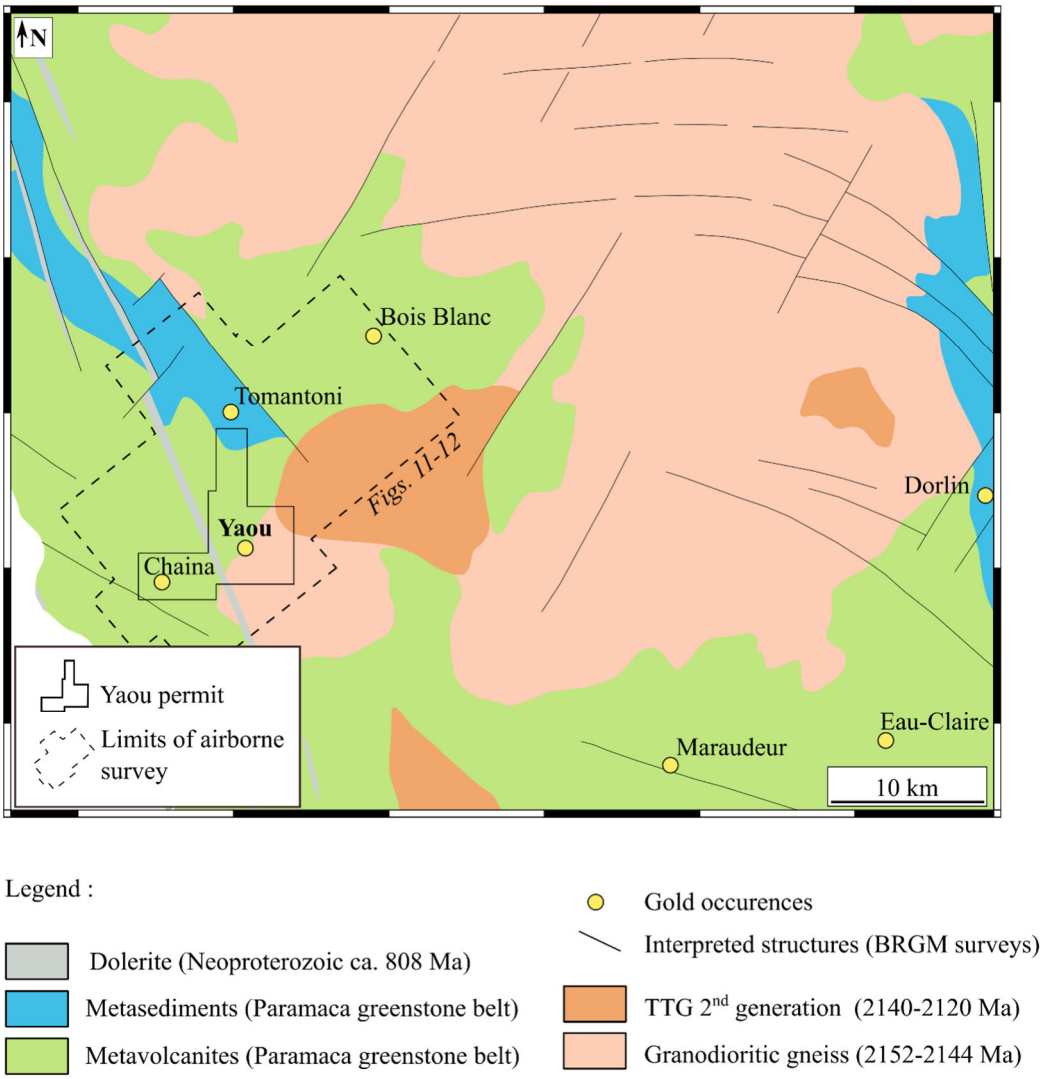

Figure 3-3 Regional geological map with location of the main Au occurences. Modified from Delor et al. (2003b). See Fig. 2 for location.

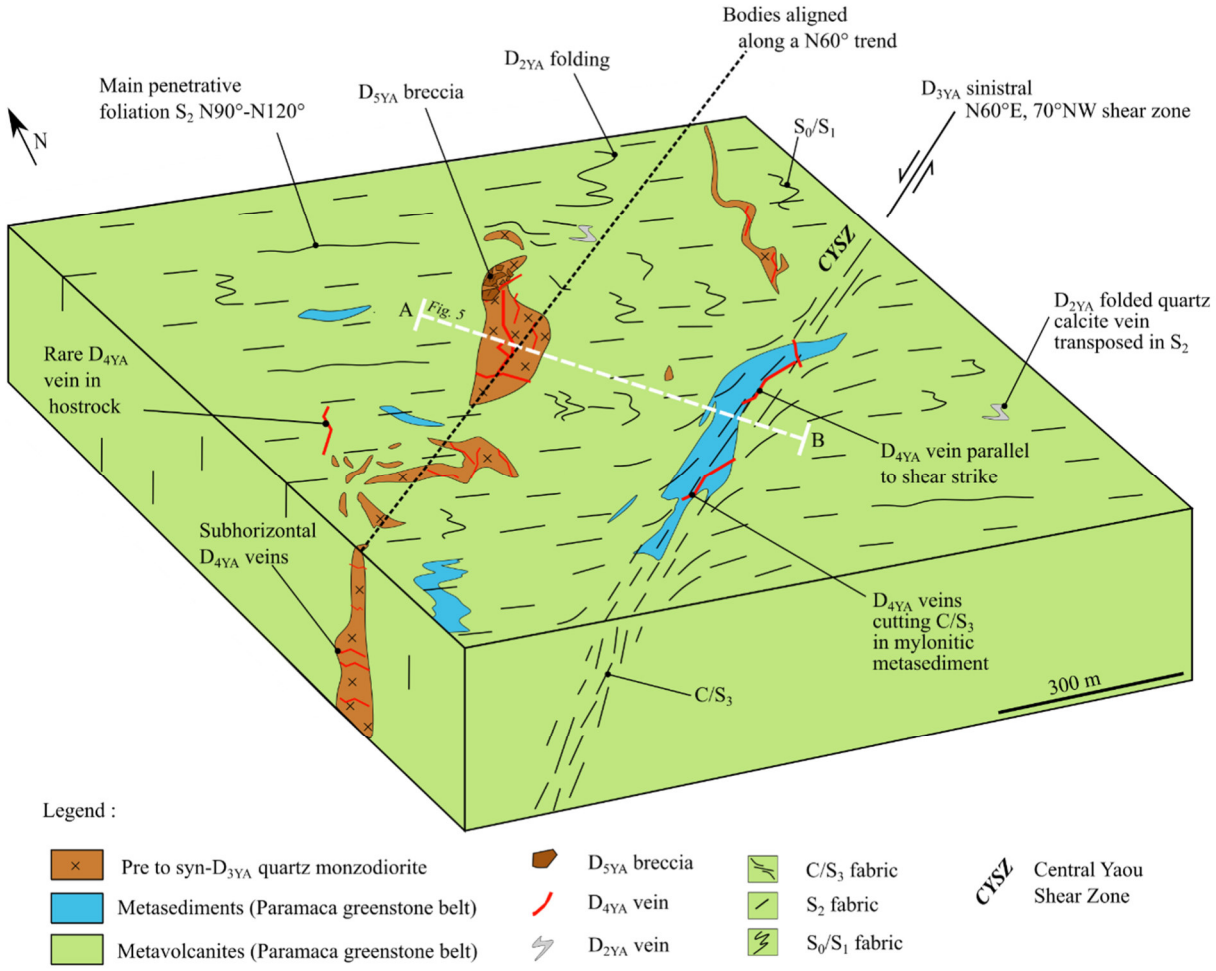

Figure 3-4 Schematic 3D block diagram of the deposit at the camp scale after all deformation/ intrusion events occured, highlighting the geometry of the CYSZ associated with the D_{3YA} deformation phase and the pre to syn- D_{3YA} intrusive bodies

With over 36 000 m drilled at Yaou (auger, RC and diamond drilling), (AMG exploration database) a precise modeling of the central part of the deposit has been drawn at the camp scale. A Leapfrog Geo view (NNW-SSE) of the model is presented on Figure 5 using assay data, where the D_{3YA} sinistral shear zone correlates with the N60°E striking $Au_{D0/D3/D4YA}$ orebodies whereas the bulk of the Au_{D4YA} orebodies are located within the quartz monzodiorite bodies giving two subparallel ore trends striking N60°E.

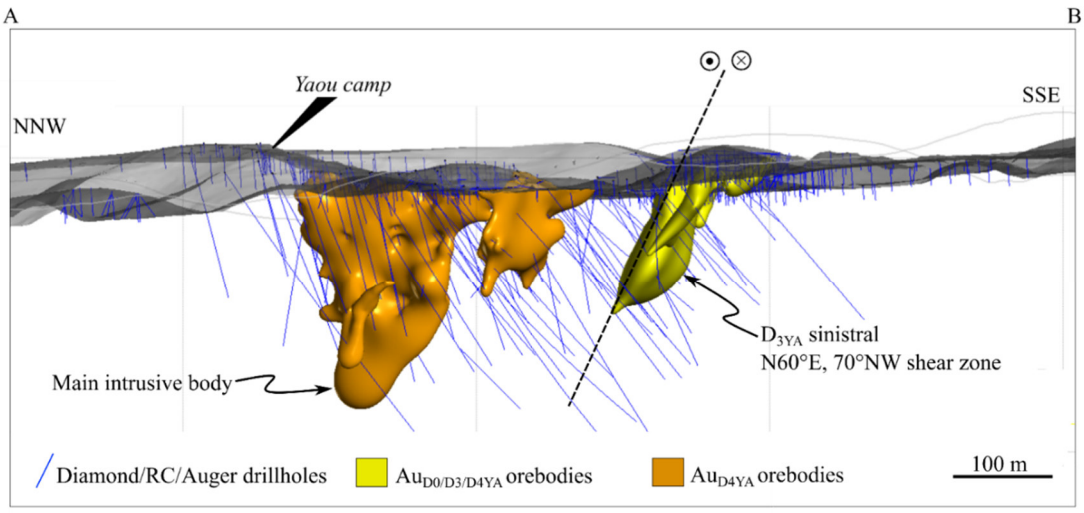

Figure 3-5 Leapfrog scene of the model with orebodies geometry at the camp scale (central part of the deposit). Orebodies associated with D_{4YA} correspond to intrusive bodies enveloppes. See Fig. 4 for location.

3. Methodology and data use

Whole-rock analyses of trace and major elements

Whole-rock analyses of trace and major elements (Table 1) were conducted on 20 cm-long half-drillcore samples at the SARM laboratory (CRPG) in Nancy, France. Veins and unfresh pieces were removed prior to crushing and pulverisation at the GeoRessources laboratory (Nancy, France). Trace elements were analysed by inductively coupled plasma mass spectrometry (ICP-MS) and oxides were analysed by inductively coupled plasma optical emission spectrometry (ICP-OES). Results are presented here for the five least altered samples out of twelve sampled cores after carefull petrographic studies of hydrothermal alteration mineralogy.

U-Pb dating and Lu-Hf isotope analyses of zircon

Zircon grains were separated from 28 kg of quartz monzodiorite saprock powdered with a jaw crusher and a roller mill at the CRPG in Nancy (France) and concentrated using first a Gemini shacker table, then by heavy liquids (diiodomethane: density = 3.31 g/cm^3) and a Frantz isodynamic magnetic separator. Individual grains were then handpicked, mounted in epoxy blocks, and polished to expose their cores. Prior to *in situ* isotope analyses the internal texture of each grain was characterised by means of cathodoluminescence (CL) and back scattered electron (BSE) imaging performed with a TESCAN VEGA 3 LM, with Gatan ChromaCL2UV at the SCMEM (GeoRessources, Nancy, France). *In situ* U-Pb and Lu-Hf isotope analyses of

zircon grains/domains were carried out by Laser Ablation Inductively Coupled Plasma Mass Spectrometry (LA–ICPMS), at the Karlsruher Institut für Technologie (Karlsruhe, Germany). Laser spots for Lu–Hf (50 µm in diameter) were placed directly on the U–Pb laser spots (33 µm in diameter). The results of U-Pb dating and Lu-Hf isotope analyses are shown in Tables 2 and 3 respectively (*supplementary material*).

Re-Os dating of pyrite

From selected drillcore intervals, centimetre-large pyrite grains (Py_4 proximal to auriferous D_{4YA} veins) were separated using a saw and then crushed (GeoRessources, Nancy, France). Re-Os analyses were performed on two aliquots of the crushed pyrite powder at the Centre de Recherches Pétrographiques et Géologiques (CRPG) in Nancy, France. Chemical separation techniques applied in this study are based on those described by Shirey and Walker (1995) for sample digestion, using an Anton Paar HPA-S high pressure asher instead of Carius tubes, and Birck et al. (1997) for osmium extraction. For each sample, ~ 200 mg of pyrite powder were spiked with precisely weighed quantities of a mixed ^{185}Re-^{190}Os tracer solution and digested in a mixture of hydrochloric acid (2 mL), nitric acid (5 mL) and hydrogen peroxide (0.1 mL) at 260 °C for 16 h, under a pressure of 100 bars. After sample digestion, Os was separated by liquid–liquid extraction into liquid bromine. The Br_2 was then evaporated and the osmium fraction was purified by microdistillation (Birck et al. 1997). The Re was extracted from the residual acidic solution by anion exchange using chromatographic columns (AG1 X8 resin). Re isotopic compositions for isotope dilution calculations were measured using a Thermo Neptune MC-ICPMS. Instrumental mass fractionation during measurements was regularly monitored and corrected for using an 0.5 ppb Re standard with an assumed $^{187}Re/^{185}Re$ ratio of 1.6738. The Os samples were loaded on platinum filaments for analysis by negative thermal ionisation mass spectrometry (N-TIMS; Creaser et al. 1991; Völkening et al. 1991), using a Finnigan MAT 262 instrument. About 0.2 µL of a saturated solution of $Ba(OH)_2$ in 0.1 N NaOH (Birck et al. 1997) was added to the samples to maximise OsO_3^- emission in the instrument. Analyses were made by peak jumping and ion counting using an ETP electron multiplier. Instrumental mass fractionation was corrected iteratively off-line by assuming that the true $^{192}Os/^{188}Os$ ratio of the sample loaded on the filament lay on a mixing line between the spike (5.00736) and natural (3.08271) values. The oxygen isotope composition determined by Nier ($^{17}O/^{16}O$ = 0.0003708 and $^{18}O/^{16}O$ = 0.002045) was used to correct for isobaric interferences from heavy oxides. Common Os, including both the natural component and any contribution from the analytical blank, was monitored using mass ^{188}Os, and a correction to ^{187}Os was applied

assuming a common $^{187}Os/^{188}Os$ value of 0.6 ± 0.5 The magnitude of this correction was about 0.02% for both aliquots. The Re blank associated with these samples was 24 ±7 pg while the total Os blank was 0.75 pg with a $^{187}Os/^{188}Os$ ratio of 6.1. The results of the Re-Os dating are shown in Table 4. All uncertainties are 2σ, and include all identified sources of uncertainty, including measurement uncertainties, blank variability, and the variation in the assumed initial $^{187}Os/^{188}Os$ ratio of the pyrite.

Airborne geophysical data processing and interpretation

Airborne geophysical data from a magnetic and radiometric survey of Auplata Mining Group are used for this study. The covered area, of 360 km^2 represents 2201 km of NW-SE striking lines, using a line spacing of 200 m with perpendicular tie lines flown every 1000 m. Data include (1) airborne radiometric data (K, Th, U) and (2) airborne magnetic data.

Airborne magnetic surveys help constraining structures and lithologies and are therefore excellent tools for constructing lithostructural maps (Aitken & Betts, 2009a, b; Baratoux et al., 2015) especially in undercover domains (Metelka et al., 2011). Raw data have been processed in order to obtain various filters. The total magnetic field data were reduced to the pole prior to further processing. Filters used include (a) the First Vertical Derivative, (b) the Tilt Derivative (TD) and (c) the Horizontal Derivative (Blakely & Simpson, 1986; Miller & Singh, 1994; Milligan & Gunn, 1997; Pilkington & Keating, 2009; Verduzco et al., 2004). Regarding the radiometric data, the original bands K, eTh, and eU and the ternary RGB (Red, Green, Blue) color composite are used. The gamma-ray signal gives information regarding the content and distribution of the radioactive elements in rocks. It can highlight anomalies due to geochemical alterations such as mineralisation, hydrothermal alterations, and weathering (Metelka et al., 2011). Finally, a SRTM digital elevation model shaded from NW is utilised as a background image.

4. Geological results

Petrography of the quartz monzodiorite

All intrusive bodies observed in drillcores are hydrothermally altered due to the high frequency of auriferous D_{4YA} veins (Combes et al., 2021). When selected away from the ore zone, the least altered quartz monzodiorite samples remain albitised (Fig. 6A). This rock is phaneritic, fine to medium grained with no internal fabric observed. The defined mineralogical assemblage is of albite, quartz, sericite and chlorite, with minor amount of ankerite, magnetite, calcite and apatite. We observe some variation within the least altered quartz monzodiorite rock with some samples showing higher amounts of chlorite and ankerite (Fig. 6B) and/or hematite (Fig. 6C). At the microscopic scale, the typical assemblage (Fig. 7A and D) is of albite, quartz and sericite with polysynthetic twinning of albite, and late sericitisation overprinting albite. Moderate to strong chloritisation is also observed (Fig. 7B). Hydrothermal interstitial ankerite (Fig. 7C and E) and hematisation in-between albite grains (Fig. 7F) are common, the latter being responsible for the typical reddish color of the rock. It is worth noticing that few occurences of K-feldspar have be observed (Fig. 7C).

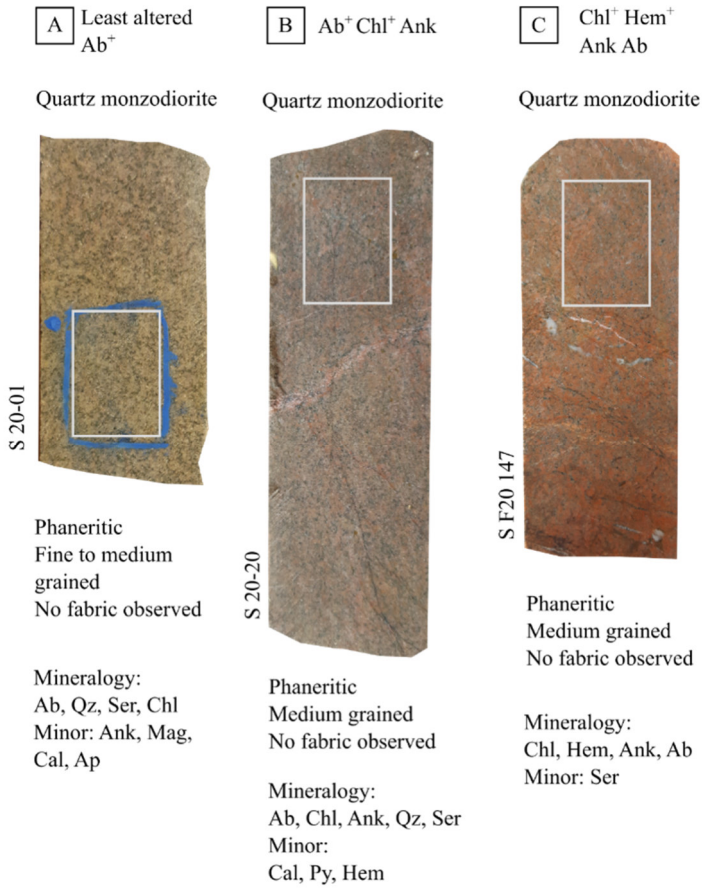

Figure 3-6 Photographs of half-drillcore intervals presenting the least altered samples of the quartz monzodiorite intrusive bodies.

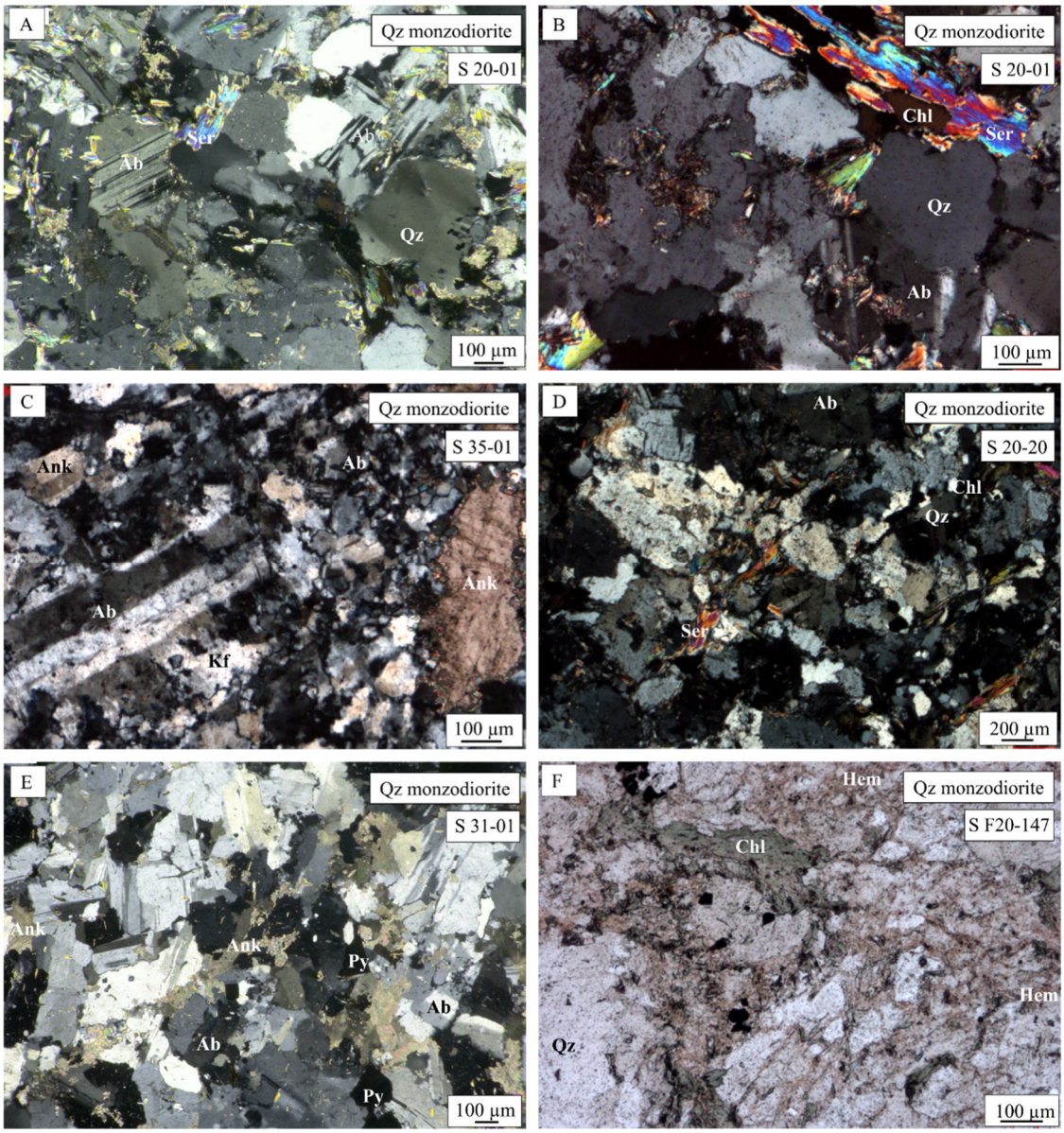

Figure 3-7 Representative micrographs of the least altered quartz monzodiorite (XPL except F. in PPL) A. B. D Typical albitisation and seritisation, C. E. Strong ankeritisation. F. Hematisation along albite grains. Abbreviations: Albite (Ab), Quartz (Qz), Ankerite (Ank), Sericite (Ser), Chlorite (Chl), Pyrite (Py), Hematite (Hem), K-feldspar (Kf).

Geochemistry of the quartz monzodiorite

Whole-rock geochemical data for the five least altered samples are provided in Table 1. SiO_2 contents range from 61.76 to 68.48 wt % while Na_2O concentrations vary from 5.61 to 7.42 wt %, and Fe_2O_3 contents range from 2.35 to 4.66 wt %. As previously mentioned in Combes et al. (2021), these samples plot in the quartz monzodiorite field in the Q-A-P normative classification diagram (Fig. 8A) and in the trondhjemite field (Fig. 8C), though this designation must be taken with caution due to the great amount of hydrothermal albite and sericite. All five representative samples plot in the same field in the relatively immobile elements Th *vs* Co diagram (Fig. 8B), arguing for a single protolith for all the least altered samples. This rock belongs to the calc-alkaline series based on the AFM diagram of Irvine and Baragar (1971).

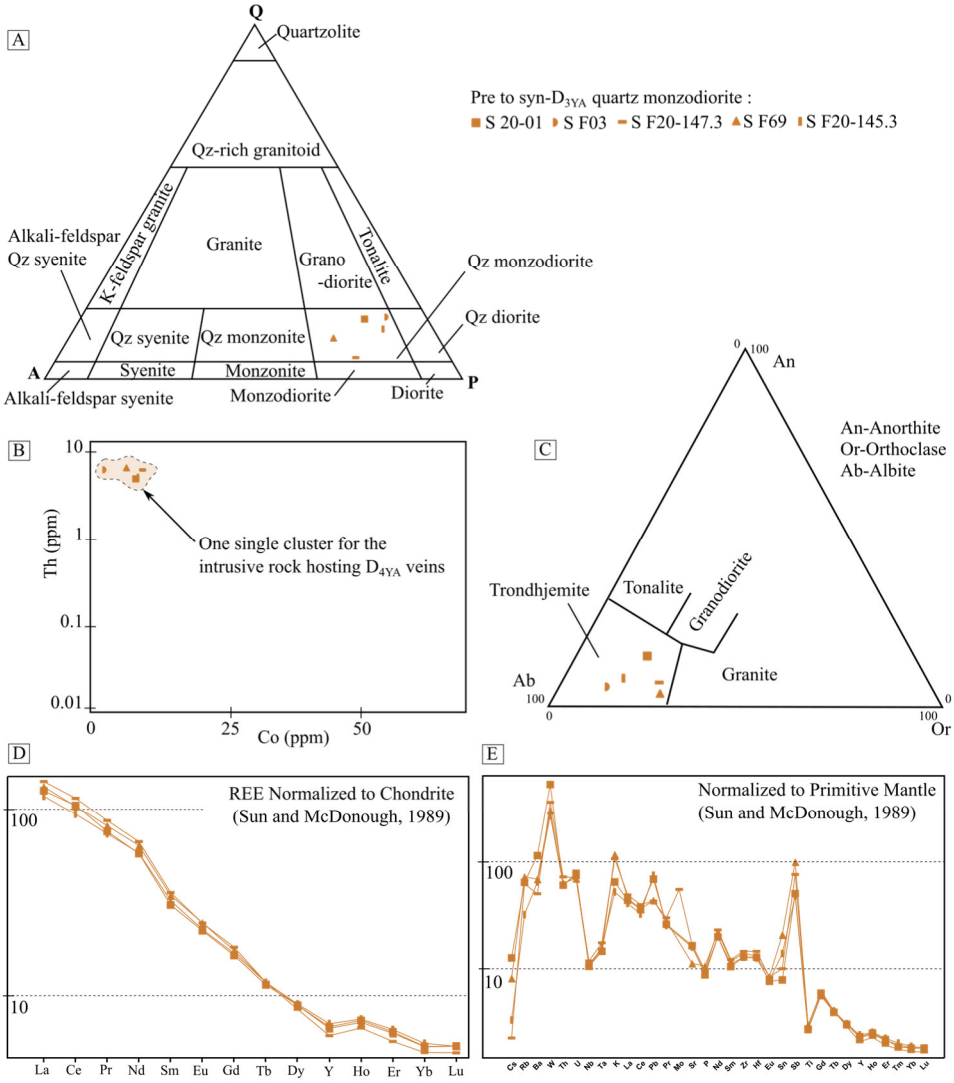

Figure 3-8 A. QAP Streckeisen ternary diagram where all samples plot in the Qz monzodiorite field. B. Least altered samples plotted in a Th vs Co diagram. C. Ternary An-Ab-Or diagram (Barker, 1979). D. REE abundances normalised to chondritic values from Sun and McDonough (1989). E. Spider plot normalised to primitive mantle values from Sun and McDonough (1989).

Regarding trace elements, the Y content is below 11 ppm for all samples. Chondrite-normalised REE patterns (Sun and McDonough, 1989; Fig. 8D) are highly reproducible and dip relatively steeply toward the HREE. We observe (1) a LREE (La, Ce, Pr, Nd) enrichment with the La_N content ranging from 90.81 to 109.23; (2) no marked Eu anomalies and (3) $[La/Yb]_N$ ratios ranging from 20.65 to 38.58. The HREE patterns are shallowly dipping toward the right with low contents of HREE (Er, Yb, Lu); the Yb_N contents range from 2.46 to 4.39.

Plots of trace elements normalised to primitive mantle abundances (Sun and McDonough, 1989, Fig. 8E), show patterns enriched in highly incompatible trace elements (LREE), depleted in HREE and enriched in large-ion lithophile elements (LILE) such as Rb, Ba, U and Pb. We observe a depletion in Cs, an enrichment in Sb and negative anomalies in Nb-Ta-Ti (Fig. 8E). The Nb/Ta ratios are subchondritic (Nb/Ta ≤ 12.57 ppm).

Table 3-1. Whole rock major (wt%) and trace element (ppm) composition of sampled intrusive rocks (dl, detection limit)

ID	SiO_2	Al_2O_3	Fe_2O_3	MnO	MgO	CaO	Na_2O	K_2O	TiO_2	P_2O_5	LOI
F69	64.07	16.09	4.66	0.02	1.63	1.21	5.91	3.55	0.64	0.23	1.79
F03	68.48	15.56	2.35	0.03	0.64	1.30	7.42	1.55	0.28	0.14	2.40
F20-147.3	61.76	16.30	4.55	0.02	1.99	1.80	6.52	3.24	0.62	0.21	2.93
F20-145.3	64.71	15.22	4.36	0.04	1.78	2.23	6.67	1.58	0.58	0.2	2.77
F20-01	64.27	15.15	4.15	0.05	1.5	3.18	5.61	1.96	0.58	0.19	3.98
dl	0.05	0.04	0.02	0.02	0.03	0.03	0.02	0.03	0.02	0.10	

ID	As	Ba	Be	Bi	Cd	Co	Cr	Cs	Cu	Ga	Ge
F69	1.93	483	1.62	0.33	0.06	9.06	17.30	0.26	43.30	21.80	1.11
F03	1.66	682	1.39	0.50	0.21	2.64	2.30	0.17	19.40	20.30	1.10
F20-147.3	1.38	353	1.36	0.58	0.04	9.70	20.30	0.07	43.90	20.90	1.10
F20-145.3	0.74	455	1.30	0.13	0.06	8.84	18.90	0.11	38.40	21.40	1.13
F20-01	0.57	807	1.10	0.17	0.05	8.83	14.30	0.40	6.19	22.29	1.21
dl	0.50	5.50	0.05	0.05	0.02	0.08	0.50	0.02	2.00	0.02	0.04

ID	Hf	In	Mo	Nb	Ni	Pb	Rb	Sb	Sc	Sn	Sr
F69	4.05	0.03	<dl	7.63	12.00	8.10	46.20	0.50	7.84	3.53	236.00
F03	3.77	<dl	3.76	5.55	<dl	8.76	22.10	1.22	2.89	159	350.00
F20-147.3	4.48	<dl	3.49	8.41	13.20	7.97	39.60	0.38	6.11	1.70	356.00
F20-145.3	3.88	0.03	<dl	7.77	12.20	13.90	20.40	0.24	7.48	2.36	336.00
F20-01	3.95	0.03	<dl	7.49	10.63	12.82	41.01	0.25	7.15	1.33	346.50
dl	0.03	0.03	0.50	0.02	2.00	0.45	0.15	0.06	0.60	0.30	0.70

ID	Ta	Th	U	V	W	Y	Zn	Zr	La	Ce	Pr
F69	0.61	5.42	1.47	91.50	6.17	10.2	64.70	156.00	31.70	64.10	7.75
F03	0.51	6.23	1.86	38.90	6.85	5.78	38.40	151.00	29.50	55.10	6.18
F20-147.3	0.72	6.18	1.50	99.00	7.42	9.35	59.40	162.00	33.90	70.80	8.27

F20-145.3	0.65	5.23	1.58	89.90	5.50	10.80	61.50	143.00	28.20	57.80	7.02	
F20-01	0.60	5.16	1.65	69.27	10.94	10.44	70.96	144.10	30.14	64.59	7.22	
dl	0.01	0.02	0.01	0.85	0.80	0.02	7.00	1.50	0.02	0.03	0.01	

ID	**Nd**	**Sm**	**Eu**	**Gd**	**Tb**	**Dy**	**Ho**	**Er**	**Tm**	**Yb**	**Lu**	**Total**
F69	29.70	5.23	1.41	3.53	0.43	2.20	0.40	1.02	0.14	0.88	0.13	99.81
F03	22.10	3.37	0.95	2.12	0.24	1.19	0.21	0.55	0.08	0.52	0.07	100.15
F20-147.3	31.20	5.41	1.40	3.68	0.43	2.10	0.37	0.92	0.13	0.82	0.12	99.93
F20-145.3	27.10	4.89	1.30	3.41	0.43	2.24	0.41	1.06	0.15	0.92	0.13	100.11
F20-01	26.89	4.64	1.28	3.32	0.42	2.21	0.41	1.03	0.14	0.88	0.13	100.62
dl	0.02	0.01	0.01	0.01	0.01	0.01	0.01	0.01	0.01	0.01	0.01	

A geochemical database of plutonic rocks sampled within French Guiana has been built for this study. To constrain the geodynamical significance of the quartz monzodiorite observed at Yaou and to integrate it into the context of known regional plutonic events, the chondrite normalised REE (Sun and McDonough, 1989) pattern of this rock is compared with patterns of the most representative samples of each main plutonic complex in the region as illustrated in figure 9. Representative samples are from the "Ile de Cayenne" Complex (Fig. 9A), the 1st generation of TTG patterns (Fig. 9B), the 2nd generation of TTG (Fig. 9C), the late 2nd generation of TTG (Fig. 9D), the Granitic suite (Fig. 9E) and the peraluminous leucogranite unit (Fig. 9F). Comparisons will be discussed in the *Discussion* section.

U-Pb geochronology and Hf isotopes

Zircon grains from the quartz monzodiorite were dated *in situ* (Table 2) and analysed for Hf isotopes (Table 3). Zircon grains are euhedral to subhedral and vary in length from 100 to 400 µm (Fig. 10A). The BSE images reveal that most zircon grains are strongly to partly altered and fractured, some with oscillatory or banded magmatic zoning (Fig. 10A). Except one, all analyses display Th/U ratios >0.1 (Table 2), which are typical for magmatic zircon. The majority of zircon analyses yielded discordant ages that plot on a Discordia line with an upper intercept age of 2128.9±5.1 Ma (Fig. 10B) whereas the lower intercept age points to a recent Pb loss event (768±210 Ma), with no geological relevance. As illustrated on Figure 10C, fifteen analyses from least altered zircon domains are concordant and define a precise U-Pb Concordia age of 2130.6±5.8 Ma (with MSWD = 0.15, Probability of concordance = 0.7 and n = 15). This age is interpreted to indicate the timing of magma crystallisation. Regarding zircon Hf isotope compositions, samples have limited variation of $^{176}Hf/^{177}Hf$ values, ranging from 0.281463 to 0.281588. Zircon grains yield suprachondritic εHf_t between +1.3 and +4.2 corresponding to hafnium (two stage) model ages between ca. 2.4 and 2.6 Ga (Fig. 10D, Table 3).

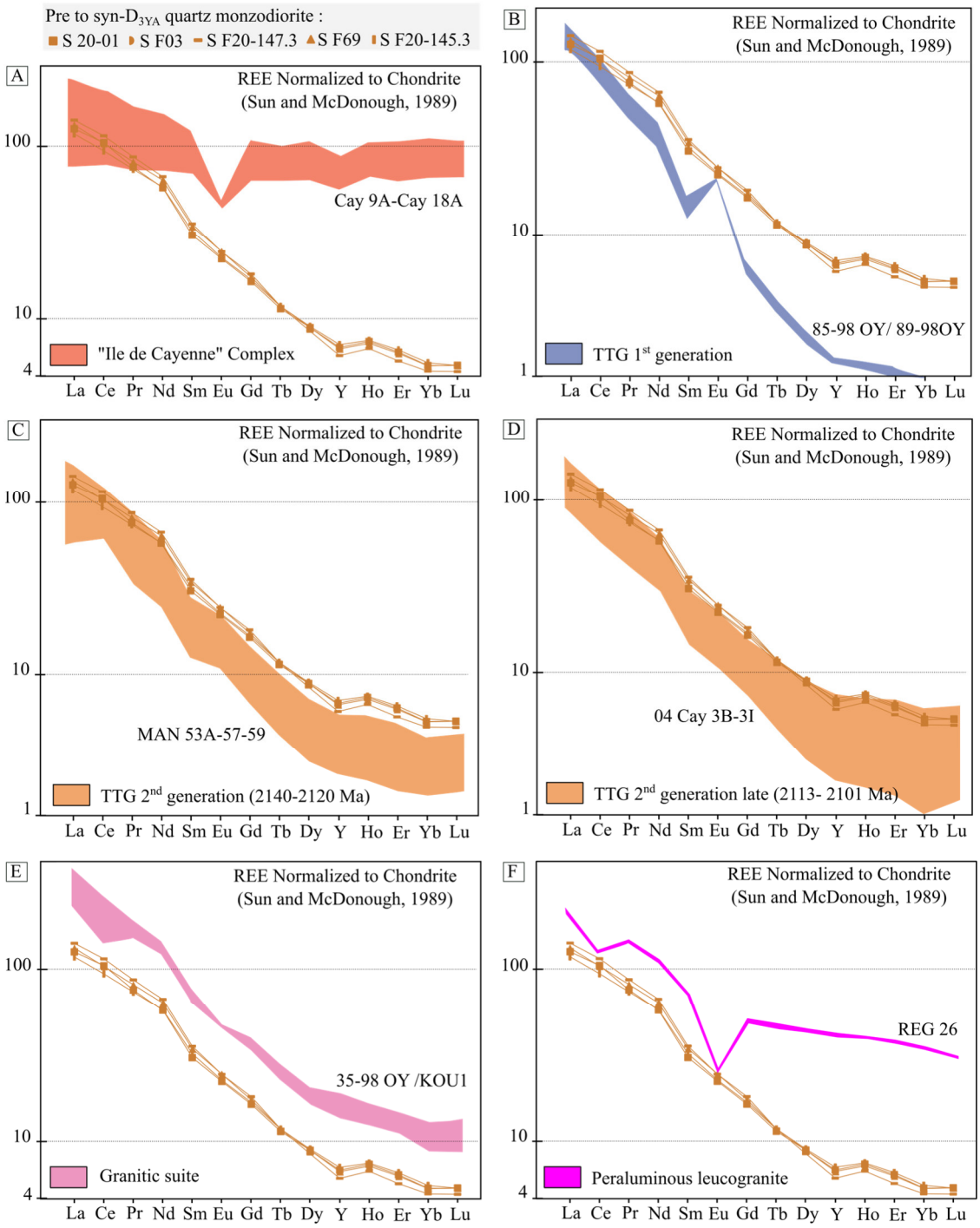

Figure 3-9 Yaou Quartz monzodiorite REE Normalised to Chondrite (Sun and McDonough, 1989) patterns compared to the main intrusive units defined in French Guiana. A. The "Ile de Cayenne" Complex patterns. B. The 1st generation of TTG patterns. C. The 2nd generation of TTG patterns. D. The late samples of the 2nd generation of TTG patterns. E. The Ganitic suite patterns. F. The peraluminous leucogranite patterns. Compared geochemical data are from Vanderhaeghe et al. (1998), Delor et al. (2003a, b) and Enjolvy (2008).

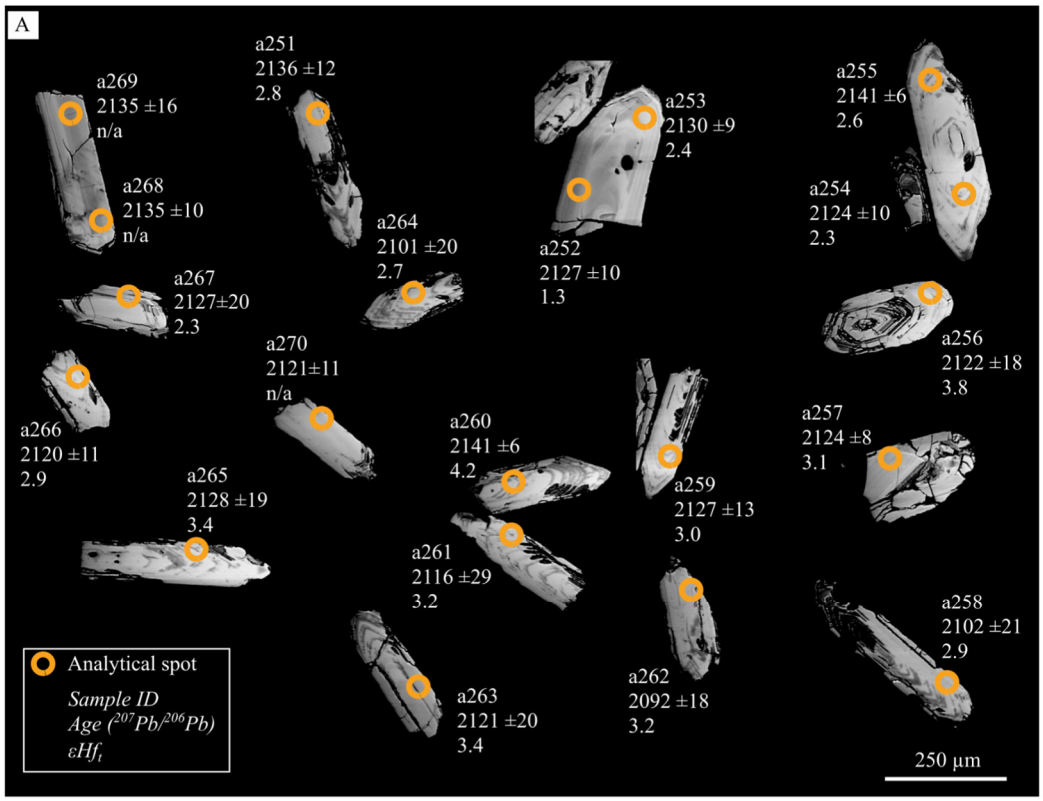
A
a269
2135 ±16
n/a
a268
2135 ±10
n/a
a267
2127±20
2.3
a266
2120 ±11
2.9
a265
2128 ±19
3.4
a251
2136 ±12
2.8
a264
2101 ±20
2.7
a270
2121±11
n/a
a260
2141 ±6
4.2
a261
2116 ±29
3.2
a263
2121 ±20
3.4
a253
2130 ±9
2.4
a252
2127 ±10
1.3
a259
2127 ±13
3.0
a262
2092 ±18
3.2
a255
2141 ±6
2.6
a254
2124 ±10
2.3
a256
2122 ±18
3.8
a257
2124 ±8
3.1
a258
2102 ±21
2.9
Analytical spot
Sample ID
Age (207Pb/206Pb)
εHft
250 µm

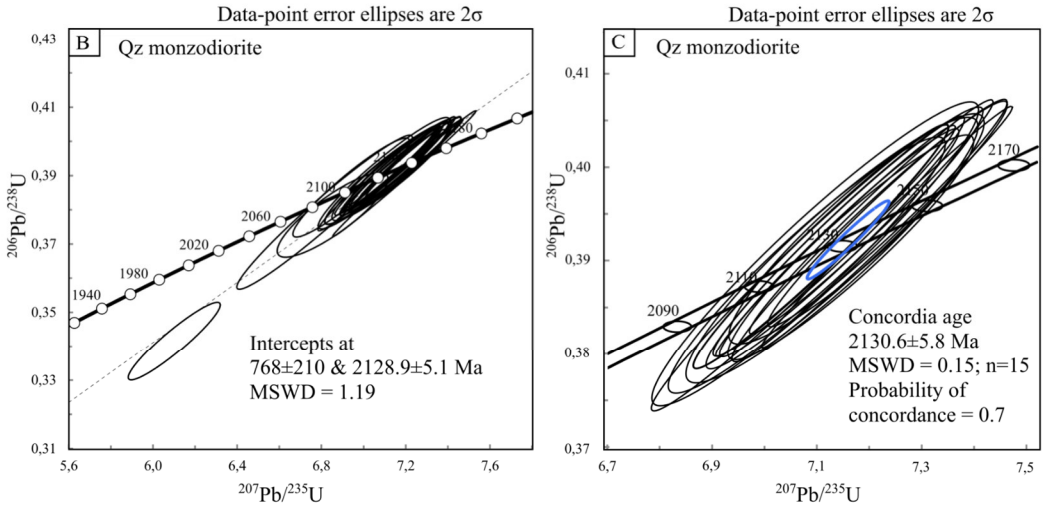
Data-point error ellipses are 2σ
B
Qz monzodiorite
Intercepts at
768±210 & 2128.9±5.1 Ma
MSWD = 1.19
206Pb/238U
207Pb/235U
Data-point error ellipses are 2σ
C
Qz monzodiorite
Concordia age
2130.6±5.8 Ma
MSWD = 0.15; n=15
Probability of
concordance = 0.7
206Pb/238U
207Pb/235U

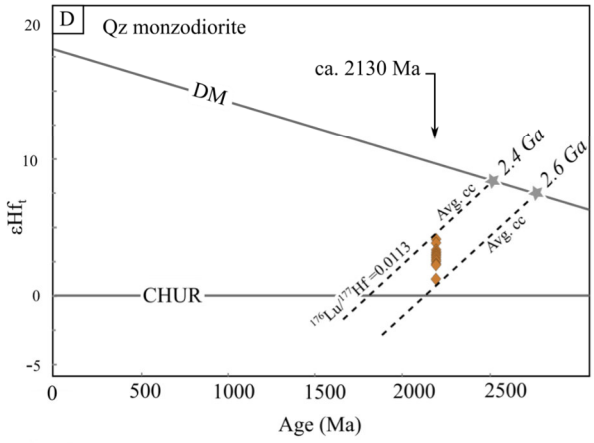
D
Qz monzodiorite
ca. 2130 Ma
DM
2.4 Ga
2.6 Ga
Avg. cc
Avg. cc
CHUR
176Lu/177Hf=0.0113
εHft
Age (Ma)

Figure 3-10 A. BSE images of representative analysed zircon grains from the quartz monzodiorite intrusion. The circles indicate Lu-Hf and U-Pb laser spots. The numbers are respectively the sample ID, the $^{207}Pb/^{206}Pb$ age and the Hf model age of the corresponding spot. B. $^{207}Pb/^{235}U$ versus *$^{206}Pb/^{238}U$ diagrams for the quartz monzodiorite (intercept). C. $^{207}Pb/^{235}U$* versus *$^{206}Pb/^{238}U$ diagrams for the quartz monzodiorite (concordance). D. εHf_t as a function of intrusion age (Ma). Crustal evolution trends (between dotted lines) are calculated with a value of $^{176}Lu/^{177}Hf = 0.0113$, value for average present-day continental crust. Stars at the intersection of depleted mantle and crustal evolution trends represent Hafnium model ages. CHUR = chondritic uniform reservoir; DM = depleted mantle.*

Re-Os geochronology on pyrite

The quartz monzodiorite is a preferential host for the main gold-bearing vein set with a strong rheological control (Combes et al. 2021). These quartz-carbonate veins characterised by a strong proximal pyritisation postdate the intrusive event and are interpreted as being synchronous to the D_{4YA} deformation phase. The Py_4 pyrite grains are coarse, homogeneous in composition, and can contain gold micro-inclusions and gold infilling fractures. Two aliquots of Py_4 from the same sample powder yield Re-Os ages of 2110±30 Ma and 2101±17 Ma (Table 4, Fig. 13).

Table 3-4. The Re-Os data obtained on Py_4 pyrite

Name	Sample wt. (g)	[Re] ppb	total uncertainty	^{187}Re M/g	total uncertainty	^{188}Os M/g	%^{188}Os from blank
Yaou (1)	0.20292	26.57	0.3789	8.93E-11	1.27E-12	5.49E-15	22.9
Yaou (2)	0.20165	26.16	0.2037	8.80E-11	6.74E-13	5.69E-15	22.4

Name	^{187}Os ppb blank corr	187 rad if $^{187}/^{188}$(initial) =0.6	Total uncertainty	$^{187}Os/^{188}Re$	$^{187}Os/^{187}Re$ uncertainty	Age (Ga)	Uncertainty
Yaou (1)	0.595	3.18E-12	6.50E-15	3.58E-02	5.15E-04	2.11	0.03
Yaou (2)	0.584	3.12E-12	6.00E-15	3.56E-02	2.83E-04	2.101	0.017

All data are blank corrected.

Radiogenic Os is estimated assuming an initial $^{187}Os/^{188}Os$= 0.6 ±0.5

Total uncertainties (2 sigma) include measurement uncertainties, uncertainty on the blank reproducibility, and assumed variation in initial $^{187}Os/^{188}Os$ ratio.

5. Geophysical interpretations

Lithological distribution

At the deposit to camp scale, the lithological distribution of the main units is relatively well identified (Combes et al., 2021) from drillcore data and historical subsurface extraction and mapping. When zooming out from the central part of Yaou, no outcrop data are available at the district scale where no recent exploration work has been carried out within this dense Amazonian forest area. Magnetic and radiometric anomalies are used here to zoom out and to produce a lithological map up to the district scale (i. e. beyond the Yaou tenement, see limits on Figure 3) with respect to the initial camp scale map. All interpretations and corroborations between geophysical data and available field/core observation are made first at the well studied camp scale. The potassium anomaly map presented in Figure 11A defines in great details the spatial distribution of the metasedimentary unit and corroborates the regional scale map proposed by Delor et al. (2003b) based mainly on the BRGM radiometric survey for the whole country (Fig. 2 and 3) and shows the presence of metasediments belonging to the Paramaca greenstone belt. At the camp scale, this correlation (positive K anomalies and metasediment distribution) is demonstrated where drilled areas with logged metasediments show positive K anomalies. The U anomaly filter delimits the northeastern U-rich plutonic body (Fig. 11B) while a clear delimitation of both TTG complexes (according to Delor et al., 2003a) is visible in the ternary map displaying the relative abundances of U, K and Th (Fig. 11C). These observations from the radiometric maps are supported by the 1VD grid (Fig. 11D) emphasing shallow features, with (1) the northeastern pluton delimited by its smooth texture, (2) the eastern pluton highlighted by its smooth texture (but to a lesser degree than the northeastern pluton), (3) the remanently magnetised dolerite striking N165°E, (4) the metasediments without stipple textures observed in the north as opposed to (5) the main area with stipple textures typical of metavolcanite formations. Finally (6) some minor mafic intrusive plugs are visible in the northern part of the surveyed area. The whole interpreted lithological map is presented in Figure 11E on a shaded-relief image. Overall, based on the internal geophysical data set of the Auplata Mining Group, the present study proposes a more detailed lithological map compared to the one established by Delor et al. (2003b) for the whole country using the BRGM regional data set. The occurrence of the metasedimentary unit is extended toward the South and the TTG complexes are more delimited at their western borders. The quartz monzodiorite bodies spatially defined with details at the camp scale could not be targeted with the resolution of the present data set.

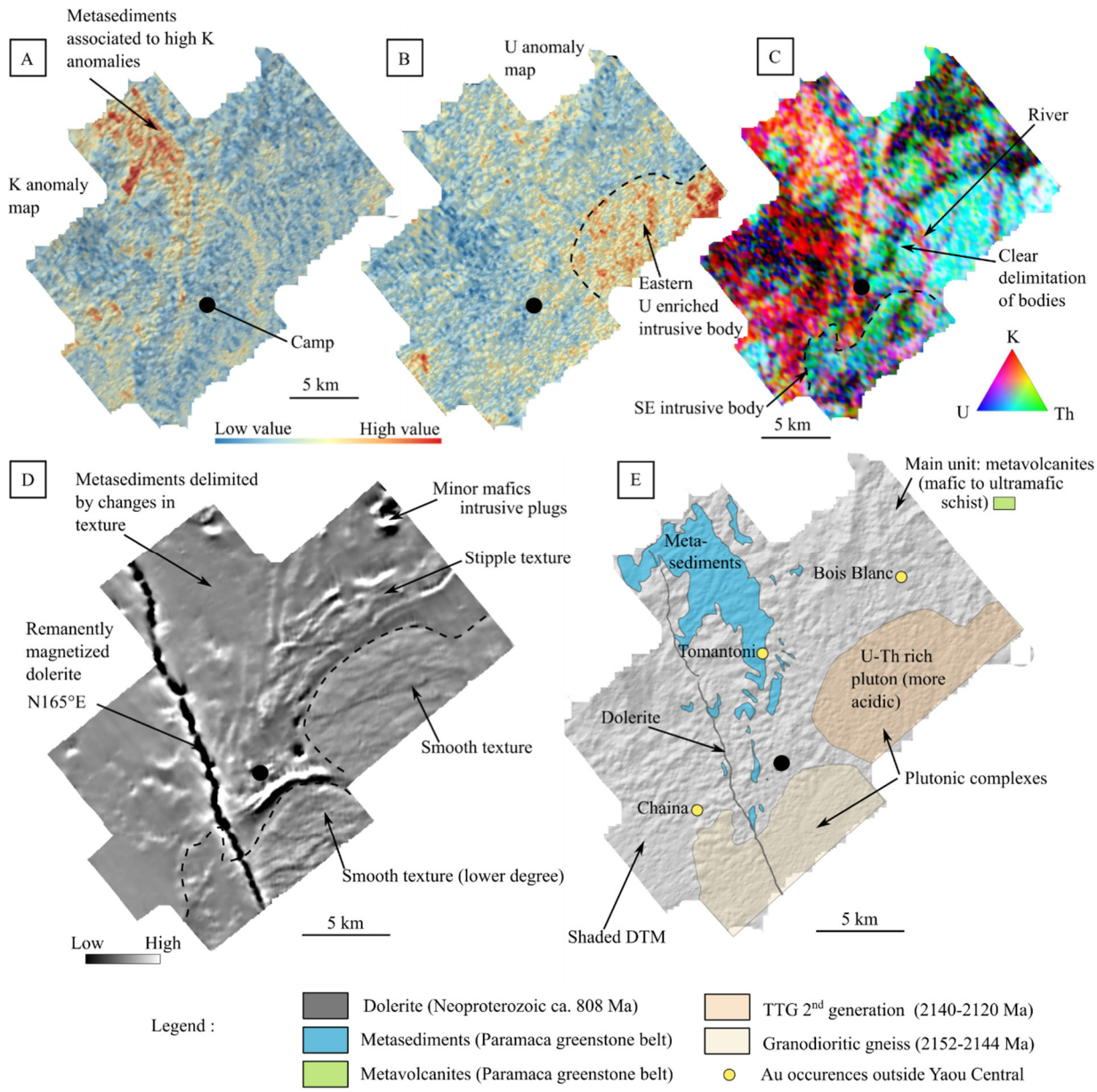

Figure 3-11 Lithological interpretations based on airborne geophysics. A. K anomaly grid used to map the metasedimentary unit. B. U anomaly map highlighting the U-rich TTG complex. C. Ternary radio-element map (relative abundance) of K, Th and U. D. 1VD image emphasizing shallow features. E. Overview of the interpreted distribution of lithologies at the district scale

Identified structures

No robust structural data are available in the area. Three airborne magnetic filters are therefore used in an attempt to identify possible structures within the Yaou district, namely the 1VD (Fig. 12C), RTP-TD (Fig. 12A), and RTP-TD-HDR (Fig. 12 B) filters (see *methods* section). This work focuses here on the supra-crustal scale only. As for the lithologic distribution, the study

focuses first on the deposit to camp scale and then zooms out. From core studies and internal reports, the identified structures at the camp scale are as follow: a main subvertical foliation striking E-W and a shear corridor striking N60° (CYSZ, Combes et al., 2021). While it is not possible with the used magnetic data set to define at this scale the main foliation, the CYSZ may correspond to a low magnetic N60°-striking lineament. Considering all filters, at the camp scale, structures observed are low and high magnetic response NE-SW- striking linear structures. Locally, they may be offset by a N140° structure. When zooming out and considering the whole surveyed area (Fig. 3 and 12) possible interpreted structures can be defined as follow:

(1) The main subvertical lineaments (symmetric features) strike roughly NE-SW (Fig. 12A, B), the RTP-TD (Tild Derivative) filter enhancing these magnetic lineaments. These main structures are troncated by the dolerite and in the east, are parallel to contacts between the metavolcanites and the TTG complexes. They locally display some folding together with some minor sinistral strike-slip faulting offsetting the main lineaments (NE of the area, Fig. 12D).

(2) Some minor fabrics within the metasedimentary unit, in the upper west part of the area, produce a lower magnetic intensity signal (Fig. 12C). In this area the main lineaments are not observed.

(3) Among the TTG complexes in the east, some internal NE-SW features are highlighted by the RTP-TD-HDR filter (Fig. 12B), meaning that the TTG complexes have been affected by the deformation phase giving the main NNE-SSW lineaments and were emplaced before the main deformation phase. Margins of these plutons show a negative magnetic anomaly (Fig. 12C).

(4) The same minor N140° faults observed at the camp scale are encountered elsewhere in the surveyed area (in red in Figure 12D) affecting the main NE-SW structures. Most gold occurrences (established by the BRGM, Guyanor and Auplata Mining Group-internal reports) are located in the vicinity of interconnections between these minor faults and the main lineaments (see Fig. 12D) with for some examples, other occurrences are not included here for confidentially issues).

The scale of the geophysical maps is not sufficiently detailed to show the CYSZ however the N60° low magnetic lineaments are continuous along strike and replicated toward the NW (Fig. 12 A, B, C and D).

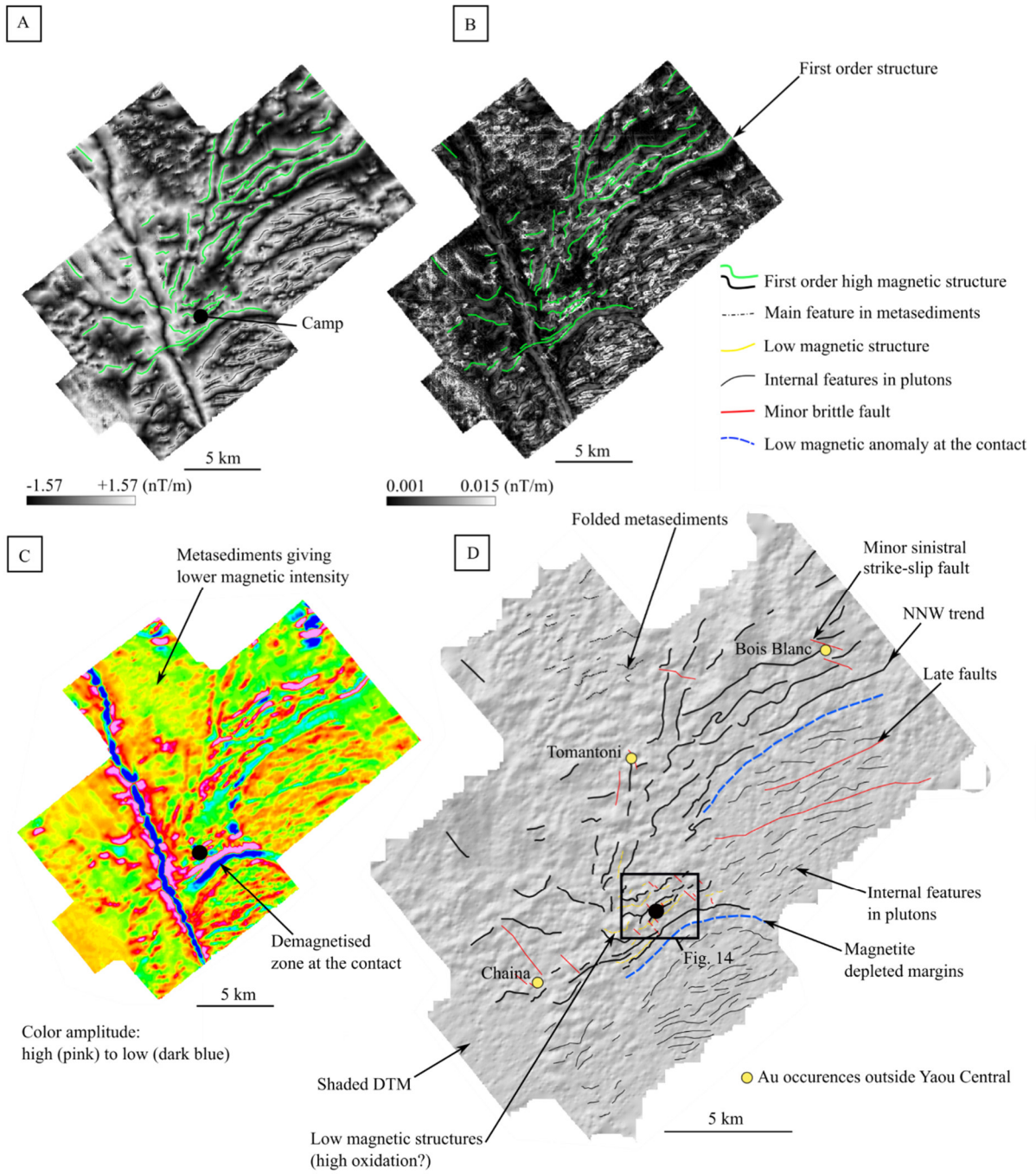

Figure 3-12 Structural interpretation using airborne geophysics A. Aeromagnetic map with RTP-TD grid enhancing magnetic lineaments. B. Aeromagnetic map with RTP-TD-HRD grid showing maximum ridges over edges of magnetic bodies. C. Aeromagnetic map with 1VD

displaying magnetic intensity with color gradient. D. Overview of main structures identified at the district scale.

6. Discussion

The Yaou intrusive event at the deposit-scale

The REE data from the Yaou quartz monzodiorite are compared to REE results from other plutonic rocks sampled within French Guiana in Fig. 9. The « Ile de Cayenne » complex samples show a flat pattern with no variation between LREE and HREE together with an Eu negative anomaly (Fig. 9A) that differs strikingly from the quartz monzodiorite's pattern. The Yaou samples share some similarities with the 1st generation of TTG but those TTG display more depleted HREE and a marked positive Eu anomaly (Fig. 9B). The Yaou quartz monzodiorite pattern clearly ressembles those of the 2nd generation of TTG (Fig. 9C), with an enrichment in LREE and a depletion of HREE. It is even better correlated with the pattern of the late samples of the same TTG generation, as visible in Figure 9D. Therefore, geochemically, the Yaou quartz monzodiorite can be interpreted as belonging to the 2nd TTG generation, also referred to as the Central TTG Complex (Delor et al., 2003a, b) and dated between ca. 2140-2120 Ma for the main magmatic phase and ca. 2113-2101 Ma (Enjolvy, 2008 ; Fig. 9) for the late phase interpreted as a continuum of the same 2nd generation TTG intrusive event. Samples of the granitic suite follow a similar pattern to those of Yaou (Fig. 9E) but with much stronger REE absolute abundances and no relative Ho enrichment. Finally, peraluminous leucogranite samples show higher absolute LREE abundances, strong negative Ce and Eu anomalies, and a slightly sloping HREE segment, with absolute HREE abundances greatly exceeding those of the Yaou samples.

The interpretation of a TTG-type intrusion at Yaou is reinforced by the similarities between the Yaou samples and the typical TTG geochemical signatures (Martin et al., 2005; Moyen and Martin, 2012). Indeed, Moyen and Martin (2012) indicates that TTGs (1) do not present Eu anomalies, as for the Yaou samples, (2) show Yb content below 1.5 ppm (below 0.8 ppm for our samples), (3) an $(La/Yb)_N > 15$ where the normalised ratios at Yaou are above 20.65 ; (4) a depletion in HREE and Y (same depletion for Yaou and a Y content below 11 ppm) and (5) Nb-Ta negative anomalies, also observed for this study with Nb/Ta < 13 ppm.

TTG magmas result from melting and/or crystallisation of hydrous, low-potassium basalts, (Moyen and Martin, 2012; Laurent et al., 2020). The geodynamic setting in which they are formed is still debated (Laurent et al., 2020). The high content of HREE implies the presence of garnet in the petrogenesis of the magma. Considering its stability field, it is therefore at a high-pressure condition. The Yaou quartz monzodiorite could have formed on an active margin context (i) by partial melting of a subducted oceanic crust, (ii) by melting of over-thickened arc roots or (iii) by fractionation of hydrous arc basalts (Laurent et al., 2020 and references therein).

The Yaou deposit, mainly hosted by the dated quartz monzodiorite, is located in the vicinity of the Central TTG Complex with two complexes in the east (Fig. 2) belonging to the 2nd generation of TTG (ca. 2140-2120 Ma). Therefore, the quartz monzodiorite intrusions identified at the camp-scale could be associated (genetically and spatially) with these TTG complexes. A field-based sampling campaign is necessary in the eastern part of the deposit, in order to sample both complexes. The age of 2130.6±5.8 Ma obtained in this study for the Yaou intrusion, falls in the age range of the 2nd generation TTG intrusions. An interpreted integration of the deposit/camp scale litho-stuctural framework in the regional scale scheme of Delor et al. (2003a, b) is presented in Figure 13 based on the robust timing of emplacement of the pre- to syn-shearing intrusion together with the geochemical comparison (REE patterns) of all types of magmatic rocks from French Guiana. Regarding the Re-Os pyrite age, the duplicate analyses are in excellent agreement and yield an average value of 2105 ±25 Ma. It suggests that the D_{4YA} phase was concomitant with the regional D_{2a} episode of Delor et al. (2003a, b) and most likely postdated the intrusive event dated at 2130.6±5.8 Ma. This is in agreement with the relative timing of Combes et al. (2021) based on core observations and is the first dating of a gold-bearing mineral in the region, allowing to bracket an absolute age of a major gold event. Considering the obtained U-Pb and Re-Os ages for the intrusive event and the D_{4YA} phase respectively, the following interpretation can be prosposed: (1) the D_{1YA}/D_{2YA} deformation phase would refer to the regional D_1 deformation phase (subduction, oceanic island arcs/back arc basins dated at ca. 2180-2130 Ma with an N-S compression); (2) the $D_{3/4YA}$ would be related to the D_{2a} phase (collision, compression to transpression dated at ca. 2110-2080 Ma). The major gold event is interpreted here to occur between ca. 2130-2125 Ma (lastest age of the intrusion; the Au-bearing pyritisation being post-intrusion) and ca. 2084 Ma (youngest age obtained on Py_4 permitted within uncertainties). The present work shows an age of intrusion emplacement at the transition between the regional D_1 and D_{2a}, therefore at the end of the magmatic arc

activity (ca. 2180-2130 Ma) and at the beginning of the collision between magmatic arcs and crustal blocks (ca. 2110-2080 Ma). We propose that the $D_{1/2YA}$ deformation phase ends earlier than initially proposed by Delor et al. (2003a) for the D_1 phase (2180-2130 Ma) as the intrusion (2130 Ma) is interpreted as post-D_{2YA} (Combes et al., 2021). Also, the D_{2a} deformation phase (dated at 2110-2080 Ma), which is interpreted to correspond to the D_{3YA} phase at Yaou, could start earlier. The D_{2a} has only been dated in the northern belt of the PGB and not in the southern belt where the Yaou deposit is located (see Fig. 13). The D_{5YA} phase may correspond to the regional D_{2b} (dextral strike slip shearing dated at 2070-2060 Ma) but no data are available to confirm this statement. Regarding the late Granitic suite (ca. 2110-2070 Ma, Pb/Pb and U-Pb on zircon dating, see Fig. 13), both their geochemical signature (Fig. 9) and the relative timing of deformation phases (Fig. 13) distinguish these rocks from the intrusive rocks of Yaou.

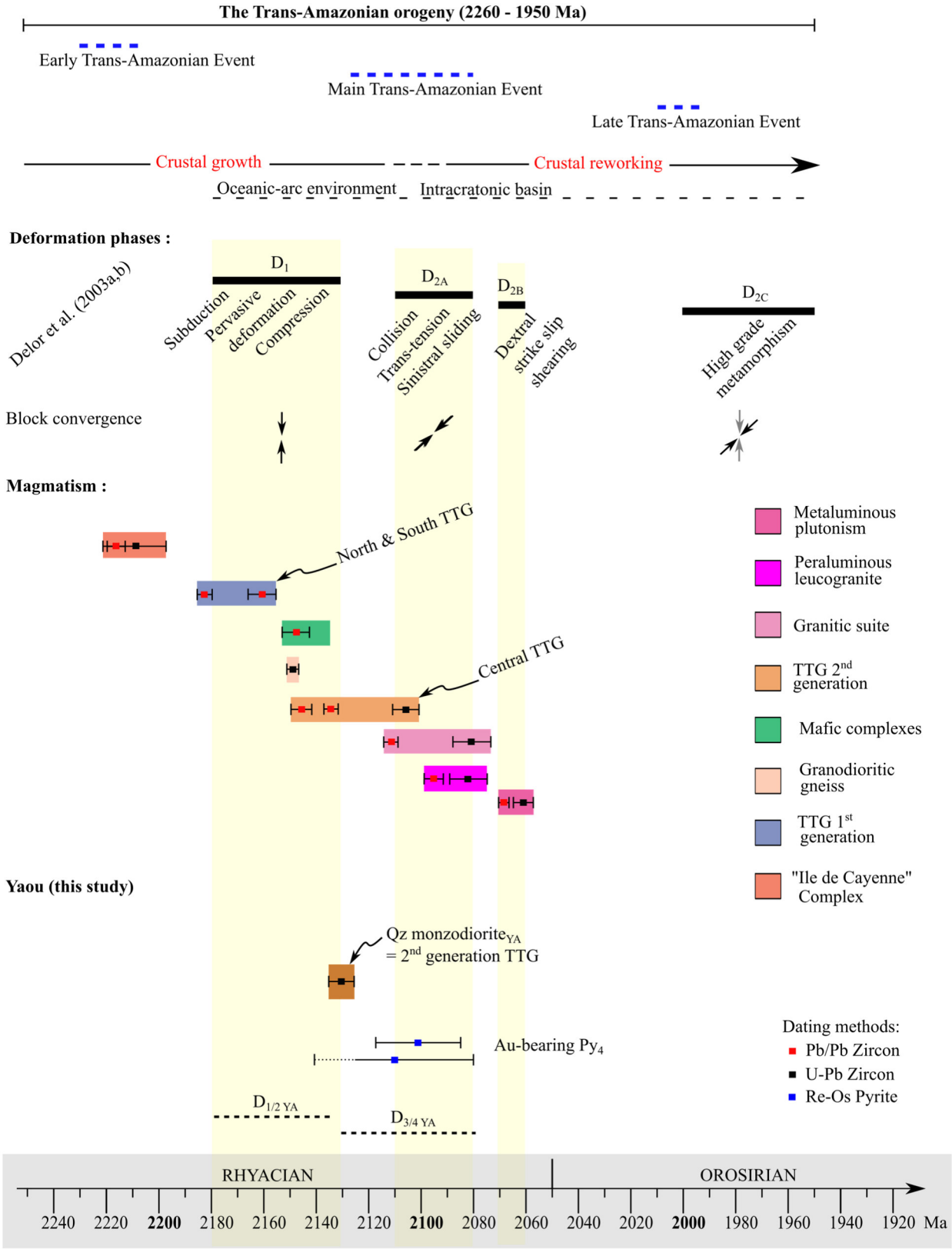

Figure 3-13 Geochronological synthesis of the Trans-Amazonian orogeny with deformation phases (Delor et al., 2003 a, b), compilation of published geochronological data of main plutonic events (zircon Pb/Pb and U-Pb; Vanderhaeghe et al., 1998; Delor et al., 2003b;

Enjolvy 2008) and interpreted integration of the Yaou camp-scale deformation phases from Re-Os dating on pyrite (Py_4) and U-Pb dating on zircon (quartz monzodiorite i.e. intrusive event) in the regional framework.

Regarding the isotopic data, zircon Hf isotope compositions are supra-chondritic suggesting that the quartz monzodiorite derives from the reworking of juvenile Trans-Amazonian crustal components as old as ca. 2.4-2.6 Ga. The juvenile character of the Yaou intrusion reinforces the interpretation of a TTG signature of the quartz monzodiorite. These Hf-isotopes signatures are similar to those calculated on the intrusive rocks studied by Para-Avila et al. (2018) in the Baoulé-Mossi domain of the southern West African Craton with $^{176}Hf/^{177}Hf_{(t)}$ values, ranging from 0.2814 to 0.2815. Thus, in analogy with what has been proposed for the West African Craton, we suggest that the Yaou samples result from an accretionary process involving an oceanic environment, reworked in an arc type or oceanic plateau system and later accreted due to continental terrane collision (Block et al., 2016; Eglinger et al., 2017; Petersson et al., 2016; Para-Avila et al., 2018). Our εHf_t values, ranging between +1.3 and +4.2 plot within the middle field of the interpreted evolution trend of εHf_t *vs* ages of Para-Avila et al. (2018) corresponding to the Eburnean phase.

Zooming out from the camp-scale, a pre- to syn-shearing intrusive event

The spatial distribution of the intrusive bodies (aligned along a N60° trend) and their 3D geometry has been defined in great details at the deposit to camp scale (Fig. 4 and 5). When zooming out from the camp scale to the district scale, no detailed interpretation has been made prior to this study, no outcrop is used/found for this work, no lineation is measured, no far-field stress is established. The only data available are the geophysical survey and its interpretation. Historical gold in soil surveys (AMG) does not help at the district scale. The use of geophysics where no ground exploration has been carried out is therefore essential although the resulting interpretation may be weak. The CYSZ precisely delimited at the camp scale and striking N60°E corresponds to a low magnetic lineament (Fig. 14C). The N60° structure remains open along strike (Fig. 14A with RTP-TD greyscale grid). A lateral repetition of N60° structures toward the northwest (Fig. 14B) with alternating first order high and low magnetic structures are interpreted. The D_{3YA} shear zone may be part of a serie of parallel shear zones as proposed in Figure 14C. Importantly, brittle faults (WNW-ESE) are interpreted as being D_{4YA}-related since these faults affect the interpreted D_{3YA} structures. Furthermore, these fauts are all located within kown aurifereous zones (near placers and/or gold showings such as Chaina, Tomantoni

and the Yaou Central area, Fig. 3) and share similar strikes with the regional N120-140° structures. Regarding the quartz monzodiorite instrusion, the resolution of the accessed geophysical maps does not allow to precisely delineate the intrusive bodies but possible occurences using a correlation (as observed within Yaou Central) between demagnetised lineaments and altered intrusions is proposed (Fig. 14C). This association could be explained by the fact that quartz monzodiorite bodies display a high frequency of D_{4YA} veins (Combes et al., 2021) which produce magnetite-depleted (and pyrite-rich) zones due to the progressive replacement of magnetite by pyrite towards the veins.

From these 2D interpretations, a 3D model can be discussed that integrates time as a component. We interprete the relative timing of the shearing event and intrusive event at the camp-scale as follow. First, the Pre-D_{3YA} phase D_{2YA} (Combes et al. 2021), is characterised by an E-W penetrative foliation (Fig. 15A) with both the metasediment and the metavolcanites being transposed in the S_2. The following syn-D_{3YA} shearing phase with the intrusive body is illustrated in Figure 15B. A 3D representation of the interpreted shearing induced intrusive event is presented in Figure 15C with opening from shearing, associated magma injection emplacement and lateral repetition of syn-kinematic intrusions and shear zones.

Two hypotheses are presented (Fig. 15C) that may explain the space opening in order to settle the intrusions between the parallel shear zones. Robust structural data would be needed to test these models. The first model implies the formation of tension gashes, which will rotate and deflect while the shearing is active. The second model implies a syn-shearing back-rotation of fabrics between the two shear zones, with an antithetic rotation. In this case the extension allowing magma injection is unsure. A structural overview at the plan view of the spatial relationship between the C/S_3 fabrics (associated with the D_{3YA} deformation phase) and the S_2 fabrics (associated with the D_{2YA} deformation phase) is proposed in Figure 15D. This relationship reflects a protracted process during which intrusion emplacement and shearing are synchroneous. Locally plutons are stretched and mylonitised when close to the shearing corridors, as also illustrated by Plissard et al. (2012).

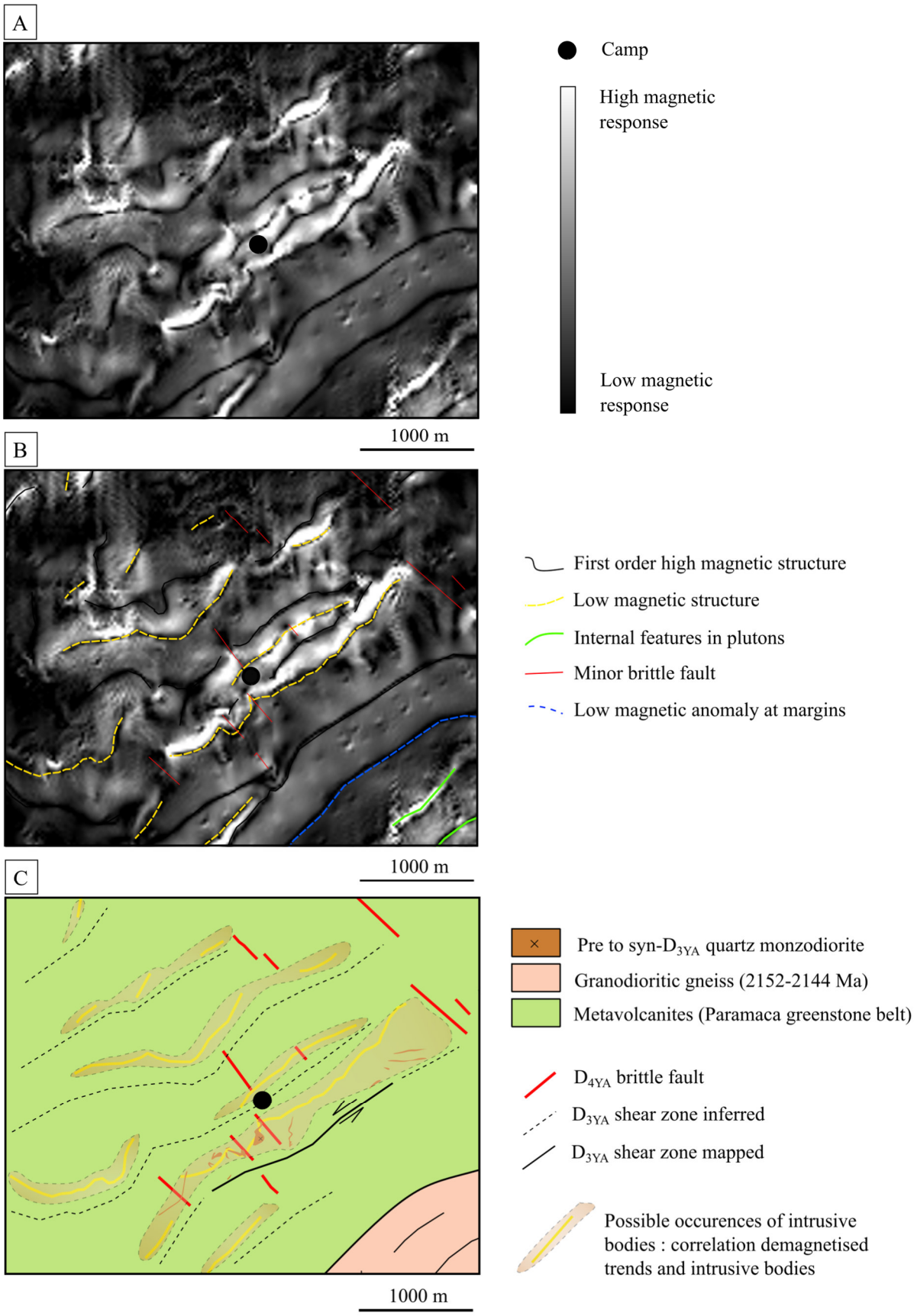

Figure 3-14 Structural interpretation of the distribution of faults, shear zones and intrusive bodies A. High to low magnetic response in greyscale (RTP TD HDR filter). B. Geophysical-

based interpretation (RTP TD HDR filter). C. Structural and lithogical interpretations displaying the proposed intrusive body trends, a serie of N60°-striking shear zones and late D_{4YA-} related faults.

Shear zone kinematic evidence (transtensional versus transpressional regime) is rare due to the lack of bedrock outcrops. Thus, it is contentious to ascertain the role of shearing. Since the CYSZ is parallel to the TTG complexes in the east, one simple interpretation could be that the shearing expressed at Yaou could be related to emplacement of these TTG Complexes. However, a more detailed structural study is needed to confirm the genetic link between shearing and magmatism at larger scale.

Based on the geometry of the deposit at the camp scale and the geophysical interpretation at larger scale, we propose that the shearing could open spaces (extensional pull-apart-like structures; Bhattacharya & Kar, 2004) enabling the magma to rise and allowing the emplacement of various intrusive bodies along the shear structure (D'Lemos et al., 1992 ; Weinberg et al., 2004). Weinberg et al. (2004) suggest *« that magma ascent in shear zones is intermittent and characterised by magma entrapment, ballooning, renewed escape, and deflation as the system develops into a number of dilational sites in shear-zone shoulders interconnected by magma sheets within the shear zones ».* The process of magma injection into a transtensional shear zone is exampled within the Variscan belt, SW Iberia by Pereira et al. (2015). Similar settings are described by Hutton (1982), Guineberteau et al. (1987) ; Joly et al. (2007) and Gébelin et al. (2007) but have been debated by Paterson and Fowler (1993), Paterson and Schmidt (1999) and Paterson et al. (2005) regarding the role/need of shear zones to provide a setting for the intrusions. An alternative model proposed by Neves et al. (1996) is a pluton-assisted shear zone nucleation (referred as pluton-induced shear zone). Here shear zones are related to magma emplacement as mentionned for the Borborema Province of north east Brazil with examples of intrusive bodies inducing strain localisation and favoring shear zone nucleation (Neves et al., 1996 ; Neves et al., 2005). More recently, Dering et al. (2019), defined intrusion-related deformation as lateral/vertical propagation and inflation of dykes that generates both seismicity and deformation (Dering et al., 2019 and references therein).

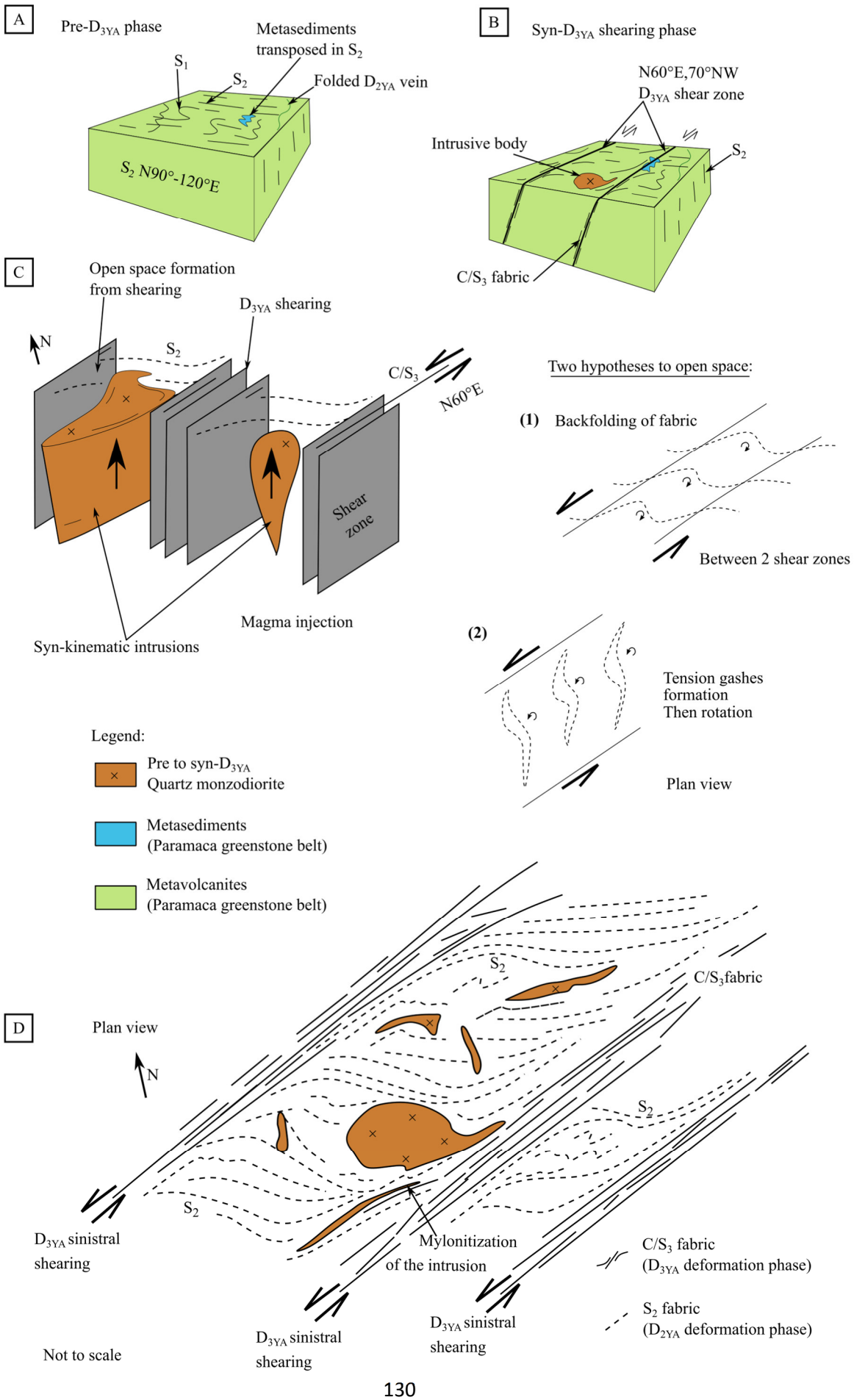
A
Pre-D3YA phase
Metasediments transposed in S2
S1
S2
Folded D2YA vein
S2 N90°-120°E
B
Syn-D3YA shearing phase
N60°E,70°NW
D3YA shear zone
Intrusive body
S2
C/S3 fabric
C
Open space formation from shearing
D3YA shearing
N
S2
C/S3
N60°E
Shear zone
Magma injection
Syn-kinematic intrusions
Two hypotheses to open space:
(1) Backfolding of fabric
Between 2 shear zones
(2)
Tension gashes formation
Then rotation
Plan view
Legend:
Pre to syn-D3YA
Quartz monzodiorite
Metasediments
(Paramaca greenstone belt)
Metavolcanites
(Paramaca greenstone belt)
D
Plan view
N
S2
C/S3fabric
S2
S2
D3YA sinistral shearing
Mylonitization of the intrusion
C/S3 fabric
(D3YA deformation phase)
S2 fabric
(D2YA deformation phase)
D3YA sinistral shearing
D3YA sinistral shearing
Not to scale

Figure 3-15 Sketches illustrating the structural settings at the camp-scale. A. The Pre-D_{3YA} phase. B. The syn-D_{3YA} shearing contemporaneous with the intrusive body. C. 3D representation of the interpreted shearing induced intrusive event with two hypotheses of formation, tension gashes or backfolding of fabric. D. Structural overview of the C/S_3 fabrics (associated with the D_{3YA} deformation phase) and the spatial relationship S_2 fabrics (associated with the D_{2YA} deformation phase).

Regarding the type of lithosphere involved in such compressive regime, two models are currently considered, namely (1) the horizontal tectonic model, followed by Vanderhaeghe et al. (1998) and Delor et al. (2003b) in the region, implying a modern-type tectonic where the lithosphere is defined as resistant and cold; and (2) the vertical tectonic model as defined by Gapais (2018) following the work of Cagnard et al. (2006a), Chardon et al. (2009) among other, with a weak and hot/buoyant lithosphere. The proposed model at the Yaou camp-scale does not allow to decipher between cold vs hot orogen but the steeply dipping deformation zones along intrusions bodies with a possible transpression component would be more applicable to the second tectonic model. Moreover, the recent work of Gapais (2018) highlights the relationships between structural patterns in weak lithosphere and mineralisation.

From the camp- to the district-scale, a new litho-structural model for gold targeting

A new litho-structural map is constructed at the district scale (Fig. 16A) based on deposit scale geological data (Combes et al., 2021), 3D modelling, geochemical characterisation of intrusions and airborne geophysical interpretations. When compared to the cross-section of Delor et al. (2003b) for the Yaou district as presented in Figure 16B the lithologic distribution is similar however the present study better defines the structural grain, the brittle faults (D_{4YA}-related) and internal fabrics within the intrusive complexes. This integrated approach, and in particular interpretation of airborne geophysical data, led to important findings and targeting previously unrecognised in the southern PGB. Indeed, best targets include (1) intersections of the main NE-SW lineaments with late N140° faults (many known occurrences follow this scheme); (2) near contacts of TTG-type intrusions and (3) areas in the NW where occurrences in metasediments are inferred. As suggested by Combes et al. (2021), the metasedimentary unit could be a primary source of gold (Au-bearing Py_0).

Upscaling progressively from the craton-scale to the ore-shoot scale, the following features are key elements for gold exploration (McCuaig and Hronsky, 2014; Wyman et al., 2016; Hronsky, 2019; Niiranen et al., 2019; Groves et al., 2020 and references therein): (1) paleo convergent

margins (outlined by airborne geophysical and large-scale geological exploration methods); (2) faults, folds and intrusions at the district scale (recognised by both geological and airborne/ground geophysical data), (e.g. Stewart et al., 2009; Metelka et al., 2011; Baratoux et al., 2015); (3) faults, folds and intrusions at the camp and deposit scale (recognised by both geological and airborne/ground geophysical data; drilling with precise 3D modelling of the geometry of the deposit), (Allibone et al., 2018; Cowan et al., 2019; Kreuzer et al., 2019); (4) locations of lithological units/facies with rheological and geochemical characteristics representing traps for ore shoots (geochemical characterisation and comparison/correlation of key lithological units at various scales) and, (5) deformation phases and associated gold events (identified when building a detailed petro-structural framework at the deposit scale with relative and absolute dating of available rocks and datable minerals), (e.g. Thébaud et al., 2018; Tedeschi et al., 2018a, b; Combes et al., 2021).

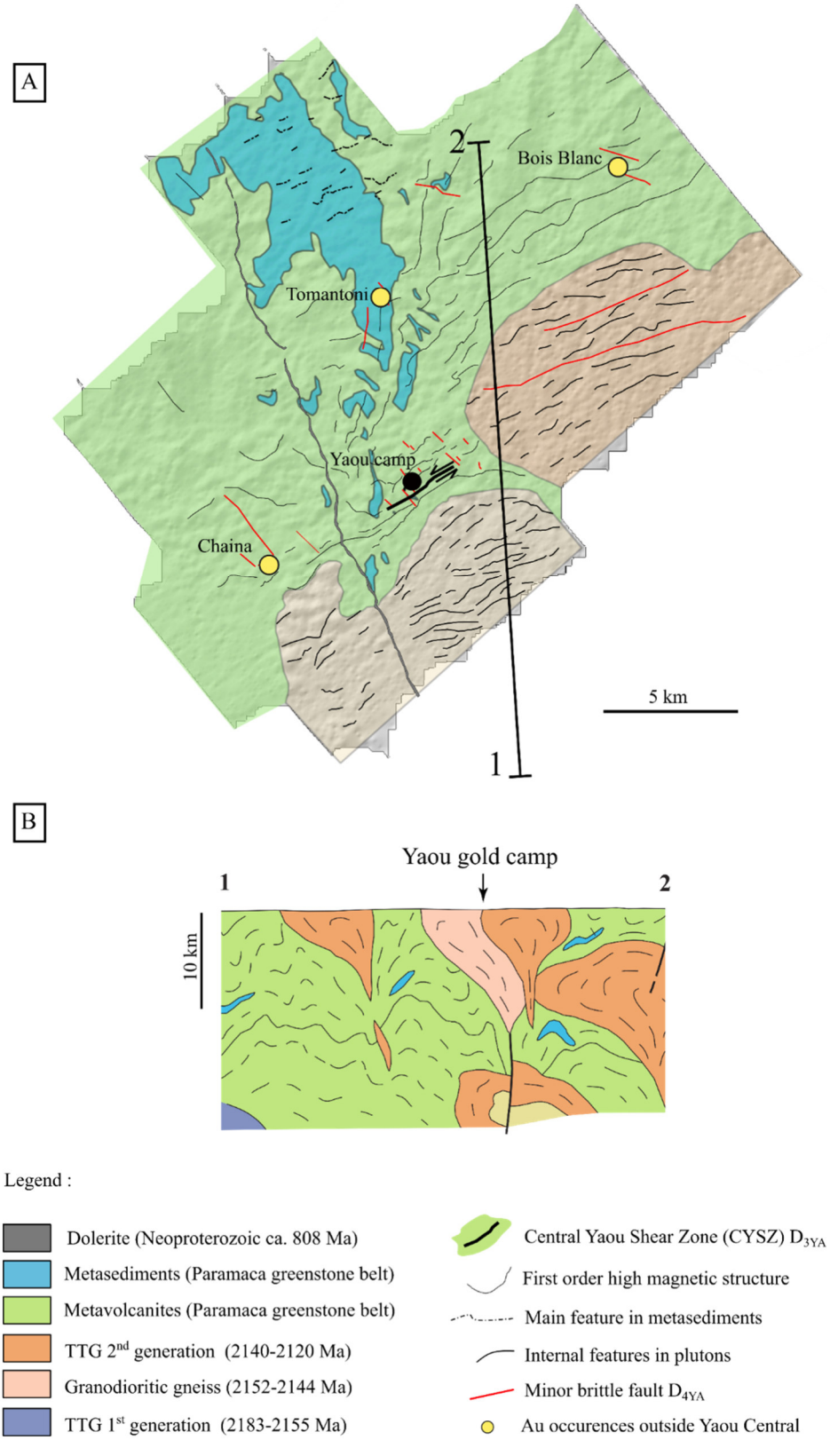

Figure 3-16 Litho-structural map produced from geological and geophysical data at the district-scale, and its integration within the geological cross-section of Delor et al.(2003b).

At the cratonic-scale, gold deposits spatially associated with intrusions within the Guiana Shield include the Omai gold deposit (Guyana), which is related to intrusive rocks dated between 2120±2 Ma and 2096±11 Ma (Norcross et al. 2000). The so-called Omai Stock (quartz monzodiorite) of Voicu et al. (1999) displays a REE chondrite-normalised pattern similar to that of the Yaou intrusion but with a slight enrichment in HREE. Like the Yaou quartz monzodiorite, the Omai intrusion postdates the regional foliation and is affected by a late phase of brittle deformation responsible for the network of Au-bearing veins (Voicu et al., 1999). The targeting of quartz monzodiorite intrusive bodies with TTG signatures, in the vicinity of shear zones, should be considered in the whole region. The intrusion-hosted, Yaou-type deposit may not be unique and similar structural settings may be good exploration targets in the Yaou and Dorlin districts.

Conclusions

The Yaou intrusion hosting the bulk of the gold mineralisation, is dated at 2130.6±5.8 Ma (U-Pb on zircon) and show supra-chondritic εHf_t indicating that this quartz monzodiorite is derived from the reworking of juvenile Trans-Amazonian crustal components. Using geochemical comparison (REE patterns) of all types of plutonic rocks from French Guiana, the quartz monzodiorite is associated to the second stage TTG rocks, which have the same age range. An integration of the deposit-scale framework is proposed where the quartz monzodiorite emplacement is defined between the regional D_1 and D_{2a} phases, therefore at the end of the crustal growth phase and at the beginning of the crustal reworking period. The main gold event hosted by this intrusion is dated by Re-Os on Au-bearing pyrite at 2105±25 Ma. In an outcrop-depleted region with no robust structural data, the multi-scale approach using airborne magnetic and radiometric data, helps to better understand the spatial distribution of the intrusions and associated shear zones. Both are interpreted as being repeated along a N60° trends and laterally toward the north west. The coupled geological and geophysical studies used in French Guiana are promising to localise/predict which structures and lithologies could be associated with gold at the district scale. The Yaou-type intrusion hosted mineralisation may be targeted along the N60° structures and where possible occurrences of intrusive bodies are defined. Moreover, minor faults offsetting the D_{3YA} N60° structures are high priority targets, knowing that the main gold event at Yaou is associated with the D_{4YA} deformation phase. This integrated approach,

and in particular interpretation of airborne geophysical data, opens some targeting possibilities, previously unrecognised within the southern Paramaca Greenstone Belt (PGB) at the province-scale.

Acknowledgment

This study is part of Vincent Combes's Ph.D. research at the Université de Lorraine within the GeoRessources laboratory, in Nancy, France. We are grateful to E. Davy of the CRPG in Nancy, France for helping us with zircon separation, to J. Perret for zircon handpicking. The airborne geophysical data were reprocessed and interpreted during the SAXI workshop held in 2019 at Paramaribo, Suriname.

Funding

This research was funded by Auplata Mining Group (AMG) and benefited from the framework of the CREGU.

References

Aitken, A.R.A., Betts, P.G., 2009a. Constraints on the Proterozoic supercontinent cycle from the structural evolution of the south-central Musgrave Province, central Australia. Precambr. Res. 168, 284–300.

Aitken, A.R.A., Betts, P.G., 2009b. Multi-scale integrated structural and aeromagnetic analysis to guide tectonic models: an example from the eastern Musgrave Province, Central Australia. Tectonophysics 476, 418–435.

Allibone, A., Blakemore, H., Gane, J., Moore, J., Mackenzie, D., Craw, D., 2018. Contrasting Structural Styles of Orogenic Gold Deposits, Reefton Goldfield, New Zealand. Econ. Geol. 113 (7), 1479–1497.

Barker, F., 1979, Trondhjemite: Definition, environment, and hypotheses of origin: p. 1-12, in Barker, F., ed., Trondhjemites, Dacites, and Related Rocks, Elsevier, Amsterdam, 659 p.

Baratoux, L., Metelka, V., Siebenaller, L., Naba, S., Naré, A., Ouiya, P., Jessell, M.W., Béziat, D., Salvi, S., and Franceschi, G., 2015. Tectonic evolution of the Gaoua region: Implications for mineralization. J. Afr. Earth Sci. 112, 419–439.

Begg, G.C., Hronsky, J.A.M., Arndt, N.T., Griffin, W.L., O'Reilly, S.Y., Hayward, N., 2010. Lithospheric, cratonic, and geodynamic setting of Ni–Cu–PGE sulfide deposits. Econ. Geol. 105, 1057–1070.

Betts, P. G., Williams, H. A., Stewart, J. R., Ailleres, L., 2007. Kinematic analysis of aeromagnetic data: looking at geophysical data in a structural context. Gondwana Res. 11(4), 582 - 583.

Bhattacharya, S., Kar, R., 2004. Alkaline intrusion in a granulite ensemble in the eastern ghats belt, India: Shear zone pathway and a pull-apart structure. J Earth Syst Sci. 113, 37–48 https://doi.org/10.1007/BF02701997

Bierlein, F.P., Groves, D.I., Goldfarb, R.J., Dubé, B., 2006. Lithospheric controls on the formation of provinces hosting giant orogenic gold deposits. Miner. Depos. 40, 874–887.

Bierlein, F.P., Groves, D.I., Cawood, P.A., 2009. Metallogeny of accretionary orogens—the connection between lithospheric processes and endowment. Ore Geol. Rev. 36, 282–292.

Birck, J.-L., Roy Barman, M., Capmas, F., 1997. Re-Os isotopic measurements at the femtomole level in natural samples. Geostand. Newsletter 20, 19–27.

Blakely, R.J., Simpson, R.W., 1986. Approximating edges of source bodies from magnetic or gravity anomalies. Geophysics 51, 1494–1498.

Blichert-Toft, J., Puchtel, I.S., 2010. Depleted mantle sources through time: Evidence from Lu-Hf and Sm-Nd isotope systematics of Archean komatiites. Earth Planet. Sci. Lett. 297, 598–606.

Block, S., Baratoux, L., Zeh, A., Laurent, O., Bruguier, O., Jessell, M., Ailleres, L., Sagna, R., Parra-Avila, L.A., Bosch, D., 2016. Paleoproterozoic juvenile crust formation and stabilisation in the south-eastern West African Craton (Ghana); new insights from UPb- Hf zircon data and geochemistry. Precambrian. Res. 287, 1–30

Bouvier, A., Vervoort, J.D., Patchett, P.J., 2008. The Lu–Hf and Sm–Nd isotopic composition of CHUR: Constraints from unequilibrated chondrites and implications for the bulk composition of terrestrial planets. Earth Planet. Sci. Lett. 273, 48–57.

Cagnard, F., Durrieu, N., Gapais, D., Brun, J.P., Ehlers, C., 2006a. Convergence tectonics within weak lithospheres : a working hypothesis with particular reference to Precambrian times. Terra Nova 18: 72–78.

Creaser, R.A., Papanastassiou, D.A., Wasserburg, G.J., 1991. Negative thermal ion mass spectrometry of osmium, rhenium and iridium. Geochim. Cosmochim. Acta 55, 397–401.

Chardon, D., Gapais, D., Cagnard, F., 2009. Flow of ultra-hot orogens: a view from the Precambrian, clues for the Phanerozoic. Tectonophysics 477: 105–118.

Chardon, D., Bamba, O., Traoré, K., Eburnean deformation pattern of Burkina Faso and the tectonic significance of shear zones in the West African craton, 2020. BSGF-Earth Sci Bull. 191, 2.

Combes, V., Eglinger, A., Andre-Mayer, A-S., Teitler, Y., Heuret, A., Gibert, P., Béziat, D., Polyphase gold mineralisation at the Yaou deposit, French Guiana. Accepted in the J. Geol. Soc. of London. Special Publication.

Cowan, E.J., 2020. Deposit-scale structural architecture of the Sigma-Lamaque gold deposit, Canada—insights from a newly proposed 3D method for assessing structural controls from drill hole data. Miner Deposita 55, 217–240. https://doi.org/10.1007/s00126-019-00949-6

Delor, C., Lahondère, D., Egal, E., Lafon, J.-M., Cocherie, A., Guerrot, C., Rossi, P., Truffert, C., Théveniaut, H., Phillips, D., Avelar, V.G.d., 2003b. 2-3-4 In: Transamazonian crustal growth and reworking as revealed by the 1:500000 scale geological map of French Guiana. Géol Fr. 5–57.

Delor, C., de Roever, E.W.F., Lafon, J.-M., Lahondère, D., Rossi, P., Cocherie, A., Guerrot, C., Potrel, A., 2003a. The Bakhuis ultrahigh-temperature granulite belt (Suriname) : II. Implications for late Transamazonian crustal stretching in a revised. Géol Fr. 2-3- 4, 207–230.

Dering, G. M., Micklethwaite, S., Cruden, A. R., Barnes, S. J., Fiorentini, M. L., 2019. Evidence for dyke parallel shear during syn-intrusion fracturing. Earth Planet. Sci. Lett. 507, 119 130. https://doi.org/10.1016/j.epsl.2018.10.024

De Roever, E.W.F., Lafon, J.-M., Delor, C., Cocherie, A., Rossi, P., Guerrot, C., Potrel, A., 2003. The Bakhuis ultrahigh-temperature granulite belt (Suriname): I. petrological and geochronological evidence for a counterclockwise P-T path at 2.07–2.05 Ga. Géol. Fr. 2-3-4, 175–205.

D'Lemos, R. S., Brown, M. and Strachan, R. A., 1992. Granite magma generation, ascent and emplacement within a transpressional orogen. J. Geol. Soc. of London. 149, 487-490.

Egal, E., Mercier, D., Itard, Y., Mounié, F., 1992. L'ouverture de bassins en pull-apart au Protérozoïque inférieur: nouveaux arguments dans le nord du craton guyanais. Comptes rendus de l'Académie des sciences. Série 2, Mécanique, Physique, Chimie, Sciences de l'univers, Sciences de la Terre 314, 1499–1506.

Eglinger A, Thébaud N, Zeh A, Davis J, Miller J, Parra-Avila LA, Loucks R, McCuiag C, Belousova E., 2017. New insights into the crustal growth of the Paleoproterozoic margin of the Archean Kénéma-Man domain, West African craton (Guinea): implications for gold mineral system. Precambrian Res 292. 258–289

Eglinger A., André-Mayer A.-S., Combes V., Teitler Y., Heuret A., 2020. Les gisements d'or de la Guyane française. Géologues 206 :36-40.

Enjolvy, R., 2008. Processus d'accrétion crustale et régimes thermiques dans le bouclier des Guyanes: signatures géochimiques et thermochronologiques au transamazonien (2250-1950Ma). PhD Thesis. Université Montpellier II-Sciences et Techniques du Languedoc, pp. 305

Fougerouse D, Micklethwaite S, Ulrich S, Miller J, Godel B, Adams DT, McCuaig TC., 2017. Evidence for two stages of mineralization in West Africa's largest gold deposit: Obuasi, Ghana. Econ Geol. 112: 3–22.

Gapais, D., 2018. Tectonics-mineralisation relationships within weak continental lithospheres: A new structural framework for Precambrian cratons. BSGF-Earth Sci Bull. 189. 14. 10.1051/bsgf/2018014.

Gébelin, A., Brunel, M., Monié, P., Faure, M., Arnaud, N., 2007. Transpressional tectonics and Carboniferous magmatism in the Limousin, Massif Central, France: structural and 40Ar/39Ar investigations. Tectonics 26, TC2008. doi:10.1029/2005TC001822.

Gerdes, A., Zeh, A., 2009. Zircon formation versus zircon alteration – New insights from combined U-Pb and Lu-Hf in-situ La-ICP-MS analyses of Archean zircons from the Limpopo Belt. Chem. Geol. 261. 230-243. 10.1016/j.chemgeo.2008.03.005.

Gibbs, A.K., Barron, C.N., 1993. The Geology of the Guiana Shield. Oxford University Press, USA, pp. 246.

Groves, D.I., Santosh, M., Zhang, L., 2020b. A scale-integrated exploration model fororogenic gold deposits based on a mineral system approach. Geosci. Front. 11 (3),719–738

Guineberteau, B., Bouchez, J.-L., Vigneresse, J.-L., 1987. The Mortagne granite pluton (France) emplaced by pull-apart along shear zone: structural and gravimetric arguments and regional implication. Geol. Soc. Am. Bull. 99, 763-770.

Hronsky, J.M.A., Groves, D.I., Loucks, R.R., Begg, G.C., 2012. A unified model for gold mineralisation in accretionary orogens and implications for regional-scale exploration targeting methods. Miner. Depos. 47, 339–358.

Hronsky, J.A., 2019. Deposit-scale structural controls on orogenic gold deposits: an integrated, physical process based hypothesis and practical targeting implications. Miner. Depos. https://doi.org/10.1007/s00126-019-00918z.

Huston, D. L., Blewett, R. S. & Champion, D. C. 2012. Australia through time: a summary of its tectonic and metallogenic evolution. Episodes, 35, 23–43.

Hutton, D. H. W., 1982. A tectonic model for the emplacement of the Main Donegal Granite, NW Ireland, J. Geol. Soc. London, 139, 615 – 631

Irvine, T.N., Baragar, W.R.A., 1971. A Guide to the Chemical Classification of the Common Volcanic Rocks. Can. J. Earth Sci. 8, 523-548

Jenkin, G., Lusty, P., Mcdonald, I., Smith, M., Boyce, A., Wilkinson, J., 2014. Ore deposits in an evolving Earth: An introduction. J. Geol. Soc. of London. Special Publications. 393. 10.1144/SP393.14.

Jessell, M., Valenta, R.K., Jung, G., Cull, J.P., Geiro, A., 1993. Structural geophysics. Geophysics. 24, 599–602.

Jessell, M.W. and Valenta, R.K., 1996, Structural geophysics: Integrated structural and geophysical modelling: Structural Geology and Personal Computers, Elsevier Science Ltd, Oxford, 303-324

Jessell MW, Begg GC, Miller MS. 2016. The geophysical signatures of the West African Craton. Precambrian Res 274: 3–24.

Joly, A., Faure, M., Martelet, G., Chen, Y., 2009. Gravity inversion, AMS and geochronological investigations of syntectonic granitic plutons in the southern part of the Variscan French Massif Central. J. Struct. Geol. 31, 421-443.

Klaver, M., De Roever, E.W.F., Nanne, J.A.M., Mason, P.R.D., Davies, G.R., 2015. Charnockites and UHT metamorphism in the Bakhuis Granulite Belt, western Suriname: evidence for two separate UHT events. Precambr. Res. 262, 1–19.

Kreuzer, O. P., Buckingham, A., Mortimer, J., Walker, G., Wilde, A., Appiah, K., 2019. An integrated approach to the search for gold in a mature, data-rich brownfields environment: A case study from Sigma-Lamaque, Quebec. Ore Geol. Rev. 111, [102977]. https://doi.org/10.1016/j.oregeorev.2019.102977

Kroonenberg, S.B., de Roever, E.W.F., Fraga, L., Reis, N., Faraco, T., Lafon, J.-M., Cordani, U., Wong, T., 2016. Paleoproterozoic evolution of the Guiana Shield in Suriname: a revised model. Neth. J. Geosci. 95, 491–522.

Ledru, P., Laserre, J.L., Manier, E., Mercier, D., 1991. Le Proterozoique inferieur nord guyanais: revision de la lithologie, tectonique transcurrente et dynamique des bassins sedimentaires. Bull. Societ. 162 (4), 627–636.

Lafrance, J., Bardoux, M., Voicu, G., Stevenson, R., Machado, N., 1999. Geological and metallogenic environments of gold deposits of the Guiana Shield; a comparative study between St-Elie (French Guiana) and Omai (Guyana). Explor. Min. Geol. 8, 117–135.

Laurent, O., Björnsen, J., Wotzlaw, J-F., Bretscher, S., Pimenta Silva, M., Moyen, J-F., Ulmer, P., Bachmann, O., 2020. Earth's earliest granitoids are crystal-rich magma reservoirs tapped by silicic eruptions. Nat. Geosci. 13. 1-7.

Martin, H., Smithies, R.H., Rapp, R.P., Moyen, J.-F., Champion, D.C., 2005. An overview of adakite, tonalite–trondhjemite–granodiorite (TTG) and sanukitoid: relationships and some implications for crustal evolution. Lithos 79, 1–24.

Metelka V, Baratoux L, Naba S, Jessell MW., 2011. A geophysically constrained litho-structural analysis of the Eburnean greenstone belts and associated granitoid domains, Burkina Faso, West Africa. Precambr. Res. 190: 48–69

McCuaig, T.C., Beresford, S., Hronsky, J., 2010. Translating the mineral systems approach into an effective exploration targeting system. Ore Geol. Rev. 38, 128–138.

McCuaig, T.C., Hronsky, J.M.A., 2014. The Mineral System Concept: the Key to Exploration Targeting. SEG 2014: Building Exploration Capability for the 21st Century, pp. 153–175.

Milesi, J., Lerouge C, Delór C, Ledru P, Billa M, Cocherie A, Egal E, Fouillac A, Lahondère D, Lasserre J, Marot A, Martel-Jantin B, Rossi P, Tegyey M, Théveniault H, Thiéblemont D, Vanderhaeghe, O., 2003. Gold deposits (gold-bearing tourmalinites, gold-bearing conglomerates, and mesothermal lodes), markers of the geological evolution of French Guiana: geology, metallogeny, and stable isotope constraints. Géol Fr, 2-3-4:257-290.

Miller, H.G., Singh, V., 1994. Potential field tilt—a new concept for location of potential field sources. J. Appl. Geophys. 32, 213–217.

Milligan, P.R., Gunn, P.J., 1997. Enhancement and presentation of airborne geophysical data. AGSO J. Aust. Geol. Geophys. 17, 63–75.

Motta, J. G., Souza Filho, C. R. d., Carranza, E. J. M., and Braitenberg, C., 2019, Archean crust and metallogenic zones in the Amazonian Craton sensed by satellite gravity data: Scientific Reports, v. 9, p. 2565

Moyen, J.F., Martin, H., 2012. Forty years of TTG research. Lithos, 148, 312–336.

Neves, S.P., Vauchez, A., Archanjo, C.J., 1996. Shear-zone controlled magma emplacement or magma-assited nucleation of shear zone? Insights from northeast Brazil. Tectonophysics 262, 349–364.

Neves, S.P., Vauchez, A., Feraud, G., 2000. Tectono-thermal evolution, magma emplacement, and shear zone development in the Caruaru area (Borborema Province, NE Brazil). Precambr. Res. 99, 1–32.

Neves, S.P., Marianoa, G., Beltrão, B.A., Correia, P.B., 2005. Emplacement and deformation of the Cachoeirinha pluton (Borborema province, NE Brazil) inferred through petrostructural studies: constraints on regional strain fields. J. S. Am. Earth Sci. 19, 127–141.

Niiranen, T., Nykänen, V., Lahti, I., 2019. Scalability of the mineral prospectivity modelling – An orogenic gold case study from northern Finland. Ore Geol. Rev. 109 :11-25.

Nykänen, V., Lahti, I., Niiranen, T., Korhonen, K., 2015. Receiver Operating Characteristics (ROC) as validation tool for prospectivity models – a magmatic Ni-Cu case study from the Central Lapland greenstone belt, Northern Finland. Ore Geol. Rev. 71, 853–860.

Norcross, C., Davis, D.W., Spooner, T.C., Rust, A., 2000. U/Pb and Pb/Pb age constraints on Paleoproterozoic magmatism, deformation and gold mineralization in the Omai area Guiana Shield. Precambr. Res. 102, 69–86.

Parra-Avila LA, Belousova E, Fiorentini ML, Eglinger A, Block S, Miller J. 2018. Zircon Hf and O-isotope constraints on the evolution of the Paleoproterozoic Baoule-Mossi domain of the southern West African Craton. Precambrian Res 306: 174–188.

Paterson, S. R., Fowler, T. K., 1993a. Re-examining pluton emplacement processes. J. Struct. Geol. 15, 191-206.

Paterson, S.R., Schmidt, K.L., 1999. Is there a close spatial relationship between faults and plutons? J. Struct. Geol. 21, 1131-1142.

Paterson, S.R., 2005. Close spatial relationship between plutons and shear zones: comment and reply. Geology 33 (1), 72.

Pereira, M.F., Chichorro, M., Moita, P., Santos, J.F., Solá, A.M.R., Williams, I.S., Silva, J.B., Armstrong, R.A., 2015. The multistage crystallization of zircon in calc-alkaline granitoids: U–Pb age constraints on the timing of Variscan tectonic activity in SW Iberia. Int J Earth Sci. 104 (5): 1167-1183.

Perrouty S, Ailleres L, Jessell MW, Baratoux L, Bourassa Y, Crawford B. 2012. Revised Eburnean geodynamic evolution of the gold-rich southern Ashanti Belt, Ghana, with new field and geophysical evidence of pre-Tarkwaian deformations. Precambrian Res 204: 12–39.

Petersson, A., Scherstén, A., Kemp, A.I.S., Kristinsdóttir, B., Kalvig, P., Anum, S., 2016. Zircon U-Pb–Hf evidence for subduction related crustal growth and reworking of Archaean crust within the Palaeoproterozoic Birimian terrane, West African Craton, SE Ghana. Precambr. Res. 275, 286–309.

Pilkington, M., Keating, P.B., 2009. The utility of potential field enhancements for remote predictive mapping. Can. J. Remote Sens. 35 (Suppl. 1), S1–S11.

Plissart, G., Diot, H., Monnier, C., Maruntiu, M., Berger, J., 2012. Relationship between a syntectonic granitic intrusion and a shear zone in the Southern Carpathian–Balkan area (Almaj Mountains, Romania):

Implications for Late Variscan kinematics and Cherbelezu granitoid emplacement. J. Struct. Geol. 39, 83–102

Sánchez, M., Allan, M., Hart, C., Mortensen, J., 2014. Extracting ore-deposit-controlling structures from aeromagnetic, gravimetric, topographic, and regional geologic data in western Yukon and eastern Alaska. Interpretation. 2. SJ75-SJ102. 10.1190/INT-2014-0104.1.

Shirey, S.B., Walker, R.J., 1995. Carius tube digestion for low-blank rhenium-osmium analysis. Anal. Chem. 67, 2136–2141.

Siddorn, J. P., Williams, P. R., Isles, D. J., Rankin, L. R. 2020. Integrated Geologic-Geophysical Interpretation of District-Scale Structural Frameworks: Systematic Approaches for Targeting Mineralizing Systems. Reviews in Econ. Geol. 21, 271–313

Stacey, J.S., Kramers, J.D., 1975. Approximation of terrestrial lead isotope evolution y a two-stage model. Earth Planet. Sci. Lett. 26, 207–221.

Stewart, J. R., Betts, P. G., Collins, A. S., Schaefer, B. F., 2009. Multi-scale analysis of Proterozoic shear zones: An integrated structural and geophysical study. J. Struct. Geol. 31(10), 1238-1254. https://doi.org/10.1016/j.jsg.2009.07.002

Sun, S.S., and McDonough, W.F., 1989, Chemical and isotopic systematics ofoceanic basalts: Implications for mantle composition and processes. Geol. Soc. Spec. Publi 42, 313–345.

Tedeschi, M., Hagemann, S.G., Davis, J., 2018a. The Karouni Gold Deposit, Guyana, South America: part I. Stratigraphic Setting and Structural Controls on Mineralization. Econ. Geol. 113, 1679–1704.

Thébaud, N., Sugiono, D., LaFlamme, C., Miller, J., Fisher, L., Voute, F., Tessalina, S., Sonntag, I., & Fiorentini, M., 2018. Protracted and polyphased gold mineralisation in the Agnew District (Yilgarn Craton, Western Australia). Precambr. Res. 310, 291-304.

Théveniaut, H., Freyssinet, Ph., 2002. Timing of lateritization on the Guiana Shield: Synthesis of paleomagnetic results from French Guiana and Suriname. Palaeogeogr. Palaeoclimatol. Palaeoecol. 178. 91-117. 10.1016/S0031-0182(01)00404-7.

Verduzco, B., Fairhead, J.D., Green, C.M., MacKenzie, C., 2004. New insights into magnetic derivatives for structural mapping. The Leading Edge 23, 116–119.

Voicu, G., Bardoux, M., Jébrak, M., Crépeau, R., 1999. Structural, Mineralogical, and Geochemical Studies of the Paleoproterozoic Omai Gold Deposit, Guyana. Econ. Geol. 94, 1277–1304.

Völkening, J., Walczyk, T., Heumann, K.G., 1991. Osmium isotope determinations by negative thermal ionization mass spectrometry. Int. J. Mass Spectrom. 105, 147–159.

Vanderhaeghe, O., Ledru, P., Thiéblemont, D., Egal, E., Cocherie, A., Tegyey, M., Milési, J.-P., 1998. Contrasting mechanism of crustal growth: Geodynamic evolution of the Paleoproterozoic granite–greenstone belts of French Guiana. Precambr. Res. 92, 165–193.

Weinberg, R.F., Sial, A.N., Mariano, G., 2004. Close spatial relationship between plutons and shear zones. Geology 32 (5), 377-380.

Wyborn, L.A.I., Heinrich, C.A., Jaques, A.L., 1994. Australian Proterozoic Mineral Systems: Essential Ingredients and Mappable Criteria. Australasian Institute of Mining and Metallurgy Annual Conference, Melbourne, pp. 109–115.

Wyman, D.A., Cassidy, K.F., Hollings, P., 2016. Orogenic gold and the mineral systemsapproach: resolving fact, fiction and fantasy. Ore Geol. Rev. 78, 322–335.

Supplementary material: *tables 2 and 3*

Table 3-2 Results of U-Pb-dating.

grain	^{207}Pb[a] (cps)	U[b] (ppm)	Pb[b] (ppm)	Th[b] U	^{206}Pbc[c] (%)	^{206}Pb[d] / ^{238}U	±2s (%)	^{207}Pb[d] / ^{235}U	±2s (%)	^{207}Pb[d] / ^{206}Pb	±2s (%)	rho[e]	^{206}Pb / ^{238}U	±2s (Ma)	^{207}Pb / ^{235}U	±2s (Ma)	^{207}Pb / ^{206}Pb	±2s (Ma)	conc.[f] (%)
a251	281477	470	208	0,49	0,29	0,39310	2,9	7,2	3,0	0,1328	0,7	0,97	2137	53	2136	27	2136	12	100
a252	87414	148	66	0,65	0,52	0,39190	2,5	7,142	2,6	0,1322	0,6	0,97	2132	46	2129	24	2127	10	100
a253	79490	135	61	0,68	0,24	0,39470	2,6	7,203	2,6	0,1324	0,5	0,98	2144	47	2137	24	2130	9	101
a254	322633	516	226	0,41	0,30	0,39260	2,7	7,141	2,7	0,1319	0,6	0,98	2135	49	2129	25	2124	10	101
a255	451003	745	310	0,20	0,10	0,39360	2,7	7,233	2,7	0,1333	0,3	0,99	2140	49	2141	24	2141	6	100
a256	206533	347	151	0,47	0,64	0,38950	2,9	7,08	3,1	0,1318	1	0,94	2121	52	2121	28	2122	18	100
a257	88528	145	58	0,01	0,01	0,39210	2,6	7,135	2,6	0,132	0,4	0,99	2133	47	2128	24	2124	8	100
a258	238939	482	207	0,74	0,85	0,37930	4,9	6,815	5,0	0,1303	1,2	0,97	2073	87	2088	45	2102	21	99
a259	259355	476	215	0,58	0,11	0,39240	2,9	7,152	3,0	0,1322	0,8	0,97	2134	53	2131	27	2127	13	100
a260	253835	502	218	0,50	0,26	0,39060	3,9	7,194	3,9	0,1336	0,4	1,00	2126	70	2136	35	2145	6	99
a261	266534	442	197	0,65	1,91	0,37850	2,7	6,853	3,1	0,1313	1,6	0,85	2069	47	2093	28	2116	29	98
a262	241511	377	147	0,51	0,44	0,34150	2,7	6,101	2,9	0,1296	1	0,94	1894	45	1990	26	2092	18	91
a263	215892	450	196	0,44	0,36	0,39070	3,4	7,096	3,6	0,1317	1,1	0,95	2126	62	2124	32	2121	20	100
a264	232006	481	211	0,50	0,85	0,38650	3,1	6,941	3,3	0,1302	1,1	0,94	2107	55	2104	29	2101	20	100
a265	274751	551	243	0,45	0,31	0,39340	2,6	7,175	2,8	0,1323	1,1	0,92	2139	47	2133	25	2128	19	100
a266	300304	541	240	0,52	0,26	0,39150	2,7	7,107	2,8	0,1316	0,6	0,98	2130	50	2125	25	2120	11	100
a267	175230	351	153	1,16	0,60	0,39110	3,0	7,128	3,2	0,1322	1,2	0,93	2128	54	2127	29	2127	20	100
a268	96299	164	78	0,93	0,48	0,39510	2,5	7,234	2,6	0,1328	0,6	0,97	2146	46	2141	23	2135	10	101
a269	162528	265	112	0,35	b.d.	0,39140	2,5	7,164	2,7	0,1328	0,9	0,94	2129	46	2132	24	2135	16	100
a270	236969	405	178	0,59	0,48	0,38920	3,2	7,067	3,3	0,1317	0,6	0,98	2119	58	2120	30	2121	11	100

Spot size = 33µm. $^{206}Pb/^{238}U$ error is the quadratic additions of the within run precision (2 SE) and the external reproducibility (2 SD) of the reference zircon. $^{207}Pb/^{206}Pb$ error propagation (^{207}Pb signal dependent) following Gerdes & Zeh (2009). $^{207}Pb/^{235}U$ error is the quadratic addition of the $^{207}Pb/^{206}Pb$ and $^{206}Pb/^{238}U$ uncertainty.

[a] Within run background-corrected mean ^{207}Pb signal in cps (counts per second).

[b] U and Pb content and Th/U ratio were calculated relative to GJ-1 reference zircon.

[c] percentage of the common Pb on the ^{206}Pb. b.d. = below dectection limit.

[d] corrected for background, within-run Pb/U fractionation (in case of $^{206}Pb/^{238}U$) and common Pb using Stacy and Kramers (1975) model Pb composition and subsequently normalised to GJ-1 (ID-TIMS value/measured value); $^{207}Pb/^{235}U$ calculated using $^{207}Pb/^{206}Pb/(^{238}U/^{206}Pb*1/137.88)$

[e] rho is the 206Pb/238U/207Pb/235U error correlation coefficient.

[f] degree of concordance = $^{206}Pb/^{238}U$ age / $^{207}Pb/^{206}Pb$ age x 100

Table 3-3 LA-ICPMS Lu-Hf isotope data of zircon.

sample	$^{176}Yb/^{177}Hf$ [a]	±2s	$^{176}Lu/^{177}Hf$ [a]	±2s	$^{178}Hf/^{177}Hf$	$^{179}Hf/^{177}Hf$	Sig_{Hf} [b] (V)	$^{176}Hf/^{177}Hf$	±2s [c]	$^{176}Hf/^{177}Hf_{(t)}$ [d]	$eHf_{(t)}$ [d]	±2s [c]	T_{DM2} [e] (Ga)	age [f] (Ma)	±2s	conc.[g]
a251	0,0378	13	0,00126	4	1,46729	0,74026	9	0,281554	28	0,281503	2,8	1,0	2,50	2127	6	100
a252	0,0032	3	0,00008	1	1,46723	0,74022	10	0,281463	27	0,281460	1,3	0,9	2,59	2127	6	100
a253	0,0244	10	0,00075	2	1,46726	0,74007	8	0,281521	26	0,281491	2,4	0,9	2,53	2127	6	100
a254	0,0325	9	0,00098	2	1,46726	0,74015	9	0,281529	32	0,281490	2,3	1,1	2,53	2127	6	100
a255	0,0394	11	0,00113	2	1,46724	0,74015	10	0,281542	30	0,281496	2,6	1,1	2,52	2127	6	100
a256	0,0375	18	0,00110	4	1,46725	0,74021	10	0,281577	26	0,281532	3,8	0,9	2,45	2127	6	100
a257	0,0343	9	0,00103	3	1,46731	0,74015	11	0,281552	37	0,281511	3,1	1,3	2,49	2127	6	100
a258	0,0374	11	0,00108	1	1,46726	0,74013	9	0,281550	29	0,281507	2,9	1,0	2,50	2127	6	100
a259	0,0325	5	0,00096	1	1,46727	0,74021	9	0,281546	30	0,281507	3,0	1,1	2,50	2127	6	100
a260	0,0422	39	0,00116	9	1,46733	0,74017	9	0,281588	34	0,281541	4,2	1,2	2,43	2127	6	100
a261	0,0344	14	0,00102	3	1,46728	0,74016	10	0,281555	28	0,281514	3,2	1,0	2,48	2127	6	100
a262	0,0301	9	0,00092	2	1,46727	0,74020	8	0,281552	26	0,281514	3,2	0,9	2,48	2127	6	100
a263	0,0360	32	0,00096	6	1,46726	0,74022	9	0,281558	37	0,281519	3,4	1,3	2,47	2127	6	100
a264	0,0280	14	0,00077	4	1,46725	0,74025	9	0,281530	31	0,281499	2,7	1,1	2,51	2127	6	100
a265	0,0349	18	0,00099	3	1,46726	0,74028	10	0,281559	26	0,281519	3,4	0,9	2,47	2127	6	100
a266	0,0639	28	0,00167	6	1,46730	0,74016	9	0,281572	32	0,281504	2,9	1,1	2,50	2127	6	100
a267	0,0509	15	0,00133	4	1,46725	0,74004	8	0,281543	29	0,281489	2,3	1,0	2,53	2127	6	100

(a) $^{176}Yb/^{177}Hf = (^{176}Yb/^{173}Yb)_{true} \times (^{173}Yb/^{177}Hf)_{meas} \times (M_{173(Yb)}/M_{177(Hf)})^{b(Hf)}$, $b(Hf) = \ln(^{179}Hf/^{177}Hf_{true} / {}^{179}Hf/^{177}Hf_{measured}) / \ln(M_{179(Hf)}/M_{177(Hf)})$, M=mass of respective isotope. The $^{176}Lu/^{177}Hf$ were calculated in a similar way by using the $^{175}Lu/^{177}Hf$ and b(Yb). Quoted uncertainties (absolute) relate to the last quoted figure. The effect of the inter-element fractionation on the Lu/Hf was estimated to be about 6 % or less based on analyses of the GJ-1 and Plesoviče zircons.

(b) Mean Hf signal in volt.

(c) Uncertainties are quadratic additions of the within-run precision and the daily reproducibility of the zircon GJ-1. Uncertainties for GJ-1 is 2SD (2 standard deviation).

(d) Initial $^{176}Hf/^{177}Hf$ and eHf calculated using the age (Ma), and the CHUR parameters: $^{176}Lu/^{177}Hf = 0.0336$, and $^{176}Hf/^{177}Hf = 0.282785$ (Bouvier et al., 2008).

(e) two stage model age in billion years using the measured $^{176}Lu/^{177}Lu$, the estimated age (Ma), a value of 0.01113 for the average coninental crust (second stage), and a depleted mantle $^{176}Lu/^{177}Hf$ and $^{176}Hf/^{177}Hf$ of 0.03933 and 0.283294 (Blichert-Toft & Puchtel, 2010).

(f) $^{206}Pb/^{238}U$ age for zircon <1.0 Ga, and $^{206}Pb/^{207}Pb$ age for zircon >1.0 Ga. *-intrusion age

(g) degree of concordance (for detrital grains)

Complementary discussion: other intrusive rocks and alteration study

Introduction

This complementary section focuses on intrusive units observed away from the ore zone and not related to the quartz monzodiorite bodies studied in chapter 4. Also, we present here an attempt to compare different samples of altered quartz monzodiorite using the isocon method of Grant (1986) as previously used by Pochon et al., (2017) among others.

Methodology

Petrography

A total of 5 thin sections was manufactured at the GeoRessources laboratory (Nancy, France) on 5 representative samples from historical drillcores in order to produce a petrographic characterisation of intrusions not related to the mineralisation (away from the ore zone). These samples were studied using optical microscopy and scanning electron microscopy (SEM; TESCAN VEGA 3 LM).

Whole-rock analyses of trace and major elements

Whole-rock analyses of trace and major elements are conducted on 20 cm-long half-drillcore samples at the SARM laboratory (CRPG) in Nancy, France. Veins are removed prior to crushing and pulverisation at the GeoRessources laboratory (Nancy, France). Trace elements are analysed by inductively coupled plasma mass spectrometry (ICP-MS) and oxides are analysed by inductively coupled plasma optical emission spectrometry (ICP-OES), (Carignan et al., 2001). Results are presented here for 4 samples of intermediate intrusive rocks, 5 least altered samples of quartz monzodiorite and 3 altered quartz monzodiorite samples, all chosen after careful petrographic studies.

Mass balance using the isocon method

Using whole-rock analyses of trace and major elements of selected altered quartz monzodiorite samples, the isocon method is utilised as a graphical tool to quantify mass and volume changes between most representative samples. Produced with the EASYGRESGRANT Excel spreadsheet program the isocon method developed by Grant (1986), illustrates the mass change due to the mobility of elements during the alteration processes (gain and loss).

Results

Other intrusions

The various intrusion units presented here are not precisely mapped and therefore not visible in the maps of chapters 3 and 4. This section is only based from logging on historical drillcores. Rarely observed at Yaou, a subvolcanic/shallow intrusive rock is encountered with both albite and quartz phenocrysts (Fig. 17A). The groundmass is composed of chlorite, albite, sericite and quartz (Fig. 17B) with some seritisation of albite grains observed (Fig. 17C). Displaying a microcrystalline texture with albite and quartz phenocryststhis unit has a trachy-andesitic geochemical signature when plotted in the Zr/Ti *vs.* Nb/Y diagram of Pearce (1996).

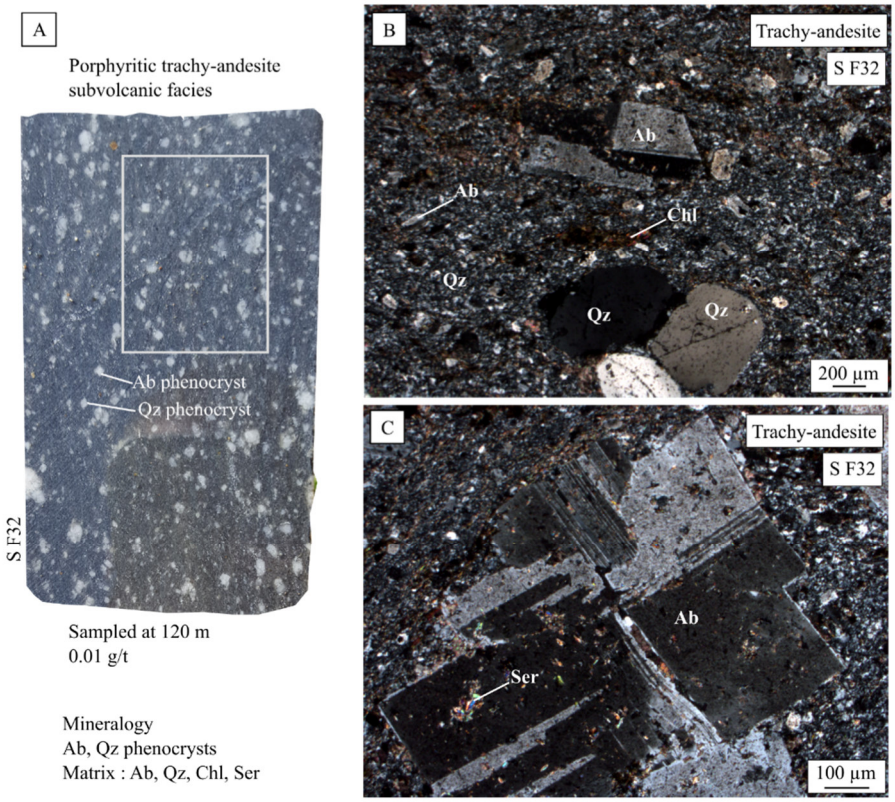

Figure 3-17. Drillcore photography (A) and associated optical microphotographs (B and C) of the subvolcanic unit. (abbreviations: Ab=albite, Qz=quartz, Chl=chlorite, Ser=sericite, Mag=magnetite).

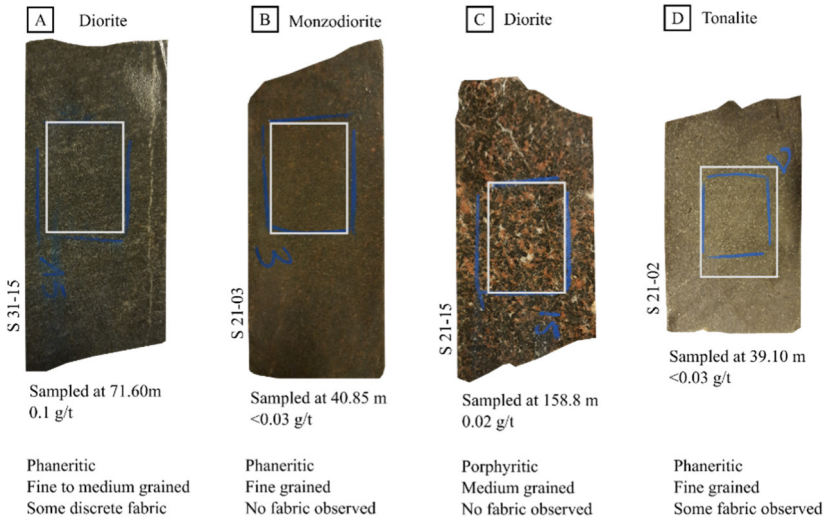

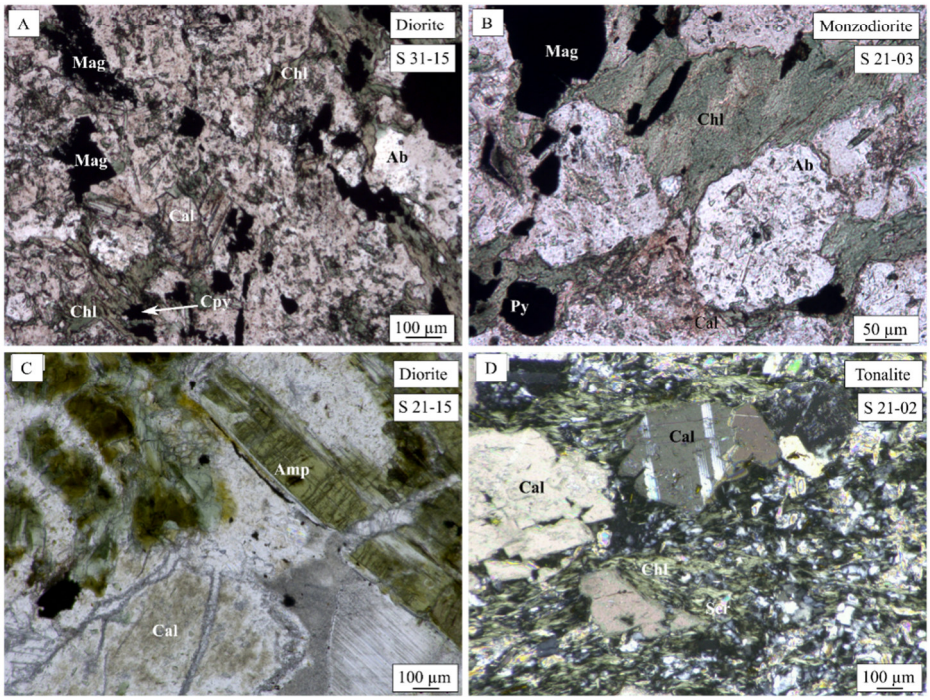

Figure 3-18. Drillcore photographs and associated optical microphotographs of intrusive rock sampled away from the mineralisation. A. Diorite. B. Monzodiorite. C. Diorite. D. Tonalite (abbreviations: Chl=chlorite, Mag=magnetite, Cal=calcite, Ab=albite, Ccp=chalcopyrite, Py=pyrite, Amp=amphibole, Ep=epidote, Ser=sericite).

Away from the mineralisation, examples of other intrusive rocks, observed in the core are presented in Figure 18. We observe a fine to medium grained diorite (Fig. 18A) displaying a discrete fabric with a matrix made of chlorite, magnetite, calcite, plagioclase and albite; a fine grained monzodiorite with no fabric composed of chlorite, albite, calcite, plagioclase and

magnetite (Fig. 18B); a porphyritic, medium grained diorite (Fig. 18C) made of coarse amphibole, epidote, calcite and sericite; but also a fine grained tonalite (Fig. 18D) composed of chlorite, calcite, magnetite and white mica.

Geochemical characterisation and comparison with the quartz monzodiorite samples

As discussed in Chapter 3, all representative samples of the Yaou quartz monzodiorite hosting the auriferous veins plot in the same field in the relatively immobile elements Th *vs* Co graph (Fig. 19A) evidencing a single protolith for all hydrothermally altered facies. The mafic/intermediate rocks presented in the previous section are distinct from the quartz monzodiorite of the Chapter 3. Moreover, as previously mentioned in the chapter 3, these samples plot in the quartz monzodiorite field in the Q-A-P normative classification diagram (Fig. 19B) while the more mafic/intermediate samples are plotting toward the plagioclase feldspar (P) corner. All samples belong to the calc-alkaline series based on the AFM diagram (Irvine & Baragar, 1971), (Fig. 19C) and plot in the arc-related field in the graph by Pearce (1984) using Rb *vs* Yb + Ta (Fig. 19D) to discriminate between fields of Magmatic arc granite, Syn collisional granite, Ocean ridge granite and Within plate granite.

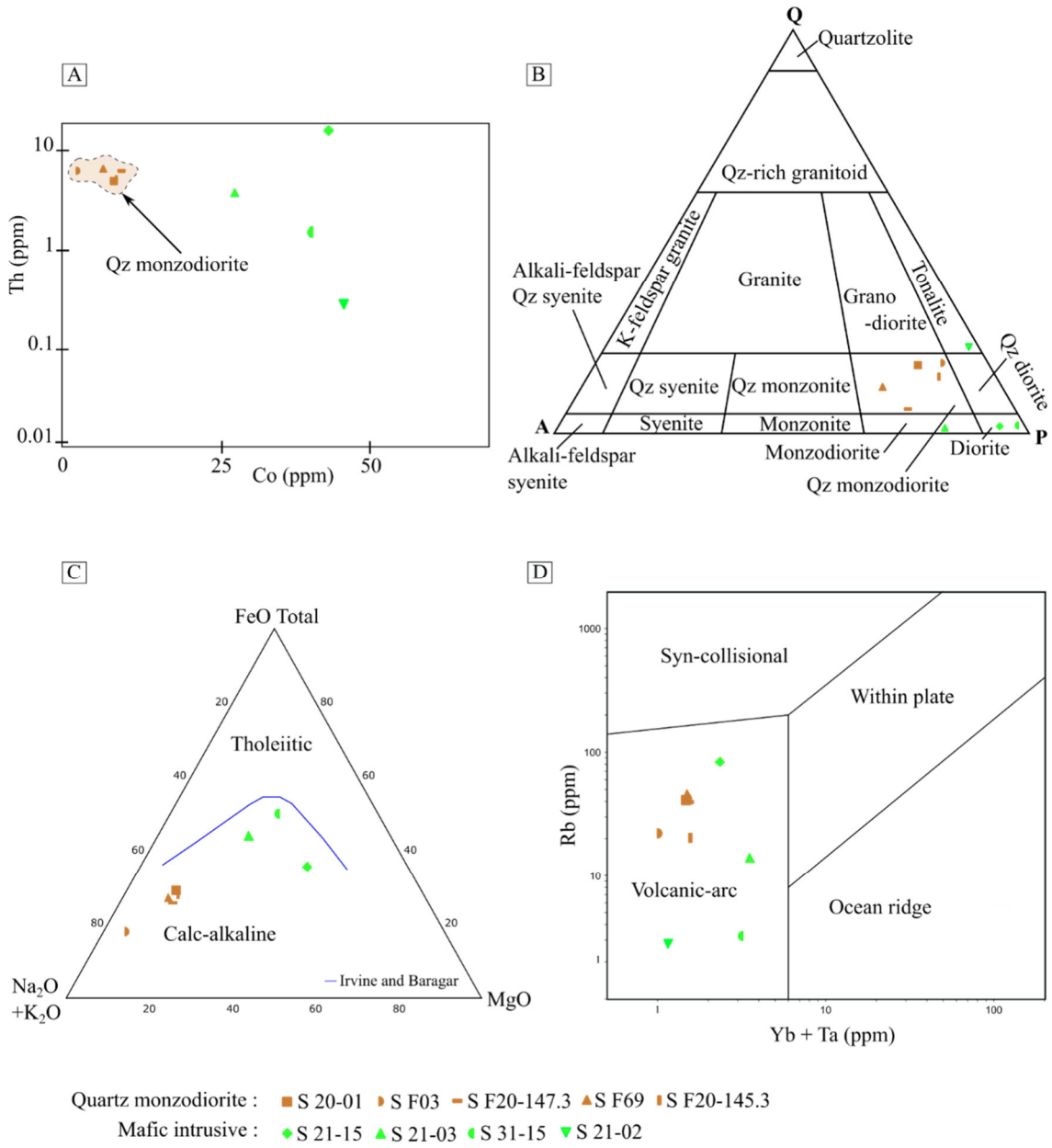

Figure 3-19 Geochemical characterisation of the Yaou quartz monzodiorite (in brown) and other intrusive rocks (in green) with A. Th vs Co graph deciphering the mafic intrusive rocks from the quartz monzodiorite of chapter 4, B. QAP (quartz (Q), Alkali feldspars (A), plagioclase feldspars (P)) graph, C. AFM diagram (Irvine & Baragar 1971) where all samples are plotting in the calc-alkaline field and D. Rb vs Yb + Ta graph of Pearce et al. (1984).

Alteration study of the quartz monzodiorite using the isocon method

Various facies of the same quartz monzodiorite protolith are logged and interpreted as being the result of different hydrothermal alteration intensity and variations of the relative amount of ankerite, hematite, chlorite, albite or sericite. The most representative facies are presented in Figure 20A to 20F. The sample *S 20-01* is considered the least altered (Fig. 19A) even if a some albitisation is identified. It has not been possible to observe an unaltered sample. Are identified:

an albite-dominant sample (Fig. 20B), an albite/chlorite-dominant sample (Fig. 20C), an ankerite/hematite-dominant sample near D_{4YA} veins (Fig. 20D), a chlorite/hematite-dominant sample (Fig. 20E) and an albite/sericite dominant sample (Fig. 20F).

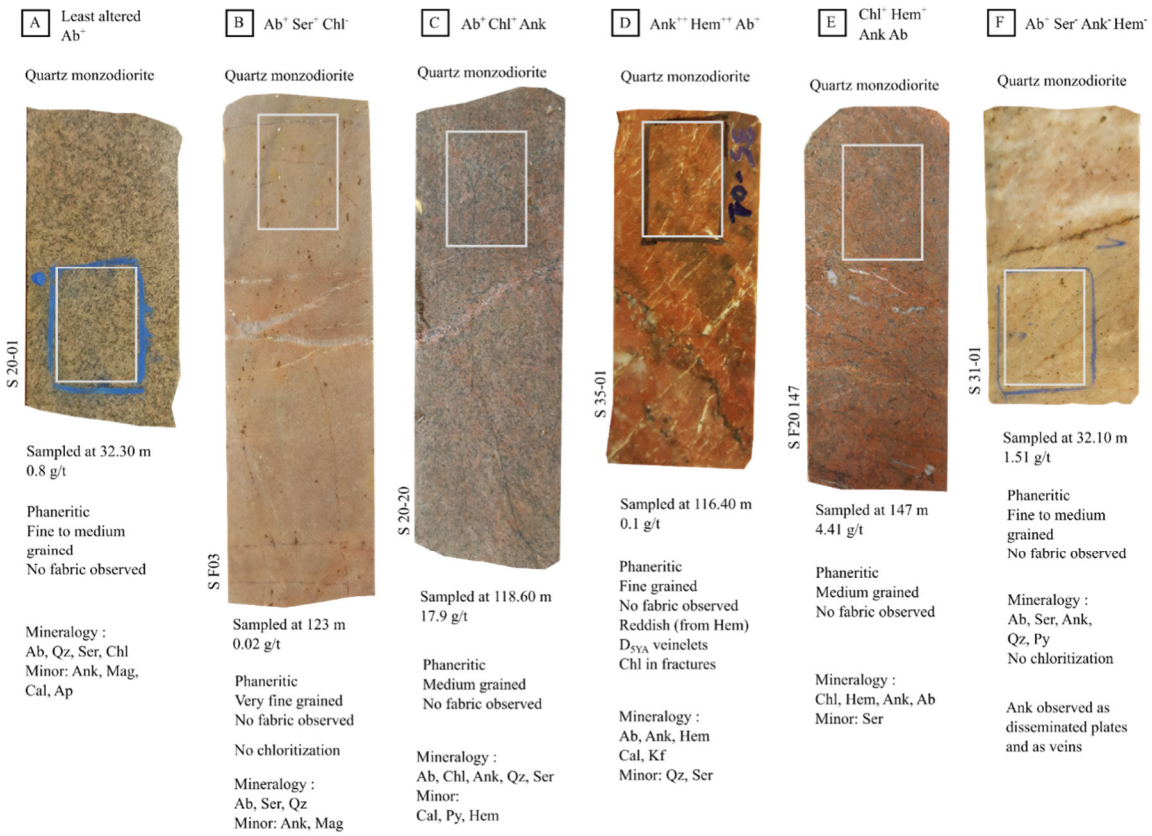

Figure 3-20 Overview of most representative alteration facies on drillcore

Following the petrographic study, selected samples are analysed for whole rock geochemistry. First, using the Hughes (1972) diagram, least altered samples are identified within the igneous spectrum (Fig. 21), near the limit with the Na-altered field. It correlates with the ones identified by petrographic observations displaying some albitisation. Three samples are in the upper left corner suggesting that they have been altered by addition of sodium.

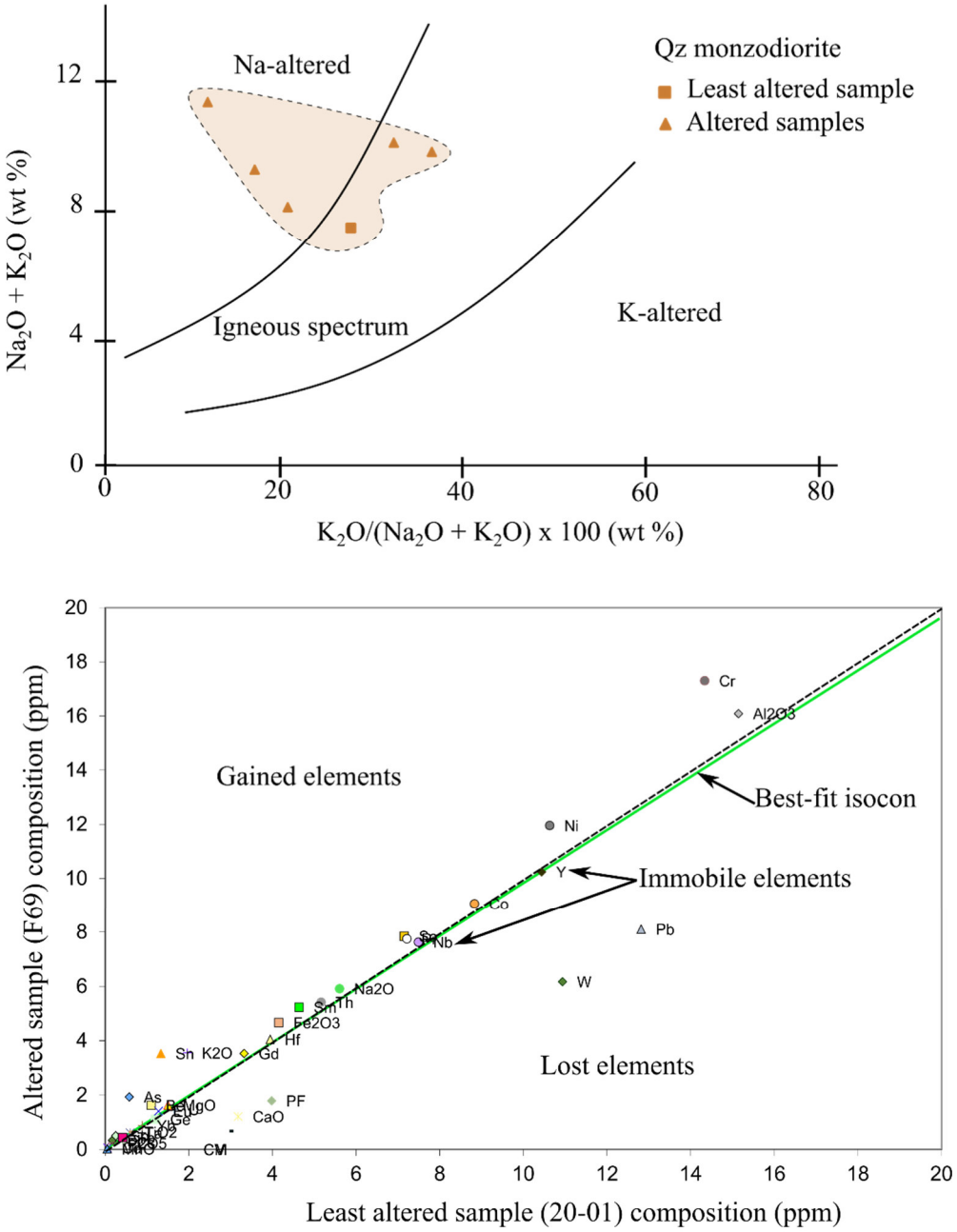

Figure 3-21 Geochemical graph of Hughes (1972) showing the Na-alteration of samples and least altered ones, and one example of isocon diagram comparing the least altered sample with an altered sample from the same quartz monzodiorite (green line= isocon, dotted black line= constant mass line).

The isocon diagram presented in Figure 21 is comparing the least altered sample with an altered sample from the same quartz monzodiorite. Elements on the dotted line through the origin have a similar geochemical behaviour with a constant mass. We define our isocon as the best-fit line

along elements considered as immobile such a Hf, Nb, Th and Y. Following the method of Grant (1986), the elements above the isocon are gained while the ones below the line are lost elements. As previously mentioned, a certain degree of alteration is present in the least altered sample and therefore the method is not working well here. Indeed, almost no gain or loss is illustrated. Nevertheless, our isocon shows that alteration is associated with (1) a very weak mass gain in Na_2O, K_2O, Cr, Ni, Sn and As; and (2) a weak mass loss in W, Pb and CaO. Overall, no significant mass change is highlighted for all tested samples.

Discussion and conclusions

Apart from the quartz monzodiorite hosting the auriferous veins, minor other intrusive rocks are observed, some being older than the intrusion as evidenced by the presence of some inherited fabrics (S_2?). Their geochemical signature is different from the quartz monzodiorite and could be assimilated to mafic input during the mesorhyacian juvenile arc formation (Delor et al., 2003).

The fact that these units are not hosting the D_{4YA} veins may be explained by their rheology (possibly less easily fractured; the diorite intrusions are possibly more sheared and altered by chlorite and thus less competent than the quatz monzodiorite bodies). As this thesis focuses on the mineralisation, no further work has been carried out here.

Regarding the isocon graphical characterisation, the results from this work is very limited (a discret gain in Na and K is possible considering the observed albitisation and seritisation), the mass balance study is biased as no truly unaltered rock is considered. It needs further findings and sampling of unaltered samples.

References

Carignan, J., Hild, P., Mévelle, G., Morel, J., Yeghicheyan, D., 2001. Routine analyses of trace elements in geological samples using flow injection and low pressure online liquid chromatography coupled to ICP-MS: a study of reference materials BR, DR-N, UB-N, AN-G and GH. Geostand. Newsl. 25, 187–198

Grant, J.A., 1986. The isocon diagram-a simple solution to Gresens' equation for metasomatic alteration. Econ Geol. 81, 1976-1982.

Hughes, D.J., 1972. The petrochemistry of the Ordovician igneous rocks of the Welsh Basin-a review. Proc. Geol. Soc. London. 128, 418.

Irvine TN, Baragar WRA., 1971. A guide to the chemical classification of the common volcanic rocks. Can J Earth Sci. 8, 523–548.

Pearce, J.A., Harris, N.B.W., Tindle, A.G., 1984, Trace element discrimination diagrams for the tectonic interpretation of granitic rocks. J of Petrology. 25, 956-983.

Pochon, A., Beaudoin, G., Branquet, Y., Boulvais, P., Gloaguen, E., Gapais, D., 2017. Metal mobility during hydrothermal breakdown of Fe-Ti oxides: insights from Sb-Au mineralizing event (Variscan Armorican Massif, France). Ore Geol. Rev. 91, 66-99.

Chapitre 4

Diversité des expressions de l'or supergène dans les latérites aurifères du prospect de Couriège, Guyane.

Résumé en français

En Guyane française, l'altération intense des gisements d'or primaires modifie la composition, la texture et la distribution de l'or hypogène. Le prospect de Couriège fournit un cas d'étude de la diversité de la distribution de l'or liée aux processus supergènes, illustrée le long de deux profils d'altération, à savoir les profils Achman Giraud et Lupe.

Dans le profil Achman Giraud, l'altération se développe sur un protolithe d'amphibolite portant des veines de quartz aurifères, et présentant une séquence verticale authigénique composée d'un bedrock, une saprolite fine, un horizon d'argiles tachetées et d'un latosol. Dans la saprolite, l'amphibolite altérée en contact avec la veine contient de l'or jusqu'à 5 ppm. Des grains d'or libre primaires sont observés au sein et à proximité de la veine. Ils présentent des caractéristiques de dissolution modérées mais croissantes de la saprolite au latosol, avec de rares sphérolites d'or secondaires sur les surfaces des grains primaires. Les grains de pyrite goethitisés présentent des micro-inclusions d'or de haute finesse interprétées comme supergène. Le caractère primaire de la plupart des grains d'or et la faible variabilité des teneurs en or plaident cependant pour une faible remobilisation supergène de l'or.

Le profil de Lupe est caractérisé par un horizon allogénique enrichi en or libre tronquant un profil latéritique stérile. Dans l'horizon détritique, l'or est présent sous forme de grains d'électrum dans des grains de pyrite détritiques partiellement oxydés, en association avec des inclusions de Bi et de la goethite contenant du Te. La grande taille et le caractère angulaire des clastes indiquent un transport limité et une exposition à l'altération latéritique du matériel allogénique, témoignant d'une source d'or relativement proximale. En revanche, la couverture transportée contient également des grains d'or libres qui présentent une forme sub-arrondie, des marques de transport mécanique en surface et des bordures appauvries en Ag, suggérant un transport et une latéritisation sur une distance et un temps important.

L’étude de la chimie de l'or, de la morphologie et l'association minérale permet d’évaluer la variabilité des types d'or primaires et l'influence des processus supergènes dans leur modification. En résulte une caractérisation relativement complexe de la distribution de l'or dans le régolithe de Couriège, comprenant (i) de l'or primaire préservé de l'altération sous forme d'or libre dans les horizons allogéniques et authigènes, des inclusions d'électrum dans la pyrite détritique dans l'horizon allogénique et (ii) de l’or supergènes comme les sphérolite sur la surface des grains d'or libre, les bordures appauvri en Ag des grains d'or libres allogéniques ou les micro-inclusions appauvries en Ag dans la pyrite oxydée proximale des veines de quartz aurifères. La faible influence des processus d'altération *in situ* sur la redistribution et la concentration d'or résulte à la fois de la faible mobilité chimique de l'or et du manque d'enrichissement résiduel significatif lors de la latéritisation. Par conséquent, le ciblage des halos de dispersion chimique à la surface à partir de l'échantillonnage des sols authigènes peut ne pas s'avérer efficace. Au contraire, comme l'érosion conduit à la remobilisation physique de l'or, les anomalies allogéniques d'or dans les sols ne sont pas indicatives de la minéralisation sous-jacente, mais peuvent aider à retracer leur source d'origine. La détermination de la nature authigénique ou allogénique des anomalies aurifères dans les levés de sol est donc essentielle pour l'exploration aurifère dans les zones de prospection en domaine latéritique.

Publication #3

(Submitted 02/2021 in the Geological Society London- Special Publication)

Diversity of supergene gold expressions within gold-bearing laterites at the Auplata Mining Group's Couriège exploration prospect, French Guiana

Vincent Combes[1, 2, *], Yoram Teitler[1], Aurélien Eglinger[1], Anne-Sylvie Andre-Mayer[1], Arnauld Heuret[3], Anthony Pochon[4], Michel Cathelineau[1], Pierre Gibert[2]

[1]Université de Lorraine-CNRS, CREGU, laboratoire GeoRessources, 54500 Nancy, France
[2]AMG, Auplata Mining Group, ZI Dégrad des Cannes, 97354, Rémire Montjoly, France
[3]Université de Guyane / Géosciences Montpellier (UMR 5243), 97300 Cayenne, France
[4]Institut des Sciences de la Terre d'Orléans (ISTO) UMR 7327, Université d'Orléans - CNRS - BRGM, Campus Géosciences, 1A rue de la Férollerie, 45071 Orléans, Cedex 2, France

* corresponding author (vincent.combes@univ-lorraine.fr)

Abstract

In French Guiana, the intense weathering of primary gold deposits modifies the composition, texture, and distribution of hypogene gold. The Couriège prospect provides good examples of the diversity of gold distribution related to supergene processes, well-illustrated along two weathering profiles, namely the Achman Giraud and the Lupe profiles. In the Achman Giraud profile, weathering develops on an amphibolitic protolith crosscut by Au-bearing quartz veins, and exhibit an authigenic vertical sequence including bedrock, saprolite, mottled clay and latosol. In the saprolite, the weathered amphibolite in contact with the vein contains gold up to 5 ppm. Primary free gold grains are observed within and proximal to the vein. They exhibit moderate but increasing dissolution features from the saprolite to the latosol, together with the formation of rare, secondary gold spherolite overgrowths on primary grain surfaces. Pyrite grains when replaced by goethite display *in situ* gold micro-inclusions of high fineness interpreted as supergene. The primary character of most gold grains and the low variability of

gold grades argue, however, for weak supergene remobilisation of gold. In the Lupe profile, an allogenic horizon enriched in free gold truncates a barren laterite profile. In the detrital horizon, gold is present as electrum grains within cm-large, partly oxidised, detrital pyrite crystals, in association with dusty Bi inclusions and Te-bearing goethite. The large size and angular character of clasts are indicative of limited transport and exposure to weathering of the allogenic material, witnessing a relatively proximal Au source. Contrastingly, the transported cover also contains free gold grains that exhibit sub-rounded shape, mechanical transportation marks on surfaces and Ag-depleted rims, suggesting transport and exposure to weathering over significant distance and time. Gold chemistry, morphology, and mineral association help to assess the variability of primary gold types and the influence of supergene processes in their modification. This yields to a relatively complex picture of Au distribution within the Couriège regolith, including (i) primary gold preserved from weathering as free gold in both allogenic and authigenic horizons, electrum inclusions in detrital pyrite in the allogenic horizon and (ii) supergene-related secondary gold such as the rare spherulite on free gold grain surface, the Ag-depleted rim of allogenic free gold grains or the Ag-depleted micro-inclusions in oxidised, authigenic pyrite proximal to Au-bearing quartz veins. The weak influence of in-situ weathering processes on the redistribution and concentration of gold results both the low chemical mobility of gold and the lack of significant residual enrichment during lateritisation. Consequently, targeting chemical dispersion haloes at surface from the sampling of authigenic soils may not prove successful. Rather, as erosion leads to the physical remobilisation of gold, allogenic gold anomalies in soils are not indicative of underlying mineralisation but may help to trace back their original source upslope. The determination of the authigenic or allogenic nature of gold anomalies in soil surveys is therefore critical for gold exploration in the prospect area as well as in deeply weathered environments in general.

Keywords: supergene gold, goethite, pyrite, lateritic profile, saprolite, French Guiana

Introduction

The Guiana Shield (Fig. 1A) in South America, is an important mineral province hosting significant gold resources which are attractive for the exploration of gold deposits (Voicu et al., 2001; Milesi et al., 2003; Daoust et al., 2011; Velasquez et al., 2014; Tedeschi et al., 2018a; Guiraud et al., 2020, Combes et al., 2021). However, due to its low latitude geographic position, the Guiana Shield is covered mainly by well-developed lateritic regolith and equatorial rainforest, representing a challenging environment for exploration (Freyssinet et al., 1989, 2005; Butt et al., 2000; Anand and Butt, 2010; Theveniaut and Freyssinet, 2002; Butt, 2015; Sunkari et al., 2019). Supergene processes can either hinder or modify primary (i.e., hypogene) gold resources (Anand et al., 2002; Chardon et al., 2018; Anand et al., 2019; Sawadogo et al., 2020) through weathering, erosion and pedimentation. In particular, the impact of weathering and laterite formation on primary gold commonly leads to the formation of secondary Au resources (Craw et al., 2015; Craw & Kerr, 2017 and references therein). Such resources are economically profitable as they represent easily accessible targets because they consist of poorly consolidated material that is readily mineable. Also, the release of gold from sulphides in these oxidised formations yield locally significant increase of gold grades.

Lateritisation processes are associated with active gold remobilisation through dissolution-reprecipitation, grain coarsening and increase in fineness with the formation of Ag-poor rims (Colin and Lecomte, 1989; Freyssinet et al., 1989; Collin et al., 1991; Bamba et al., 2002; Larizatti et al., 2008; Falconer and Crow, 2009; Fairbrother et al., 2012). Experimental studies confirm that, under these conditions, gold is dissolved and transported as gold chloride and thiosulfate complexes (Benedetti & Boulègue, 1991; Pokrovski et al., 2014; Perera et al., 2005; Zotov et al., 2018). The rate of gold dispersion remains, however, somewhat limited but insufficiently known (Bowell et al., 1993; Vishiti et al., 2015; Horbe et al., 2019). Understanding the influence of supergene processes on gold mobility is, therefore, of critical importance for the exploration of gold resources in regolith-dominated terranes, in particular in French Guiana.

In French Guiana, gold occurs in orogenic gold deposit hosted by greenstone belts (Milesi et al., 2003; Combes et al., 2021). This region is submitted since Cretaceous times to equatorial climate and underwent significant weathering as lateritic fronts. The relative impact of

weathering on primary gold ore remains poorly studied at the scale of the lateritic profile,

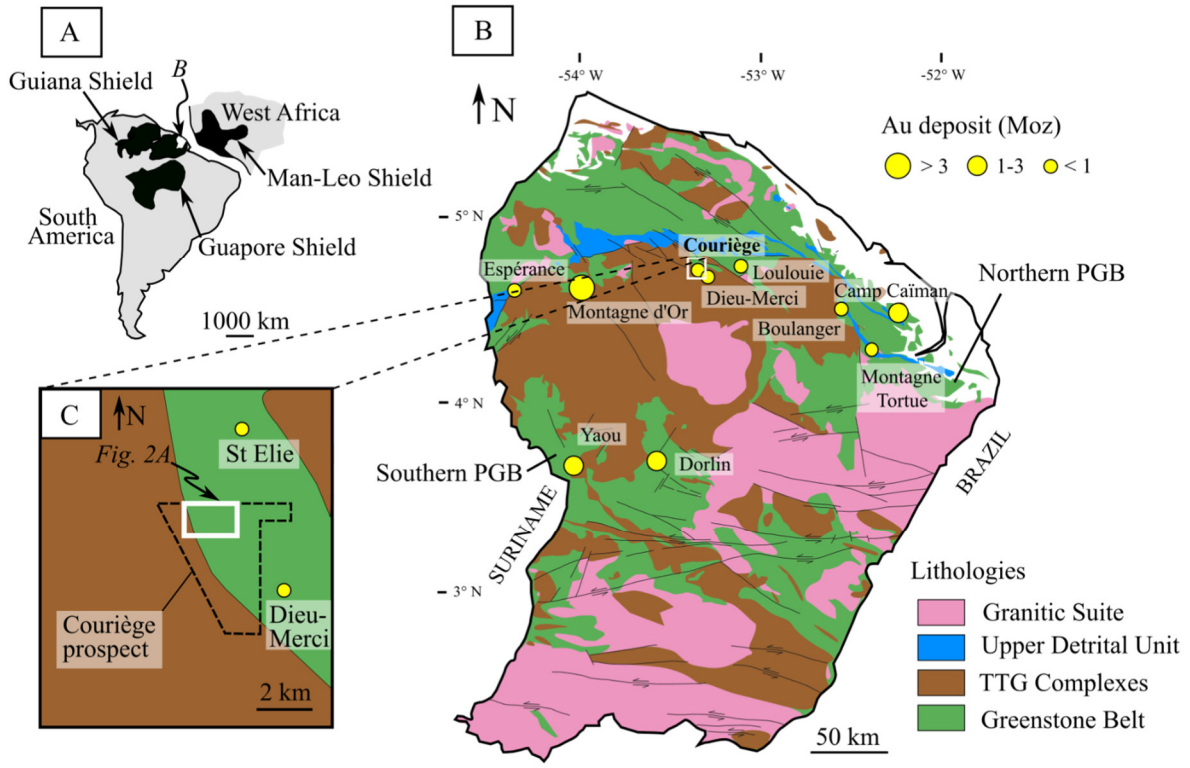

Figure 1 (A). Simplified overview of the Precambrian shields located in South America and Western Africa namely the Guapore Shield, the Man-Leo Shield, and the Guiana Shield. (B). Map of simplified Paleoproterozoic formations located in French Guiana (modified from Delor et al., 2003b; Eglinger et al., 2020). (C). Couriège prospect lithology map. The deposit is located at the contact between the northern Paramaca greenstone belt and the central TTG complex.

encouraging a detailed study of laterite profiles developed on areas where primary gold-ores are known within the bedrock. The Couriège prospect in French Guiana provided excellent conditions of sampling of such profiles. Two Au-bearing lateritic profiles were selected for the diversity of their supergene gold expressions (residual *vs* transported), (Fig.1B and C). Laterite profiles were therefore studied to (1) document the mineralogical and geochemical changes associated with the lateritisation processes, (2) assess the scale of the vertical and lateral gold dispersion from auriferous veins, (3) evaluate the compositional and morphological evolution of gold grains during weathering and (4) discuss the supergene processes involved during lateritisation. Particular attention was devoted to the *in situ* distribution of gold in the poorly consolidated latosols, mottled and saprolite horizons, which represent important targets for lateritic gold exploration within the Guiana Shield (Dardenne & Schobbenhaus, 2003).

Regional geology

The geologic environment of the Couriège prospect, owned by AMG (Auplata Mining Group), is intimately related to the Trans-Amazonian orogeny. The Trans-Amazonian cycle begins with an Eorhyacian oceanic stage (ca. 2.26-2.20 Ga) between the West African and North Amazonian Archean cratons (Vanderhaeghe et al., 1998; Delor et al., 2003a, b). The closure of this domain by subduction during the Mesorhyacian (ca. 2.18-2.13 Ga) induces the emplacement of TTG-type intrusions related to magmatic arcs. Volcano-sedimentary formations are also developed during the subduction-related D_1 deformation phase (Ledru et al., 1991; Milési et al., 1995; Vanderhaeghe et al., 1998; Delor et al., 2003a, b). The end of the subduction process is marked by the tectonic accretion of the different sets of magmatic arcs and the closure of the volcano-sedimentary basins during the Neorhyacian period (ca. 2.11-2.08 Ga) with regional scale sinistral strike-slip faults referred as the D_{2a} stage (Delor et al., 2003a, b). These transcurrent tectonic events allow the development of late extensional basins (Ledru et al., 1991) filled by detrital sediments (the Upper Detrital Unit; Fig. 1B) during a D_{2b} deformation phase (2.07-2.05 Ga) marked by crustal stretching and metaluminous to peraluminous granites emplacement (Vanderhaeghe et al., 1998; Delor et al., 2003a, b).

To sum up, the geological formations outcropping and then weathered in French Guiana can be divided into five lithotectonic units (Vanderhaeghe et al., 1998; Delor et al., 2003a, b and references therein), namely (1) the “Ile de Cayenne” complex witnessing a potential juvenile oceanic crust, (2) the Paramaca Greenstone Belts characterised by volcano-sedimentary sequences, (3) the TTG complexes represented by tonalite-trondhjemite-granodiorite suites, (4) the Upper Detrital Unit dominated by conglomerates, pelites and sandstones and (5) the metaluminous to peraluminous granites.

Within this tectono-lithological framework, four types of gold-bearing deposits are currently identified: (1) Au-rich VMS (Volcanogenic Massive Sulphide) deposit as characterised by Franklin et al. (2000) and Guiraud et al. (2017, 2020) at Montagne d’Or; (2) stratiform/stratabound gold-bearing tourmalinites with disseminated sulphides as observed at Dorlin (Milesi et al., 2003) with an overprinting of late orogenic gold mineralisation dated at ca. 2.06 Ga (Marcoux and Milési, 1993); (3) gold-bearing polygenic conglomerates hosted by the Upper Detrital Unit, exampled at Montagne Tortue (Milesi et al., 1995) where the mineralisation is multi-stage with an orogenic gold overprinting expressed by quartz-

tourmaline veining (Milesi et al., 2003) and (4) orogenic gold deposits as observed at Yaou, Esperance, Loulouie, Boulanger and Camp Caïman (Milesi et al., 2003). In this latter deposit-type, mineralisation mainly consists of visible gold (e. g., micro-inclusions in sulphides and free gold) as exampled at the Yaou deposit (Combes et al., 2021). This primary (hypogene) gold resource only represents a fraction of the global gold resource in French Guiana. Indeed, according to Picot & Chevillard (2015), alluvial placers resources could represent about 167 tons of gold while laterite-bearing and primary gold would account for 210 tons of gold altogether. Also, it is worth noticing that, as previously mentioned by Voicu et al. (2001), average Au grades are ranging between 1.3 and 2.3 g/t Au for most gold deposits of the Guiana Shield considering both primary and secondary types gold, the contribution of each types being unstudied in the region.

The formation of lateritic and placer gold deposits in French Guiana and more generally across the Guiana Shield is assumed to be related to the recent (i.e. Phanerozoic) geomorphological and weathering history that shaped the modern landscape of the region (Theveniaut and Freyssinet, 2002). Lateritisation and erosion-transport processes affected primary gold occurrences and deposits, resulting in the development of deeply weathered gold-bearing regolith and placers, respectively. Across French Guiana, Theveniaut and Freyssinet (2002) recognised a succession of lateritisation and erosion phases associated with the formation of secondary gold deposits, including: (1) early (Paleocene-Eocene) lateritic weathering corresponding to the Sul Americano lateritisation cycle at ca. 50-40 Ma resulting from the warm and perhumid conditions that prevailed during the Paleocene–Eocene Thermal Maximum (PETM); (2) a substantial erosion period during the Oligocene, at ca. 30-23 Ma; and (3) a late Miocene lateritisation event, known as the Late Velhas cycle at ca. 13-5 Ma. Regarding the time scale of lateritisation, Freyssinet & Farah (2000) estimated, along with a lateritic profile at Yaou, a saprolitisation and a latosol development rate of 7.5 and 4.5 m/Ma, respectively, thus resulting in a chemical thickening rate of 3 m/Ma. Girard et al. (1997, 2000) propose, from oxygen and hydrogen isotopic composition of goethite and kaolinite in laterites from Yaou, a change in climatic regime from tropical wet and dry (seasonal) in the past (possibly as old as Upper Jurassic or Cretaceous) to equatorial in the present day.

So far, no real constraints exist on the age of lateritic gold deposits in French Guiana, although they are presumably related to the Sul Americano and the Late Velhas lateritisation periods and formed from residual accumulations of gold during the Eocene to the Late Tertiary (Miocene-

Pliocene) (Dardenne & Schobbenhaus, 2003). Although Costa et al. (1993) highlighted that supergene enrichment has been essential for increasing the gold concentration at the Cassiporé deposit in NE Brazil, it is not clearly demonstrated that the contribution of supergene processes is of major importance in upgrading the primary gold budget in the Guiana region.

The Couriège prospect is located in the Northern Paleoproterozoic Paramaca Greenstone Belt in French Guiana (Fig. 1B), more precisely at the contact between the Lower Volcano-sedimentary unit (Paramaca) at the East and the Central TTG complex at the West (Fig. 1C).

Prospect-scale geology and topography

The Couriège prospect is located within the St Elie district, with at the East the Dieu-Merci concessions (Fig. 1C) characterised by subvertical pyrite-rich shear veins are spatially associated with subhorizontal extensional veins (Auplata Mining Group internal reports). They display similar features than those described in the nearby Devis and Michel zones (St Elie district), (Lafrance et al., 1999) where Au-bearing quartz veins are associated with ductile shear zones. The Couriège area is an exploration-only tenement, explored since the 1990s by Guyanor and later by Auplata Mining Group with indications of a 3 km-long mineralised zone with discontinuous, 2 to 15 m large orebodies that coincide with the presence of dismantled, subhorizontal, Au-bearing quartz±pyrite veins at the subsurface, that can be classified as orogenic gold. The elevation of the Couriège prospect is moderate and ranges from 56 m to 225 m above sea level (AMG Digital Elevation Model). Morphology includes dissected ferricrete plateaus, flattened hills, landslides, together with alluvial plains that host placer gold resources (Fig. 2A and B). Although no comprehensive regolith mapping is available in the prospect area, a preliminary analysis of the topographic context at the prospect-scale is proposed, based on the identification of planation surfaces from Digital Elevation Model (Fig. 2A). In the prospect area, topographic transects indicate that the highest relief corresponds to a single hill (referred to the Lupe Hill) with a maximum elevation of about 225 m above sea level. The top of the Lupe Hill is the relict of an old, now dismantled, duricrust surface (S1), as supported by local exposures of residual ferricrete (Fig. 2B). Geomorphology transects revealed two other planation surfaces at intermediate elevations. The S2 surface corresponds to the top

of flat hills at altitudes of about 130-140 m; it is not clear whether this surface represents

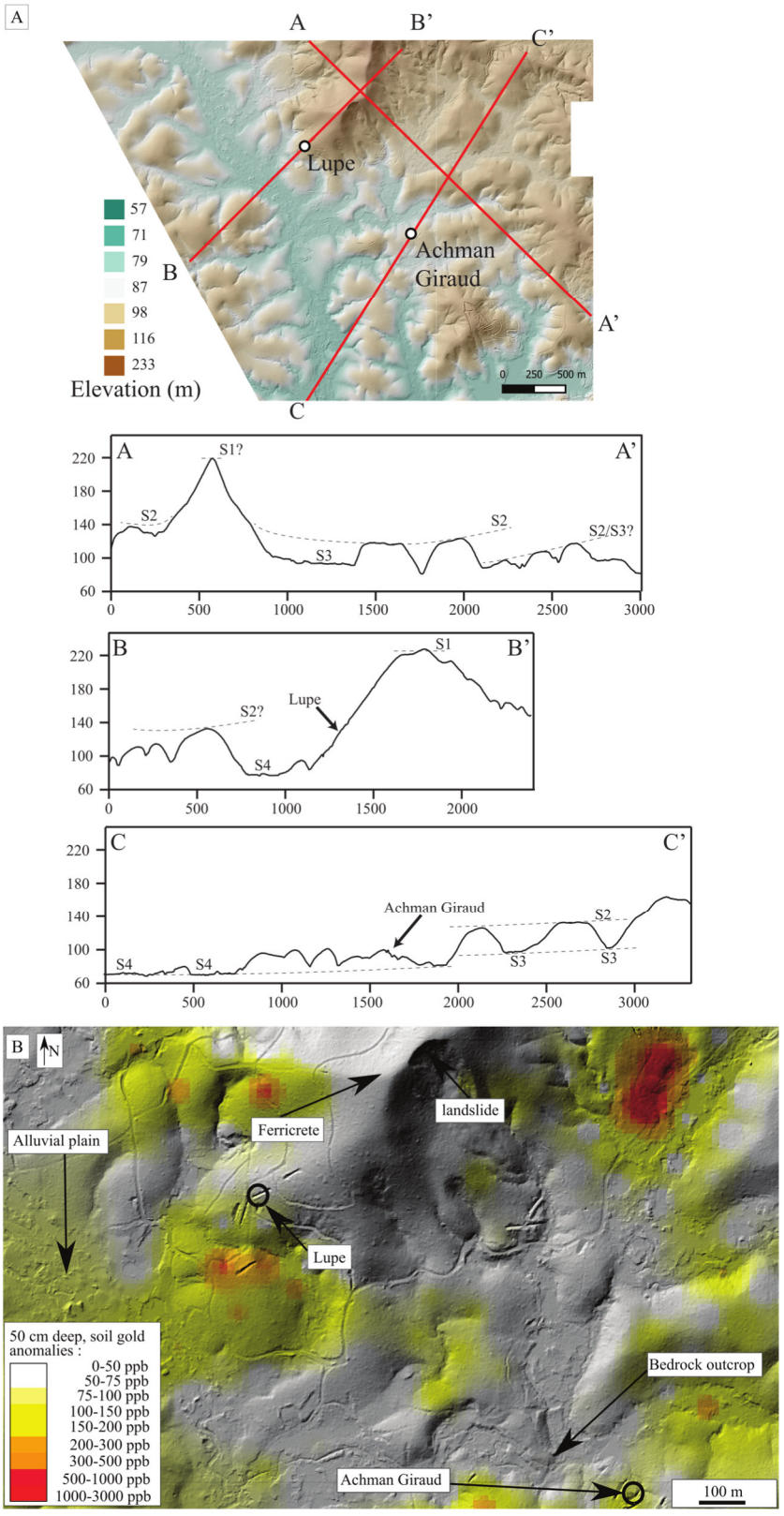

Figure 2 (A). Digital Elevation Model of the NW part of the Couriège tenement with locations of the two studied sites (Achman Giraud and Lupe) and cross-sections highlighting the geomorphology of the prospect characterised by moderate variations in elevation with

dissected ferricrete plateaus, flattened hills, landslides, and alluvial plains. Interpreted surface S1: a relic of an old, now dismantled duricrusted surface, S2: top of flat hills remnants of duricrusted plateaus (in situ) or ancient glacis surface, S3: the alluvial plain of an almost closed, kilometric watershed and S4: the main active alluvial plain. (B). Soil gold anomalies distribution in the studied area with locations of Lupe, Achman Giraud and the sampled bedrock outcrop.

remnants of duricrust plateaus formed *in situ* from chemical weathering only, or whether it corresponds to an ancient glacis surface. The S3 surface corresponds to the alluvial plain of an almost closed, kilometric watershed located in the northeastern part of the prospect, at an elevation of about 100 m (Fig. 2A), only connected to (yet not levelled with) the main watershed through a narrow, stepped exutory. The S4 surface corresponds to the main watershed alluvial plain representing the active pediplanation surface at elevations of about 70-80 m. According to Chardon et al. (2018), field investigations and topographic interpretations conducted at the scale of a few square kilometres are generally not sufficient to properly constrain the landscape chronology due to the lateral variability of the paleo-landform preservation, so that the proposed topographic analysis must be considered cautiously. A 50 cm deep, soil gold geochemical survey was conducted in the studied area in 1997 (data from AMG; over 5 000 analyses of soil samples) with returning assay values ranging from below detection limit to 3000 ppb Au (Fig. 2B). Based on available exploration data, the lateritic gold occurrences are usually located on the slopes of flattened hills, near the base of slopes that flanks the S3 planation surface (Fig. 2B). There is a limitation in the use and interpretation of the soil geochemistry anomalies in this area as transported covers, and alluvial horizons are present in various places. The prospect, with no drillcore data and only moderate exploration trenches data available, is nearly devoid of bedrock outcrops although few exposures have been identified distal to the mineralised zones delimited by the AMG subsurface trenching campaign.

Sampled material and analytical methods

The Achman Giraud site, located in the central part of the Couriège tenement near the top of a small hill (Fig. 2) at intermediate elevation between the S2 surface and the active S4 alluvial plain, was selected for the accessibility to a semi-complete weathering profile that hosts partly dismantled, high grade (1.4 to 39.5 g/t Au) quartz veins (exploration data AMG), together with

the accessibility to nearby bedrock exposures. The Lupe site, located in the NW part of the Couriège prospect (about 1 km SE from Lupe) within the southern, lower slope portion of the Lupe hill (Fig.2), was selected for the documented presence of an auriferous transported cover. The two trenches at the Achman Giraud and Lupe sites were prepared for mapping and sampling the trench wall surfaces (trench dimensions: 12 m long – 8 m deep at Achman Giraud, 20 m long – 4.5 m deep at Lupe). At Achman Giraud, channel sampling was conducted along two vertical profiles to account for the vertical gradation of the weathering sequence, including one profile that intersects a 50 cm-thick auriferous quartz vein. Sampling was also conducted along two lateral profiles, i.e., from the mineralised vein outwards, at different positions within the weathering sequence, and one unaltered bedrock sample was collected along a nearby stream (Fig. 2B). At Lupe, channel sampling was conducted along two vertical profiles and complemented with hand sampling of cm-large detrital pyrite crystals. Samples collected from channel sampling were processed for (1) whole-rock gold grade analysis; (2) whole-rock trace and major element analysis; (3) whole-rock mineralogical analysis (XRD); (4) free gold flakes collection (panning) and (5) thick (200 µm) section manufacturing for optic and scanning electronic microscopy, electron probe and XRF microanalysis. Detrital pyrite crystals collected at the Lupe site were prepared as polished sections.

Whole-rock gold grade analyses

Twenty-six samples (mostly from the Achman Giraud site) were analysed for whole-rock gold grades at the Filab laboratory in Paramaribo, Suriname. Analyses were conducted using Fire Assay (ICP-AES) on 50 g pulps obtained from drying, crushing, splitting, and pulverising of ~1000 g samples.

Whole-rock analyses of trace and major elements

Twenty-three hand specimens (mostly from the Achman Giraud site) were split and crushed using an agate bowl pulveriser at GeoRessources Laboratory (Nancy, France). Pulps were analysed for whole-rock major- and trace-element geochemistry at the SARM analytical service of the CRPG (Carignan et al., 2001). Major element oxides were analysed using an iCap6500 ICP-OES with Li borate fusion. Trace elements were analysed using an iCapQ ICP-MS with Li borate fusion followed by nitric acid digestion. Loss on ignition (LOI) was determined by

drying sample powders, ignition at 1100 °C and subsequent measurement of the weight loss. Analytical accuracy (2σ standard deviation) lies within typical uncertainty of the analytical data for both major oxides and trace elements, that is <1% for major oxides and <5% for most trace elements. The laboratory procedure for whole-rock analyses excludes the Te and Ag.

XRD analyses on powder

Mineral assemblages were identified using X-ray diffraction (XRD) analysis performed on rock powders. X-ray diffraction patterns were collected at the GeoRessources laboratory using a D2 phaser X-ray diffractometer, operating in step scan mode, with CuKα radiation (30 kV, 10 mA). Patterns were collected in the range 2–90° 2θ with a step size of 0.016° and a rate of 0.4 s per step.

Imagery and geochemistry of free gold grains

Lateritic materials collected along the two investigated sites were panned on the field. Collected heavy minerals were dried, and gold grains were handpicked under a binocular microscope at the GeoRessources laboratory. It is worth noticing that the manual panning method permits to recover large gold grains (>300 µm) but results in the loss of smaller-sized gold grains, thus leading to significant sampling biases. For optical examination of morphology and surface, 42 grains were placed on the double taped band. They were examined using a 3D macroscope (VHX 2000 Keyence) followed by high-resolution Scanning Electron Microscopy (SEM) observations on a Hitachi FEG S4800 using SE imaging mode with beam conditions of 10 kV and 10 nA at the SCMEM at the GeoRessources laboratory (Nancy, France).

Selected representative grains from each horizon were then polished and mounted in a resin mount. Grains were classified according to their morphology and studied by SEM (TESCAN VEGA3) and electron probe micro analyser, EPMA (CAMECA SX-100) at the GeoRessources laboratory with an acceleration voltage of 20 kV and beam current of 20 nA : 116 spot analyses were performed for Au, Ag, As, Bi, Te, Sb, Cu, Ni, Co and Fe. Standard specimens used for calibration were FeS_2 (for Fe) and pure metals for Au, Ag, As, Te, Cu, Ni and Co. Only Ag, Au and rarely Cu present contents above detection limits. Chemical zonations have been tested on 7 representative grains by performing X-rays maps (EPMA) of Au, As, Cu, Te and Ag.

Trace element composition of gold grains was further investigated from LA-ICP-MS analyses at the BRGM laboratory in Orléans (France). The following elements were analysed: ^{52}Cr, ^{33}S, ^{55}Mn, ^{58}Ni, ^{59}Co, ^{63}Cu, ^{64}Zn, ^{75}As, ^{76}Se, ^{78}Se, ^{82}Se, ^{103}Rh, ^{105}Pd, ^{106}Pd, ^{107}Ag, ^{109}Ag, ^{112} Cd, ^{114}Cd, ^{118}Sn, ^{120}Sn, ^{121}Sb, ^{123}Sb, ^{130}Te, ^{195}Pt, ^{197}Au, ^{202}Hg, ^{208}Pb and ^{209}Bi. Sulphur (^{33}S), ^{57}Fe and ^{48}Ti were monitored to detect eventual signal interference of sulphides and Fe-Ti oxides inclusions, respectively. LA-ICP-MS system consists of an excimer laser (193 nm) CETAC Excite coupled to ThermoScientific X serie II quadrupole plasma mass spectrometer. The laser is equipped with a HelEx® 2 volume ablation cell that optimises the material transport to the ICP-MS. The ablated material is carried by He, which is then mixed with N_2 and Ar, before injection into the plasma source. The alignment of the instrument and mass calibration was performed before each analytical session on the NIST SRM 612 reference material. To enhance the signal and reach very low detection limits for analysed trace elements, a beam diameter of 85 µm was used, and ablation areas were carefully selected to avoid solid micro-inclusions. One single analysis consists of 20 s of gas blank followed by 40 s of ablation. A laser pulse frequency of 8 Hz, and a laser beam energy of 3.06 J/cm^2 were used during analyses. Quantification of gold was carried out using ^{107}Ag as internal standard. For each analytical session, we used the following standard bracketing procedure: one analysis of the RAuP7 and RAuP3 gold reference materials from MBH every 10 analyses of gold grains and one analysis of the NA-Au-31 and NA-Au-30 gold standards (Kovaks et al. 2009) for every twenty analyses of gold grains. This sequence was then repeated up to the end of the session. Calibration of Ni, As, Cd, Sn and Te was performed using reference material NA-Au-31. For the remaining elements, the RAuP7 gold standard was used for calibration. To monitor the quality of analyses, we used the reference materials NA-Au-30 and RAuP3. The NA-Au-30 and RAuP3 standards measurements were treated as unknowns and used to control the reproducibility and accuracy of analyses. Data reduction was carried out using Iolite software (Patton et al., 2011). Analyses of RAuP3 show high accuracy and excellent precision, with a mean relative difference (RD) ~4.4% and relative standard deviations (RSD) ~9.8% for all considered elements. ^{121}Sb and ^{208}Pb are slightly overestimated by 12-14 %. Note that ^{209}Bi have the largest RSD of 32%. Regarding the NA-Au-30, analyses show good accuracy and excellent precision, with a mean RD of ~8 % and a mean RSD of ~8.8%. ^{114}Cd and ^{118}Sn are underestimated by 25%.

Microscopic observations and analysis on thick sections

A total of 13 impregnated (epoxy resin) thick sections have been manufactured, including 11 thick sections encompassing all the horizons observed at Achman Giraud and 2 thick sections of cm-large detrital pyrites collected at Lupe. Thick sections were examined using reflected/transmitted light and scanning electron microscopy (TESCAN VEGA3 and JEOL J7600F providing backscattered electron mode images, at an acceleration voltage of 20 kV) to characterise mineral assemblages, parageneses and possible occurrences of *in situ* gold. EPMA spot analysis was conducted on microscopic (*in situ*) gold occurrences identified from optical and scanning electron microscopy, with analytical conditions identical to those used for EPMA spot analysis of large (> 300 µm) free gold grains. Chemical micro-XRF maps were acquired using the M4 TORNADO analyser with beam conditions of 50 kV and 600 mA, 25 µm spatial resolution and 12 ms/pixel dwell time. Micro-XRF maps were processed to obtain quantitative mineral maps using the open-source MARCIA Python routine (Meyer and Cauzid, 2020). MARCIA permits mineral classification by defining masks that are a linear combination of elemental intensities in spectra. EPMA mapping was also conducted on one mm-large crystal of goethite pseudomorph after pyrite from the Achman Giraud site (analysed elements are Si, Fe, S, Bi, Ti, Ag, Al, Te and Au).

Results

Macroscopic observations

Achman Giraud profile

The weathering profile at the Achman Giraud site, exposed along a SSW-NNE trench, presents an undisturbed succession of weathering horizons (Fig. 3). The base of the profile consists of a mafic-derived, fine grained purplish saprolite wherein the primary fabric is partly preserved (Figs. 3 and 4D, F). The saprolite horizon sharply grades upwards into the mottled zone, characterised by a kaolinite-rich matrix locally containing cm-scale, hematite-bearing mottles with typical reddish colouration (Figs. 3 and 4C, F). The mottled zone, whose thickness does not exceed a few tens of centimetres, is laterally discontinuous and locally pinches out in the central part of the exposed profile. Upwards, there is an evolution into the pulverulent red latosol wherein kaolinite still represents the predominant mineral phase. Diffuse hematisation results in a homogeneous reddish colouration of this horizon (Figs. 3 and 4B). Above, the

uppermost metre of the profile consists of a light brownish horizon (brown latosol) wherein ochreous goethite (limonite) forms at the expense of hematite (Figs. 3 and 4A). Sigmoidal, moderately dipping quartz veins about 10 to 60 cm-thick (Figs. 3 and 4G), are observed in all horizons except within the brown latosol.

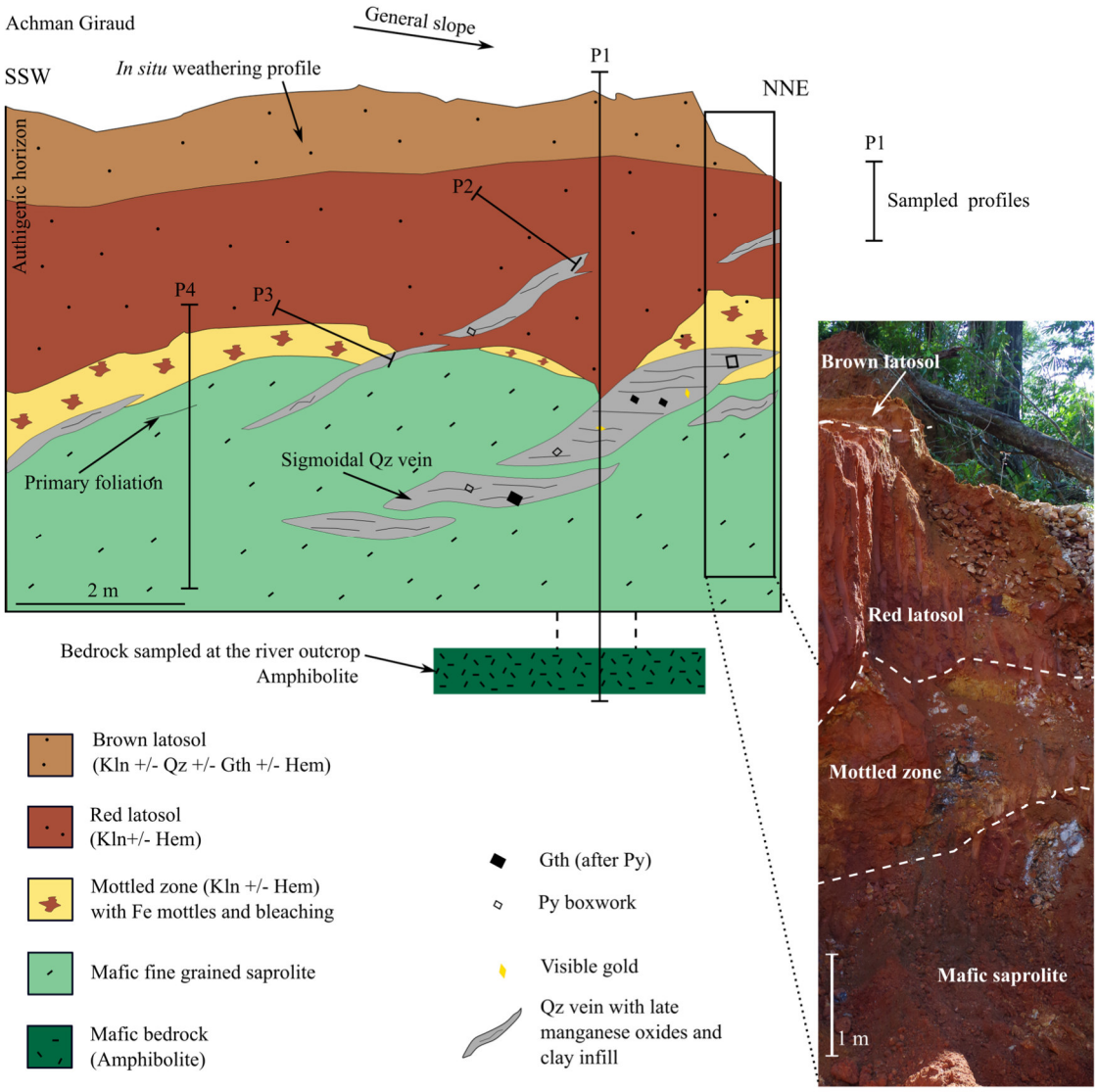

Figure 3 Schematic cross section of the Au-bearing regolith of the Achman Giraud site with location of sampled profiles. (Abbreviations: Qz=quartz, Hem=hematite, Gth=goethite, Kln=kaolinite, Py=pyrite).

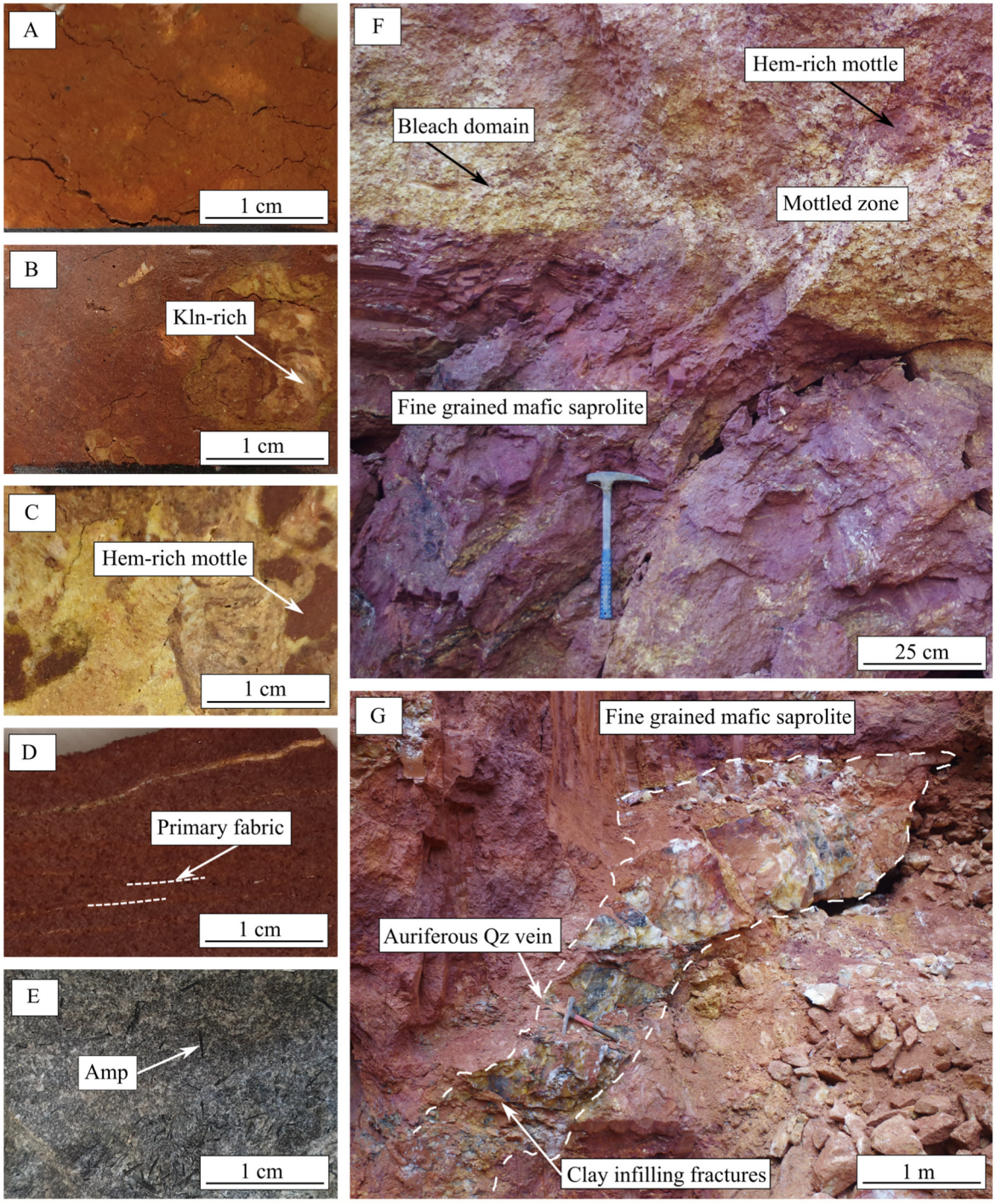

Figure 4 Macroscopic photographs, from the Achman Giraud site. (A). Brown latosol. (B). Red latosol. (C). Mottled zone. (D). Saprolite. (E). Amphibolite bedrock. (F). Contact zone between the fine grained mafic saprolite and the mottled zone. (G). The auriferous quartz vein within the saprolite horizon. (Abbreviations: Qz=quartz, Amp=amphibole, Hem=hematite, Kln=kaolinite).

This observation, together with the gradual evolution from the red latosol to the brown latosol and the apparent absence of any clastic beds, further support the assumption that the entire weathering profile is authigenic. Quartz veins are weakly to moderately dismantled and locally contain late manganese oxides and clay infills where fractured. Importantly, goethite pseudomorphs after mm-to cm-large pyrite crystals exhibiting boxwork alteration textures as well as visible, mm-large gold flakes, occur in the quartz vein. Neither the saprock nor the unweathered bedrock was directly exposed within the sampled trench. Nevertheless, one sample of unweathered, foliated amphibolite was collected along a stream located about 180 m NW from the Achman Giraud was collected along a stream situated about 180 m NW from the Achman Giraud site (Figs. 2B and 3). As a preliminary conclusion, the Achman Giraud weathering profile probably developed on the amphibolite observed more in-depth in the bedrock.

Lupe

The weathering profile at the Lupe site is exposed along an E-W trench and consists of a sequence of authigenic horizons truncated by an allogenic cover (Fig. 5). The base of the exposed profile is characterised by a >2m-thick mottled zone predominantly composed of kaolinite and includes cm-thick mottles that contain minor amounts of hematite (Figs. 5, 6E). The mottled zone evolves upwards into a red latosol, characterised by a relative increase in the proportion of hematite, which homogeneously stains the kaolinitic matrix. The red latosol is sharply truncated by an allogenic, detrital cover (Figs. 5 and 6A), with clear evidence for an erosional contact at its base. A poorly consolidated limonitic matrix characterises the transported cover containing numerous clasts of heterogeneous size and nature, including angular quartz, pisolithic bauxite, vesicular and massive duricrust clasts, together with millimetric to pluricentimetric pyrite crystals transformed into goethite (Figs. 5 and 6B, C, D). Subhorizontal, cm to dm-thick quartz±pyrite veins cut the mottled zone and the red latosol. These veins exhibit intense dismantling, thus contrasting with the relatively well-preserved veins observed in the mottled zone of the Achman Giraud profile. Together with the greater thickness of the mottled zone, the greater intensity of quartz vein dismantlement (Fig. 6E) at the Lupe site compared to the Achman Giraud site suggests that the weathering profile exposed at Lupe is more mature in terms of weathering intensity.

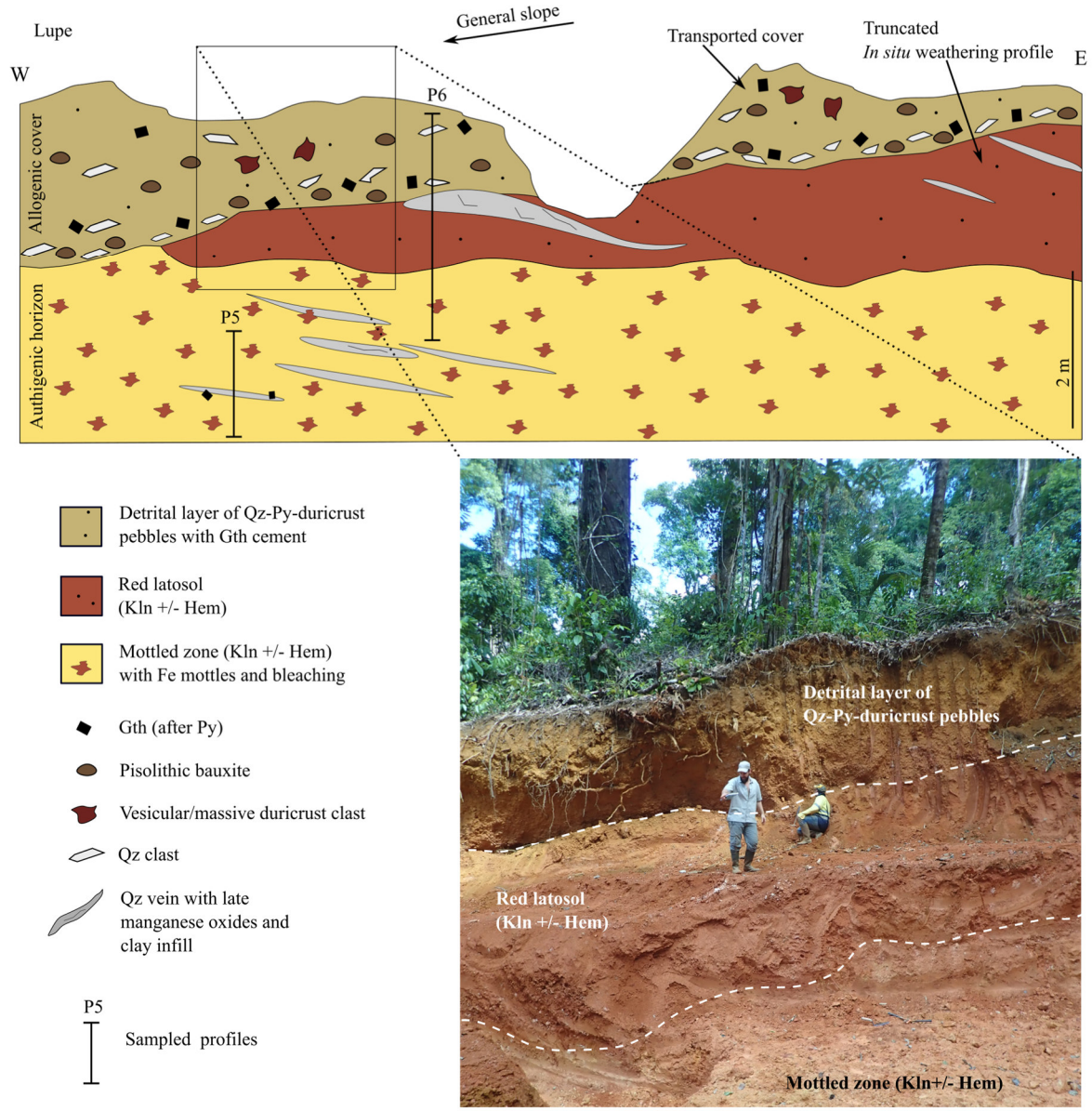

Figure 5 Schematic cross section of the Au-bearing regolith of the Lupe site with location of sampled profiles. (Abbreviations: Qz=quartz, Hem=hematite, Gth=goethite, Kln=kaolinite, Py=pyrite).

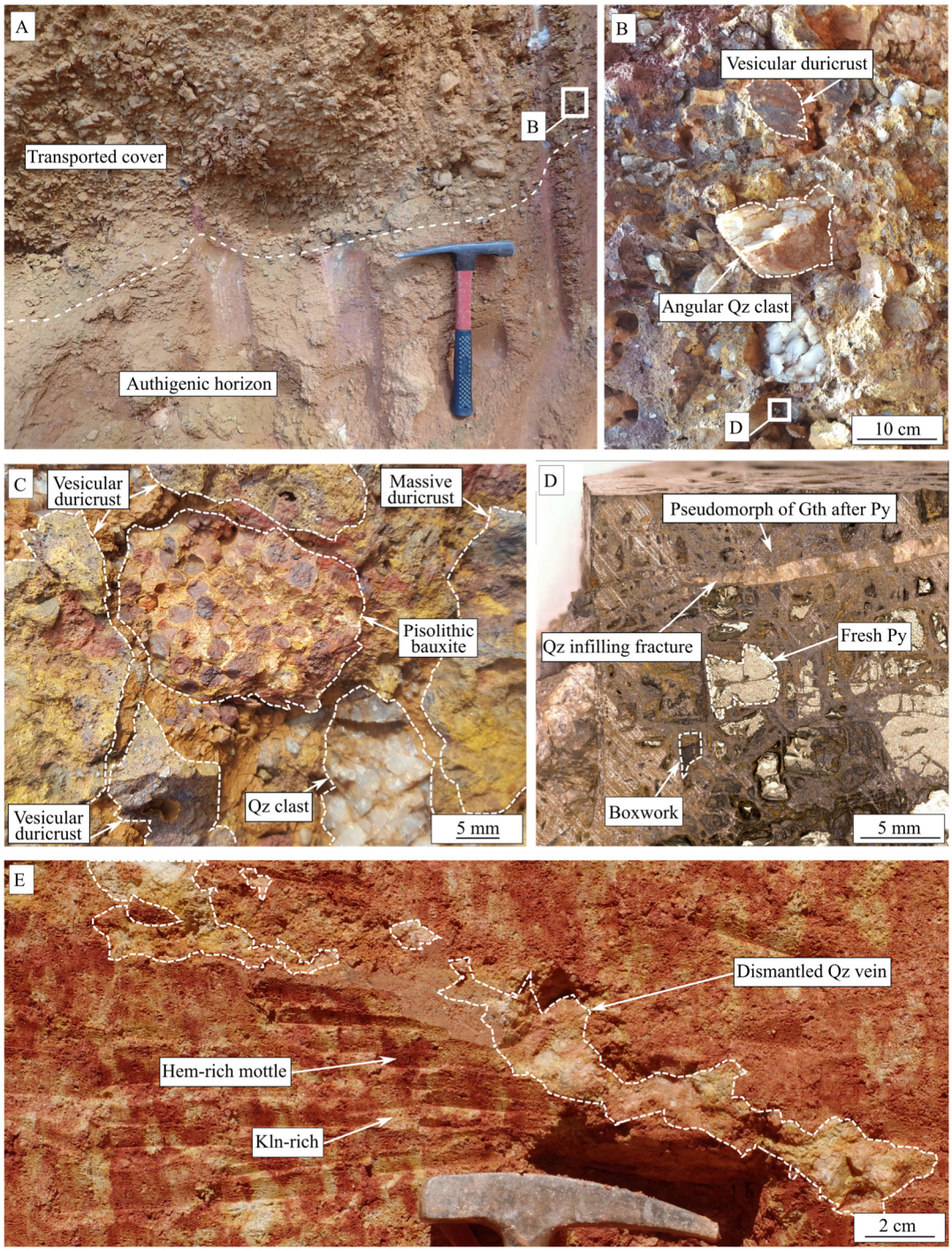

Figure 6 Macroscopic photographs (A). The contact between the transported cover and the authigenic horizon. (B). Zoom on the transported cover with vesicular duricrust clasts and angular quartz clasts. (C). Zoom in the transported cover displaying pisolithic bauxite, vesicular and massive duricrust clasts, and quartz clasts within a limonitic matrix. (D). Half-cut, detrital goethitised pyrite located in (B). (E). Highly dismantled quartz vein within the mottled zone. (Abbreviations: Qz=quartz, Hem=hematite, Gth=goethite, Kln=kaolinite, Py=pyrite).

Whole-rock geochemistry

The Achman Giraud site was sampled for whole-rock geochemistry as the profile is complete. Biplots of Th, Hf, Ta, TiO_2, Fe_2O_3 and Al_2O_3 against Zr concentrations are shown in Figure 7. Variations of major oxides and trace element concentrations along the main vertical transect (P1) are shown in Figure 8 and 9, respectively. Results of major and trace element compositions of collected samples are summarised in Table 1. The unweathered amphibolite, collected along a nearby stream, displays a dioritic composition (TAS diagram, Middlemost 1994) with SiO_2, Al_2O_3, Fe_2O_3 and CaO contents of approximately 60, 15, 7 and 6 wt.%, respectively. MgO, Na_2O, P_2O_5, K_2O and TiO_2 contents are below 3 wt.%. Compared to the parent amphibolite, the lateritic profile exposed at Achman Giraud exhibits systematic changes in major and trace element compositions. Elements may be classified into three groups depending on their behaviour. Group 1 includes Fe, Ti, Zr, Hf, Th and Ta. These elements were nearly immobile during weathering and display increasing concentrations upwards in the profile (Figs. 7 and 9). High Field Strength Elements (HFSE) such as Zr, Hf, Ta and Th show strong positive correlations and co-enrichments throughout the weathering profile, suggesting that they represent the least-mobile elements during lateritisation and that all samples are derived from a chemically homogeneous parent rock (Fig. 7). It is worth noticing that the bedrock sample, collected at a certain distance from the weathering profile, fits in the HFSE correlation trends but yields slightly higher HFSE concentrations that one saprolite sample (Fig. 7). It is therefore suggested that the weathering profile exposed at the Achman Giraud site derives from a protolith that is not entirely equivalent yet chemically similar to the sampled unweathered amphibolite. Poorly mobile elements including Fe and Ti, whose concentrations globally increase throughout the profile (Fe_2O_3 from 7 to 12 wt.%, TiO_2 from 0.6 to 1.0 wt.%), exhibit enrichment patterns similar to that of least mobile elements (Figs. 7 and 8). Nevertheless, significant dispersion from the correlation trends is observed in Fe_2O_3 vs. Zr and TiO_2 vs. Zr biplots (Fig. 7), suggesting that Fe and Ti were slightly remobilised during weathering. Group 2 elements include Al, Si and most of the analysed trace elements (Pb, Cu, Zn, Mn, Ni, Co, Cr, Bi), which were largely redistributed within the lateritic profile during weathering. Contrasting with SiO_2 which remains relatively constant (around 60 wt.%) throughout the profile, Al_2O_3

increases upwards from the bedrock and reaches maximum concentrations of about 25 wt.% in the saprolite and the lower portion of the red latosol.

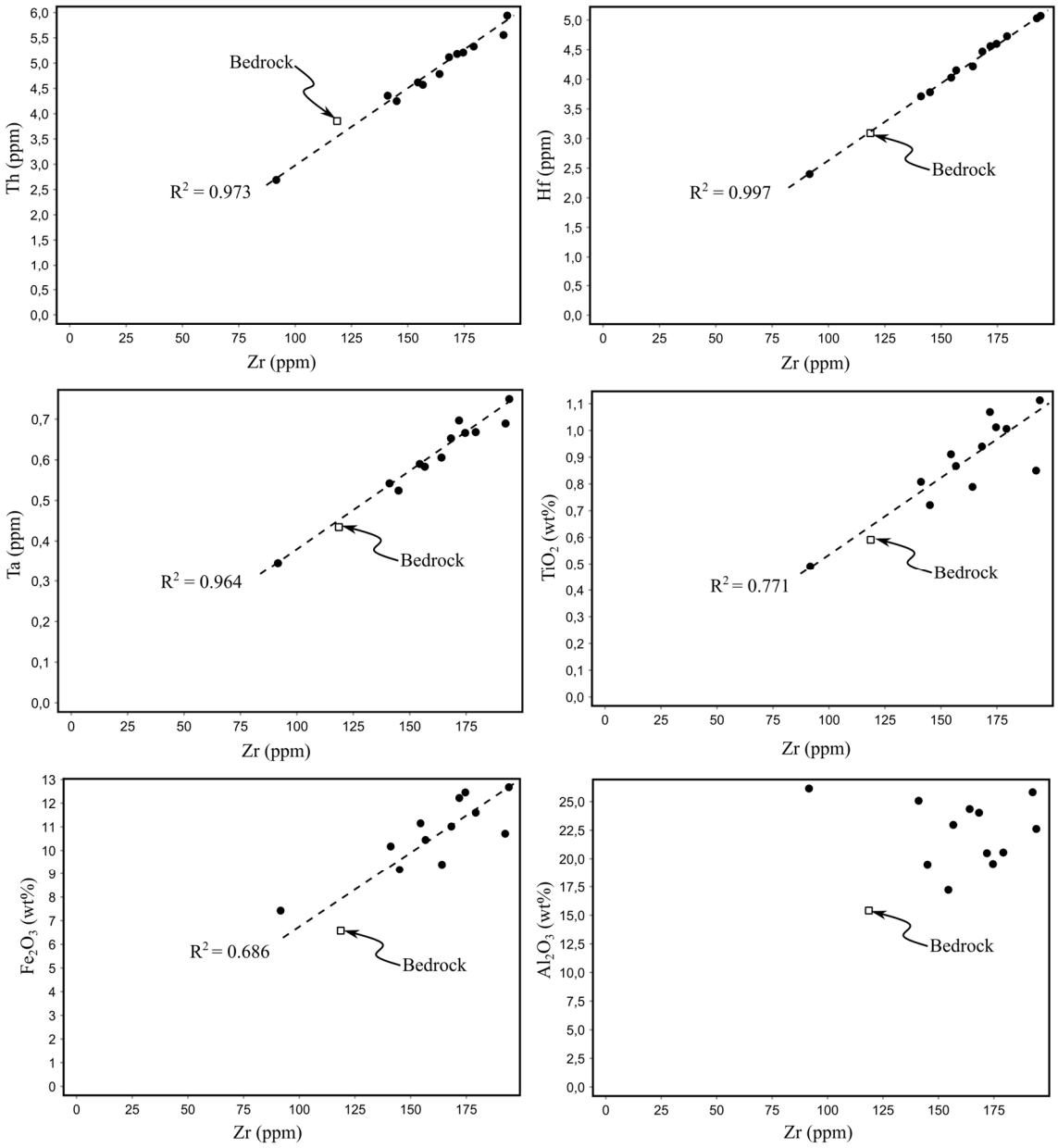

Figure 7 Correlation plots of Th, Hf, Ta, TiO_2, Fe_2O_3 and Al_2O_3 against Zr, along the Achman Giraud profile.

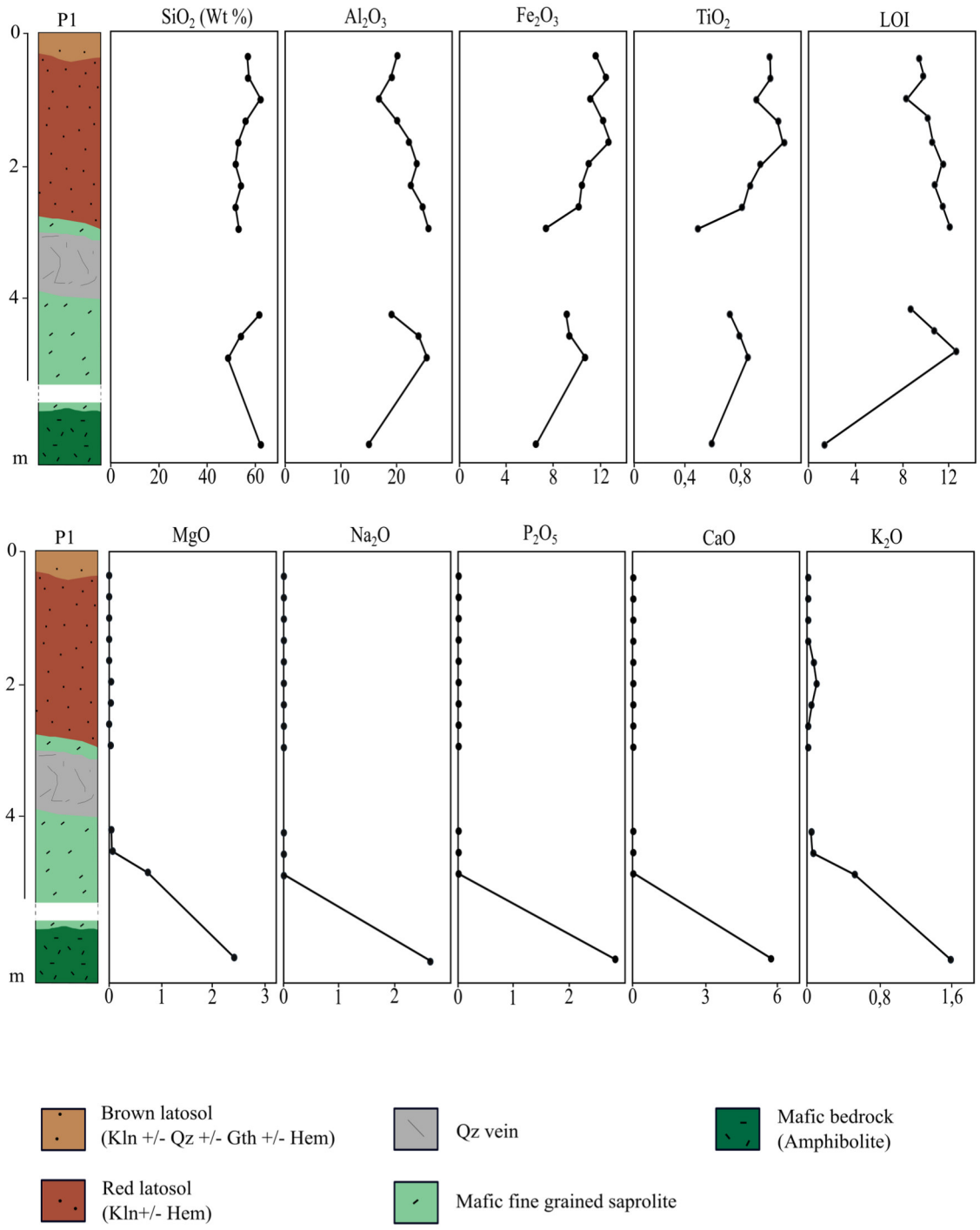

Figure 8 Variations of major element concentrations (wt. %) along depth in the P1 transect at Achman Giraud.

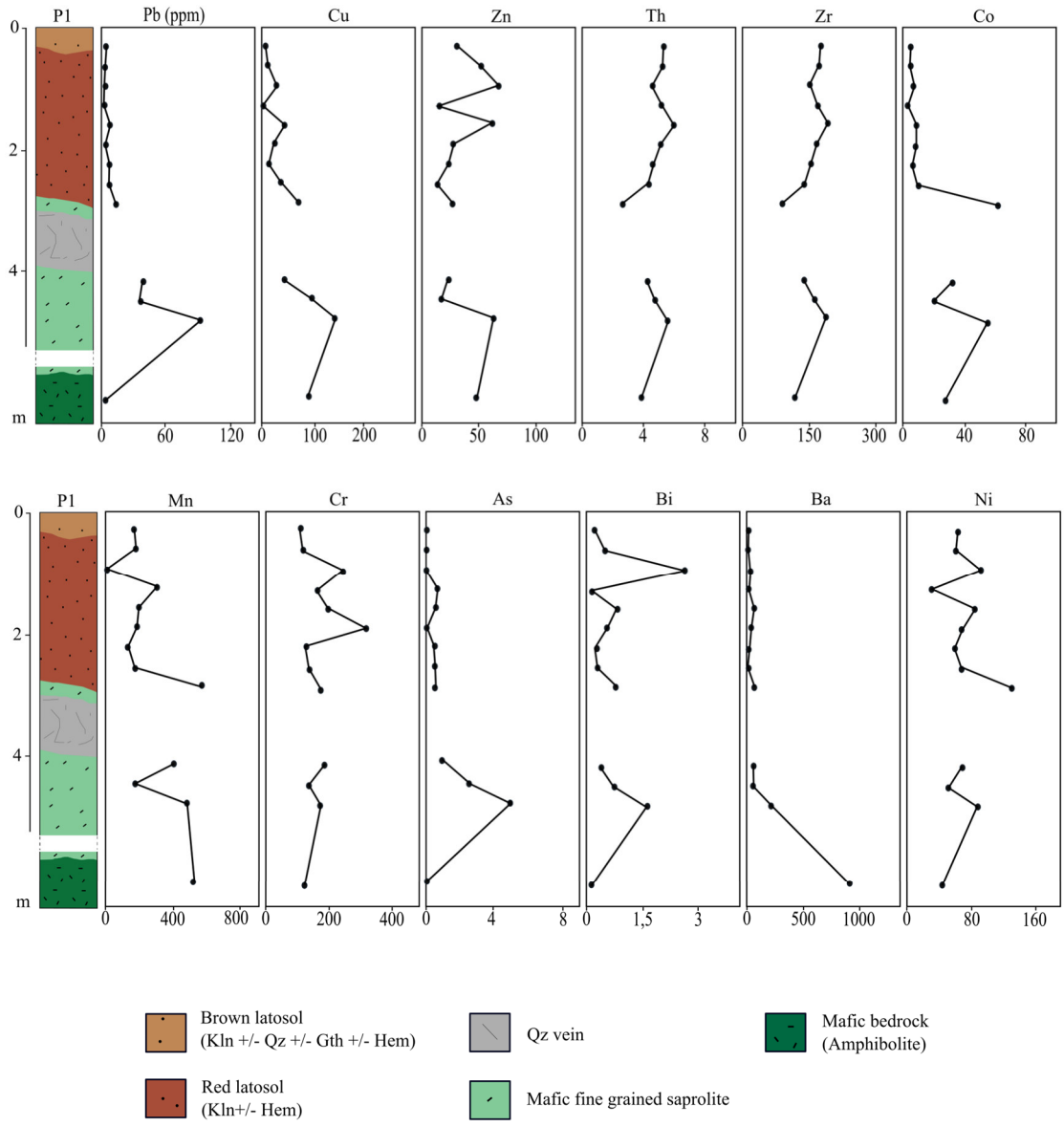

Figure 9 Variations of selected trace elements (ppm) along in the P1 transect at Achman Giraud.

Above, Al_2O_3 concentrations slightly decrease down to 15-20 wt.%. Although these elements were partly retained and residually enriched in the profile, they appear miscorrelated with least and poorly mobile elements (e.g. Al_2O_3 vs. Zr in Fig. 7), supporting the assumption that they were significantly remobilised. Group 3 represents elements that were largely removed from the weathering profile, including MgO, Na_2O, P_2O_5, CaO, K_2O and Ba. Nevertheless, the depletion of Mg and K in the saprolite zone remains less pronounced than that of other mobile cations. There, Mg and K may have been temporally preserved from leaching in mineral phases

such as smectite and white mica, respectively. In addition, it is worth noticing that the LOI content increases from about 1 wt.% in the bedrock to about 10 wt.% along the profile, following the formation of weathering-related phyllosilicates and oxy-hydroxides.

Gold grade variation

Variations of gold grades (Fig. 10) have been investigated both along the vertical profile P1 and along the two lateral profiles P2 and P3, i.e., from the Au-bearing quartz vein outwards. Whole-rock Au grades range from 0.03 to 7.14 ppm along the P1 profile (Fig. 10A), with 3 samples grading above 2 ppm: one sample collected at the hanging wall of the Au-bearing quartz vein (grading 5.38 ppm) and two samples collected in the upper part of the weathering profile (at the top of the red latosol and within the brown latosol, grading 4.89 and 7.14 ppm, respectively). The vein itself was not analysed to avoid nugget effect as mm large gold flakes are observed within the vein. Both lateral profiles realised within the red latosol (P2 profile, Fig. 10B) and mottled zone (P3 profile, Fig. 10C), exhibit a decrease in gold concentration from the Au-bearing quartz vein outwards. On the P2 profile, the Au grade decreases from 1.1 to < 0.1 ppm within the first 30 cm from the vein edge. Similarly, on the P3 profile, the Au grade decreases from 0.6 to < 0.2 ppm within the first 20 cm from the vein edge. In both profiles, no sample located farther than 1.5 m from the vein returns gold grade above the detection limit (0.005 ppm). Whole-rock gold grades (Table 2) must be considered with caution as the sampled quantity was limited (up to 3 kg per sample) and the nugget effect may be important.

Paragenetic sequence at the Achman Giraud profile

The amphibolitic bedrock is mostly composed of amphibole, in association with quartz, ilmenite and magnetite (Fig. 11A), whereas the Au-bearing quartz vein contains minor euhedral pyrite and white mica. In the saprolite horizon, kaolinite represents the predominant mineral phase with up to 50 µm-large sheeted grains, possibly developed after amphibolite grains (Fig. 11B), and thin sticks in the matrix (Fig. 11C). Locally, hematite forms at the expense of coarse kaolinite along grain borders and within kaolinite sheets or crystallise as micrometric crystals in the matrix porosity. Millimetre-large gibbsite veins are locally observed within the saprolite

(Fig. 11B). In the mottled zone, segregation of Fe leads to the formation of hematite-bearing mottles within a kaolinitic matrix that is essentially devoid of iron oxides (Figs. 11D, E, 12A).

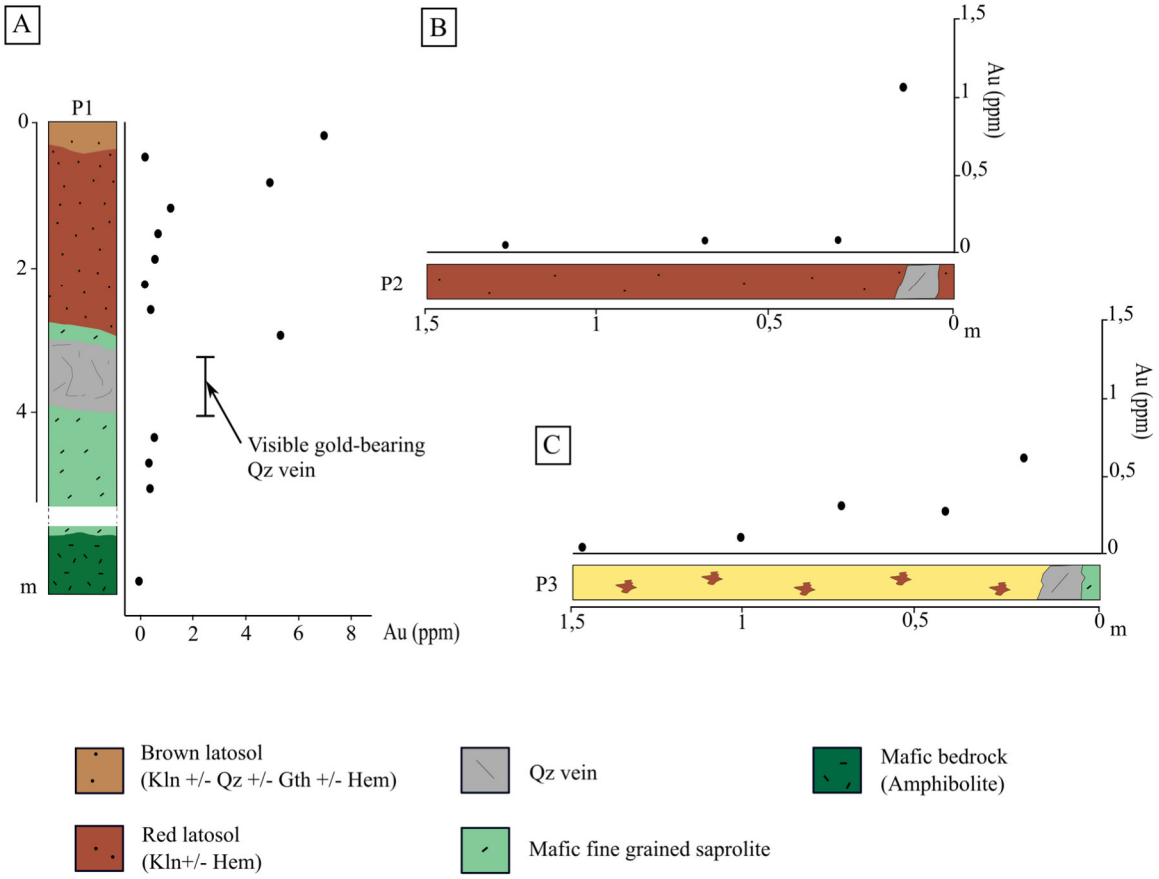

Figure 10 (A). Variations of the whole-rock gold grade (ppm) along depth in the P1 transect. (B). Lateral variation of the whole-rock gold grade (ppm) along the P2 transect. (C). Lateral variation of the whole-rock gold grade (ppm) along the P3 transect. All data are from the Achman Giraud site.

The contact between mottles and the kaolinite matrix is usually sharp (Figs. 11D, E, 12A). In the mottles, hematisation of kaolinite along grain borders and within kaolinite sheets is well-developed (Fig. 11F). Quartz grains, present both in the iron-bearing mottles and in the kaolinite matrix, appear mostly unaffected by mottle development. The iron-bearing mottles exhibit a depletion in Al and Ti compared to the kaolinite matrix, together with enrichments in Fe, as well as Cr along mottle edges (Fig. 12B). In the red latosol, a significant portion of pre-existing

coarse kaolinite grains appear most entirely replaced by hematite (Fig. 11I), and fine-grained

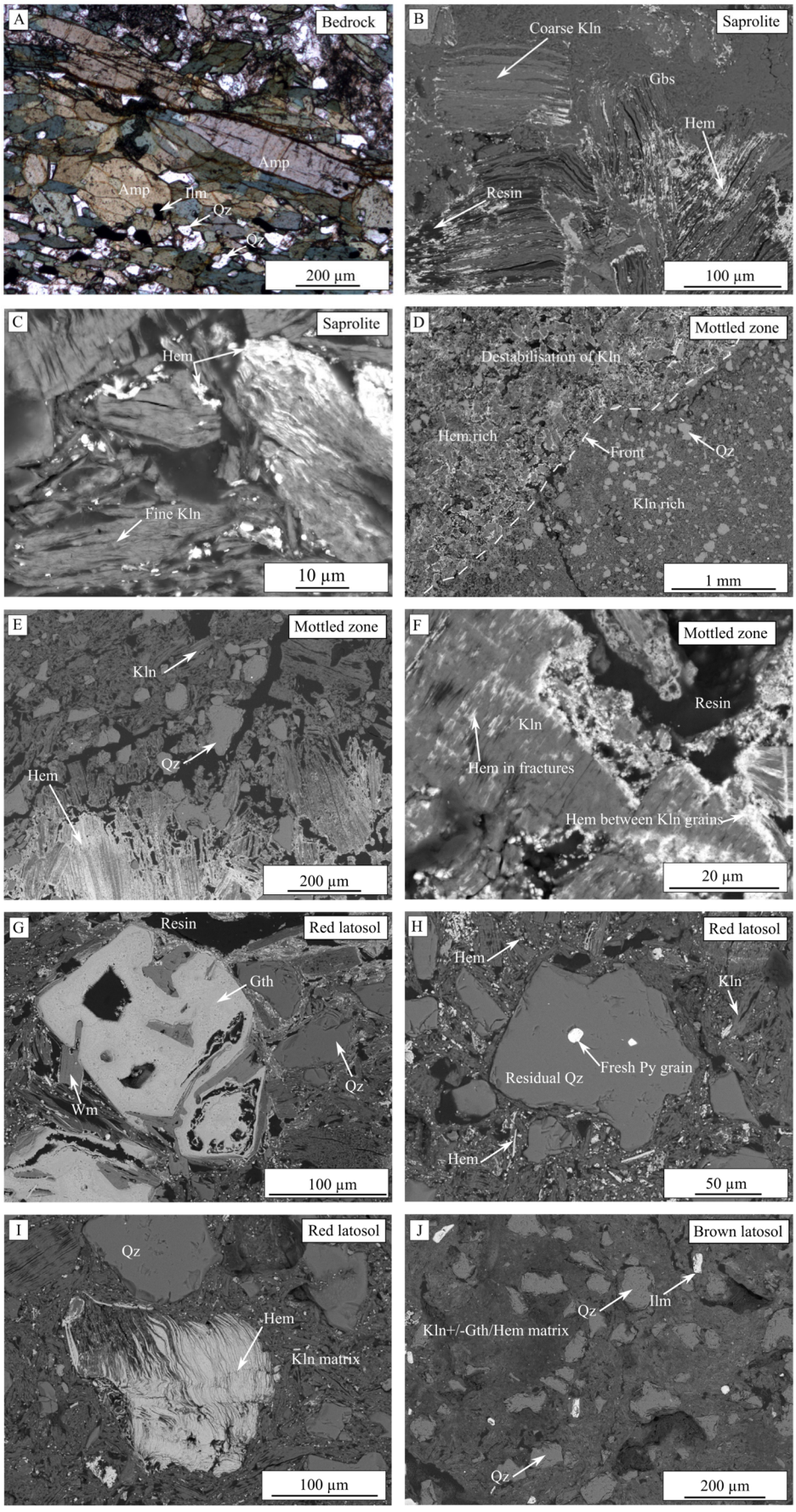

Figure 11 BSE images (except for bedrock in optical microphotography) of typical mineral associations. (A). The amphibolite bedrock displaying amphibole grains, ilmenite and quartz, (B). The saprolite with typical coarse kaolinite grain and associated hematisation along kaolinite sheets and grain borders. (C). Partial replacement of kaolinite by hematite and formation of hematite within the porosity. (D). Border of an iron-rich mottle within kaolinite matrix, with formation of hematite at the expense of kaolinite. (E). Zoom on the hematisation front associated with iron-rich mottles. (F). The mottled zone with a strong hematisation in fractures and between the kaolinite grains. (G). Goethitised pyrite crystal interlocked with primary sericite in the red latosol. (H). Residual quartz grain displaying a preserved fresh pyrite inclusion in the red latosol. (I). Complete hematisation of a coarse kaolinite grain within the red latosol and (J.) The kaolinite and goethite/hematite rich matrix in the brown latosol. (Abbreviations: Qz=quartz, Ilm=ilmenite, Amp=amphibole, Hem=hematite, Gbs=gibbsite, Kln=kaolinite, Py=pyrite).

hematite also develops within the kaolinitic matrix (Fig. 11H). In the brown latosol, hematite is mostly transformed into goethite, and the matrix is composed of kaolinite +/- goethite and hematite (Fig. 11J) and the global iron oxide content further increases at the expense of kaolinite. Throughout the weathering profile, only few of the pre-existing mineral phases remain resistant to weathering, most notably quartz, ilmenite, zircon and rare magnetite. Samples collected proximal and distal from the main quartz vein display relatively similar abundance of residual quartz grains (Fig. 11C, E), suggesting that quartz grains inherited from the protolith dominates the global quartz budget in the profile. This is supported by the persistence of quartz grains in the red and brown latosols, i.e., above the main quartz vein. Nevertheless, the occurrence of fresh pyrite inclusions within some of the quartz grains in the red latosol (Fig. 11E, 11H) suggests that additional quartz±pyrite veins may have been present in the upper part of the profile but underwent complete goethitised pyrite crystals are also observed throughout the weathering profile, some of which are interlocked with sericite (Fig. 11G). The presence of oxidised pyrite crystals within the profile is thus interpreted to result from the dismantlement of either quartz±pyrite veins or pyrite-bearing alteration haloes. Importantly, goethitised pyrite locally contains gold inclusions. In the following section, textural changes of goethitised pyrite along the profile and association with gold are documented.

XRD analyses have been carried out and confirm petrographical observations *(Supplementary material*).

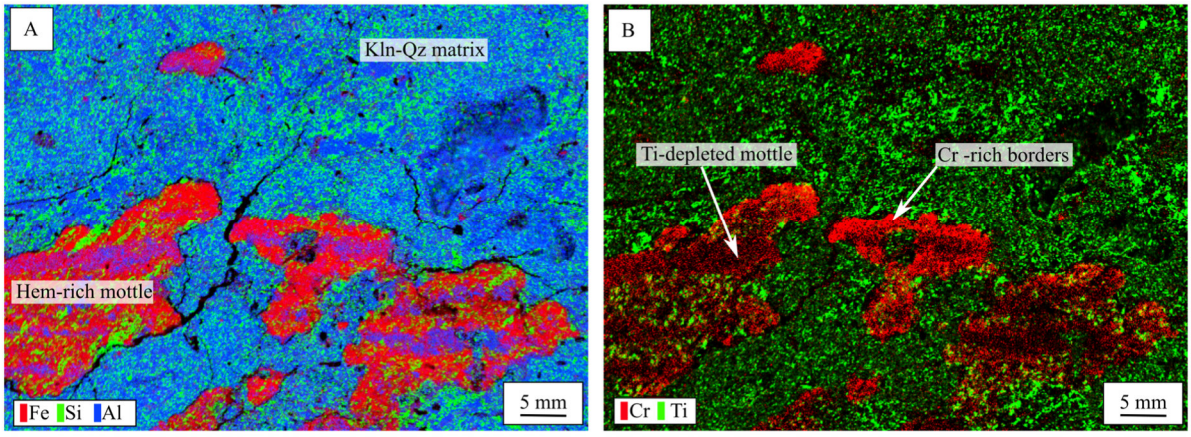

Figure 12 µXRF maps of the mottled zone. (A). Fe-Si-Al maps highlighting Fe-rich mottles (red) within the kaolinitic Al-rich matrix (blue), together with quartz grains (green) displaying a discrete fabric present in both the mottles and the matrix. (B). Ti-depleted mottles with Cr-rich margins (red). (Abbreviations: Qz=quartz, Hem=hematite, Kln=kaolinite).

Supergene alteration of pyrite and associated *in situ* gold inclusions

The supergene alteration of pyrite crystals contained within the Achman Giraud lateritic profile is associated with progressive changes in crystal textures (Fig. 13). Unweathered, subhedral to euhedral pyrite crystals are rarely observed in the saprolite horizon (Fig. 13G), as most of the crystals are already pseudomorphed into fine-grained, massive goethite (Fig. 13E, D, B). In the saprolite and in the red latosol, the rims of goethitised pyrite crystals commonly exhibit colloform textures with significant micro-porosity, resulting from dissolution and reprecipitation of goethite. The reprecipitation of colloform goethite rims is also accompanied with the incorporation of Si and Al at the expense of Fe (*Supplementary material*).

Micron-scale Au-inclusions are observed within the goethitised pyrite, both within grain cores and within the colloform rims (Fig. 13). Some micro-fractures within goethitised pyrite are locally filled with gold inclusions (Fig 13C and F), suggesting that the formation of gold micro-inclusions is related to supergene alteration. Nevertheless, although no fresh pyrite containing gold micro-inclusions were identified, the relative timing between gold precipitation and goethitisation of pyrite remains unclear. Consequently, the hypogene or supergene nature of gold inclusions cannot be deciphered from textural observations alone. In the brown latosol,

goethitised pyrite grains are largely altered and exhibit extensive dissolution features

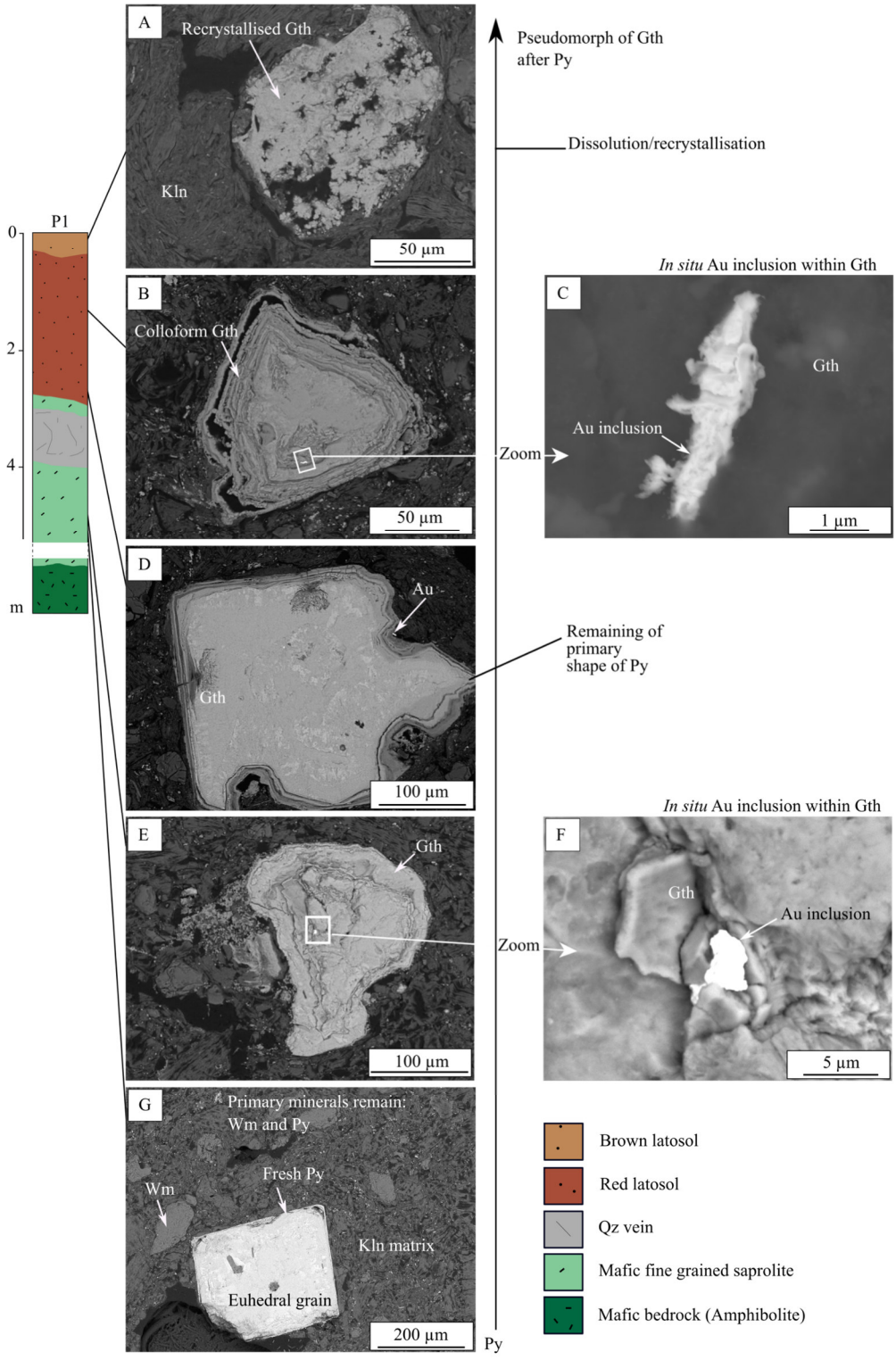

Figure 13 Textural evolution of goethitised pyrite through the P1 transect with evidence for dissolution-reprecipitation of goethite (A, B, D, E, G) with examples of in situ gold micro-inclusions (C) and (F). (Abbreviations: Qz=quartz, Gth=goethite, Kln=kaolinite, Py=pyrite, Wm=white mica).

throughout the entire grains (Fig. 13A). Although the brown latosol yields elevated gold grades up to 6 ppm, no gold micro-inclusions have been identified within goethitised pyrite originating from this horizon. EPMA analyses on *in situ* gold micro-inclusions do not show the presence of Ag or other metallic elements, it is therefore pure gold (see the synthesis of Ag and Au data for all types of gold in next sections).

At the Lupe site, cm-scale goethitised detrital pyrite crystals (Fig. 14A) collected in the transported horizon contain unweathered pyrite cores and macroscopic porosity, indicative of the incomplete supergene alteration of the crystals (Fig 14B). There, goethite exhibits characteristic boxwork textures with boxwork strips consisting of massive, Te-bearing goethite (up to ~2 wt.% Te) and locally containing electrum inclusions up to 200 µm large (with Ag contents ranging from 29,3 wt.% to 35 wt.%) as well as dusty, micrometric to sub-micrometric Bi inclusions (Fig. 14 C, D, E, G, H, I and J). Infill material of the boxwork consists of Te-free, tabular goethite aggregates associated with micro-porosity (Fig. 14C, D).

Morphology and geochemistry of free gold grains

At Achman Giraud, visible gold grains located within quartz veins are associated with pyrite and/or quartz grains and display angular and irregular shapes and outlines with no porous surfaces (Fig. 15). Panned grains sampled within the saprolite and the mottled zone horizons similarly exhibit irregular shapes with typical textures of tabular gold crystal intergrowths and often remain interlocked with relict quartz crystals (Fig 15A, B, C and D). Typical micrometre-high, sharp terraces (Fig. 15B) are observed on the surface of grains from the saprolite while micrometric subcircular dissolution pits with striation and microglobules of secondary gold are visible on the surface of grains from the mottled zone (Fig. 15D).

Panned grains collected within the overlying red latosol also exhibit irregular shapes and outlines with moderately blunt edges, together with jagged rims, flaky structures, and inverse prints of dissolved quartz and/or pyrite crystals (Fig. 15 F and G). Although similar in shape, gold grains from the red latosol differ from the grains collected in the underlying horizons in that they more frequently display dissolution pits, (Fig. 16 F, G and H) as well as 5 µm-thick spherulitic overgrowths of secondary Au on grain surface (Fig. 16E).

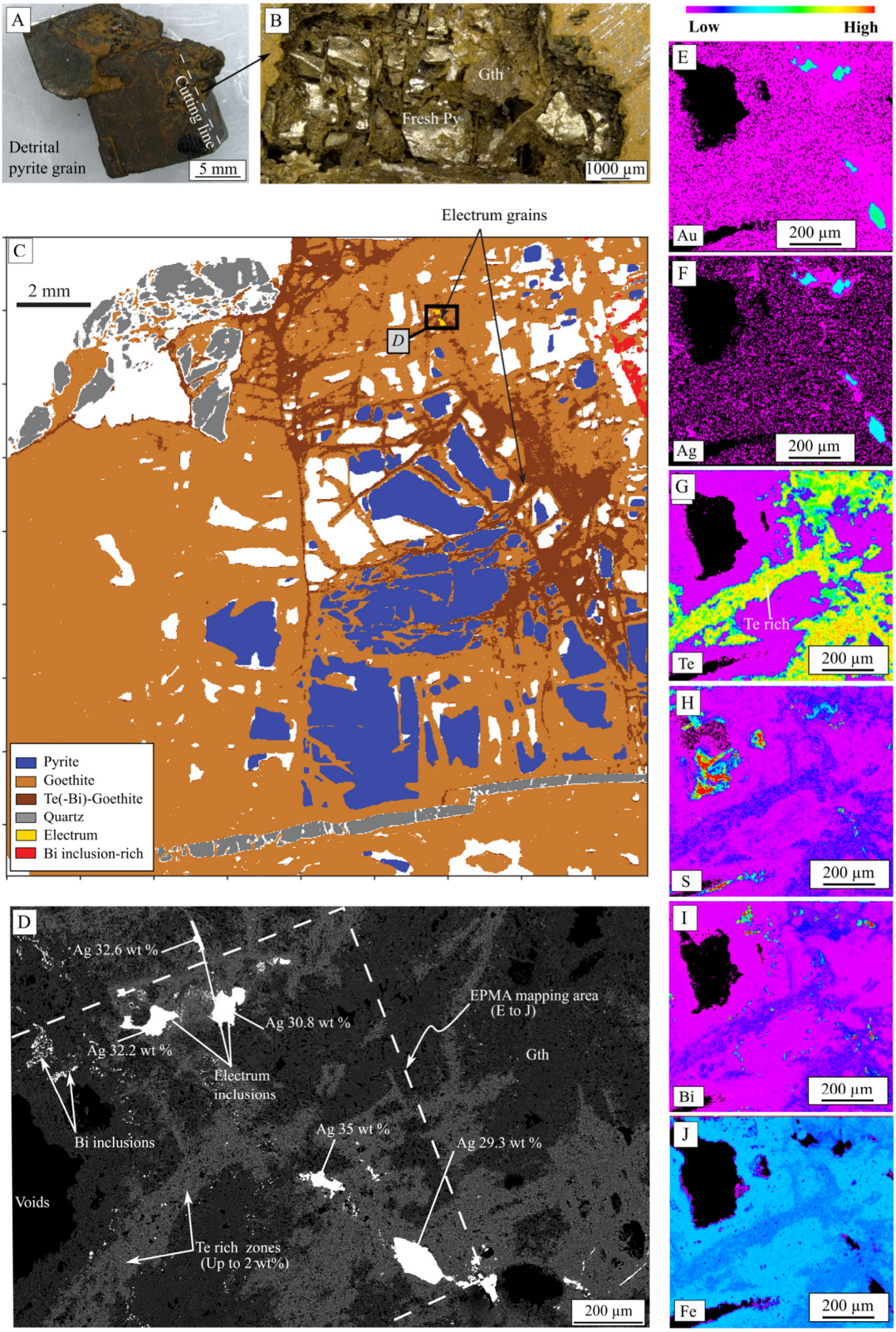

Figure 14 (A). Overview of a detrital pyrite crystal from the transported cover of the Lupe site. (B). Macroscopic image of a half-cut pyrite crystal with fresh pyrite relics and partial goethite replacement. (C). Interpreted mineral map from µXRF data on the partly goethitised pyrite showing boxwork textures enriched in Te, together with electrum and Bi inclusions. (D). In situ

EPMA analyses of electrum micro-inclusions within goethitised pyrite. (E-J). Au, Ag, Te, S, Bi and Fe X-ray maps by EPMA of the Au-Ag-Te-Bi-bearing goethitised pyrite. (Abbreviations: Gth=goethite, Py=pyrite).

Contrastingly, in the Lupe profile, where gold grains were only recovered from the uppermost 20 cm of the red latosol horizon and from the transported cover, all panned grains are rounded to subrounded with strongly blunt surfaces, and some exhibit transportation marks, mechanical scratching, and etching features (Fig 16). EPMA X-ray maps (Fig. 17) and spot analysis (Fig. 18 and Table 3) conducted on representative free gold grains from both sites indicate that Ag is the only detectable element apart from Au, although traces of Cu, Pd, Cd and Pt were also detected from LA-ICP-MS analysis (Table 4). All the analysed free gold grains from Achman Giraud (collected in the saprolite, mottled zone and red latosol) are chemically homogeneous regarding Ag and Au contents (Fig. 17 A, B and C). These yield Ag contents ranging from 1.5 and 7 wt.% depending on the analysed grain (Fig. 18) together with Cu and Pd concentrations of 200 to 1000 ppm and 0.2 to 1 ppm, respectively. Contrastingly, all the analysed grains from Lupe, collected in the red latosol and in the transported cover, exhibit 5 to 20 µm-large outer rims depleted in Ag (below 2.7 wt.%) and relatively homogeneous cores (from 6.4 to 9.8.wt. %, depending on the analysed grain), with sharp contact between both (Fig. 17 D, E and Fig. 18). Free gold grains from Lupe also yield trace Cu concentrations (200-400 ppm) and Pd with contents between 0.1 and 1.2 ppm. The Cu content of gold grains is thus lower at Lupe (200-400 ppm) than at Achman Giraud (up to 1000 ppm).

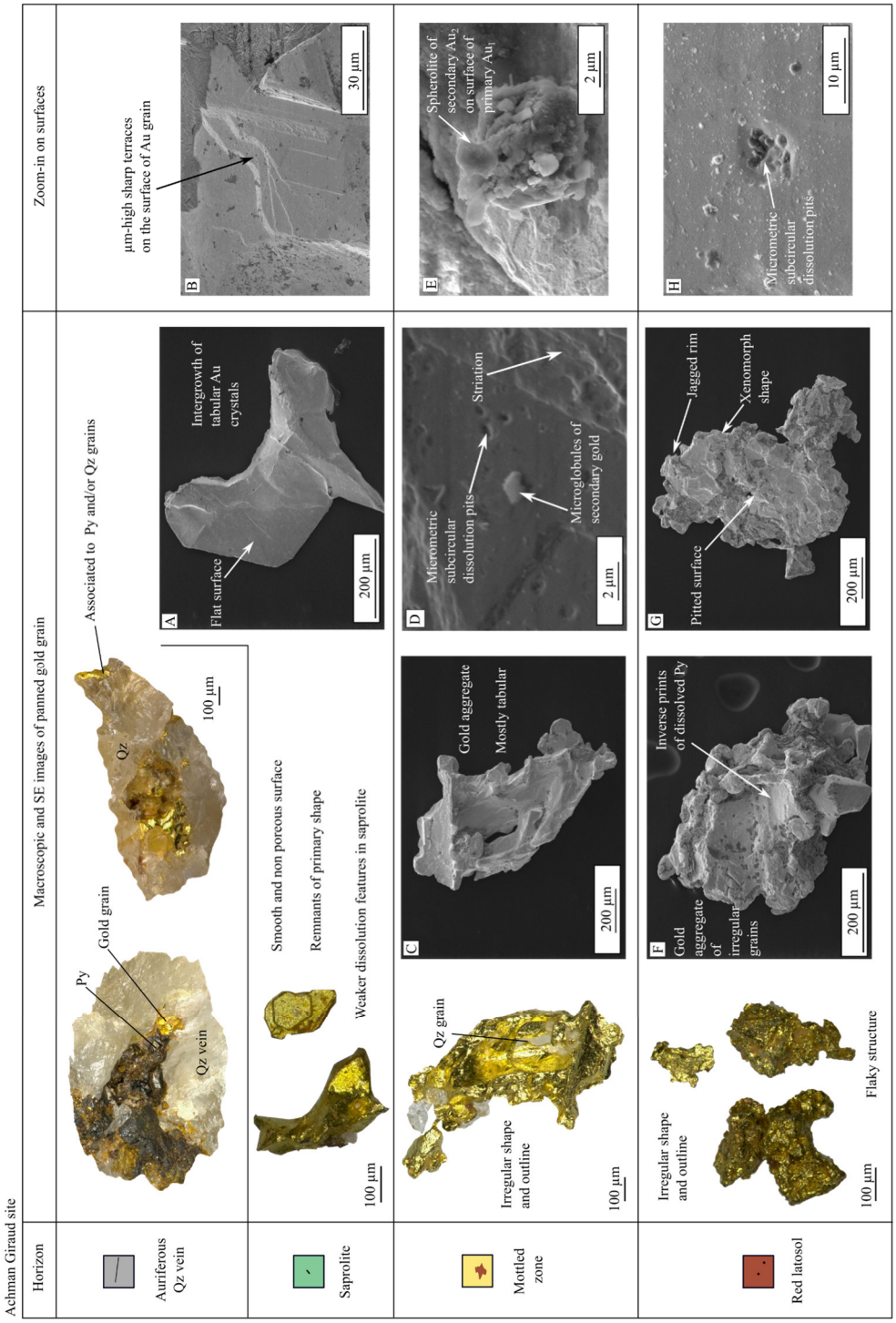

Figure 15 Representative macroscopic images of panned gold grains from each studied horizon at the Achman Giraud site with main characteristics regarding morphologies and surfaces of sampled grains. (A). Tabular grain sampled in saprolite. (B). Typical sharp terraces. (C). Gold aggregate from the mottled zone. (D). A zoom on subcircular dissolution pits and microglobules of secondary gold. (E). Spherolite of secondary Au. (F). An aggregate of irregularly shaped gold grains. (G). Xenomorph grain with pitted surface from the red latosol and (H). Zoom on a subcircular dissolution pit.

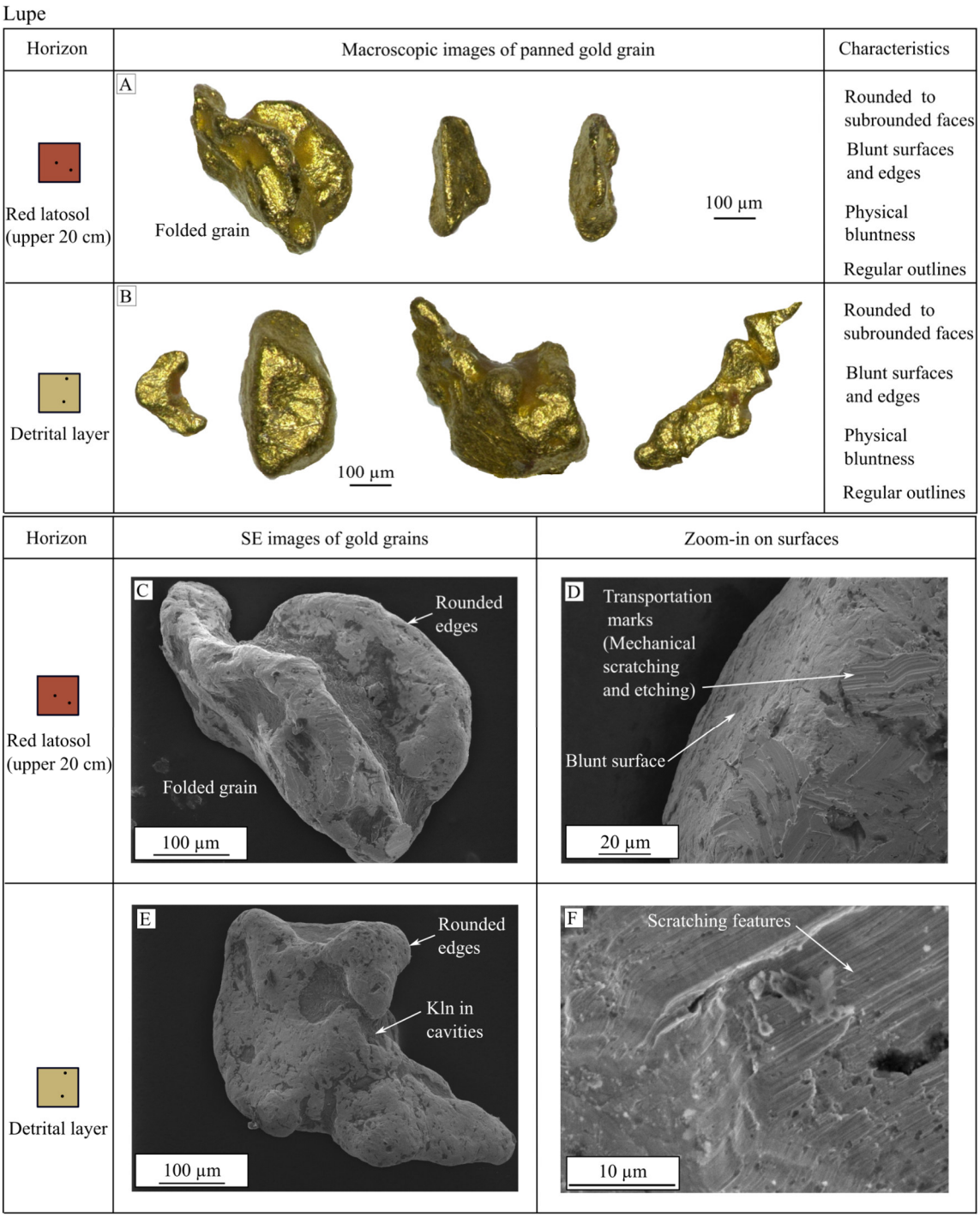

Figure 16 Macroscopic images of grains from the Lupe site. (A). The upper 20 cm of the red latosol. (B). The detrital layer; with SE images (SEM) of (C). Rounded grain from the uppermost red latosol. (D). Rounded grain sampled in the same horizon displaying transportation marks. (E). Rounded grain displaying transportation marks from the detrital layer and (F) Scratching features on a grain from the grain presented in (E).

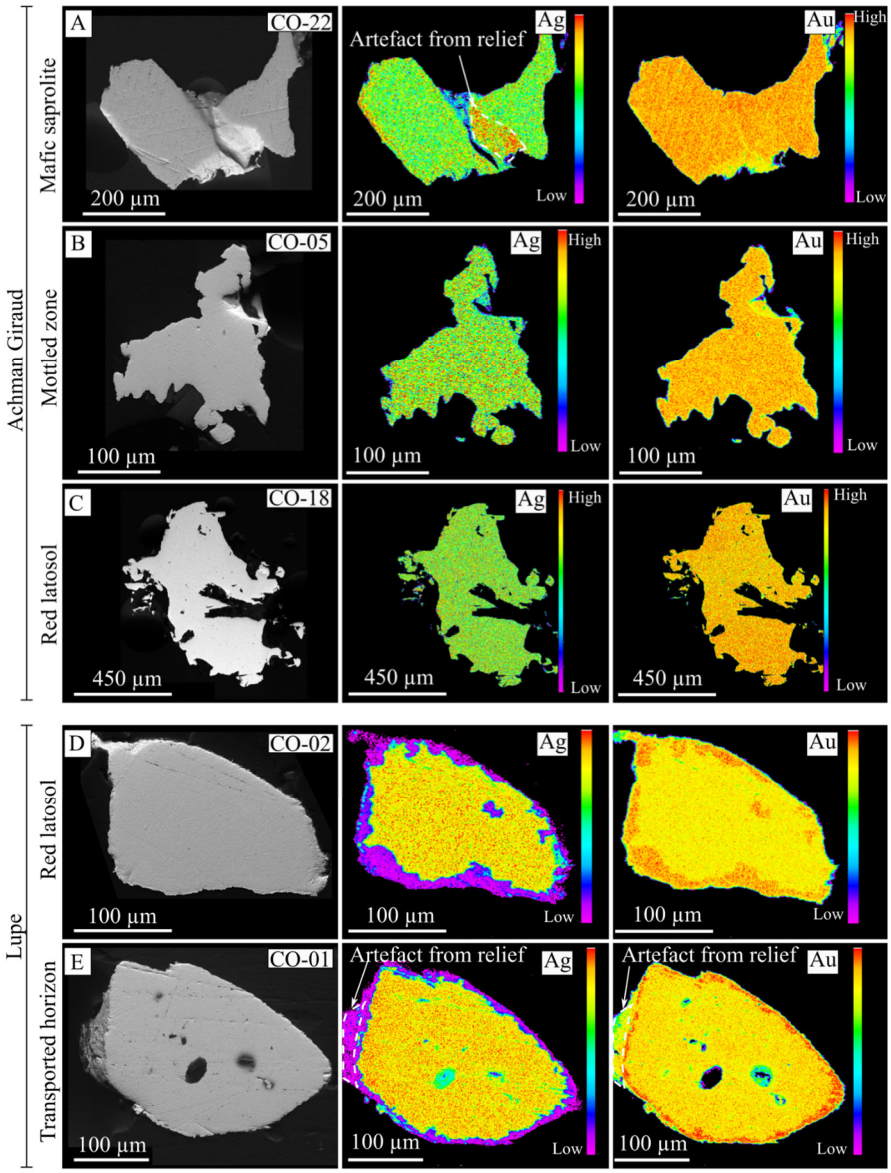

Figure 17 Examples of EPMA mapping (Au and Ag) on panned grains. (A). Homogeneous grain from the saprolite at Achman Giraud. (B). Homogeneous grain from the mottled zone at Achman Giraud. (C). Homogeneous grain from the red latosol at Achman Giraud. (D). Heterogeneous grain from the red latosol at Lupe with Ag-depleted rim and (E). Heterogeneous grain from the transported cover at Lupe with Ag-depleted rim.

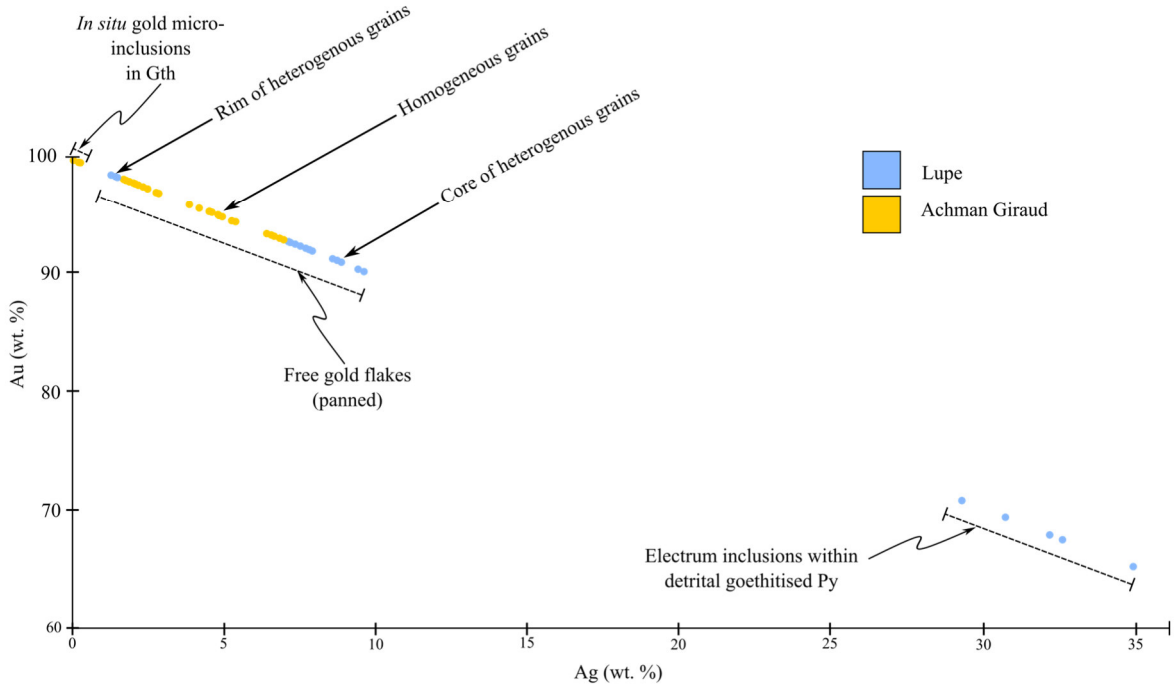

Figure 18 Plot of Au vs Ag in wt. % from EPMA analyses on in situ micro-inclusions in goethite grains and panned grains from all horizons of both sites.

Discussion

Styles, timing and controls on supergene processes at Couriège

The succession of weathering horizons exposed in the Achman Giraud and Lupe lateritic profiles results from the combination of *in situ* weathering, erosion and pedimentation processes related to the regolith landform regimes in which they are situated (Anand et al., 2019; Butt 2016; Chardon et al., 2018). The saprolite horizon is only exposed in the Achman Giraud profile. There, the preservation of the primary rock fabric unequivocally testifies of a purely residual (i.e., not transported) inheritance. Primary pyrite is readily pseudomorphed into goethite in the saprolite; such process is interpreted to take place at the weathering front near the bedrock-saprolite interface (Girard et al., 1997). The nature of the overlying mottled zone and latosol horizons, i.e., *in situ* or remobilised, is more difficult to apprehend, as primary textures are most entirely destroyed. Although it cannot be excluded that material transported

over a lateritic profile may be subsequently weathered to develop mottle textures, the upwards evolution from the saprolite to the mottled clay zone (see Fig. 4C) is mostly typical of in *situ* lateritic weathering, following bleaching of primary lithostructure and segregation of Fe (Tardy et al., 1991; Ghosh & Guchhait, 2015). It is worth noticing that the formation of the mottles seems also accompanied with the segregation of other elements, most notably the preferential incorporation of Cr along mottle edges and the depletion of Ti in the mottles (Fig 12B). Also, the presence of quartz vein relics that persist in the mottled and latosol zones, the absence of stone lines, and the progressive transition between the successive horizons, indicate that latosol and mottled horizons do not derive from transported material. At both sites, the mottled zone directly grades upwards into the latosol horizon while the duricrust is absent. The latosol is therefore interpreted to have formed at the expense of the ancient duricrust, and/or the underlying mottled zone where the duricrust had been eroded away. At Achman Giraud, further support for the authigenic character of the entire exposed profile is provided by the collinear increase of immobile element (Zr, Hf, Th, Ta) concentrations from the unweathered amphibolite to the brown latosol. Such increase in concentration is interpreted to be solely residual, following the leaching and removal of most base cations (including MgO, Na_2O, CaO, K_2O and Ba), which are usually highly mobile under the intense chemical weathering typical of tropical environments (Freyssinet et al., 2005). Noteworthily, goethitised pyrite remains largely preserved throughout the profile with only minor dissolution/recrystallisation features developing at the grain edges, except in the uppermost brown latosol where goethitised pyrite is itself largely recrystallised, as previously described at the Yaou deposit by Girard et al. (2000).

At Lupe, the detrital horizons result from the dismantlement, transport and redeposition of quartz vein and ferricrete carapace material originally situated at a higher elevation. Transport distance was probably short as quartz and duricrust clasts are angular and up to 15 cm-large. Considering (i) the situation of the Lupe site, i.e. on the lower slope portion of the Lupe hill which represents the highest relief of the prospect, (ii) the presence of residual ferricrete locally observed on the hilltop, (iii) the orientation of the red latosol – transported cover interface that is subparallel to the present-day local slope and (iv) the proximal to intermediate nature of transported clasts, it is, therefore, most likely that the detrital cover at the Lupe site comes directly from uphill. Such interpretation suggests that the source of the gold-bearing detrital pyrite is also situated uphill at a moderate distance from the sampling site. Because (i) the limonitic matrix of the transported cover is not duricrusted, (ii) it overlies an already mature

weathering profile as supported by latosol development and intense dismantlement of quartz vein and (iii) the detrital goethitised pyrite crystals often preserve unweathered pyrite cores, it is suggested that the transportation and deposition of the transported cover are relatively recent. Therefore, erosion to redeposition of the transported cover observed at the Lupe site may not only postdate the abandonment of the S1 weathering surface but may also postdate subsequent planation/duricrust formation episodes. Conversely, at the Achman Giraud site, the absence of a transported cover indicates that *in situ* weathering and erosion regimes dominate over deposition regime.

Effects of lateritisation on gold distribution, grades and styles

In supergene environments, residual enrichment, chemical dissolution/reprecipitation, and physical transport are the main processes involved in gold redistribution (Freyssinet et al., 2005). According to Webster and Mann (1984), the style and intensity of gold mobilisation depend on the climate, the bedrock composition, and geomorphological factors. The distribution of gold grades along the investigated profiles, together with the compositional and morphological characteristics of gold, allows to assess the mobility of gold during weathering. The Achman Giraud site provides the opportunity to assess the extent of gold redistribution in a residual lateritic profile developed after a mineralised quartz vein and its host rock. A number of models suggest that the gold redistribution in such residual lateritic profiles may exhibit two mushroom-shaped dispersion zones from the mineralised vein, located at the surficial Fe-rich crust and at the base of the saprolitic horizon (e.g. Costa et al., 1993; Freyssinet et al. 1989a, b; Butt & Smith, 1980 ; Colin and Vieillard, 1991 ; Freyssinet, 1993 ; Freyssinet & Itard, 1997). Such model cannot be verified at the Achman Giraud site as these two horizons were not exposed in profile. Contrarily, our investigations highlight the lack of lateral dispersion of gold (Fig. 10B and C) in the saprolite, mottled zone and red latosol horizons, as Au anomamies are still close to the mineralised veins. This argues either for a limited migration of the gold away from the primary source, or no migration at all, the 20-30 cm corresponding to a primary Au-bearing alteration halo around the vein as commonly observed in orogenic lode gold deposits (Dubé & Gosselin, 2007). On the other hand, it is worth noticing that two samples from the upper red latosol and brown latosol return high grades (> 5 ppm) but are not spatially associated with vein. This may be explained by a redistribution of gold from another mineralised vein situated above and now entirely dismantled, leading to a strong dispersion in the upper

ferruginous horizon, as stated by Freyssinet & Itard, (1997). The relative contribution of the host rock and the quartz veins to the residual quartz budget in the latosol is unclear, as some relicts of quartz-sericite-pyrite aggregates probably inherited from veins are observed. It is nevertheless suggested that the weakly dismantled, main mineralised vein exposed in the profile, contribute little to the global quartz budget of the profile.

The angular morphology, the Au-Ag contents (average fineness of 971) and the Au-Ag homogeneous distribution in free gold grains from the saprolite to the latosol argue that these grains are primary and inherited. Such grains underwent moderate dissolution-reprecipitation, expressed through (i) the increasing presence of circular pits on surfaces and irregular shapes following Au dissolution after exposure to weathering solutions as already shown elsewhere by several authors (Colin et al., 1989; Colin & Vieillard, 1991; Bamba et al., 2002; Larizzatti et al., 2008) and (ii) the rare occurrences of secondary Au_2 spherolites (Fig. 15E) observed on surfaces of primary gold (Au_1), similar to the description of Bamba et al. (2002). It is worth mentioning that according to Freyssinet et al. (1987) secondary gold overgrowths can be destroyed by panning, therefore the few observation of such Au_2 on grain surfaces may not indicate a rare reprecipitation of secondary gold. Santosh and Omana (1991) also describe fine secondary grains in cavities of panned grains but such features have not been observed at Couriège. At the opposite, gold micro-inclusions in the altered pyrite crystals are Ag-free (average calculated fineness of 998) from the saprolite and the red latosol (Fig. 13) and result probably from dissolution of primary Au and reprecipitation (Freyssinet & Butt, 1988; Hough et al., 2007) during the supergene pseudomorphism of pyrite to goethite. Although, a supergene signature is supported by the elevated Au fineness (Mann, 1984; Butt, 1989; Freyssinet et al., 2005 ; Larizzatti et al., 2008), it remains unclear whether these inclusions formed during weathering, or were already present in pyrite and were subsequently depleted in Ag during weathering. The presence of hypogene gold inclusions in unweathered pyrite is indeed common in many orogenic gold deposits where it forms the bulk of the Au mineralisation in association with quartz-carbonate veining (e.g., Combes et al., 2021 and references therein). Together with the lack of lateral gold dispersion from the vein, the primary character of large gold grains and the restricted evidence for secondary gold precipitation argue for a limited influence of supergene processes in the chemical redistribution of gold through the profile, with no clear evidence for supergene enrichment or dispersion. The lack of any significant supergene enrichment can be explained by (1) the weak dismantlement of quartz veins, with gold grains remaining trapped within veins, (2) a poorly developed alteration halo along Au-bearing veins,

with therefore minor amount of gold remobilised in the hostrock, and (3) a limited residual enrichment due to the retention of Si within the profile. Such observations are similar to that of Bowell (1992) at Ashanti in Ghana, with a lack of lateral dispersion of gold and a limited migration of the Au-complexes with mostly local dissolution and re-precipitation. The absence of a mushroom-shape enrichment halo in the Achman Giraud profile is best explained by the lack of duricrust within the truncated profile. Indeed, such haloes have mostly been documented in the uppermost horizons of lateritic profiles (Freyssinet et al., 2005; Sawadogo et al., 2020).

At the Lupe site, gold grains were observed only in the transported cover and within the uppermost 20 cm of the red latosol. Rounded grains with transportation marks clearly demonstrate the involvement of physical transport processes. Moreover, the gold grains collected within the upper red latosol also exhibit some physical transport features; even though this horizon is interpreted as authigenic, it is suggested that mechanical mixing between the transported cover and the underlying latosol may have affected the uppermost 20 cm of the red latosol, so that allogenic gold grains may physically contaminate the barren red latosol. The main geochemical characteristic of rounded grains collected at Lupe is the presence of Ag-poor rims (average fineness of 933 and up to 997 ppm in grain cores and rims, respectively) suggesting that Ag may be removed while Au reprecipitates (Butt & Zeegers, 2015). Such Ag-depleted rims are common within the upper horizons of the lateritic profiles as previously evidenced by Colin & Lecomte (1989); Freyssinet et al. (1989); Collin et al. (1991); Bamba et al. (2002); Larizatti et al. (2008); Falconer & Crow (2009); Fairbrother et al. (2012) and Vishiti et al. (2015) among others. According to Gray et al. (1992), "galvanic reactions on the grain surface, involving simultaneous solution of Ag^{+} and Au^{+} ions", would produce such Ag-poor rims. Contrastingly, the chemical homogeneity and the low average fineness (680 ppm) of the large (up to 200 µm) electrum inclusions hosted by cm-large detrital pyrite grains suggest a primary origin. Nevertheless, the association of these electrum inclusions with Bi dusty inclusions and Te-rich goethite along boxwork textures in the pyrite raises questions about the potential effect of goethitisation on their remobilisation. As for its detrital nature, gold at Lupe is interpreted to be spatially sourced from quartz±pyrite veins likely situated uphill on the Lupe hill (Fig. 2), following physical transport. Whereas the zonation of free gold grains suggest that they underwent significant weathering during or after transport, the absence of zonation in pyrite-hosted electrum grains together with the incomplete goethitisation of pyrite suggest limited effect of weathering on the detrital pyrite. Such observations may suggest a multiple

source of Au in the transported cover, combining material exposed long enough to weathering to produce zonation rims on gold grains with material freshly exposed to weathering so that pyrite goethitisation and Ag leaching in electrum is absent or incomplete. Alternatively, it cannot be excluded that goethitisation of pyrite crystal rims makes it more resistant to weathering compared to free gold grains, thus preserving pyrite core and inclusions from subsequent weathering while free grains become depleted in Ag along their borders. Also, the primary electrum in Lupe detrital pyrite chemically differs from any of the primary gold grains observed at Achman Giraud, suggesting some variability in primary gold styles at the prospect scale. To summarise, the Au-Ag content variations observed at Couriège, as shown in Figure 19, display different types of gold within the lateritic profiles, showing variations in composition (from electrum to Ag-bearing gold) but also supergene chemical modifications such as dissolution and refinement of gold. It is worth noting that our investigations focus on visible gold but do not provide constraints on the potential contribution of invisible gold to the gold budget, in particular in the primary pyrite and in its goethitised supergene counterpart. Nevertheless, it has been suggested that gold sorption is much less efficient on goethite than on pyrite, so that goethite is unlikely to host significant amounts of invisible gold, contrasting with pyrite (Schoonen et al., 1992).

Implications for gold exploration

Gold exploration in weathered and covered terrains commonly relies on the analysis of surface or shallowly collected soil samples that may or may not have a direct genetic relationship with the underlying basement. Comprehensive characterisation of the regolith landscape is therefore required, especially regarding the relict, erosional or depositional nature of the regolith surface (Butt et al., 2000; Arhin and Nude, 2009; Chardon et al., 2018; Sawadogo, 2020). The distinction between *in situ* and transported material within lateritic profiles may rely on several types of observation at different scales. Careful investigation of the relative geomorphic position and lateral extension of landscape elements allow to distinguish residual, erosional and depositional contexts. When exposed, iron duricrusts may prove useful for geochemical vectoring as the formation of residual ferricrete may lead to Au remobilisation and enrichment (Anand, 2019). Such approach requires to distinguish purely residual duricrusted surfaces from duricrusts developed on glacis (Chardon et al., 2018; Sawadogo et al., 2020) through field-based investigations including regolith mapping and textural observations.

Investigations conducted on the truncated, *in situ* laterite profile at Achman Giraud, highlight no significant dispersion of gold from the mineralised veins in saprolite and mottled horizons, although the dispersion may be more pronounced in the overlying residual latosol. In such context where the ferricrete is absent, it is therefore suggested that soil sampling should be prioritised on latosols rather than on mottled zones or saprolites, so that broader dispersion haloes may be more easily identified. On the other hand, the purely *in situ* inheritance of latosol horizons is usually more challenging to assess, and gold anomalies in latosols that are entirely or even partly developed after transported material may lead to false positives and spurious genetic relationships with underlying horizons. The usefulness of pathfinder elements such as Pb, Cu, As, Bi, Te and Ag needs to be further assessed as they may positively correlate with Au (Anand and Butt, 2010; Sunkari et al., 2019). Nonetheless, at Couriège, no specific association of Au with other metals was identified, at the exception that the elevated Au and Bi grades in some samples from Achman Giraud latosol may suggest a potential primary association, (note that Ag and Te were not analysed for whole rock composition). In all cases, the minimisation of the nugget effects requires to sample significant rock volumes.

In detrital-covered profiles, such as the Lupe site, gold surficial enrichment is not indicative of buried mineralisation but derives from one or several sources located at higher elevations in the paleolandscape that prevailed during their transport. Together with surface/soil sampling, the reconstruction of landscape chronology may prove useful in targeting the source of gold anomalies in transported covers and identify false negative and false positive responses at the surface. The morphological and chemical characteristics of transported clasts and gold grains may also provide information on the proximal or distal character of the source. At Lupe, the rather proximal character suggested by the presence of large and angular clasts together with the relative preservation of detrital pyrite is in apparent contradiction with the intermediate to distal character suggested by the presence of rounded and Ag-depleted gold grains. This discrepancy, which may result either from a multiple source and/or a differential alteration of the transported material, highlight that the evaluation of the proximal to distal character of transported covers may be challenging.

Conclusions

This study investigates the style and distribution of gold mineralisation in two lateritic profiles at the Couriège prospect, French Guiana. First, the Achman Giraud profile consists of an *in situ* lateritic profile exposed from the saprolite to the latosol wherein the primary gold mineralisation is associated with sigmoidal quartz±pyrite veins. There, vertical and lateral Au grade distribution demonstrates a weak dispersion of gold not extending farther than 30 cm from the Au-bearing vein into the lateritised host rock. No clear evidence of supergene-related enrichment was found but dispersion is more pronounced in the residual latosol. Gold is observed as (i) free primary Au grains, with increasing dissolution features in the upper horizons together with rare secondary (supergene-related) spherolitic gold overgrowths of high fineness, and (ii) *in situ* supergene micro-inclusions of high fineness within goethitised pyrite crystals. Secondly, the Lupe profile consists of a gold-bearing detrital horizon truncating a barren lateritic profile. The size and angular nature of transported clasts suggest a proximal to intermediate source. Within this horizon, gold is present as (i) free gold grains displaying sub-rounded shapes, mechanical transportation marks on surfaces as well as Ag-depleted rims resulting from supergene leaching of silver, and (ii) primary electrum inclusions within cm-large, partly goethitised pyrite crystals, in association with Bi dusty inclusions and Te-goethite. A complex distribution of gold types within the lateritic profiles is therefore evidenced, witnessing primary differences in composition (from electrum to Ag-bearing gold), supergene chemical modifications (dissolution, refinement of gold, secondary Au formation) and mechanical concentration in allogenic horizons. The identified gold grades are in agreement with Voicu et al. (2001) stating that average Au grades within bedrock- to saprolite-hosted orebodies are ranging between 1.3 and 2.3 g/t Au for most gold deposits of the Guiana Shield. The limited extent of authigenic gold anomalies at surface, due to the weak chemical redistribution of gold during lateritisation, represents a challenge for exploration based on soil sampling. The occurrence of allogenic gold anomalies in soils must also be accounted for, as these are not indicative of underlying mineralisation but may help to trace back an original gold source upslope.

Acknowledgements

This study is part of Vincent Combes's Ph.D. research at the Université de Lorraine within the GeoRessources laboratory, in Nancy, France. We are grateful to O. Rouer and A. Lecomte at the SCMEM and A. Flammang for thin sections manufacturing at the GeoRessources laboratory, in Nancy, France.

Funding

This research was funded by Auplata Mining Group (AMG) and benefited from the framework of the CREGU.

References

Allard, T., Gautheron, C., Riffel, S., Balan, E., Fernandes Soares, B., 2018. Combined dating of goethites and kaolinites from ferruginous duricrusts. Deciphering the Late Neogene erosion history of Central Amazonia. Chem Geol. 479, 136-150.

Anand, R.R., Paine, M., 2002. Regolith geology of the Yilgarn Craton, Western Australia: implications for exploration. Aust. J. Earth Sci. 49, 1–163.

Anand, R.R., Butt, C.R.M., 2010. A guide for mineral exploration through the regolith in the Yilgarn Craton. Aust. J. Earth Sci. 57, 1015–1114.

Anand, R.R., Hough, R.M., Salama, W., Aspandiar, M.F., Butt, C.R.M., Gonzalez-Alvarez, I., Metelka, V., 2019. Gold and pathfinder elements in ferricrete gold deposits of the Yilgarn Craton of Western Australia: a review with new concepts. Ore Geol. Rev. 104, 294-355.

Arhin, E. and P.M. Nude, 2009. Significance of regolith mapping and its implication for gold exploration in Northern Ghana: A case study at Tinga and Kunche. Geochem. Explor. Env. A., 9, 63-69.

Ballo, I., Hein, K.A.A., Guindo, B., Sanogo, L., Ouologuem, Y., Daou, G., Traoré, A., 2016. The Syama and Tabakoroni goldfields, Mali. Ore Geol. Rev. 78, 578-585.

Bamba, O., Parisot, J.C., Grandin, G., Beauvais, G., 2002. Ferricrete genesis and supergene gold behaviour in Burkina Faso, West Africa. Geochem. Explor. Environ. Anal. 2, 3–14.

Benedetti, M., Boulegue, J., 1991. Mechanism of Au transfer and deposition in a supergene environment. Geochim. et Cosmochim Ac. 55, 1539–1547.

Bowell, R.J., Foster, R.P., Gize, A.P., 1993. The mobility of gold in tropical rain forest soils. Econ. Geol. 88, 999–1016.

Butt, C.R.M. and Smith, R.E. (Compilers and Editors), 1980. Conceptual models in exploration geochemistry, 4: Australia. J Geochem Explor. 12: 89-365

Butt, C.R.M., 1989. Genesis of supergene gold deposits in the lateritic regolith of the Yilgarn Block, Western Australia. In: In: Keays, R.R., Ramsay, W.R.H., Groves, D.I. (Eds.), The Geology of Gold Deposits: The Perspective in 1988 8. Econ Geol. Monograph, 460–470.

Butt, C.R.M., 1998. Supergene gold deposits. AGSO J. Geo. Geophys. 17, 89–96.

Butt, C.R.M., Lintern, M., Anand, R.R., 2000. Evolution of regoliths and landscapes in deeply weathered terrain - implications for geochemical exploration. Ore Geol. Rev. 16, 167–183.

Butt, C.R.M., Zeegers, H. (Eds.), 2015. Regolith Exploration Geochemistry in Tropical and Subtropical Terrains Handbook of Exploration Geochemistry 4. Elsevier, Amsterdam (607 pp.).

Butt, C.R.M., 2015. The Development Of Regolith Exploration Geochemistry In The Tropics And Sub-Tropics. Ore Geol Rev. 73, 10.1016

Chardon, D., Grimaud, J.L., Beauvais, A., Bamba, O., 2018. West African lateritic pediments: landform-regolith evolution processes and mineral exploration pitfalls. Earth Sci. Rev. 179, 124–146.

Carignan, J., Hild, P., Mévelle, G., Morel, J., Yeghicheyan, D., 2001. Routine analyses of trace elements in geological samples using flow injection and low pressure on-line liquid chromatography coupled to ICP-MS: a study of reference materials BR, DR-N, UB-N, AN-G and GH. Geostandards Newsletter 25, 187-198.

Chardon, D., Grimaud, J.-L., Beauvais, A., Bamba, O., 2018. West African lateritic pediments: landform-regolith evolution processes and mineral exploration pitfalls. Earth- Sci. Rev. 179, 124–146.

Colin, F., Lecomte, P., Boulange, B., 1989. Dissolution feature of gold particles in a lateritic profile at Dondo Mobi, Gabon. Geoderma 45, 241–250.

Colin, F., and Vieillard, P., 1991, Behavior of gold in lateritic equatorial environment: Weathering and surface dispersion of residual gold particles at Dondo Mobi, GabonJ Appl Geochem. 6, 279–290.

Colin, F., Vieillard, P., and Ambrosi, J. P., 1993, Behavior of gold in lateritic equatorial environment: Mass transfer and thermodynamic study. Earth and Planetary Sci. Lett. 114, 269–285

Combes, V., Eglinger, A., Andre-Mayer, A-S., Teitler, Y., Heuret, A., Gibert, P., Béziat, D., Polyphase gold mineralisation at the Yaou deposit, French Guiana. Accepted at the Geological Society London Special Publication.

Costa M.L., Costa J.A.V., Angélica R.S. 1993. Gold bearing bauxitic laterite in a tropical rain forest climate: Cassiporé, Amapá, Brazil. Chronique de la Recherche Minière, 510, 41-51.

Costa, L.M., 1993. "Gold distribution in lateritic profiles in South America, Africa and Australia: applications to geochemical exploration in tropical regions. J. Geochem. Explor. 47, 143-163.

Craw, D., MacKenzie, D., 2015. Supergene gold mobility in orogenic gold deposits, Otago Schist, New Zealand. N. Z. J. Geol. Geophys. 58 (2), 123–136.

Craw, D., Kerr, G., 2017. Geochemistry and mineralogy of contrasting supergene gold alteration zones, southern New Zealand. J Appl Geochem. 85:19-34.

Daoust, C., Voicu, G., Brisson, H. and Gauthier, M., 2011, Geological setting of the Paleoproterozoic Rosebel gold district, Guiana Shield, Suriname. J South Am Earth Sci. 32, 222–245.

Dardenne, M.A., Schobbenhaus, C., 2003. Metallogeny of the Guiana Shield. Geol. Fr. 2–4, 291–319.

Davy, R., El Ansary, M., 1986. Geochemical patterns in the laterite profile at the Boddington Gold Deposit, Western Australia. J. Geochem. Explor. 26, 119–124.

Delor, C., Lahondère, D., Egal, E., Lafon, J.-M., Cocherie, A., Guerrot, C., Rossi, P., Truffert, C., Théveniaut, H., Phillips, D., Avelar, V.G.d., 2003b. 2-3-4 In: Transamazonian crustal growth and reworking as revealed by the 1:500000 scale geological map of French Guiana. Géol Fr, 5–57.

Delor, C., de Roever, E.W.F., Lafon, J.-M., Lahondère, D., Rossi, P., Cocherie, A., Guerrot, C., Potrel, A., 2003a. The Bakhuis ultrahigh-temperature granulite belt (Suriname) : II. Implications for late Transamazonian crustal stretching in a revised. Géol Fr. 2-3- 4, 207–230.

Dubé, B., and Gosselin, P., 2007, Greenstone-hosted quartz-carbonate vein deposits, in Goodfellow, W.D., ed., Mineral Deposits of Canada: A Synthesis of Major Deposit-Types, District Metallogeny, the Evolution of Geological Provinces, and Exploration Methods: Geological Association of Canada, Mineral Deposits Division, Special Publication No. 5, 49-73.

Eglinger A., André-Mayer A.-S., Combes V., Teitler Y., Heuret A., 2020. Les gisements d'or de la Guyane française. Géologues 206 :36-40.

Fairbrother, L., Brugger, J., Shapter, J., Laird, J.S., Southam, G., Reith, F., 2012. Supergene Au transformation: Biogenic secondary and nano-particulate Au from arid Australia. Chem. Geol. 320, 17–31.

Falconer, D., Craw, D., 2009. Supergene gold mobility: a textural and geochemical study from gold placers in southern New Zealand. Econ Geol. Special Publication 14, 77–93.

Franklin, J., Bertoni, C., Boudrie, M., Bout, J., Costelloe, D., Lillie, F., Millo, L., Sauvage, J., 2000. The Paul Isnard gold–copper occurrence, French Guiana: the first volcanogenic massive sulphide occurrence in the Guiana Shield? In: Sherlock, R., Logan, M.A.V. (Eds.), VMS Deposits of Latin America, Geological Association of Canada, Mineral Deposits Division. Special Publication, pp. 509–542

Freyssinet, P., Zeegers, H. and Tardy, Y., 1987. N6oformation d'or dans les cuirasses latéritiques : dissolution, migration, pr6cipitation. C.R. Acad. Sci., 305 (II): 867-874.

Freyssinet, Ph., Butt, C.R.M., 1988. Morphology and geochemistry of gold in a lateritic profile, Bardoc Mine, Western Australia. Restricted Report, MG 59R. CSIRO Australia, Division of Exploration Geoscience, Perth, pp. 19

Freyssinet, Ph., Lecomte, P., Edimo, A., 1989. Dispersion of gold and base metals in the Mborguene laterite profile. J. Geochem. Explor. 32, 99–116.

Freyssinet, Ph., 1993. Gold dispersion related to ferricrete pedogenesis as South Mali: Application to geochemical exploration. Chron Rech Min. 510, 25–40.

Freyssinet, P., Itard, Y., 1997. Geochemical Mass Balance of Gold Under Various Tropical Weathering Conditions: Application to Exploration, In "Proceedings of Exploration 97: Fourth Decennial International Conference on Mineral Exploration" edited by A.G. Gubins, 347–354

Freyssinet, Ph., Butt, C.R.M., Morris, R.C., Piantone, P., 2005. Ore-forming processes related to lateritic weathering. In: Hedenquist, J.W., Thomson, J.F.H., Goldfarb, R.J., Richards, J.P. (Eds.), Economic Geology 100th Anniversary Volume, Econ Geol. 681–722

Freyssinet, P., Farah, A., 2000. Geochemical mass balance and weathering rates of ultramafic schists in Amazonia. Chem Geol.170, 133-151.

Girard, J.-P., Razanadranorosoa, D., Freyssinet, P., 1997. Laser oxygen isotope analysis of weathering goethite from the lateritic profile of Yaou, French Guiana: paleoweathering and paleoclimatic implications. Appl. Geochem. 12, 163– 174.

Girard J.-P., Freyssinet P., and Chazot G., 2000. Unravelling climatic changes from intraprofile variation in oxygen and hydrogen isotopic composition of goethite and kaolinite in laterites: An integrated study from Yaou, French Guiana. Geochim. et Cosmochim Ac. 64, 409-426

Ghosh, S., Guchhait, S., 2015. Characterization and evolution of primary and secondary laterites in northwestern Bengal Basin, West Bengal, India. Jof Palaeogeography. 4, 203 -230.

Gray, D.J., Butt, C.R.M., Lawrance, L.M., 1992. The geochemistry of gold in lateritic terrains. In: Butt, C.R.M., Zeegers, H. (Eds.), Regolith Exploration Geochemistry in Tropical and Subtropical Terrains. Handbook of Exploration Geochemistry, 4. Elsevier, Amsterdam, pp. 461–482.

Guiraud, J., Tremblay, A., and Jebrak, M., 2017, The Rhyacian Montangne d'Or auriferous volcanogenic massive sulphide deposit, French Guiana, South America: Stratigraphy and geochronology [ext. abs.]: Society for Geology Applied to Mineral Deposits, 14th Biennial Meeting, Québec City, August 20–23, 2017, Extended Abstracts, p. 237–240.

Guiraud, J., Tremblay, A., Jébrak, M., Ross, P-S., Lefrançois, R., 2020. Stratigraphic setting and timing of the Montagne d'Or deposit, a unique Rhyacian Au-rich VMS deposit of the Guiana Shield, French Guiana, Precambr. Res. 337, 105551.

Horbe, A.M.C., Martins-Ferreira, M.A.C., Lima, R.S., 2019. Supergene gold characterization by geochemistry, grain morphology and Au-Ag-Cu-Te classification. J. S. Am. Earth Sci. 95, 102315.

Hough, R., Noble, R., Reich, M., 2011. Natural gold nanoparticles. Ore Geol Rev. 42, 55-61

Kovacs, R., Schlosser, S., Staub, S., Schmiderer, A., Pernicka, E., Günther, D., 2009. Characterization of calibration materials for trace element analysis and fingerprint studies of gold using LA-ICP-MS. J Anal At Spectrom. 24. 10.1039/b819685k.

Larizzatti, H., Oliveria, S.M.B., Butt, C.R.M., 2008. Morphology and composition of gold in a lateritic profile, Fazenda Pison "Garimpo", Amazon, Brazil. J. S. Am. Earth Sci. 25, 359–376

Lafrance, J., Bardoux, M., Voicu, G., Stevenson, R., Machado, N., 1999. Geological and metallogenic environments of gold deposits of the Guiana Shield; a comparative study between St-Elie (French Guiana) and Omai (Guyana). Explor. Min. Geol. 8, 117–135.

Ledru, P., Lasserre, J., Manier, E., Mercier, D., 1991. Le Proterozoique inferieur nord guyanais ; revision de la lithologie, tectonique transcurrente et dynamique des bassins sedimentaires.
Bull Soc Geol Fr. 162, 627–636.

Mann, A.W., 1984. Mobility of gold and silver in lateritic weathering profiles, some observations from Western Australia. Econ Geol. 79, 38–49.

Marcoux, É., Milési, J.-P., 1993. Lead isotope signature of early Proterozoic ore deposits in western Africa; comparison with gold deposits in French Guiana. Econ. Geol. 88, 1862–1879.

MacFarlane, M.J., 1983. Laterites. In: A.S. Goudie and K. Pye (Editors), Chemical sediments and Geomorphology. Academic Press Inc., London, 430 pp.

McGregor, G.R., Nieuwolt, S., 1998. Tropical Climatology. Wiley., 339 pp.

Meyer, H., Cauzid, J., 2020. Hameye /MARCIA: MARCIA v 0.1.0. doi:10.5281/zenodo.3929745

Middlemost E.A.K., 1994. Naming materials in magma/igneous rock system. Earth Sci Rev 37:215–224

Milési, J.-P., Egal, E., Ledru, P., Vernhet, Y., Thiéblemont, D., Cocherie, A., Tegyey, M., Martel-Jantin, B., Lagny, P., 1995. Les minéralisations du Nord de la Guyane française dans leur cadre géologique. Chron Rech Min. 518, 5–59.

Milesi, J., Lerouge C, Delór C, Ledru P, Billa M, Cocherie A, Egal E, Fouillac A, Lahondère D, Lasserre J, Marot A, Martel-Jantin B, Rossi P, Tegyey M, Théveniault H, Thiéblemont D, Vanderhaeghe, O., 2003. Gold deposits (gold-bearing tourmalinites, gold-bearing conglomerates, and mesothermal lodes), markers of the geological evolution of French Guiana: geology, metallogeny, and stable isotope constraints. Géol Fr, 2-3-4:257-290.

Nahon, D., Introduction to the Petrology of Soils and Chemical Weathering, 1991. John Wiley & Sons, Inc., New York. 313 p.

Patton, C., Hellstrom, J., Paul, B., Woodhead, J. Hergt, J., 2011. Iolite: freeware for the visualization and processing of mass spectrometry data. J. Anal. At. Spectrom. 26: 2508–2518.

Perera, W., Senanayake, Ga., Nicol, M., 2005. Interaction of gold(I) with thiosulfate–sulfite mixed ligand systems. Inorg Chim Acta. 358, 2183-2190.

Picot, J. C, Chevillard, M., 2015. Potentiel aurifère de la Guyane - Note de synthèse BRGM

Pokrovski, G., Akinfiev, N., Borisova, A., Zotov, A., Kouzmanov, K., 2014. Gold speciation and transport in geological fluids: Insights from experiments and physical-chemical modelling. 10.1144/SP402.4.

Santosh, M., Omana, P.K., 1991. Very high gold from lateritic weathering profiles of Nilambur, southern India. Geology 19, 46–749.

Sawadogo, B., Bamba, O., Chardon, D., 2020. Landform-regolith mapping in the West African context. Ore Geol Rev.126, 103782.

Schoonen, M.A.A., Fisher, N., Maryann, W., 1992., Gold sorption onto pyrite and goethite: A radiotracer study. Geochim Cosmochim Acta. 56, 1801-1814

Sunkari, E. D., Appiah-Twum, M., Lermi, A. 2019, Journal of African Earth Sciences, 158, 103519

Tardy, Y., Kobilsek, B., Paquet, H., 1991. Mineralogical composition and geographical distribution of African and Brazilian periatlantic laterites: The influence of continental drift and tropical paleoclimates during the past 150 million years and implications for India and Australia. J Afr Earth Sci. 12(1-2): 283-295.

Tedeschi, M., Hagemann, S.G., Davis, J., 2018. The Karouni Gold Deposit, Guyana, South America: part I. Stratigraphic Setting and Structural Controls on Mineralization. Econ Geol. 113, 1679–1704

Théveniaut, H., Freyssinet, Ph.,2002. Timing of lateritization on the Guiana Shield: Synthesis of paleomagnetic results from French Guiana and Suriname. Palaeogeography, Palaeoclimatology, Palaeoecology. 178. 91-117.

Vanderhaeghe, O., Ledru, P., Thiéblemont, D., Egal, E., Cocherie, A., Tegyey, M., Milesi, JP., 1998. Contrasting mechanism of crustal growth: Geodynamic evolution of the Paleoproterozoic granite–greenstone belts of French Guiana. Precambrian Res. 92:165–193.

Velásquez, G., Béziat, D., Salvi, S., Siebenaller, L., Borisova, A.Y., Pokrovski, G.S., and De Parseval, P., 2014, Formation and deformation of pyrite and implications for gold mineralization in the El Callao district, Venezuela. Econ Geol. 109, 457–486.

Vishiti, A., Suh, C., Lehmann, B., Egbe, J.A., Shemang, E., 2015. Gold grade variation and particle microchemistry in exploration pits of the Batouri gold district, SE Cameroon. J Afr Earth Sci. 111. 1-13.

Voicu, G., Bardoux, M., Stevenson, R., 2001. Lithostratigraphy, geochronology and gold metallogeny in the northern Guiana Shield, South America: a review Ore Geol Rev. 18, 211–236.

Webster, J. G.; Mann, A. W. 1984: The influence of climate, geomorphology and primary geology on the supergene migration of gold and silver. J. Geochem. Explor. 22, 21-42.

Zotov, A., Kuzmin, N., Reukov, V., Tagirov, B., 2018. Stability of $AuCl2^-$ from 25 to 1000 °C at Pressures to 5000 bar and Consequences for Hydrothermal Gold Mobilization. Minerals. 8. 286.

Supplementary material:

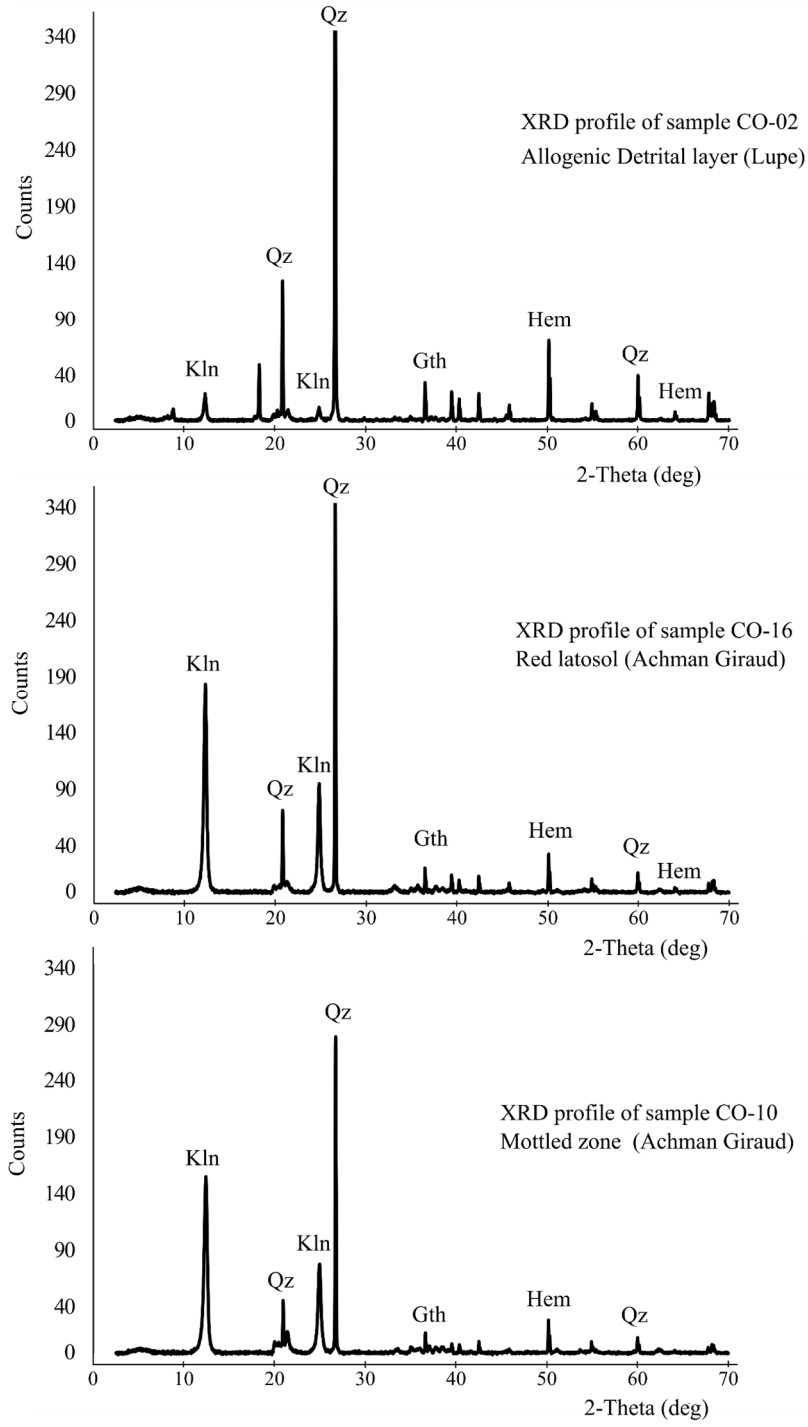

Figure 19 Example of X-ray diffraction (XRD) patterns of samples from different horizons (detrital layer, red latosol and mottled zone). Abbreviations: Qz= quartz, Gth=goethite, Hem=hematite, Kln=kaolinite.

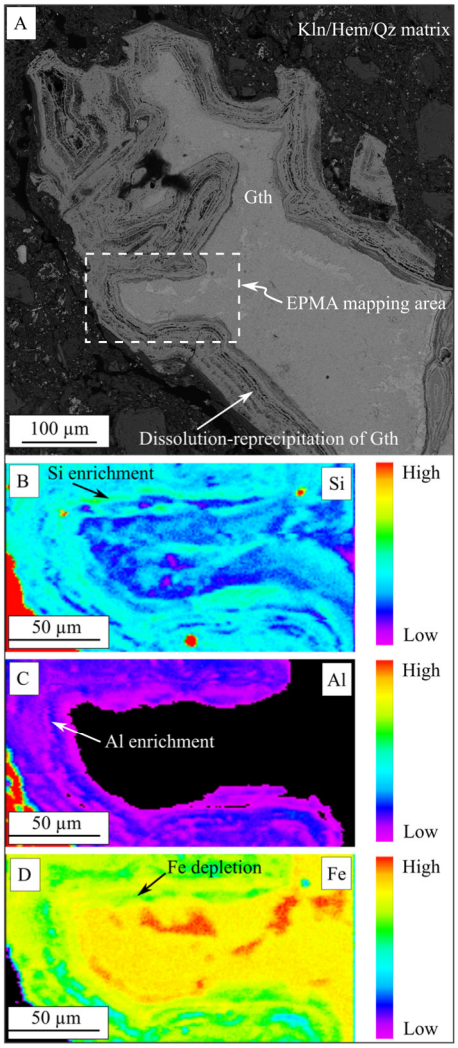

Figure 20 (A). BSE image of a goethitised pyrite with colloform dissolution-reprecipitation at the rim. (B-D). Si, Al and Fe X-ray maps by EPMA showing Si-Al enrichment and Fe depletion along the colloform rims. (Abbreviations: Gth=goethite).

Tables

Table 1. Major and trace element compositions of samples collected along the vertical P1 transect at Achman Giraud

Sample ID	Horizon	Zr_ppm	As_ppm	Ba_ppm	Be_ppm	Bi_ppm	Cd_ppm	Co_ppm	Cr_ppm	Cs_ppm	Cu_ppm	Ga_ppm	Ge_ppm	Hf_ppm	In_ppm	Mo_ppm	Nb_ppm	Ni_ppm	Pb_ppm	Rb_ppm	Sb_ppm
CO-14	Red latosol	179,24	bdl	11,37	0,55	0,22	0,04	4,56	109,23	0,06	40,49	29,14	1,81	4,73	0,07	0,6	7,43	64,45	8,86	0,47	0,07
CO-15	Red latosol	174,58	bdl	17,56	0,76	0,49	0,03	4,9	119,89	0,04	46,46	28,16	1,77	4,6	0,06	bdl	7,28	62,04	7,86	0,39	bdl
CO-16	Red latosol	154,46	bdl	21,18	0,72	2,65	0,03	6,72	242,94	0,05	65,96	27,7	1,8	4,03	0,07	0,62	6,67	92,56	7,57	0,49	bdl
CO-17	Red latosol	171,87	0,67	10,66	0,45	0,2	0,03	3,52	167,23	0,07	34,45	27,36	1,64	4,56	0,07	1,07	7,67	32,52	8,12	0,43	0,09
CO-18	Red latosol	194,13	0,53	64,67	0,9	0,87	0,04	9,13	191,03	0,09	82,53	38,44	2,09	5,07	0,12	bdl	8,91	84,85	11,75	1,53	0,07
CO-19	Red latosol	168,3	bdl	35,42	0,74	0,56	0,04	8,44	315,13	0,1	61,08	32,03	2,05	4,47	0,1	bdl	7,49	68,79	9,98	2,57	bdl
CO-20	Red latosol	156,69	0,51	18,51	0,72	0,3	0,05	6,76	128,93	0,07	49,89	25,57	1,89	4,15	0,06	bdl	6,45	59,64	12,31	1,03	0,07
CO-21	Red latosol	141,06	0,54	17,87	0,59	0,31	0,05	10,13	140,48	0,06	73,69	23,65	1,92	3,71	0,06	bdl	5,98	67,94	12,38	0,53	0,08
CO-22	Saprolite	91,62	0,5	60,41	0,46	0,78	0,04	60,06	174,31	0,07	115,21	18,53	2,02	2,4	0,05	0,87	3,96	130,28	19,72	0,6	0,06
CO-23	Saprolite	145,05	0,77	50,96	0,64	0,43	0,07	31,86	180,88	0,07	80,82	24,82	1,9	3,78	0,05	0,76	5,83	69,71	48,78	1,23	0,11
CO-24	Saprolite	164,08	2,47	48,96	0,61	0,76	0,21	20,58	139,54	0,09	143,66	28,5	1,68	4,22	0,05	0,54	6,65	52,17	46,08	1,67	0,35
CO-25	Saprolite	192,47	4,93	198,14	0,62	1,65	0,36	54,09	176,55	0,48	196,07	33,69	2,33	5,03	0,06	1,59	7,42	89,31	109,55	18,14	0,7
CO 33	Bedrock	118,61	bdl	893,64	0,92	0,17	0,06	26,95	120,68	0,66	136,02	18,35	1,39	3,09	0,05	0,68	4,53	44,36	7,21	44,93	0,07

Sample ID	Horizon	Sc_ppm	Sn_ppm	Sr_ppm	Ta_ppm	Th_ppm	U_ppm	V_ppm	W_ppm	Y_ppm	Zn_ppm	Zr_ppm	La_ppm	Ce_ppm	Pr_ppm	Nd_ppm	Sm_ppm	Eu_ppm	Gd_ppm	Tb_ppm	Dy_ppm
CO-14	Red latosol	24,35	1,33	bdl	0,67	5,33	1,89	203,65	0,88	2,15	49,62	179,24	1,17	12,09	0,4	1,63	0,51	0,23	0,45	0,09	0,61
CO-15	Red latosol	27,32	1,52	0,85	0,67	5,21	2,05	219,97	5,84	2,89	71,91	174,58	1,62	11,23	0,47	1,83	0,59	0,29	0,58	0,13	0,89
CO-16	Red latosol	23,95	1,49	bdl	0,59	4,62	1,98	192,48	4,01	2,91	85,67	154,46	1,09	6,36	0,35	1,37	0,5	0,25	0,54	0,13	0,93
CO-17	Red latosol	32,28	1,4	1,63	0,7	5,18	1,65	207,87	bdl	2,76	32,85	171,87	2,6	19,84	0,68	2,63	0,62	0,22	0,55	0,09	0,64
CO-18	Red latosol	30,54	2,36	1,16	0,75	5,94	2,51	275,62	2,8	3,88	81,34	194,13	2,04	11,15	0,5	1,95	0,7	0,34	0,79	0,18	1,28

CO-19	Red latosol	30,52	1,87	0,74	0,65	5,12	2,63	259,05	1,99	3,63	45,5	168,3	2,07	13,13	0,45	1,76	0,61	0,3	0,67	0,15	1,05
CO-20	Red latosol	24,84	1,35	3,4	0,58	4,57	2,7	189,65	0,88	3,22	42,51	156,69	6,06	13,9	0,89	2,93	0,72	0,3	0,68	0,13	0,9
CO-21	Red latosol	23,73	1,4	4,24	0,54	4,36	2,41	171,67	bdl	2,93	32,78	141,06	5,37	17,23	0,89	3,03	0,68	0,26	0,6	0,12	0,8
CO-22	Saprolite	24,94	0,97	0,91	0,35	2,69	2,15	152,6	1,18	2,18	45,31	91,62	2,2	605,62	0,54	1,9	0,54	0,21	1,69	0,12	0,59
CO-23	Saprolite	24,22	1,49	17,56	0,52	4,25	2,33	168,94	1,62	4,33	42,02	145,05	93,54	260,29	12,94	33,47	4,53	1,17	2,79	0,34	1,74
CO-24	Saprolite	30,05	3,11	9,97	0,61	4,79	2,36	179,8	2,03	3,58	35,61	164,08	30,45	134,26	5,35	15,68	2,39	0,68	1,52	0,2	1,09
CO-25	Saprolite	26,83	5,79	12,74	0,69	5,56	2,48	212,07	2,09	20,72	82,64	192,47	86,65	285,87	19,27	73,06	12,32	3,25	7,86	0,87	4,6
CO 33	Bedrock	18,99	1,04	662,82	0,43	3,85	1,51	132,42	bdl	12,65	67,43	118,61	21,74	43,41	5,36	21,04	4,03	1,25	3,04	0,42	2,42

Sample ID	Horizon	Ho_ppm	Er_ppm	Tm_ppm	Yb_ppm	Lu_ppm	SiO_2_wt. %	Al_2O_3_wt. %	Fe_2O_3_wt. %	MnO_wt. %	MgO_wt. %	CaO_wt. %	Na_2O_wt. %	K_2O_wt. %	TiO_2_wt. %	P_2O_5_wt. %	P_wt. %	Total
CO-14	Red latosol	0,13	0,4	0,07	0,66	0,11	57,49	20,55	11,6	0,02	bdl	bdl	bdl	bdl	1,01	bdl	9,35	100,02
CO-15	Red latosol	0,19	0,56	0,1	0,86	0,14	57,56	19,54	12,46	0,02	bdl	bdl	bdl	bdl	1,01	bdl	9,67	100,26
CO-16	Red latosol	0,19	0,58	0,11	0,92	0,15	62,82	17,22	11,15	bdl	bdl	bdl	bdl	bdl	0,91	bdl	8,23	100,33
CO-17	Red latosol	0,14	0,42	0,08	0,66	0,11	56,53	20,49	12,22	0,04	bdl	bdl	bdl	bdl	1,07	bdl	10,04	100,39
CO-18	Red latosol	0,26	0,76	0,14	1,17	0,18	53,49	22,61	12,68	0,03	bdl	bdl	bdl	0,06	1,11	bdl	10,33	100,31
CO-19	Red latosol	0,22	0,67	0,12	1,03	0,16	52,42	24,03	11,02	0,02	0,04	bdl	bdl	0,09	0,94	bdl	11,36	99,92
CO-20	Red latosol	0,18	0,54	0,1	0,84	0,14	54,59	22,97	10,45	0,02	0,03	bdl	bdl	0,04	0,87	bdl	10,74	99,69
CO-21	Red latosol	0,17	0,5	0,1	0,8	0,13	52,36	25,07	10,17	0,02	bdl	bdl	bdl	bdl	0,81	bdl	11,52	99,95
CO-22	Saprolite	0,13	0,38	0,07	0,59	0,1	53,58	26,14	7,42	0,08	0,03	bdl	bdl	bdl	0,49	bdl	11,95	99,69
CO-23	Saprolite	0,29	0,77	0,13	1,02	0,17	62,26	19,49	9,17	0,05	0,04	bdl	bdl	0,04	0,72	bdl	8,62	100,4
CO-24	Saprolite	0,19	0,53	0,09	0,76	0,13	54,57	24,35	9,4	0,02	0,07	bdl	bdl	0,06	0,79	bdl	10,86	100,11
CO-25	Saprolite	0,89	2,37	0,36	2,42	0,39	49,21	25,82	10,71	0,07	0,75	bdl	bdl	0,52	0,85	bdl	12,45	100,37
CO 33	Bedrock	0,47	1,28	0,19	1,25	0,19	62,91	15,41	6,58	0,07	2,43	5,77	2,63	1,58	0,59	0,15	1,42	99,52

Table 2. Gold grade analyses for each sample from Achman Giraud and Lupe sites.

Sample ID	Horizon	Au (ppm)
CO-02	Red latosol	0,23
CO-03	Mottled zone	0,05
CO-04	Mottled zone	0,07
CO-05	Mottled zone	0,61
CO-06	Mottled zone	0,28
CO-07	Mottled zone	0,3
CO-08	Mottled zone	0,1
CO-09	Mottled zone	0,03
CO-10	Mottled zone	0,48
CO-11	Saprolite	0,64
CO-14	Red latosol	7,14
CO-15	Red latosol	0,22
CO-16	Red latosol	4,89
CO-17	Red latosol	0,37
CO-18	Red latosol	1,01
CO-19	Red latosol	0,41
CO-20	Red latosol	0,16
CO-21	Red latosol	0,3
CO-22	Saprolite	5,39
CO-23	Saprolite	0,31
CO-24	Saprolite	0,24
CO-25	Saprolite	0,28
CO-26	Red latosol	0,05
CO-27	Red latosol	0,08
CO-28	Red latosol	0,07
CO-29	Red latosol	1,11

Table 3. EPMA analyses of Ag and Au for all gold types sampled at Achman Giraud and Lupe.

Sample ID	Horizon	Gold type	Ag (ppm)	Au (ppm)
P1-g18-1	Red latosol	Free gold (panned)	1,99	99,25
P1-g18-2	Red latosol	Free gold	2,2	98,68
P1-g18-3	Red latosol	Free gold	2,4	98,56
P1-g18-4	Red latosol	Free gold	1,76	99,35
P1-g5-1	Mottled zone	Free gold	2,31	97,82
P1-g5-2	Mottled zone	Free gold	2,33	98,25
P1-g5-3	Mottled zone	Free gold	2,45	98,39

Sample ID	Horizon	Gold type	Ag (ppm)	Au (ppm)
P3-g22-3	Saprolite	Free gold	2,91	98,81
P3-g19-1	Red latosol	Free gold	2,05	99,28
P3-g19-2	Red latosol	Free gold	2,06	98,13
P3-g19-3	Red latosol	Free gold	2,06	99,16
P3-g19-4	Red latosol	Free gold	1,71	98,14
P3-g19-5	Red latosol	Free gold	4,27	97,22
P3-g19-6	Red latosol	Free gold	4,73	98,01

P2-g5-1	Mottled zone	Free gold	2,3	98,92	P3-g19-7	Red latosol	Free gold	4,6	96,65
P2-g5-2	Mottled zone	Free gold	2,3	99,38	P3-g19-8	Red latosol	Free gold	4,84	96,48
P2-g5-3	Mottled zone	Free gold	2,33	100,32	P4-g02-1	Red latosol	Free gold	7,79	94,21
P2-g5-4	Mottled zone	Free gold	2,4	97,62	P4-g02-2	Red latosol	Free gold	7,28	92,96
P2-g5-5	Mottled zone	Free gold	2,26	98,85	P4-g02-3	Red latosol	Free gold	7,78	93,92
P2-g5-6	Mottled zone	Free gold	2,15	97,89	P4-g02-4	Red latosol	Free gold	7,85	93,01
P2-g5-7	Mottled zone	Free gold	2,33	98,33	P4-g02-5	Red latosol	Free gold	7,38	92,67
P2-g5-8	Mottled zone	Free gold	2,34	99,5	P4-g01-2	Detrital layer	Free gold	2,64	98,14
P2-g5-9	Mottled zone	Free gold	2,67	98,27	P4-g01-3	Detrital layer	Free gold	2,44	98,87
P2-g5-10	Mottled zone	Free gold	2,83	97,44	P4-g01-4	Detrital layer	Free gold	0,28	101,54
P2-g2-1	Red latosol	Free gold	7,69	93,29	P4-g01-5	Detrital layer	Free gold	8,98	93,09
P2-g2-2	Red latosol	Free gold	7,72	93,25	P4-g01-6	Detrital layer	Free gold	8,77	93,17
P2-g2-3	Red latosol	Free gold	7,98	93,74	P4-g01-7	Detrital layer	Free gold	9,82	93,08
P2-g2-4	Red latosol	Free gold	7,5	93,22	P4-g01-8	Detrital layer	Free gold	8,75	92,33
P2-g2-5	Red latosol	Free gold	3,85	95,27	P4-g19-1	Red latosol	Free gold	2,11	98,87
P2-g2-6	Red latosol	Free gold	6,42	91,56	P4-g19-2	Red latosol	Free gold	2	97,96
P2-g18-1	Red latosol	Free gold	1,98	99,12	P4-g19-3	Red latosol	Free gold	1,34	94,93
P2-g18-2	Red latosol	Free gold	1,74	99,53	P4-g19-4	Red latosol	Free gold	4,8	94,28
P2-g18-3	Red latosol	Free gold	2,26	99,46	P4-g19-5	Red latosol	Free gold	5,45	96,92
P3-g27-1	Red latosol	Free gold	1,47	99,72	P4-g19-6	Red latosol	Free gold	5,43	95,58
P3-g27-2	Red latosol	Free gold	1,56	99,24	P4-g21-1	Red latosol	Free gold	6,82	93,92
P3-g27-3	Red latosol	Free gold	1,84	97,32	P4-g21-2	Red latosol	Free gold	6,68	94,24
P3-g27-4	Red latosol	Free gold	1,78	100,26	P4-g21-3	Red latosol	Free gold	7,17	94,33
P3-g27-5	Red latosol	Free gold	1,98	98,55	P4-g21-4	Red latosol	Free gold	6,9	94,04
P3-g27-6	Red latosol	Free gold	1,46	98,38	P4-g21-5	Red latosol	Free gold	6,3	91,87
P3-g18-1	Red latosol	Free gold	1,85	97,87	P4-g21-6	Red latosol	Free gold	2,46	99,31
P3-g18-2	Red latosol	Free gold	2,12	99,42	P4-g21-7	Red latosol	Free gold	2,07	98,25
P3-g18-3	Red latosol	Free gold	1,74	99,65	P4-g21-8	Red latosol	Free gold	2,31	98,26
P3-g18-4	Red latosol	Free gold	2,2	98,5	P4-g21-9	Red latosol	Free gold	1,41	98,58
P3-g18-5	Red latosol	Free gold	2,19	99,35	P4-g21-10	Red latosol	Free gold	1,72	98,86
P3-g16-1	Red latosol	Free gold	2,28	98,47	P4-g21-11	Red latosol	Free gold	1,61	99,06
P3-g16-2	Red latosol	Free gold	2,26	98,44	P4-g21-12	Red latosol	Free gold	1,84	98,22
P3-g16-3	Red latosol	Free gold	2,22	97,2	P4-g21-13	Red latosol	Free gold	1,92	99,77
P3-g16-4	Red latosol	Free gold	2,09	97,2	16-IN-1	Red latosol	Micro-inclusion	0,1	99,5
P3-g16-5	Red latosol	Free gold	4,57	96,52	16-IN-2	Red latosol	Micro-inclusion	0,1	99,5
P3-g16-6	Red latosol	Free gold	4,29	97,71	16-IN-3	Red latosol	Micro-inclusion	0,1	99,5
P3-g16-7	Red latosol	Free gold	4,88	94,72	16-IN-4	Red latosol	Micro-inclusion	0,1	99,5
P3-g16-8	Red latosol	Free gold	4,68	96,66	16-IN-5	Red latosol	Micro-inclusion	0,1	99,5
P3-g05-1	Mottled zone	Free gold	2,39	99,12	32A	Detrital layer	Micro-inclusion	32,6	67,4
P3-g05-2	Mottled zone	Free gold	2,92	97,73	32A	Detrital layer	Micro-inclusion	32,2	67,8
P3-g05-3	Mottled zone	Free gold	2,62	98,22	32A	Detrital layer	Micro-inclusion	30,8	69,2

P3-g05-4	Mottled zone	Free gold	2,69	98,92	32A	Detrital layer	Micro-inclusion	35	65
P3-g22-1	Saprolite	Free gold	2,49	99,33	32A	Detrital layer	Micro-inclusion	29,3	70,7
P3-g22-2	Saprolite	Free gold	2,69	96,73					

Table 4. Trace element compositions of panned free gold grains (LA-ICPMS) and corresponding EPMA analyses of Ag at the same spot. (**= EPMA)

Sample ID	Horizon	Cu	Pd	Cd	Cr	Fe	Rh	Sb	Pt	Bi	Cd	Ag109 (*), (ppm)	Ag (**), (wt%)
Detection limit *maximum value*		0,519	0.098	0.026	0.266	5.645	0.008	0.029	0.009	0.004	0.026	0,421	
P1-01	Red latosol	688	0,42	0,61	bdl	bdl	bdl	bdl	0.023	bdl	0.612	40590	4,04
P1-3	Red latosol	454,8	0,23	0,31	bdl	bdl	bdl	bdl	bdl	bdl	0.309	30070	3,76
P1-4	Red latosol	431,4	0,28	0,22	bdl	bdl	bdl	bdl	0.014	bdl	0.218	20260	2,28
P1-5	Red latosol	422	0,56	0,27	bdl	bdl	bdl	bdl	bdl	bdl	bdl	19790	2,67
P1-6	Red latosol	1021	0,33	0,9	bdl	bdl	0.008	bdl	0.014	bdl	0.903	19770	2,2
P1-7	Red latosol	1017	0,36	1,1	bdl	bdl	0.010	bdl	0.010	bdl	1.097	19990	2,2
P1-8	Red latosol	1023	0,37	1,07	bdl	bdl	bdl	0.090	0.013	bdl	1.066	19870	2,4
P1-9	Mottled zone	777	0,91	0,48	bdl	bdl	bdl	bdl	bdl	bdl	bdl	20010	2,2
P1-10	Saprolite	739	0,31	0,03	bdl	bdl	0.008	bdl	0.017	bdl	0.027	30020	4,22
P1-11	Saprolite	766	0,28	0,02	bdl	bdl	bdl	bdl	0.013	bdl	bdl	29730	4,08
P1-12	Saprolite	759	0,33	0,02	bdl	bdl	0.011	bdl	bdl	bdl	bdl	29800	3,98
P1-13	Saprolite	757	0,56	0,02	bdl	bdl	bdl	bdl	0.010	bdl	bdl	30200	3,88
P1-14	Saprolite	770	0,29	0,03	bdl	bdl	bdl	bdl	0.015	bdl	0.029	30140	3,98
P1-15	Mottled zone	686	0,79	0,29	bdl	bdl	bdl	bdl	bdl	bdl	bdl	20290	2,33
P2-1	Mottled zone	616	0,32	0,32	bdl	bdl	bdl	0.111	0.017	0.018	0.375	19840	2,33
P4-4	Red latosol	262	0,21	0,14	bdl	bdl	bdl	bdl	bdl	bdl	bdl	10100	1,34
P3-3	Red latosol	504	0,34	0,42	bdl	bdl	bdl	bdl	0.018	bdl	0.417	20450	2,37
P3-4	Red latosol	512	0,3	0,29	bdl	bdl	bdl	bdl	bdl	bdl	bdl	30160	3,81
P3-7	Red latosol	1152	0,45	1,81	bdl	bdl	bdl	bdl	bdl	bdl	bdl	19920	2,19
P3-8	Red latosol	442,3	0,24	0,84	bdl	bdl	bdl	bdl	bdl	bdl	bdl	20180	2,22
P3-9	Red latosol	376,8	0,22	0,71	bdl	bdl	bdl	bdl	bdl	bdl	bdl	19970	2,28
P3-10	Red latosol	432	0,54	0,14	bdl	bdl	bdl	bdl	bdl	bdl	bdl	39100	4,88
P3-11	Mottled zone	466	0,43	0,5	0.320	bdl	bdl	bdl	0.016	bdl	0.498	19520	2,92
P3-12	Mottled zone	461	0,45	0,57	bdl	7.100	bdl	bdl	0.016	0.008	0.571	20260	2,62
P3-14	Saprolite	299,6	0,21	0,1	bdl	bdl	bdl	bdl	0.012	bdl	0.095	19880	2,91

P3-15	Saprolite	300,4	0,2	0,1	bdl	bdl	bdl	bdl	0.010	bdl	0.096	20160	2,91
P3-16	Saprolite	615	0,5	3,14	bdl	bdl	bdl	bdl	bdl	bdl	bdl	19790	2,91

* correspond to ^{109}Ag because the ^{107}Ag is used as the internal standard

Chapitre 5

Discussion générale, conclusions et perspectives

Dans cette thèse, le couplage de données structurales, pétro-géochimiques, isotopiques, géochronologiques et géophysiques a permis de définir (1) le cadre pétro-structural des phases de minéralisation primaire à l'échelle du gisement de Yaou, (2) l'architecture litho-structurale et son évolution temporelle à l'échelle du district de Yaou et (3) les processus d'enrichissement supergènes dans le prospect de Couriège.

A partir des apports fermes découlant des travaux de cette thèse, mais également d'aspects plus spéculatifs inévitables considérant le peu de données disponibles (forages non orientés, peu d'affleurement de roche fraiche), les interprétations proposées permettent de discuter des minéralisations aurifères en Guyane française dans le cadre du système métallogénique (Wyborn et al., 1994 ; McCuaig and Hronsky, 2014 ; Wyman et al., 2016 ; Hronsky, 2019 et Groves et al., 2020b) en considérant les paramètres critiques (Fig. 1) que sont :

- *Une architecture lithosphérique propice*
- *Un cadre géodynamique favorable*
- *Une fertilité géochimique en éléments sidérophiles*
- *Et une préservation post-minéralisation du dépôt primaire*

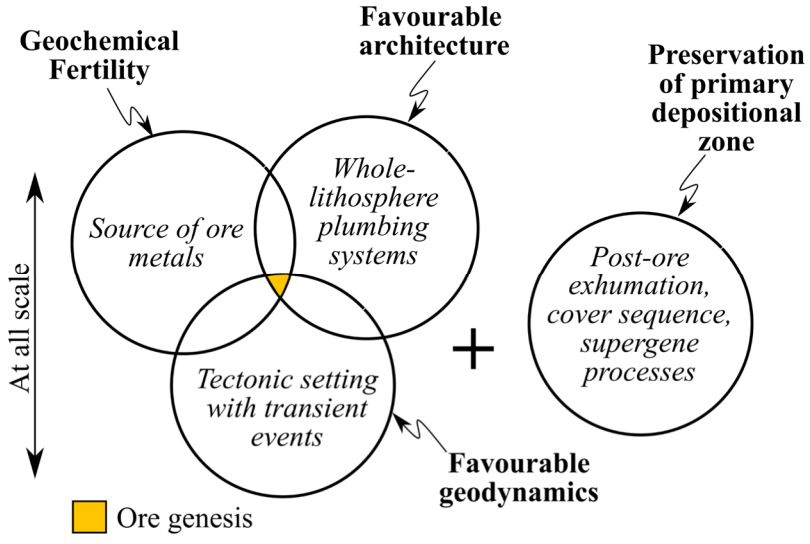

Figure 5-1 Éléments critiques d'un système métallogénique (modifié d'après McCuaig & Hronsky, 2014). Le dépôt aurifère se produit lorsque les paramètres suivants sont réunis. : architecture lithosphérique favorable, cadre géodynamique favorable, fertilité géochimique et préservation post-minéralisation du gisement primaire.

Architecture lithosphérique propice

Dans un système métallogénique de type or orogénique, une architecture favorable à l'échelle de la lithosphère est nécessaire pour assurer la circulation des fluides aurifères au travers de la croûte (McCuaig and Hronsky, 2014, Groves et al., 2020b). En effet, les travaux de synthèse de Groves et al. (2000) ou Goldfarb et al. (2005) soulignent la relation spatiale des minéralisations aurifères avec des zones de déformation qu'elles soient dans le domaine fragile (faille) ou ductile (zone de cisaillement). Pour cette thèse, aucun travail n'a été réalisé à cette échelle mais il est important de préciser que les deux sites minéralisés de cette étude, Yaou et Couriège, sont situés à proximité de grandes zones de cisaillement à l'échelle lithosphérique héritées de l'orogenèse transamazonienne (Fig. 2 ; Vanderhaeghe et al., 1998) comme la *SGSZ* (South Guiana Shear Zone ; Lasserre et al., 1989) au sud de Yaou et la *NGT* (North Guiana Trough ; Ledru et al., 1991) au nord de Couriège.

A plus petites échelles, celles du district (10^2 à 10^4 km²) et du camp (1 à 10^2 km²), cette thèse a caractérisé l'architecture litho-structurale (chapitres 2 et 3) en proposant un modèle sur la distribution des intrusifs de type Yaou et leur relation spatiale et temporelle avec de possibles couloirs de cisaillement interprétés en géophysique. Ici un modèle spéculatif est proposé n'ayant pas de données structurales à cette échelle. Néanmoins nos résultats et ce modèle permettent une meilleure compréhension de la géologie du district et apportent des pistes pour le ciblage de l'or dans la région.

Cette approche multiscalaire a été également conduite à encore plus petites échelles, celles du gisement (10^{-2} à 1 km²) et de la minéralisation (macro- à microscopique) en intégrant dans un cadre pétro-structural (chapitre 2) les évènements aurifères de Yaou. L'ensemble des observations et interprétations qui dérivent de cette approche est illustré sur la Figure 2. A partir des observations de terrain (cartographie et carottes de forage) et de pétrographie que les intrusifs de type Yaou (quartz monzodiorite) ont été interprétés comme anté- à syn-déformation, se mettant en place dans des couloirs de cisaillement orientés N60°. La minéralisation aurifère à Yaou étant principalement encaissée par ces intrusifs, les couloirs de cisaillement orientés N60° deviennent alors des métallotectes pour prospecter de futurs indices à l'échelle du district. Afin de poursuivre cette étude, de nouvelles données géophysiques (relevé magnétique au sol avec inversion par exemple) seraient nécessaires afin de définir précisément la localisation et la géométrie de ces corps intrusifs.

A l'échelle du camp minéralisé, ces nombreux corps intrusifs de quartz monzodiorite sont effectivement alignés le long de la *Central Yaou Shear Zone* (*CYSZ* ; Fig. 2), zone de cisaillement sénestre qui s'étend sur plus de 4,5 km avec une direction NE-SO. Un modèle pétro-structural en cinq phases de déformation à l'échelle du gisement est proposé à partir de données découlant de l'étude des carottes mais également d'aspects plus spéculatifs, notamment les données structurales en contexte saprolitique :

- Deux phases de déformation ductile $D_{1/2YA}$ qui se traduisent par une schistosité subverticale principale et pénétrative S_2 observée dans les métavolcanites et métasédiments, ainsi que par la présence de veines à quartz-calcite transposées dans cette fabrique régionale ;
- Une phase de déformation non-coaxiale, notée D_{3YA}, qui s'exprime, à l'échelle cartographique par la déflection de la schistosité régionale S_2 le long d'une zone de cisaillement, et à l'échelle macroscopique à microscopique par de le développement d'une fabrique de type C/S (interprétée comme C/S_3) affectant principalement les métasédiments ; L'événement intrusif (quartz monzodiorite) est identifié comme étant anté à syn-cisaillement D_{3YA} ;
- Une phase de déformation fragile-ductile D_{4YA} représentée par un ensemble de veines de quartz-carbonate, subhorizontales hébergées préférentiellement dans les corps intrusifs par contraste rhéologique ;
- Une dernière phase de déformation fragile D_{5YA} caractérisée par le développement de brèches affectant localement ces veines centimétriques D_{4YA}, observées dans les corps intrusifs.

L'étude de la déformation à partir de carottes de forage a suivi une approche par phase permettant de mieux contraindre les évènements aurifères à l'échelle du gisement sachant que (1) l'âge absolu de chaque phase n'est pas connu excepté pour la phase D_{4YA} de façon indirecte (datation Re-OS des Py_4) et (2) qu'aucune orientation des contraintes locales n'est établie (pas orientation des carottes). Alternativement, une approche par continuum proposant une déformation progressive (Fossen et al., 2019) est envisageable, avec une activation de la schistosité régionale S_2 effective tout au long du fonctionnement de la zone de cisaillement, et la formation de veines de quartz-carbonates subhorizontales syn- à tardi- cisaillement.

À l'échelle macroscopique, l'étude pétro-structurale des carottes de forage de Yaou, associée à une caractérisation de la distribution des teneurs or en roche totale et du cadre structural précédemment défini, permet d'identifier deux événements hydrothermaux aurifères qui contrôlent l'enrichissement global en or de Yaou. Ils sont associés respectivement aux phases de déformation D_{3YA} (associé aux Py_3) et D_{4YA} (associé aux Py_4). Le stade économique D_{4YA}, avec or visible, est associé à une forte pyritisation (Py_4) localisée dans un halo d'altération à ankérite-hématite-albite.

Cette étude démontre ainsi un polyphasage de l'enrichissement en or avec successivement un contrôle :

(1) Lithologique pour l'or Au_{D0YA} hébergé dans des unités métasédimentaires au sein de pyrite diagénétique et/ou hydrothermales avec une association Au-As comme décrit précédemment par Large et al., (2009 ; 2011) notamment ;
(2) Structural pour l'or Au_{D3YA} hébergé dans la zone de cisaillement. Ce contrôle, documenté dans les gisements d'or orogénique (Chauvet, 2019b, Blenkinsop et al., 2020 par exemple) est essentiel pour le ciblage de zones minéralisées ;
(3) Rhéologique pour l'or Au_{D4YA} hébergé par les corps intrusifs où la fréquence des veines économiques D_{4YA} est élevée. Ce contrôle est aussi observé dans le Bouclier Guyanais à Omai au Guyana (Voicu et al., 1999) et à Karouni (Tedeschi et al., 2018a, b) au Guyana également, où les veines aurifères se développent préférentiellement dans des corps intrusifs.

Afin de compléter cette étude, de nouveaux forages orientés sont nécessaires à Yaou, afin d'obtenir des mesures structurales robustes, notamment l'orientation des veines D_{4YA}.

Pour conclure, le gisement de Yaou se forme donc par phases successives d'apport et/ou de remobilisation d'or lors d'évènements hydrothermaux associés à une histoire tectonique complexe enregistrée par le Bouclier Guyanais au cours du Paléoprotérozoïque. Les travaux de thèse apportent une meilleure compréhension de l'architecture à différentes échelles dans un contexte où les données structurales sont rares.

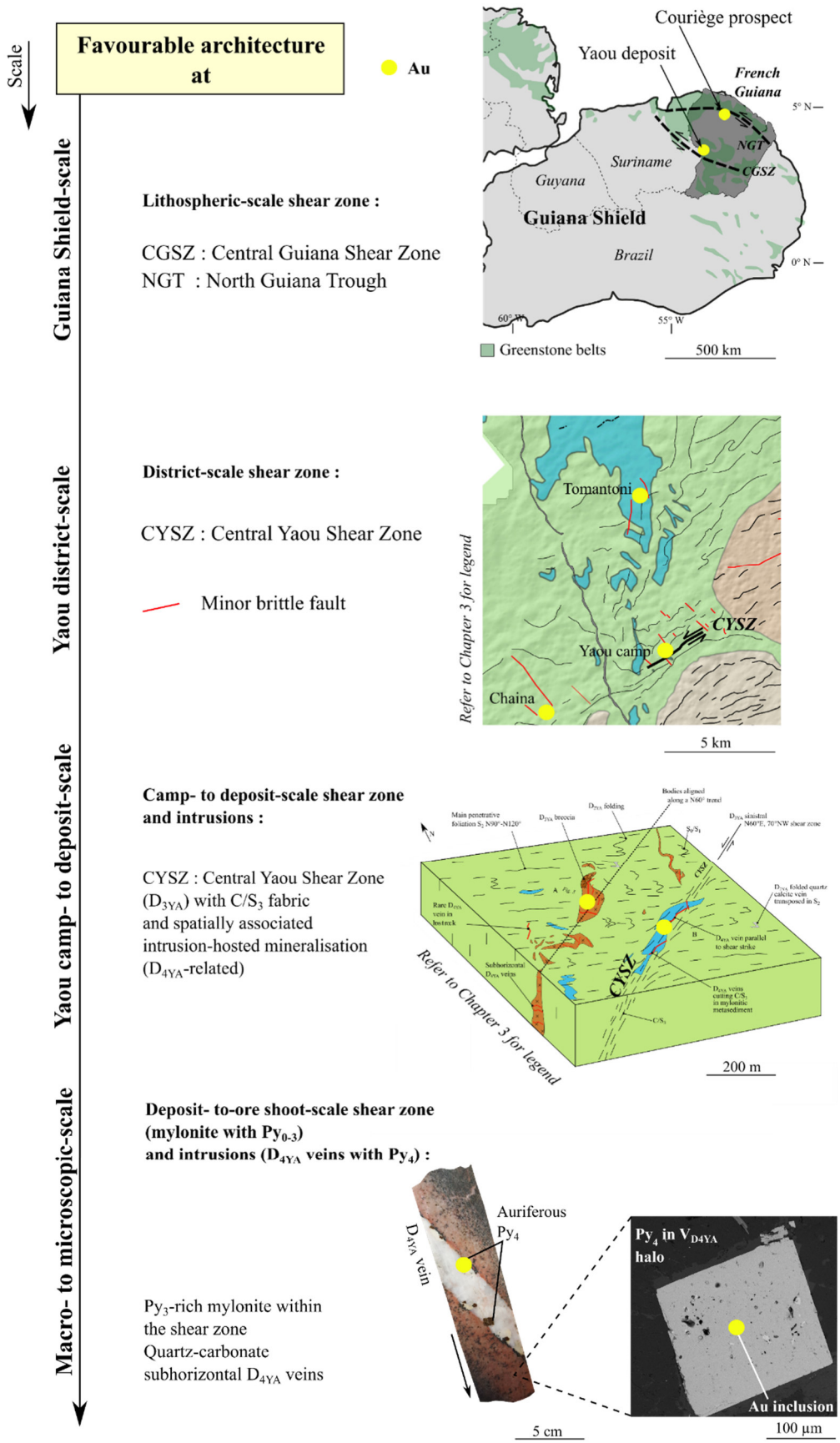

Figure 5-2 Importance d'une architecture favorable multi-échelle pour le piégeage de l'or.

Cadre géodynamique favorable

Le cadre géodynamique du district de Yaou est peu contraint par manque d'étude et de datation absolue.

Cette thèse a permis la datation de l'événement magmatique (quartz monzodiorite datée par U-Pb sur zircon), de l'évènement de pyritisation aurifère Py_4 (datation Re-Os sur pyrite) mais également de proposer un calage relatif de la phase de cisaillement (chapitres 2 et 3). Une tentative d'intégration de ces résultats dans le cadre régional établi par les travaux de Gibbs (1980), Ledru et al. (1991), Gibbs and Barron (1993), Vanderhaeghe et al. (1998), Voicu et al. (2001), Delor et al. (2003a, b), Enjolvy (2008) et Kroonenberg et al. (2016) est proposé dans le chapitre 3 et dans la figure de synthèse suivante (Fig. 3) en considérant les datations absolues disponibles pour quelques gisements du Bouclier Guyanais. Les phases de déformation établies à l'échelle du gisement (notées D_{XYA}) peuvent se corréler avec les phases proposées par Delor et al. (2003a, b) comme suit : (1) $D_{1/2YA}$ ferait référence à la phase de déformation régionale D_1 (formation d'arc(s) magmatique(s) en contexte de subduction, ~2180-2130 Ma) avec une convergence N-S ; (2) la phase D_{3YA} serait lié à la phase régionale D_{2a} (collision arcs/continent et tectonique transcurrente, ~2110-2080 Ma) et (3) la D_{4YA}/D_{5YA} pourrait également correspondre au D_{2a} régional selon la datation Re-Os à 2110±30 Ma et 2101±17 Ma. Néanmoins, au regard de la dispersion du peu de données géochimiques et géochronologiques à l'échelle de la Guyane française, il est évident que cette évolution est sujette à débat et que localement ces fourchettes d'âge (incluant leurs incertitudes) ne coïncident pas avec les données acquises. Ici, nous suggérons que la phase de compression D_1 (équivalente du $D_{1/2YA}$) se termine plus tôt qu'initialement proposé par Delor et al. (2003a) car l'intrusion (datée à ~2130 Ma) est clairement post-D_{2YA}. De plus, la phase de déformation D_{2a} (datée entre ~2110 et 2080 Ma), interprétée comme correspondant à la phase D_{3YA} à Yaou, pourrait commencer plus tôt comme illustré sur la Figure 3 qui synthétise les différentes phases de déformation et périodes de magmatisme (âge absolu + erreur) au cours de l'orogenèse transamazonienne. La phase de déformation D_{2a} n'a été datée que dans la ceinture nord du PGB et non dans la ceinture sud où se trouve le gisement de Yaou ce qui peut expliquer le diachronisme entre le modèle de Delor et al. (2003a, b) et celui de cette étude. Concernant l'évènement aurifère principal, il succède à la phase de convergence régionale D_1 ($D_{1/2YA}$) et se produit durant la phase de tectonique transcurrente ($D_{2a, b}$) soit entre ~2130 et 2050 Ma. L'étude géochronologique de l'intrusif principal de Yaou indique un évènement magmatique à 2130,6 ± 5,8 Ma (U-Pb sur zircon) en

accord avec la seconde génération de TTG (Enjolvy, 2008). La minéralisation aurifère est postérieure à cet âge, les veines aurifères étant clairement post-intrusion et datés indirectement par la méthode Re-Os sur pyrites Py_4. Notre étude confirme les conclusions de Milesi et al. (2003) considérant que lors du second stade de recyclage crustal (tardi-D_1) et d'accrétion tectonique (D_2 régionale), les minéralisations aurifères orogéniques se sont mises en place en Guyane. Cependant, ces mêmes travaux définissent de « petits stocks de granite tardi-D_2 régionale » comme porteurs préférentiels de veines aurifères. Les datations relatives et absolues provenant de cette thèse montrent que les corps intrusifs de quartz monzodiorite sont clairement anté-D_{4YA} et de ce fait pré-à syn-D_2 régionale (D_{3YA}) et non tardi-D_2. Une intégration du système minéralisé de type or orogénique à l'échelle du Bouclier Guyanais est malheureusement hasardeuse du fait du manque d'études approfondies. Cependant, on peut citer les récents travaux menés à Karouni (Guyana) où la minéralisation aurifère a été datée à 2084 ± 15 Ma (U-Pb sur titanite) par Tedeschi et al. (2019).

Pour conclure, bien que les données de datation disponibles soient peu nombreuses, les apports de cette thèse permettent de proposer une phase aurifère principale à Yaou bien intégrée dans un cadre géodynamique favorable régionale, à savoir lors de la phase de déformation $D_{2a/b}$ régionale (Vanderhaeghe et al., 1998 ; Delor et al., 2003a, b) marquée par un processus de coulissage sénestre des blocs continentaux convergents (Delor et al., 2003a).

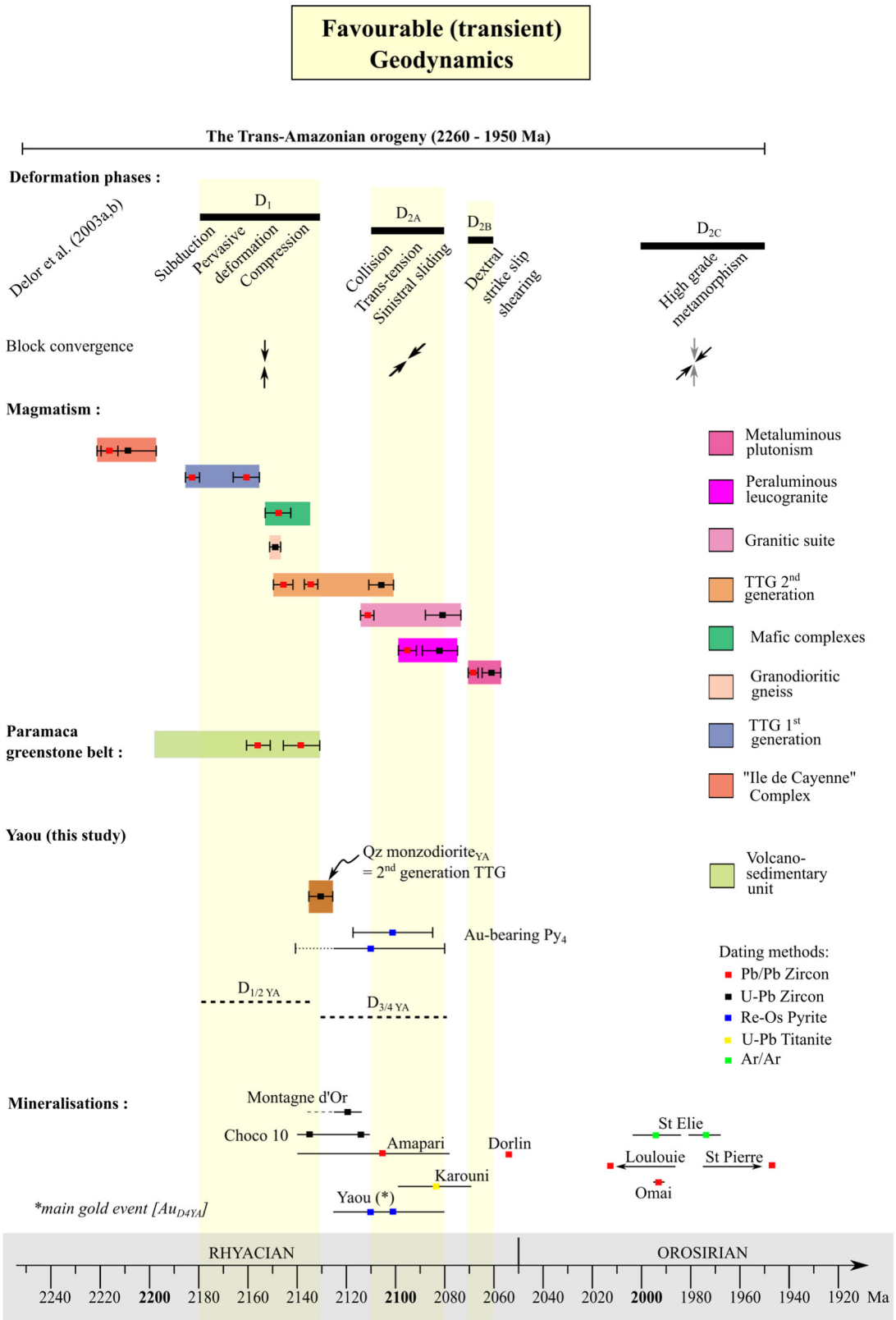

Figure 5-3 Le gisement de Yaou au sein de l'orogenèse transamazonienne, références datation Vanderhaeghe et al. (1998) ; Lafrance et al. (1999) ; Lerouge et al. (1999) ; Voicu et al. (2001), Delor et al. (2003a, b) ; Enjolvy (2008) ; Kroonenberg et al. (2016) ; Padoan et al. (2014) ; Tedeschi et al. (2019) ; Guiraud et al. (2020) and Combes et al. (2021).

Fertilité géochimique en éléments sidérophiles

Différentes caractéristiques lithologiques, géochimiques et isotopiques traduisent la fertilité géochimique de la ceinture de roches vertes du Paramaca, partie nord et sud qui héberge les gisements de Yaou et Dieu-Merci. Cependant, cet aspect n'a que très peu été étudié au cours de cette thèse, c'est pourquoi ce chapitre est assez succinct. De nouvelles données géochimiques et isotopiques à l'échelle du craton seraient nécessaires pour avoir une réflexion plus globale.

A Yaou, comme à Couriège, l'encaissant principal de la zone appartient à l'unité du Paramaca (métavolcanite à Yaou et amphibolite à Couriège). Les lithologies observées dans cette unité du Paramaca sont peu différenciées, constituées principalement de roches magmatiques ultramafiques à mafiques ainsi que de roches volcano-sédimentaires de composition mafique à intermédiaire. A l'échelle du Bouclier Guyanais, comme le montrent les travaux de Cassard et al. (2008), les indices en or connus ou supposés sont localisés préférentiellement dans les métavolcanites et métasédiments du Paramaca (*Lower Volcano-sedimentary unit*) ou aux contacts entre ces derniers et les complexes de TTG (Milesi et al., 2003 ; Delor et al.,2003b). Ces roches (métavolcanites et métasédiments) représentent ainsi des sources potentielles d'or orogénique (Phillips and Groves, 1983 ; Groves et al. 1998 ; Pitcairn et al., 2006 ; Large et al., 2009 ; Phillips and Powell, 2010) par leur faible différenciation (Patten et al., 2020). En ce sens, les données isotopiques εHf_t de l'intrusif de Yaou daté à 2.13 Ga varient entre +1.3 and +4.2 pour un âge modèle entre 2,4 et 2,6 Ga (Fig. 3-10) et traduisent donc cet apport juvénile avec la remobilisation d'une croûte rhyacienne (Fig. 3-10).

Ces données peuvent être opposées à celles récemment publiées par Vianna et al. (2020) sur des granitoïdes d'âge paléoprotérozoïque du domaine de Lourenço dans la région de l'Amapá (Nord Brésil), toujours dans le Bouclier Guyanais. Les signatures εHf_t comprises entre −3.5 à −4.3 et −6.6 à −12.5 (dite sub-chondritiques) sont obtenues sur zircon témoignent quant à elles toujours d'une remobilisation d'une croûte juvénile mais aussi d'une contribution de fragments d'une croûte continentale d'âge Archéen (nucléus Archéen adjacent, Amapá) lors de la collision arc(s)-continent (Vianna et al., 2020).

Préservation post-minéralisation du gisement primaire

La préservation d'un gisement primaire est essentielle. En contexte latéritique comme en Guyane française, la préservation et la modification sont à prendre en considération. La minéralisation préexistante est affectée par des processus supergènes associés au développement de profils d'altération latéritique. Une synthèse est présentée Figure 4 illustrant l'histoire hypogène Rhyacienne et supergène (Eocène à tardi-Miocène) à partir des observations issues des chapitres 2 et 4.

L'étude de ces processus secondaires supergènes est importante en Guyane, où les gisements exploités actuellement ou par le passé sont uniquement de type secondaire (saprolitique *in situ*, colluvionnaire ou alluvionnaire). L'exploitation de telles minéralisations se fait dans des horizons latéritiques (essentiellement dans l'horizon saprolitique facilement exploitable) et dans les placers ou paléo-placers. Le gisement de Yaou, bien qu'exploité par le passé (2006 à 2013) dans sa partie saprolitique, ne se prêtait pas à une étude détaillée des enrichissements supergènes. En effet, les affleurements sont quasi-inexistants lors de la réalisation de cette thèse et les carottes de forage étudiées n'intersectaient pas de zones minéralisées affectées par des processus supergènes. Il est à noter que des travaux antérieurs portant sur les profils latéritiques de Yaou ont été réalisés. La pédologie, minéralogie et géochimie du profil de Yaou sont décrits par Freyssinet (1994) et Farah (1994) avec un profil latéritique tronqué comprenant un sol ferralitique, un horizon humique marron, un horizon ocre, un horizon de transition orange pale conservant des textures primaires ainsi qu'une saprolite développée sur schistes mafiques et intrusifs intermédiaires. Une étude détaillée des processus supergènes similaires à celle faite dans le prospect de Couriège serait intéressante une fois la découverture de zones d'échantillonnage réalisée.

Les travaux de thèse présentés dans les chapitres précédents ont ainsi permis de comparer et de corréler les processus primaires et secondaires à partir des sites de Yaou et Couriège. Bien que la minéralisation hypogène ne soit pas observée en profondeur sur le second site, cette étude met en évidence une diversité des types d'or au sein du régolite de Couriège, témoignant à la fois de différences de composition d'or primaire et de modifications chimiques supergènes.

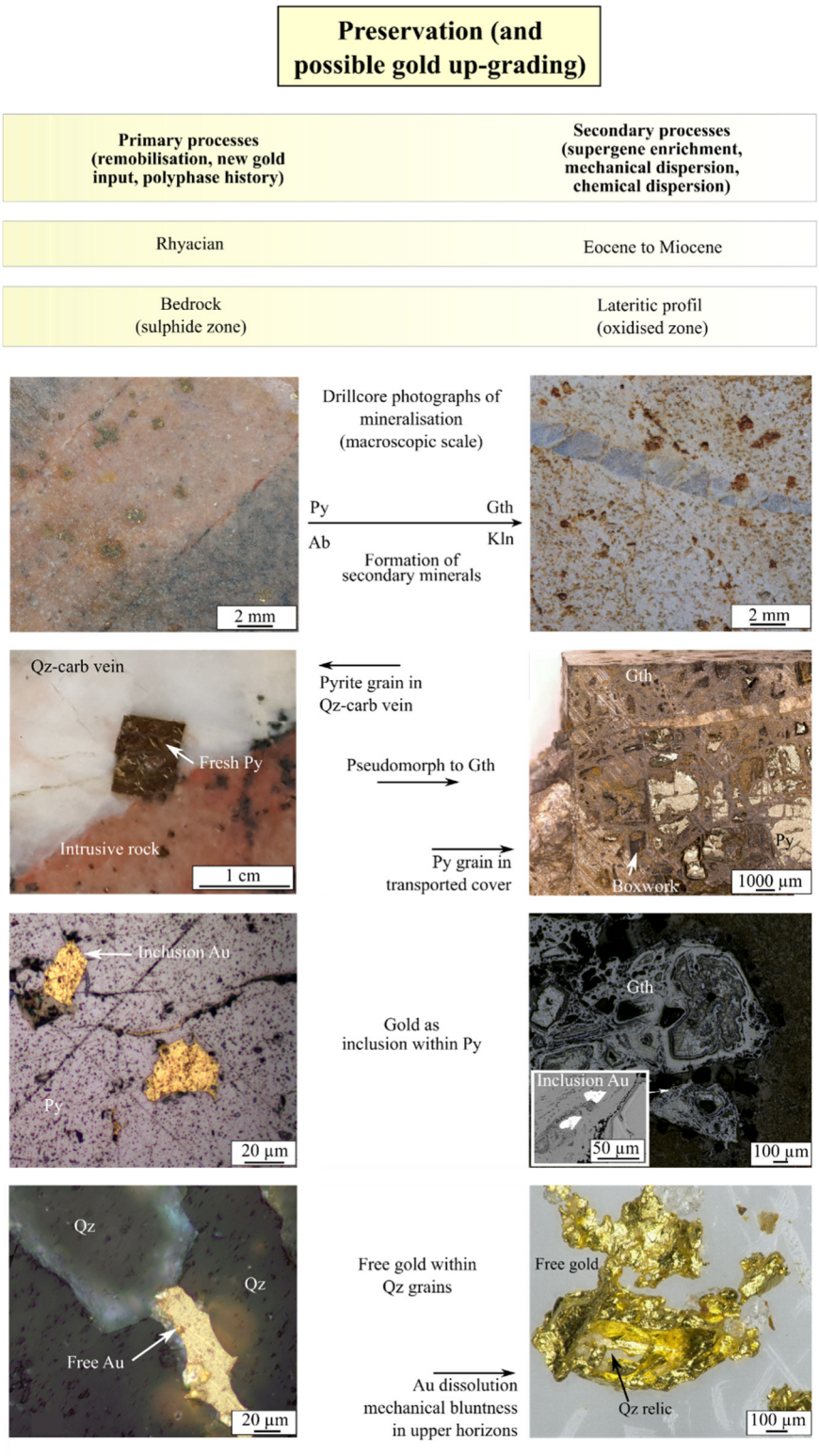

Figure-5-4 Vue d'ensemble des processus primaires et secondaires avec des exemples des deux gisements étudiés (Yaou et Couriège).

Un enrichissement par des processus supergènes n'est pas démontré à Couriège, les teneurs en or en roche totale ne sont pas supérieures au teneurs moyennes des estimations de ressources publiées par les compagnies minières au sein du Bouclier Guyanais (entre 1.3 and 2.3 g/t selon Voicu et al., 2001). Ainsi le gisement de Couriège comme celui de Yaou est préservé lors de la latéritisation avec une faible modification des concentrations en or. La dispersion mécanique avec ces horizons transportés comme sur la zone d'échantillonnage de Lupe est la modification la plus notoire par des processus post-minéralisation, comme en témoigne également les nombreuses occurrences identifiées d'or alluvionnaire. Ces travaux de thèse ont permis une meilleure identification du type de réponse en surface des minéralisations hypogènes dans le cadre de campagne d'exploration en géochimie sol notamment, dans un contexte latéritique avec des horizons tronqués, déplacés et possiblement minéralisés (Fig. 5). Afin de poursuivre ces travaux sur les modalités de l'enrichissement primaire aux processus secondaires, une étude de la minéralisation primaire de Couriège à partir de carottes de forages (si Auplata Mining Group réalise une campagne de forage carottés dans le secteur) serait essentielle. Ceci permettrait de caractériser les phases de déformation et évènements aurifères à l'échelle du prospect mais aussi la typologie de l'or (primaire) et les concentrations hypogènes en éléments associés tel l'argent.

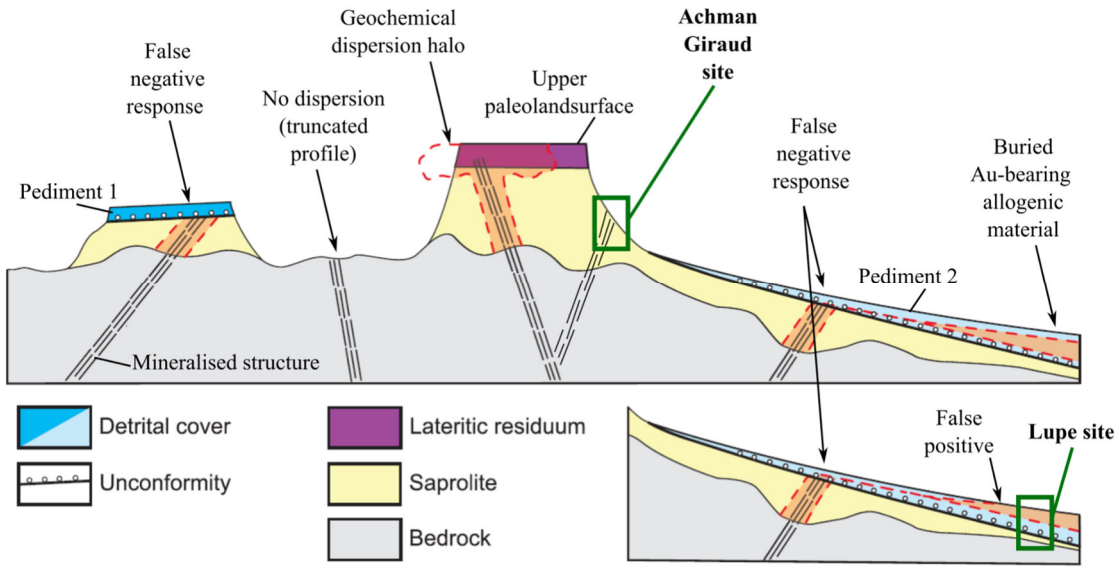

Figure 5-5 Différents types de dispersion et réponses en surface avec intégration des deux sites d'étude (Achman Giraud et Lupe). Modifié après Sawadogo et al. (2020).

Système métallogénique à l'échelle du supercontinent Columbia

Comparé au craton Ouest Africain, la compréhension de la métallogénie aurifère du Bouclier Guyanais en est à un stade précoce. Néanmoins, après les récents travaux de Tedeschi et al. (2019) au Guyana, Guiraud et al. (2020) et cette thèse en Guyane, on observe (1) des architectures lithosphériques similaires et continues entre les deux cratons (Kroonenberg et al., 2016 ; Chardon et al., 2020 et références associées) ainsi que (2) des types de gisements aurifères similaires. Peuvent être cités, des minéralisations aurifères de type VMS *(Volcanogenic Massive Sulphide*) formées dans des bassins d'arrière-arc : Montagne d'Or en Guyane (Guiraud et al., 2020) et Perkoa au Burkina Faso (Schwartz and Melcher, 2003) ; des gisements d'or détritique formés dans des bassins sédimentaires syn-orogéniques : Tarkwa au Ghana (Milesi et al., 1991) et Montagne Tortue en Guyane (Milesi et al., 2003) ; et des gisements d'or orogénique formés pendant la période de collision voire post-collisionnelle : Obuasi au Ghana (Fougerouse et al., 2017) et Yaou en Guyane. Ainsi, tous ces gisements aurifères primaires découverts aussi bien sur le Bouclier Guyanais que Ouest-Africain peuvent alors être vus comme des marqueurs des environnements géodynamiques dans lesquels ils se sont formés ou ont été remobilisés au cours de la période du Rhyacien, respectivement durant les cycles orogéniques Transamazonien et Eburnéen.

Références

Blenkinsop, T. G., Oliver, N.H.S., Dirks, P.G.H.M, Nugus, M. Tripp, G., Sanislav, I., 2020. Structural Geology Applied to the Evaluation of Hydrothermal Gold Deposits. Society of Economic Geologists. Reviews in Economic Geology. 21, 1–23.

Cassard, D., Billa, M., Lambert, A., Picot, J., Husson, Y., Lasserre, J., Delor, C., 2008. Gold predictivity mapping in French Guiana using an expert-guided data-driven approach based on a regional-scale GIS. Ore Geol. Rev. 34. 471-500.

Chardon, D., Bamba, O., Traoré, K., Eburnean deformation pattern of Burkina Faso and the tectonic significance of shear zones in the West African craton, 2020. BSGF-Earth Sci Bull. 191, 2.

Chauvet A., 2019b. Structural Control of Ore Deposits: The Role of Pre-Existing Structures on the Formation of Mineralised Vein Systems. Minerals, 9, 56.

Delor, C., Lahondère, D., Egal, E., Lafon, J.-M., Cocherie, A., Guerrot, C., Rossi, P., Truffert, C., Théveniaut, H., Phillips, D., Avelar, V.G.d., 2003b. 2-3-4 In: Transamazonian crustal growth and reworking as revealed by the 1:500000 scale geological map of French Guiana. Géol Fr. 5–57.

Delor, C., de Roever, E.W.F., Lafon, J.-M., Lahondère, D., Rossi, P., Cocherie, A., Guerrot, C., Potrel, A., 2003a. The Bakhuis ultrahigh-temperature granulite belt (Suriname) : II. Implications for late Transamazonian crustal stretching in a revised. Géol Fr. 2-3- 4, 207–230.

Enjolvy, R., 2008. Processus d'accrétion crustale et régimes thermiques dans le bouclier des Guyanes : signatures géochimiques et thermochronologiques au transamazonien (2250-1950 Ma) : Phd thesis Université Montpellier II-Sciences et Techniques du Languedoc 305 p.

Farah, A. S., 1994. Bilan de l'érosion chimique et mécanique en forêt amazonienne, Exemple du bassin versant de Yaou (Guyane Française), Rapport BRGM, No. R37993, p. 153.

Fougerouse D, Micklethwaite S, Ulrich S, Miller J, Godel B, Adams DT, McCuaig TC., 2017. Evidence for two stages of mineralization in West Africa's largest gold deposit: Obuasi, Ghana. Econ Geol 112: 3–22.

Freyssinet P., 1994. Gold mass balance in lateritic profiles from savanna and rain forest zones. Catena 21, 159-172.

Gibbs, A.K., 1980, Geology of the Barama-Mazaruni Supergroup of Guyana: Unpublished Ph.D. thesis, Cambridge, Harvard University, p. 385.

Gibbs, A.K., Barron, C.N., 1993. The Geology of the Guiana Shield. Oxford University Press, 246.

Goldfarb, R. J., Groves, D. I., and Gardoll, S., 2001, Orogenic gold and geological time: a global synthesis. Ore Geol. Rev. 18, 1–75.

Goldfarb, R., Baker, T., Dubé, B., Groves, D.I., Hart, C.J.R., Gosselin, P., 2005. Distribution, Character, and Genesis of Gold Deposits in Metamorphic Terranes. Econ Geol 100th Anniversary Volume, 407-450.

Groves, D. I., Goldfarb, R. J., Gebre-Mariam, M., Hageman, S. G., and Robert, F., 1998, Orogenic gold deposits: A proposed classification in the context of their crustal distribution and relationship to other deposit types. Ore Geol. Rev.13, 7–27.

Groves, D.I., Santosh, M., Zhang, L., 2020b. A scale-integrated exploration model fororogenic gold deposits based on a mineral system approach. Geosci. Front. 11 (3),719–738

Guiraud, J., Tremblay, A., Jébrak, M., Ross, P-S., Lefrançois, R., 2020. Stratigraphic setting and timing of the Montagne d'Or deposit, a unique Rhyacian Au-rich VMS deposit of the Guiana Shield, French Guiana. Precambr Res. 337, 105551.

Hronsky, J.A., 2019. Deposit-scale structural controls on orogenic gold deposits: an integrated, physical process-based hypothesis and practical targeting implications. Miner. Depos.

Kroonenberg, S.B., de Roever, E.W.F., Fraga, L., Reis, N., Faraco, T., Lafon, J.-M., Cordani, U., Wong, T., 2016. Paleoproterozoic evolution of the Guiana Shield in Suriname: a revised model. Neth. J. Geosci. 95, 491–522.

Lafrance, J., Bardoux, M., Voicu, G., Stevenson, R., Machado, N., 1999. Geological and metallogenic environments of gold deposits of the Guiana Shield: A comparative study between St-Elie (French Guiana) and Omai (Guyana). Explor. Min. Geol. 8, 117–135.

Large, R.R., Danyushevsky, L.V., Hollit, C., Maslennikov, V., Meffre, S., Gilbert, S., Bull, S., Scott, R., Emsbo, P., Thomas, H., and Foster, J., 2009, Gold and trace element zonation in pyrite using a laser imaging technique: Implications for the timing of gold in orogenic and Carlin-style sediment hosted deposits. Econ Geol. 104, 635−668.

Large, R.R., Bull, S.W., and Maslennikov, V.V., 2011, A carbonaceous sedimentary source-rock model for Carlin-type and orogenic gold deposits. Econ Geol. 106 (3), 331–358.

Lasserre J.L., Ledru P., Manier E., Mercier D., 1989. Le Protérozoïque de Guyane. Révision lithostructurale. Implications pour la formation détritique Orapu et la gîtologie de l'or. Rapport BRGM 89 GUF023, 52 p.

Ledru P., Lasserre J.L., Manier E., Mercier D., 1991. Révision de la lithologie du Paléoprotérozoïque du craton guyanais. Tectonique transcurrente et dynamique des bassins sédimentaires. Bull. Soc. Geol. Fr., 162(4), 627-636.

Lerouge, C., Milési, J.-P., Fouillac, A.M., 1999. The Paleoproterozoic Dorlin gold deposit French Guiana: genetic constraints of the stable isotope geochemistry. Chem. Geol. 155, 131–149.

McCuaig, T.C., Hronsky, J.M.A., 2014. The Mineral System Concept: the Key to Exploration Targeting. Building Exploration Capability for the 21st Century. 153–175.

Milesi, J., Ledru, P., Ankrah, P., Johan, V., Marcoux, E., Vinchon, Ch., 1991. The metallogenic relationship between Birimian and Tarkwaian gold deposits in Ghana. Miner. Depos. 26. 228-238.

Milesi, J., Lerouge C, Delór C, Ledru P, Billa M, Cocherie A, Egal E, Fouillac A, Lahondère D, Lasserre J, Marot A, Martel-Jantin B, Rossi P, Tegyey M, Théveniault H, Thiéblemont D, Vanderhaeghe, O., 2003. Gold deposits (gold-bearing tourmalinites, gold-bearing conglomerates, and mesothermal lodes), markers of the geological evolution of French Guiana: geology, metallogeny, and stable isotope constraints. Géol Fr, 2-3-4:257-290.

Padoan, M., Rossetti, P., Rubatto, D., 2014. The Choco 10 gold deposit (El Callao, Bolivar State, Venezuela): petrography, geochemistry and U-Pb geochronology. Precambr. Res. 252, 22–38.

Patten; C.G.C., Pitcairn, I.K, Molnár, F., Kolb, J., Beaudoin, G., Guilmette, C., Peillod. A., 2020. Gold mobilization during metamorphic devolatilization of Archean and Paleoproterozoic metavolcanic rocks. Geology. https://doi.org/10.1130/G47658.1

Pitcairn, I., Teagle, D.A.H., Craw, D., Olivo, G.R., Kerrich, R. and Brewer, T.S., 2006. Sources of metals and fluids in orogenic gold deposits: insights from the Otago and Alpine schists, New Zealand. Econ Geol. 101 (8), 1525-1546.

Phillips, G. N., Groves, D. I., 1983. The nature of Archaean gold-bearing fluids as deduced from gold deposits of Western Australia. J Geol Soc Aust. 30:1-2, 25-39,

Phillips, G.N., and Powell R., 2010, Formation of gold deposits: a metamorphic devolatization model. J Metam Geol. 28, 689–718.

Sawadogo, B., Bamba, O., Chardon, D., 2020. Landform-regolith mapping in the West African context. Ore Geol. Rev. 126, 103782.

Schwartz, MO., Melcher, F., 2003. The Perkoa zinc deposit, Burkina Faso. Econ Geol 98:1463-1485

Tedeschi, M., Hagemann, S.G., Davis, J., 2018. The Karouni Gold Deposit, Guyana, South America: part I. Stratigraphic Setting and Structural Controls on Mineralization. Econ Geol. 113, 1679–1704.

Tedeschi, M., Hagemann, S.G., Roberts, M.P. and Evans, N.J., 2018b. The Karouni Gold Deposit, Guyana, South America: Part II. Hydrothermal Alteration and Mineralization. Econ Geol. 113(8), 1705-1732.

Tedeschi, M. T., Hagemann, S. G., Kemp, A. I. S., Kirkland, C. L., Ireland, T. R., 2019. Geochronological constrains on the timing of magmatism, deformation and mineralization at the Karouni orogenic gold deposit: Guyana, South America. Precambr. Res. 105329.

Vanderhaeghe, O., Ledru, P., Thiéblemont, D., Egal, E., Cocherie, A., Tegyey, M., Milesi, JP., 1998. Contrasting mechanism of crustal growth: Geodynamic evolution of the Paleoproterozoic granite–greenstone belts of French Guiana. Precambrian Res 92:165–193.

Vianna, Sâ. Queiroz., Lafon, J.M., Milhomem Neto, J., Balieiro Silva, D.P., Eduardo de Mesquita Barros, C., 2020. U–Pb geochronology, Nd–Hf isotopes, and geochemistry of Rhyacian granitoids from the Paleoproterozoic Lourenço domain (Brazil), southeastern Guiana Shield. J South Am Earth Sci. 104, 102937.

Voicu, G., Bardoux, and M., Stevenson, R., 2001, Lithostratigraphy, geochronology and gold metallogeny in the northern Guiana Shield, South America: a review: Ore Geol. Rev. 18, 211–236.

Wyborn, L.A.I., Heinrich, C.A., Jaques, A.L., 1994. Australian Proterozoic Mineral Systems: Essential Ingredients and Mappable Criteria. Australasian Institute of Mining and Metallurgy Annual Conference, Melbourne, 109–115.

Wyman, D.A., Cassidy, K.F., Hollings, P., 2016. Orogenic gold and the mineral systems approach: resolving fact, fiction and fantasy. Ore Geol. Rev. 78, 322–335.

Résumé : Les minéralisations aurifères situées en Guyane (France, Amérique du Sud) sont localisées au sein de terrains d'âge rhyacien (2.3-2.05 Ga), témoins de l'orogenèse transamazonienne. Ces gisements du Bouclier Guyanais sont masqués par une forêt dense sous laquelle des profils latéritiques bien développés laissent peu d'affleurement de roche non altérée (« *bedrock* »). Considérant ce contexte spécifique, cette thèse s'intéresse à définir (i) quels sont les processus de minéralisation d'or primaire et (ii) quel est leur préservation et enrichissement (ou non) au cours des processus supergènes secondaires et se base sur deux sites d'étude : le gisement de Yaou et le prospect de Couriège. L'approche scientifique retenue pour ces travaux de thèse est celle du système métallogénique qui nécessite une intégration dans le temps, dans l'espace et à différentes échelles des processus géologiques et métallogéniques. Ainsi, cette thèse intègre différentes disciplines des géosciences à savoir la géologie structurale (et microstructurale), la métallographie, la pétrographie, la géochimie, la géochronologie et la géophysique pour étudier la formation de ces objets minéralisés (primaires et secondaires), caractériser leur typologie et discuter des processus métallogéniques associés.

À Yaou, des corps intrusifs (quartz monzodiorite), encaissant principalement la minéralisation aurifère, sont alignés le long d'une zone de cisaillement à cinématique sénestre affectant un ensemble volcano-sédimentaire. Une évolution tectono-magmatique polyphasée, impliquant 5 phases de déformation, est proposée à l'échelle du camp minéralisé. Sont associés à cette séquence de déformation, deux événements aurifères (contrôlés pendant les phases D_{3YA} et D_{4YA} datée à 2105±25 Ma (Re-Os sur pyrite aurifère)) qui contrôlent le budget aurifère global du gisement. Cette étude confirme que des gisements d'or orogéniques peuvent être formés par remobilisation et/ou nouveaux apports d'or lors de multiples événements de déformation et de d'hydrothermalisme. L'intrusion porteuse de la minéralisation est datée à 2130,6±5,8 Ma (U-Pb sur zircon). Une intégration à l'échelle du district est proposée où la mise en place de l'intrusion correspond à la transition entre les phases régionales D_1 et D_{2a}. Le modèle litho-structural défini à l'échelle du camp et du district montre que les minéralisations hébergées par des intrusions de type Yaou peuvent ainsi être ciblées le long de grands couloirs de cisaillement à l'échelle du district. Cette approche 4D associant géologie, géophysique et géochronologie relative/absolue aide à la prédiction de nouvelles cibles minéralisées jusqu'alors non reconnues dans la branche Sud de la ceinture de roche verte du Paramaca. Elle considère l'ensemble du système métallogénique d'or orogénique comprenant une architecture lithosphérique propice, un cadre géodynamique favorable, une fertilité géochimique en éléments sidérophiles et une préservation post-minéralisation.

Les modalités des processus supergènes sont étudiées dans le prospect de Couriège, qui comportent plusieurs indices aurifères associés soit à des veines de quartz riches en pyrite au sein de profils latéritiques en place, soit à des colluvions et alluvions. Deux profils latéritiques ont été étudiés pour évaluer le rôle des processus supergènes dans la modification des minéralisations primaires (hypogènes). Le profil du site d'Achman Giraud est caractérisé par un profil d'altération authigénique développé sur un protolithe d'amphibolite avec des veines de quartz aurifères. La dispersion verticale et latérale de l'or peu importante, le caractère principalement primaire des grains d'or et les preuves limitées de reprécipitation de l'or supergène, plaident en faveur d'une faible remobilisation supergène sans preuve évidente d'enrichissement au cours de la latéritisation. Le profil du site de Lupe expose un horizon colluvionnaire aurifère tronquant un profil latéritique stérile. L'or est présent sous forme d'inclusions d'électrum dans des cristaux de pyrite détritiques centimétriques partiellement goethitisés et sous forme de grains d'or libres qui présentent une forme subarrondie, des marques de transport mécanique et des bordures appauvries en Ag, suggérant un transport significatif ainsi qu'une altération supergène. Ces observations remettent en question l'évaluation du caractère proximal à distal de la source de cet or allogénique.

Abstract : Gold deposits located in French Guiana (France, South America) within Rhyacian terranes (2.3-2.05 Ga), are the witnesses of the Trans-Amazonian orogeny. These deposits, in the Guiana Shield, are covered by a dense rainforest where well-developed lateritic profiles leave little outcrop of unaltered bedrock. Considering this specific context, this thesis is interested in defining (i) what are the primary gold mineralisation processes and (ii) what is their preservation and enrichment (or not) during secondary supergene processes, and is based on two case studies: the Yaou deposit and the Couriège prospect. The scientific approach adopted for this work follow the mineral system concept, which requires integration in time, space and at different scales of geological and metallogenic processes. Thus, this thesis integrates different disciplines of geosciences namely structural geology (and microstructural), metallography, petrography, geochemistry, geochronology and geophysics in order to study the formation of these mineralised (hypogene and supergene) objects, characterise their typology and discuss the associated metallogenic processes.

At Yaou, intrusive bodies (quartz monzodiorite), mainly hosting gold mineralisation, are aligned along a sinistral shear zone affecting a volcano-sedimentary sequence. A polyphase tectono-magmatic evolution, of 5 deformation phases, is proposed at the scale of the mineralized camp. Associated with this deformation framework are two gold events (controlled during phases D_{3YA} and D_{4YA} dated at 2105±25 Ma (Re-Os on Au-bearing pyrite)) which control the overall gold budget of the deposit. This study confirms that orogenic gold deposits can be formed by remobilisation and/or new gold inputs during multiple deformation phases, veining and hydrothermal events. The intrusion hosting the mineralisation is dated at 2130.6±5.8 Ma (U-Pb on zircon). An integration at the district-scale is proposed where the emplacement of the intrusion is at the transition between the regional phases D_1 and D_{2a}. The litho-structural model defined at the camp- and district-scale shows that mineralisation hosted by Yaou-type intrusions can thus be targeted along shear zones within the Yaou district. This 4D approach combining geology, geophysics and relative/absolute geochronology helps to define new targets previously unrecognised in the Southern Paramaca greenstone belt. It considers the whole orogenic gold mineral system encompassing a favourable lithospheric architecture, a favourable geodynamic framework, a geochemical fertility in siderophile elements and a post-mineralisation preservation.

The modalities of supergene processes are studied at the Couriège prospect, which includes several gold occurrences associated either with pyrite-rich quartz veins within in situ lateritic profiles, or with colluvial and alluvial horizons. Two profiles were studied to assess the role of supergene processes in the modification of primary (hypogene) mineralisation. The Achman Giraud site is characterised by an authigenic alteration profile developed on an amphibolite protolith with gold-bearing quartz veins. The weak vertical and lateral dispersion of gold, the predominantly primary character of the gold grains, and the limited evidence of supergene gold reprecipitation, argue for minor supergene remobilisation without clear evidence for gold enrichment during lateritisation. The Lupe site exposes a gold-bearing detrital horizon truncating a barren lateritic profile. Gold is present as electrum inclusions in partially goethitised detrital pyrite crystals and as free gold grains exhibiting a sub-rounded shape, mechanical transport marks and Ag-depleted rim, suggesting transport and exposure to weathering over significant distance and time, respectively. These observations question the evaluation of the proximal to distal character of transported gold.

UNIVERSITÉ DE LORRAINE | SIReNa